Summer 8-15-2015

Optimal Battery Operations and Design Considering Capacity Fade Mechanisms

Bharatkumar Suthar
Washington University in St. Louis

WASHINGTON UNIVERSITY IN ST. LOUIS

School of Engineering & Applied Science
Department of Energy, Environmental, and Chemical Engineering

Dissertation Examination Committee:
Venkat R. Subramanian, Co-Chair
Pratim Biswas, Co-Chair
Richard D. Braatz
Milorad P. Duduković
Hiro Mukai
Palghat Ramachandran
Shriram Santhanagopalan

Optimal Battery Operations and Design Considering Capacity Fade Mechanisms

by
BharatKumar Suthar

A dissertation presented to the
Graduate School of Arts & Sciences
of Washington University in
partial fulfillment of the
requirements for the degree
of Doctor of Philosophy

August 2015
St. Louis, Missouri

Table of Contents

List of Figures

List of Tables

Acknowledgments

First and foremost, I would like to express my sincere gratitude to my advisor, Professor Venkat R. Subramanian, for his advice, encouragement, and constructive criticism. I would like to thank him for giving me an opportunity to be a part of MAPLE research group. I have received guidance from him on a verity of projects, both related to my thesis as well as several others under the broader scope of multi-scale systems. I have gained invaluable experience working under his supervision. I am especially thankful to him for pushing me to be more productive during my doctoral studies and working with me on the problems.

I also wish to express my deep sense of gratitude to Professor Pratim Biswas for having faith in me and giving me an opportunity to be a part of McDonnell International Scholar Academy. I would also like to thank him for making us feel like a part of AAQRL group during the final year of my stay at Washington University. I would like to thank Professor Palghat Ramachandran for his guidance on transport phenomena, and Professor Milorad P. Duduković for teaching us reaction engineering principles through one of the best (read toughest) coursework I have ever come across.

I would like to thank Professor Hiro Mukai and Dr. Shriram Santhanagopalan for their valuable comments, and critical suggestions throughout the period of my Doctoral work. I would like to thank Professor Richard D. Braatz, at MIT for his continuous guidance in the field of optimization and multi-scale simulation. I feel privileged for the timely support I received from the committee members despite their extremely busy schedule.

I wish to gratefully acknowledge the financial support from McDonnell International Scholar Academy at Washington University in St. Louis, and the United States Government, Advanced Research Projects Agency-Energy (ARPA-E), U.S. Department of Energy, award number DE-

AR0000275. I am thankful to Chancellor Mark S. Wrighton for the unique initiative of McDonnell International Scholar Academy, which provided me with invaluable experience with international exposure and leadership qualities. I would like to thank Professor Pratim Biswas, Professor James Wertsch, and Professor Henry Biggs along with the McDonnell International Scholar Academy staff: Kristine Williams, Angie Rahaman and Carla Koberna for their help and support. My sincere thanks to all the administrative and IT staff in the Department of Energy, Environmental and Chemical Engineering: Rose, Kim, Jim, Tim, Beth, Lesley, Trisha, and Lynn for helping us with our stupid and incessant question, and making my life much easier during my stay at Washington University.

And now MAPLE lab, I feel fortunate that I had the most helpful seniors in EECE department: Dr. Venkat R., Dr. Paul, and Dr. Sumitava. As my research work is based on Paul and Venkat R's work on reformulation and optimization, standing on the shoulders of GIANTS would be both literally and metaphorically true. I would take this opportunity to thank both of them for their constant encouragement and guidance. Venkat R. is one of the most helpful persons on earth, he always knows the best/quickest/smartest way to solve any problem. I still regret buying a phone without his consultation. Sumitava is truly a people's person; it is amazing the number of people he can remember and keep track. I am thankful to him for his guidance in my postdoc applications. I am also grateful to Dr. Paul and Matt for explaining the American culture in significant details and tolerating (and defending) my idiosyncrasies (such as using excessive black pepper in my food). Matt shared an office with me for four years with whom I enjoyed many constructive discussions; I thank him for it. I would also like to thank Dr. Thiagu, Dr. Dayaram, Pierre, Manan, Seongbeom, Nathan for their support.

I would like to thank my fellow graduate student for making this a memorable experience. Now coming to the '*Padhai ka Mandir*', (aka temple of study, our home in Saint Louis), I am fortunate to have Akshay and Onkar as my roomies. Onkar is a gem of a person. You should know you have issues in your life if you start having problems with a guy like Onkar. I am thankful to Akshay and Onkar for trying their best to push me for having a driving license, although both failed miserably. I will miss the marathon chats sessions with Akshay on *Joey Chairs* leading to very weird arguments which are won by proving oneself poorer with a rural background.

I take this opportunity to express my gratitude to Professor Ravindra Gudi, Professor Santosh Noronha, and Professor Sachin Patwardhan, at IITB for motivating me to pursue Ph.D. I am very thankful to Dr. S. B. Pandey for his guidance, and making me understand the importance of higher education.

Finally, I would like to thank my parents and brothers, who never hesitated in giving me the support and encouragement. I owe them more than I can try to payback. Their calls were a motivation for me to move forward. As I thank them for continued bearing with my problems and being good listeners, I ask for their forgiveness for not being there and available when needed. To them, I owe all my accomplishment.

BharatKumar Suthar

Washington University in St. Louis

August 2015

Dedicated to my family

ABSTRACT OF THE DISSERTATION

Optimal Battery Operations and Design Considering Capacity Fade Mechanisms

by

BharatKumar Suthar

Doctor of Philosophy in Energy, Environmental, and Chemical Engineering

Washington University in St. Louis, 2015

Professors Pratim Biswas & Venkat R. Subramanian, Co-Chairs

Safely and capacity fade are the key issues that restrict the use of the lithium-ion battery for many applications. These issues are being tackled in a variety of ways. This dissertation focuses on using detailed continuum-level electrochemical models to study transport, kinetics, and mechanical processes in the lithium-ion batteries. These models can be used to quantify the effect of capacity fade mechanisms (side reactions and mechanical degradation) and improve the safety aspects of the lithium ion batteries. Three capacity-fade mechanisms—solid electrolyte interface side reaction, lithium-plating side reaction and mechanical degradation due to intercalation-induced stresses—are considered in the dissertation. Monitoring and control of plating side reaction is also very critical for battery safety.

Two main focus areas of the dissertation are:

1) Optimal battery operation (design of charging/discharging protocols) considering three capacity fade mechanisms mentioned previously along with safety issues
2) Rational battery design (choice of porosity, thicknesses of electrodes, etc.) considering discharge capacity and capacity fade mechanisms

Chapter 1

Introduction

> The fuel cell is just a fundamentally inferior way of delivering electrical energy to an electric motor than batteries.
>
> **Elon Musk**

Energy is critical to sustain life. Demand for energy is constantly on the rise, increasing the carbon footprint of fossil fuels. The implications of global climate change have motivated and accelerated research in renewable sources of energy. Most of the renewable sources of energy are intermittent in nature (e.g. solar, wind energy, etc.), which limits their penetration in the grid power supply and also their reliability for many other applications. This challenge can be addressed by using cheap energy storage technologies, where electrochemical energy storage can be of significant importance. On the other hand, innovation and breakthroughs in electrochemical energy storage technologies will significantly affect many applications such as electrification of cars, reliability of mobile electronics, etc.

1.1 Electrochemical Energy Storage

Electrical energy storage (EES) technologies can be divided into four broad categories based on power and energy densities: capacitors, electrochemical double layer capacitors (EDLC), batteries, and fuel cells. A qualitative picture of EES systems is presented in Figure 1-1. Electrical capacitors, which offer high power density and long life, find limited use in applications which require higher energy densities. EDLC have lower power densities as they have narrower voltage window and additional transport resistances compared to capacitors. Both, in capacitors and EDLC, the energy is stored in an electric field, but EDLC have higher energy density they take the advantage offered

by high surface area of the nanomaterials (e.g. graphene). EDLC involve non-faradic surface storage where no electron transfer occurs, and opposite charges cling to each other without crossing the interface. Batteries, on the other hand, stores energy in the bulk of the materials. In capacitors and EDLC, charges are restricted to surfaces causing smaller energy density compared to batteries which utilize the bulk of the material. The non-faradic nature of the storage mechanism in an EDLC makes them highly reversible (~10,000 cycles) compared to batteries (~1000 cycles). Batteries involve faradic reactions where charge transfer kinetics plays a major role. In intercalation batteries (e.g. lithium-ion battery), the charge is stored in the bulk of the material, hence they offer high energy density. The bulk of the intercalation batteries is accessible only by diffusion transport, which offers additional resistance to the kinetic resistance. These additional resistances (diffusion and kinetic resistances) reduce the power density of intercalation batteries compared to EDLC. For applications where high energy capacity is required, flow batteries and fuel cells can be used. Flow batteries store energy in the electrolyte with electroactive materials held externally (in tanks) and get introduced in the system depending on the demand for electricity.

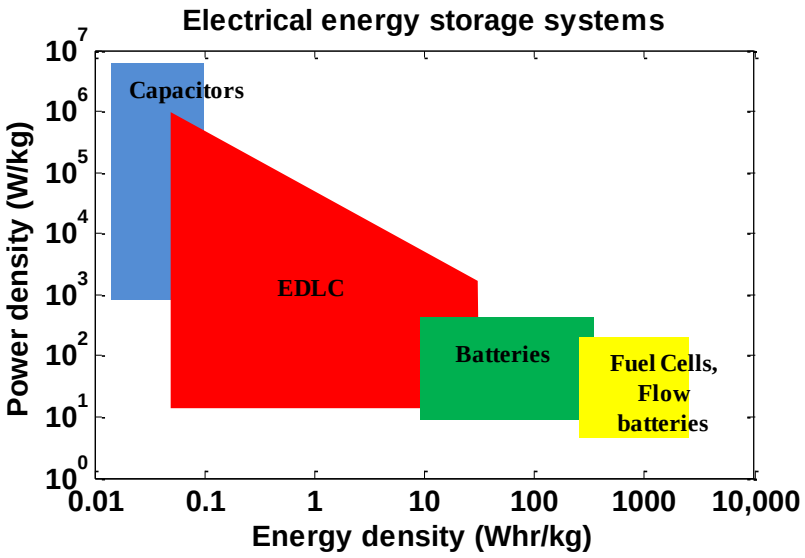

Figure 1-1: Power and energy density of electrical energy storage systems, (figure adapted from Nguyen and Savinell.[1] Reproduced by permission of The Electrochemical Society)

Progress in nano-engineered materials has enabled batteries with high energy and high power density. Though batteries and EDLC have distinct mechanisms of storing energy, the line between batteries and supercapacitors (EDLC) is blurred at nano-scale as both mechanisms contribute significantly to the energy storage. Simon *et al.*[2] have presented a clear picture of intercalation and capacitance storage phenomena in the article titled "*Where Do Batteries End and Supercapacitors Begin?"*

1.2 Comparison of Rechargeable Battery Technologies

Lithium-ion chemistries are attractive for many applications due to the high cell voltage, high volumetric and gravimetric energy density (100 Wh/kg), high power density (300 W/kg), good temperature range, low memory effect, and relatively long battery life compared to other rechargeable battery technologies.[3] A comparison of various rechargeable batteries is shown in Figure 1-2 with the focus on future goals to address the challenges of the transportation sector.

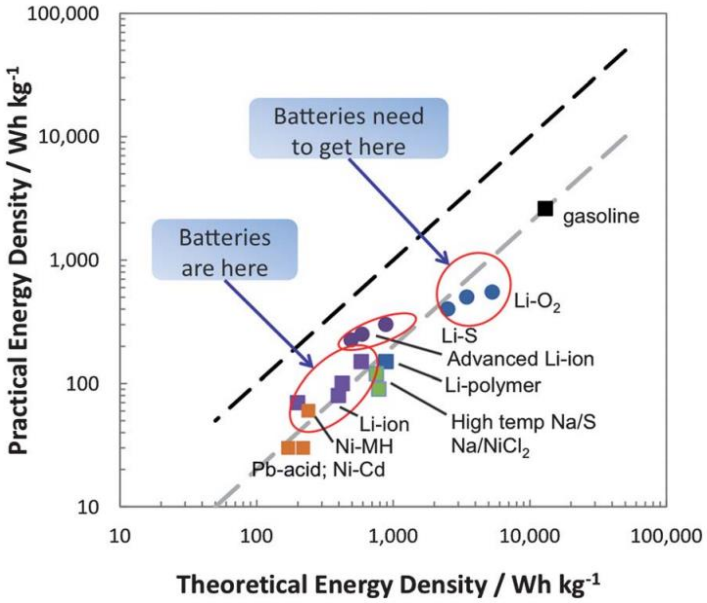

Figure 1-2: Theoretical specific energy of various rechargeable battery systems compared to their practical specific energies and the energy density requirement for transportation (figure reproduced by the permission of The Royal Society of Chemistry (RSC), 2012 from Thackeray *et al.*[4])

Compared to the conventional rechargeable batteries such as lead-acid (Pb-acid), nickel-metal hydride (Ni-MH) and nickel-cadmium (Ni-Cd), lithium-ion batteries have higher energy density but are more expensive.

1.3 Working Principle of the Lithium-ion Battery

In a lithium-ion battery, energy is stored by converting electrical energy into chemical energy (specifically, by storing lithium in host materials). Solid materials which can host the guest lithium in their interstitial spaces are called insertion materials. Lithium stored in some host materials (e.g. graphite) have more energy compared to other host materials (e.g. $LiMnO_2$). While discharging, lithium moves from a high energy configuration to a low energy configuration. This spontaneous movement of lithium produces useful work. These materials are engineered to react with lithium ions reversibly which is essential for rechargeable batteries. Winter *et al.*[5] describe the electro-insertion process (which includes intercalation as a special case) as follows:

> "The term electroinsertion refers to a host/guest solid-state redox reaction involving electrochemical charge transfer coupled with insertion of mobile guest ions from an electrolyte into the structure of a solid host, which is a mixed electronic and ionic conductor. The major structural features of the host are kept after the insertion of the guests."[5]

Lithium-ion battery is also known as *rocking chair*, *swing*, and *shuttlecock* battery as lithium moves between the anode and the cathode while charging and discharging (Figure 1-3). Lithium ions can easily be inserted in the interstitial spaces of the solid host due to its small size. During discharge, lithium deintercalates from the anode by giving up an electron and converting into a lithium ion. At the other end, the lithium ion accepts an electron and intercalates in the cathode as lithium. Depending on the insertion materials, lithium can exist as neutral lithium or a lithium ion and an electron pair where the electron may reside with the host elements. The electrolyte—typically consists of ethylene carbonate (EC), dimethyl carbonate (DMC), propylene carbonate

(PC) with lithium salt—facilitates the transportation of lithium ions between the anode and the cathode. The entire process, including electrochemical reactions, diffusion in the electrode materials, and diffusion in the electrolyte needs to be highly reversible for a good cycle life (1,000 to 10,000 cycles). Even 99% reversibility per cycle is very bad for practical use of batteries.

As progress in materials for the lithium-ion batteries has progressed, various intercalation pathways have been observed for different materials. Lithium can be stored in host materials using different (or combinations of) mechanisms at different intercalation levels. From Figure 1-4, it is clear that the intercalation process is a complicated phenomenon as the materials can go through various types of transformations. Some materials may go through homogeneous insertion, where lithium is distributed in the solid matrix of the host uniformly, while others may undergo heterogeneous insertion where the host material will phase separate into a lithium-rich phase and a lithium-poor phase. For example, $LiFePO_4$ is one material of great technological importance which is being investigated extensively for its strong phase separation behavior and its dependence on particle size.[6,7]

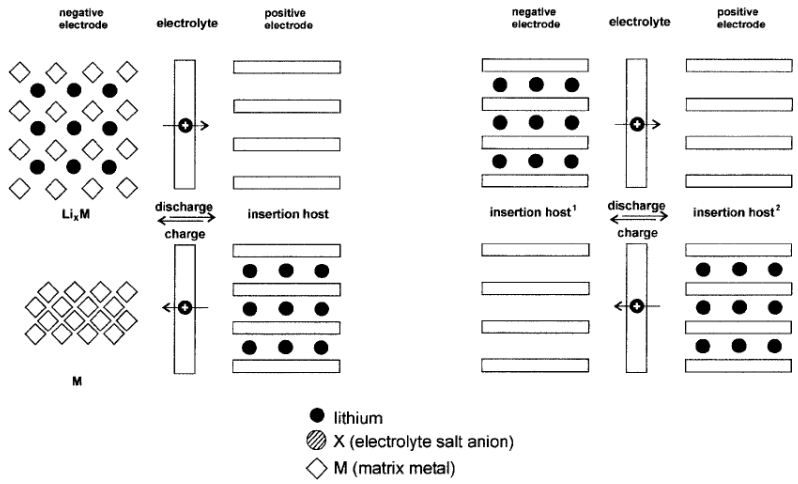

Figure 1-3: Basic working of the lithium-ion battery, Left: Negative electrode: dimensionally unstable insertion host (Li alloy, Li_xM); positive electrode: dimensionally stable insertion host. Right: Both negative and positive electrodes are dimensionally stable insertion hosts (Figure reproduced with permission from Winter *et al.*,[5] Copyright 1998, Wiley)

Flux expressions based on Fick's law can model homogeneous insertion (and to some extent alloying) reasonably well, but may find limited applicability for other pathways such as heterogeneous intercalation ($LiFePO_4$), conversion (lithium intercalation in Fe_3O_4), etc. Intercalation of lithium ion in tin and silicon can be categorized as alloying. While these materials give large capacity ($Li_{4.4}Sn$), they suffer from high volume expansion (300–400%). For accurate modeling of intercalation in such materials, a moving boundary formulation is required. In 'conversion' process, the transition metal is completely reduced to its metallic state creating nanoparticles (e.g. Fe_3O_4 gives metallic Fe nanoparticles) embedded in a Li_2O matrix (Figure 1-4). Material dependent thermodynamic approach is necessary in order to model the behavior of the electrode materials accurately. It should be noted here that for nanomaterials, surface storage can also contribute significantly as compared to intercalation capacity (such behavior is observed in anatase TiO_2 nanoparticles[8]), which makes the differentiation between electrochemical capacitors and batteries difficult.[2]

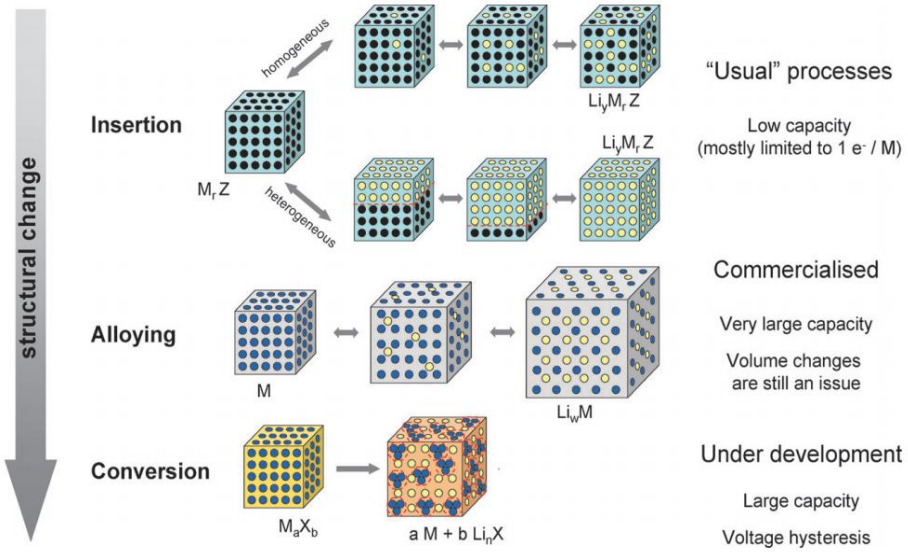

Figure 1-4: Different pathways to host lithium in host matrix, Black circles: voids in the crystal structure, blue circles: metal, yellow circles: lithium. (figure reproduced by the permission of The Royal Society of Chemistry (RSC), 2009 from Palacin[9])

Figure 1-5 shows the schematic of lithium ion battery with three sections: anode, separator and cathode. Cathode and anode are porous structures made up of small particles to increase the surface area for reaction and reduce the diffusion resistance of solid particles. The electrolyte is present in all three regions and helps in facilitatating the transport of lithium ions.

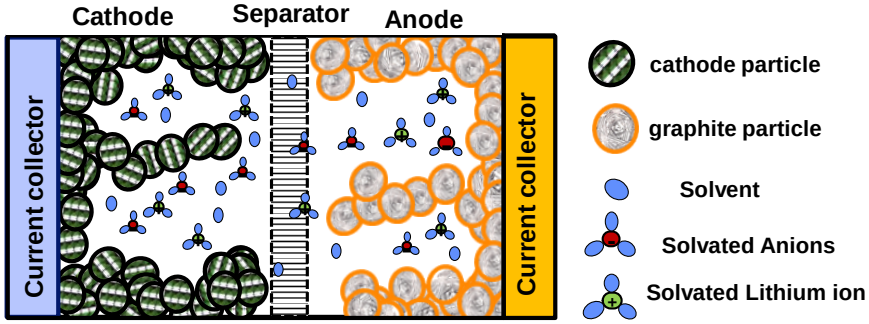

Figure 1-5: Schematic of a porous electrode lithium-ion battery cell sandwich

1.4 Materials for the Lithium-ion Battery

Figure 1-6 shows the electrode materials that are actively being considered for next generation lithium-ion battery technology. Ideally, one would like to have a large difference in potential between the anode and cathode so as to make a battery that offers high voltage. Charging and discharging an array of cells (in series and parallel configuration) requires a cell balancing/equalizing system for efficient and uniform use. Having large voltage difference per cell is advantageous as it reduces the number of cells to be used to produce the desired power output. Hence system level losses are reduced. Finding electrolytes that work well in large voltage window can be a challenge. Figure 1-6 shows voltage and energy densities associated with cathode and anode materials, which correspond to their thermodynamic limits. The voltage obtained during finite rate of discharging will always be smaller than the thermodynamic voltage due to ohmic, diffusion (both in solid phase and electrolyte phase) and kinetic losses inside the battery.

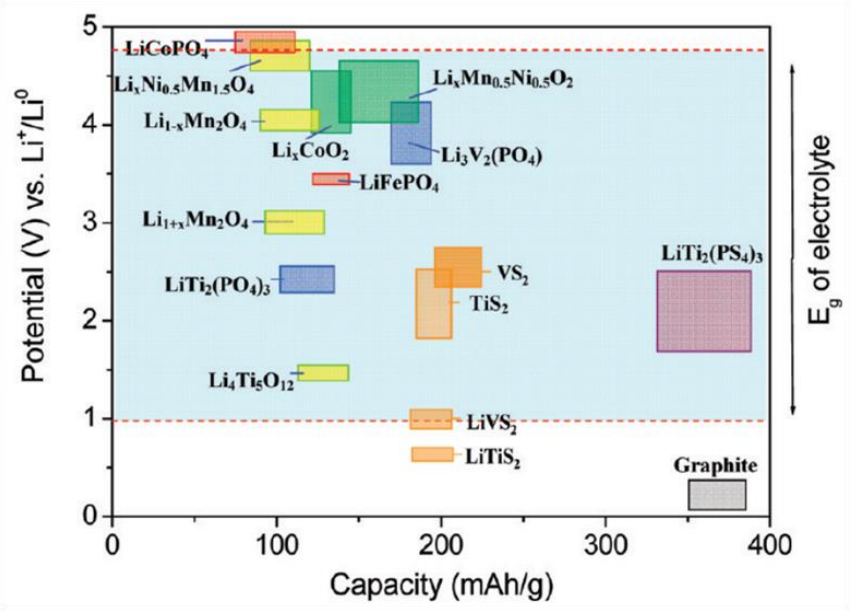

Figure 1-6: Potential versus charge capacity of electrode materials for the lithium-ion battery relative to thermodynamic window of stability of the electrolyte (Eg of electrolyte, explained later in this chapter) 1 M $LiPF_6$ in EC/DEC (1:1). (Figure reproduced with permission from Goodenough and Kim,[10] Copyright 2010 American Chemical Society.)

The four components of a battery: anode, cathode, separator, and electrolyte are discussed briefly in the next section.

1.4.1 Anode

The use of lithium metal as an anode material is desired for two reasons: 1) wide electrochemical potential window and 2) high gravimetric and volumetric energy density. However, deposition (and dissolution) of lithium ions on (and from) the lithium anode is usually not uniform, which create safety issues. Dendrite structures are also formed during deposition of lithium ions on lithium foil,[11] which can puncture the separator and potentially cause short circuits (see Figure 1-7). Due to safety concerns associated with dendrite formation, lithium metal is not used for rechargeable batteries. Insertion materials, like graphite, provide an excellent alternative to lithium metal anode from a safety and cyclability point of view with small compromises on the cell voltage, specific charge, and rate capability.[5,12] Though, graphite is preferred compared to lithium

metal as the former stores lithium in its interstitial spaces between graphite planes, it also suffers from plating side reaction (deposition of lithium in metallic form on the surface of anode particle). The slightly more positive potential of lithiated graphite (LiC_6) compared to Li metal, inherits the problem of lithium plating during charging[11] at high rates and even at low rates if the temperature is low (0.2 C at $-20\,^{\circ}C$).[13,14] Alternative materials to graphite such as TiO_2 and SnO_2 are actively being investigated and improved upon, as they are much less vulnerable to plating reactions.[15]

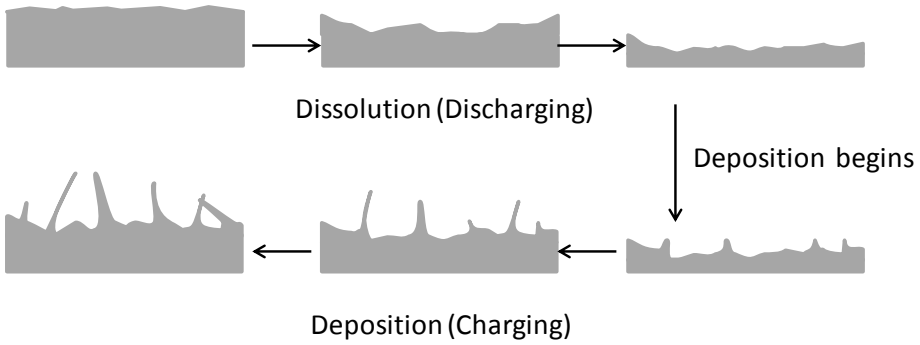

Figure 1-7: Dendrite formation on lithium metal which makes the lithium-metal batteries unsafe (figure adapted from Xu,[16] Copyright 2004 American Chemical Society)

Graphite and its disordered forms are most commonly used as anode materials for the lithium-ion batteries. Carbon black is one of the most common carbonaceous anode materials for lithium ion batteries. Carbon black is a form of paracrystalline carbon.[17] Paracrystalline structures have short to medium range of ordering in their lattice. Figure 1-8 (left) shows the ordering of a layered structure in a carbon black particle. Different manufacturing methods are employed to produce variants of carbon black (channel black, furnace black, lamp black, thermal black and acetylene black). Figure 1-8 (right) shows a model of a cutaway of a single carbon black particle. The ordering is prominent at the outer layer of the particle, but the ordering is diminished in the center.[17] The ordering of these synthetic materials can be improved by heat treatment. The transport properties such as the diffusivity of lithium and the initial capacity loss due to the formation of an inert layer surrounding the particle (solid electrolyte interface (SEI) layer) are

strongly affected by the heat treatment of these materials Particles in which the ordering of the lattice is not very strong can be modeled using Fick's law assuming homogeneous insertion (see Figure 1-1).

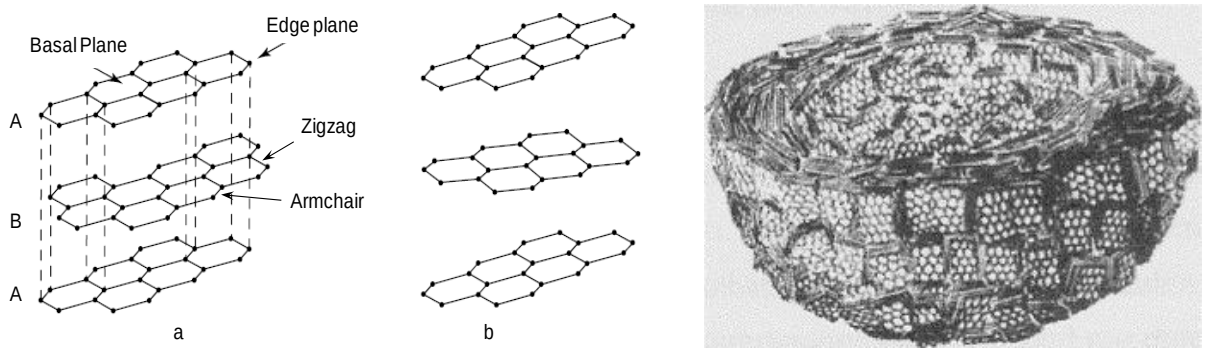

Figure 1-8: Left: Crystalline (a) and amorphous (b) graphite based carbonaceous material and Right: Model showing cutaway of single carbon black particle (Image reproduced with permission from Wissler *et al.*,[17] Copyright 2006, Journal of Power Sources)

1.4.2 Cathode

Insertion material for positive electrodes can be divided into three categories: 1) inorganic transition-metal oxides and chalcogenides, 2) organic molecules and 3) polymers. Transition-metal oxides or sulfides are common in modern-day batteries. Storage in transition-metals depends on the type of void available. Figure 1-9 shows different types of void spaces and an example cathode material corresponding to the void spacing. The interstitial spaces in cathode materials are accessible to only lithium ions as these materials develop passivating layers during the first few cycles. $LiFePO_4$, a phase change material with one-dimensional channel for lithium transport, is one of the best candidates for a cathode in the lithium-ion batteries (Figure 1-9) Though being introduced as low power materials,[18] due to several technological advancements, $LiFePO_4$ is now one of the best cathode materials for high-power lithium-ion batteries.

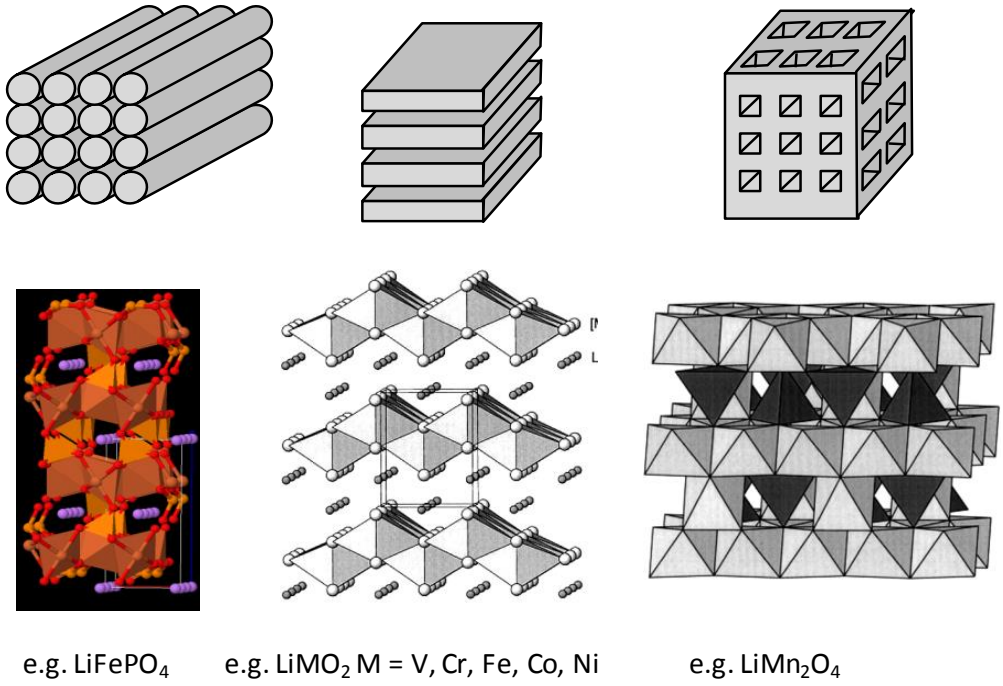

Figure 1-9: One, two and three-dimensional void spaces in transition-metal oxides and chalcogenides (figure adapted and reproduced with permission from Winter *et al.*,[5] copyright 1998, Wiley and materialsproject.org[19])

1.4.3 Electrolyte

The lithium-ion battery voltage window is around 3–5 V depending on the specific chemistry. Aqueous and most non-aqueous electrolytes do not have a wide enough thermodynamic potential window (difference between HOMO and LUMO orbital of electrolyte) to sustain such an aggressive environment.[5] Ideally, one would like to have an electrolyte which has a HOMO level lower than the electrochemical potential of cathode and a LUMO level higher than the electrochemical potential of anode,[20] in order to prevent the electrolyte from being oxidized or reduced. This configuration favors the intercalation reaction over side reactions and improves reversibility of battery (see left plot of Figure 1-10). If the thermodynamic window is not wide enough, the electrolyte will react and form a passivating film which will prevent further oxidation/reduction of electrolyte. The passivating film effectively widens the stability windows and makes the efficient working of the lithium ion battery possible (right plot of Figure 1-10).

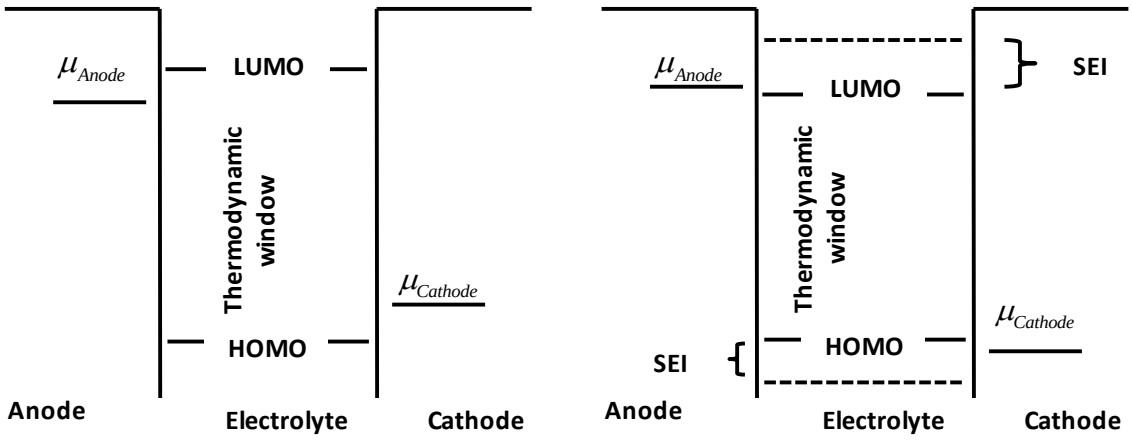

Figure 1-10: Left: ideal electrolyte having broader thermodynamic window, Right: formation of passivating layer due to smaller thermodynamic window of electrolyte (figure adapted with permission from Goodenough and Park,[20] Copyright 2013, American Chemical Society)

Three categories of electrolytes are used in the lithium-ion batteries: liquid, solid and polymer. In liquid electrolyte, three families of liquid solvents (ethers, esters and alkyl carbonates) are used in Li-ion battery with ethylene carbonate (EC) as the mandatory component. Since these electrolytes operate far beyond the thermodynamic stability range (right plot of Figure 1-10), they decompose at voltages that are typical for the lithium-ion batteries. The products from the decomposition of the salt (e.g. $LiPF_6$) and the electrolyte form a passive layer (SEI layer). The SEI layer allows the transport of lithium ions but suppresses the transport of solvent molecules (e.g. EC, PC, and DMC) slowing down further oxidation/reduction of the solvent molecules. The choice of solvent is also determined by the desired properties of the SEI layer. Solvents with high polarity, wide temperature range, sufficiently low toxicity and acceptable safety features are preferred. Common lithium based salts are: $LiPF_6$, $LiBF_4$, $LiN(SO_2CF_2CF_3)_2$, (LiBETI), $LiBC_4O_8$(LiBOB), $LiPF_3(CF_2CF_3)_3$(LiFAP), and LiN(SO2$CF_3)_2$(LiTFSI). Figure 1-6 shows the thermodynamic stability of 1 M $LiPF_6$ in EC/DEC (1:1) mixture with different electrode materials. Note that 1 M $LiPF_6$ in EC/DEC (1:1) will not be thermodynamically stable with graphite, leading to the SEI layer formation around solid graphite particles. It must be noted that Figure 1-6 shows the stability

limit when the battery is at thermodynamic equilibrium (net zero current). At nonzero current, the voltages of the anode and cathode may be pushed beyond the stability limit of the electrolyte causing further SEI layer growth.

1.4.4 Separator

A microporous separator separates the insertion material based anode and cathode. The separator is placed to facilitate ionic transport and prevent electronic current. The separator is designed to sustain wide temperature ranges, aggressive mediums (potential range of a typical lithium-ion battery), and stress generated by battery operations. With the recent advancements in the separators, the two most interesting developments are: 1) shutdown and 2) high-temperature integrity.[21] Due to short circuiting or overcharging, the temperature inside the battery can increase significantly. Shutdown refers to the increase in the impedance of the battery at high temperature. Moreover, the separator material should not lose mechanical integrity in order to be able to provide shutdown functionality at high temperature. These two features are essential in the high powered lithium-ion batteries as safety features. The design and selection of separator vary from high-power to the high-energy battery. The high-power batteries require thinner electrodes with large surface area compared to the high-energy batteries; hence they require more separator layers to deliver the required energy. In the case of a high-power battery, sometimes the cost of the separator dominates the cost of the battery. Usually polypropylene (PP) and polyethylene (PE) are used as separator materials. A tri-layer of PP/PE/PP can provide a durable and thermally stable separator with shutdown functionality.[21]

1.5 Transport and Kinetics of the Lithium-ion Battery

1.5.1 Transport in the Solid Phase

Figure 1-4 outlines different pathways for intercalation of lithium in the solid phase. Graphite intercalation compounds (GIC) show *staged phenomena*, in which intercalated layers are periodically arranged between empty graphene layers (instead of a uniform distribution of lithium between all graphene layers). Thermodynamically, periodic layers of lithium are preferred over the uniform distribution of lithium due to the high energy requirement in overcoming van der Waals forces between graphene layers. The number of graphene layers between two intercalate layers is called the stage index (n = 1 to 4). The stage index depends on the concentration of lithium (higher concentration leads to tighter packing and hence less free graphene sheets). The voltage plateau observed in Figure 1-11 for a range of concentration can be ascribed to the coexistence of two phases.[5]

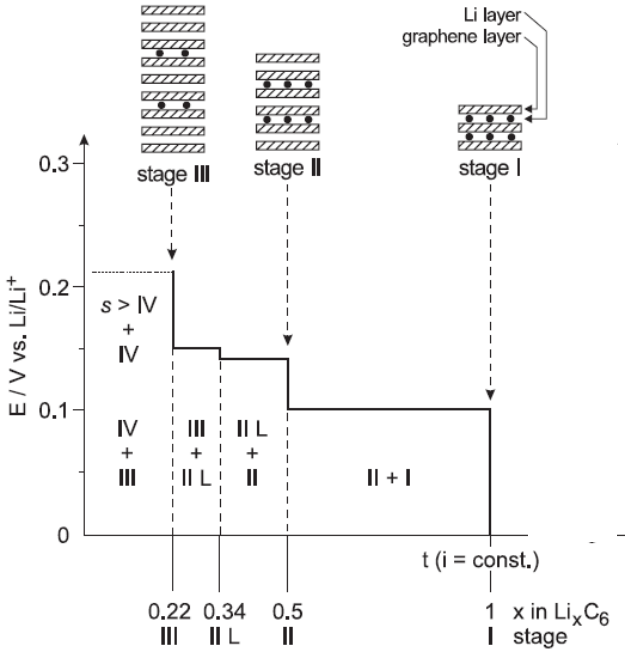

Figure 1-11: Stages formed during intercalation of lithium into graphite (constant current charging). (Image reproduced with permission from Winter *et al.*[5] copyright 1998, Wiley)

After a lithium ion (in electrolyte) reacts at the surface of the electrode, the '*lithium ion-electron*' entity may reside as a lithium ion in the interstitial sites of crystal structure and an electron may bind to either the transition metal sites (as in the case of $LiFePO_4$[22]) or oxygen sites (as in the case of Li_xCoO_2[23]). Materials in which homogeneous insertion occurs during intercalation, the transport of electrons and lithium ions in the solid phase can be modeled[22] either by Fick's law (assuming lithium ion and electron as one neutral entity) or Poisson-Nernst-Planck equation[22] (treating transport of both electrons and lithium ions separately). For materials with strong phase separation behavior (e.g. $LiFePO_4$), shrinking core models[24] or phase field models can be used.[25] In materials with high volume expansion (alloying phenomena), moving boundary formulation needs to be adapted to capture the increasing/decreasing radius of the particle.

1.5.2 Transport in the Electrolyte Phase

Typical electrolytes for a lithium-ion battery consist of some combination of Ethyl carbonate, dimethyl carbonate, propylene carbonate (EC/DMC/PC) with a lithium based salt (e.g. $LiPF_6$, typically 1 M). While charging and discharging at high rates, the local concentration of lithium ions can range from 0–5 M. Simulation of the charge/discharge of a lithium-ion battery using the infinitely dilute solution theory was published by West *et al.*[26] in 1982 where the Nernst-Planck equations and electroneutrality was assumed to model diffusion and migration of lithium ions in the electrolyte. Newman *et al.*[27] used the concentrated solution theory for the flux expressions to model diffusion and migration in the electrolyte. For the case of a binary salt, the final form of the equations derived by the concentrated solution theory can be simplified significantly to look similar to the equations for infinitely dilute solution theory and offers minimal additional computational burden,[28] hence treatment based on concentrated solution theory are very common in battery modeling and simulation literature. The equations associated with the transport of

lithium ions with concentrated solution theory are listed in Chapter 2 and the derivation of equations for transport of lithium ions in electrolyte using dilute solution theory is given in Appendix B.

1.5.3 Heterogeneous Reaction Kinetics

The reversible faradic reaction occurring at the surface of electrodes are usually modeled as Butler-Volmer kinetics, where the rate of reaction has exponential dependence on surface overpotential (difference between electrode potential (ϕ_s) and electrolyte potential (ϕ_e), denoted by symbol $\eta = \phi_s - \phi_e$). For intercalation reactions, surface overpotential also includes the open circuit voltage of the electrode (U), which is dependent on the lithium concentration at the surface of the solid particles. The lithium intercalation reaction from a liquid electrolyte and a solid host can be described as[27]

$$\mathrm{Li}^+ + e^- + \theta_s \underset{\leftarrow \text{Anodic}}{\overset{\text{Cathodic} \rightarrow}{=}} \mathrm{Li} - \theta_s, \tag{1.1}$$

where θ_s is a site in solid electrodes. The Bulter-Volmer equation is given as

$$i = \overbrace{i_o \left[\exp\left(\frac{\alpha_a F \eta}{2RT} \right) \right]}^{\text{Anodic direction}} - \overbrace{i_o \left[\exp\left(\frac{(1-\alpha_a) F \eta}{2RT} \right) \right]}^{\text{Cathodic direction}}, \tag{1.2}$$

Where $\eta = \phi_s - \phi_e - U$, α is the apparent transfer coefficient, which relates to how the applied potential difference favors either of the reactions, i_o is the exchange current density that depends on lithium ion concentration in the electrolyte and lithium concentration at the surface of the solid particle. The derivation of Butler-Volmer kinetics is presented in Appendix A. Since intercalation

is a reversible reaction, the first term in equation (1.2) represents the reaction rate in the anodic direction (*i.e.* oxidation, not to be confused with the reaction at the anode) and the second term represents reaction rate in the cathodic direction. At equilibrium, the net rate of reaction is zero. Positive over-potential $(\eta \geq 0)$ leads to positive current (net oxidation and release of electrons) as the rate in the anodic direction dominates the rate in the cathodic direction. For phase change materials (like $LiFePO_4$), where it is shown that reactions mainly occur at the interface between two phases (phase boundary), the expressions for reaction kinetics is modified and presented in Bazant.[6] Figure 1-12 shows the schematic of one pathway of intercalation phenomena where the lithium ion diffuses through the SEI layer and reacts at the graphite-SEI interface.

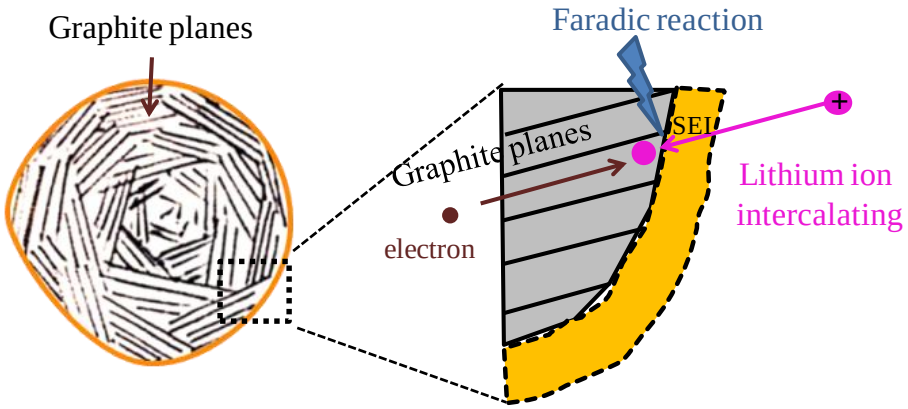

Figure 1-12: Intercalation in the graphite particle, note that lithium ion diffuses through SEI layer, and faradic reaction occurs at the graphite-SEI interface (SEI layer is considered part of the electrolyte)

1.6 Issues and Challenges with the Lithium-ion Batteries

Though lithium-ion battery technology is better in terms of energy density, power density, and cycle life when compared to other battery technologies; there is still a lot of scope for improvement of these batteries. Capacity fade and safety remain critical areas which need to be addressed for expanded applications of the lithium-ion battery technology.

One factor that affects the safety of lithium-ion batteries is the lithium plating reaction. As mentioned before, the shift from the lithium-metal anode to the lithiated-graphite anode was motivated by safety issues associated with dendrite formation on lithium metal. Graphite offers a good alternative to lithium metal but at the cost of energy density. Though, graphite avoids the problem of dendrites formation, at higher charging rates or lower temperatures[14] the plating reaction can still occur.[13,14] Figure 1-13 shows the conceptual diagram of plating reaction consuming active materials and causing capacity fade. Plating reactions not only pose safety issues but also cause capacity loss as they are only partially reversible.[14]

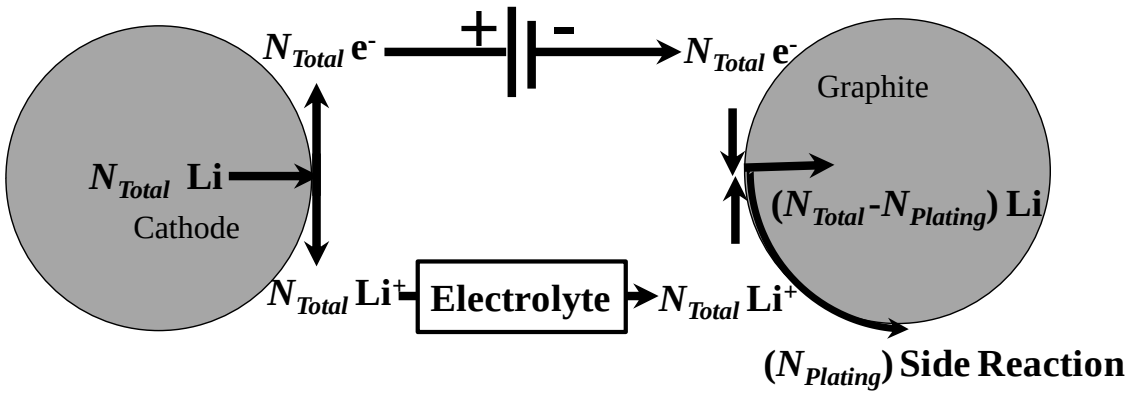

Figure 1-13: Conceptual diagram of the plating reaction at the surface of solid particle during charging

Capacity fade is another important issue that limits the applicability of lithium-ion batteries. Three main factors that affect the capacity of a battery are thermal degradation of electrolyte, SEI layer growth and cracking of particles due to intercalation induced stresses. Electrolytes have a safe operating temperature and potential range beyond which capacity fade can be accelerated.[29] A critical review of thermal issues for lithium-ion batteries can be found in Bandhauer *et al.*[29]

Even though the SEI layer slows down the oxidation of the electrolyte by restricting the transport of solvent molecules, its continuous formation consumes active material consistently over the life span of the battery. As mentioned earlier, charging/discharging of batteries at higher rates increases

the rate of SEI layer formation. Formation of the passive layer introduces an additional voltage drop along with the consumption of active materials. The dual impact of the SEI layer limits the reversibility of lithium-ion batteries. Figure 1-14 shows a graphite particle with short-range ordering in graphene planes (left) and a comparison between intercalation and new SEI layer formation at anode-SEI interface.[30] Note that the new SEI layer is formed at the graphite electrolyte interface and not at the SEI-electrolyte interface.

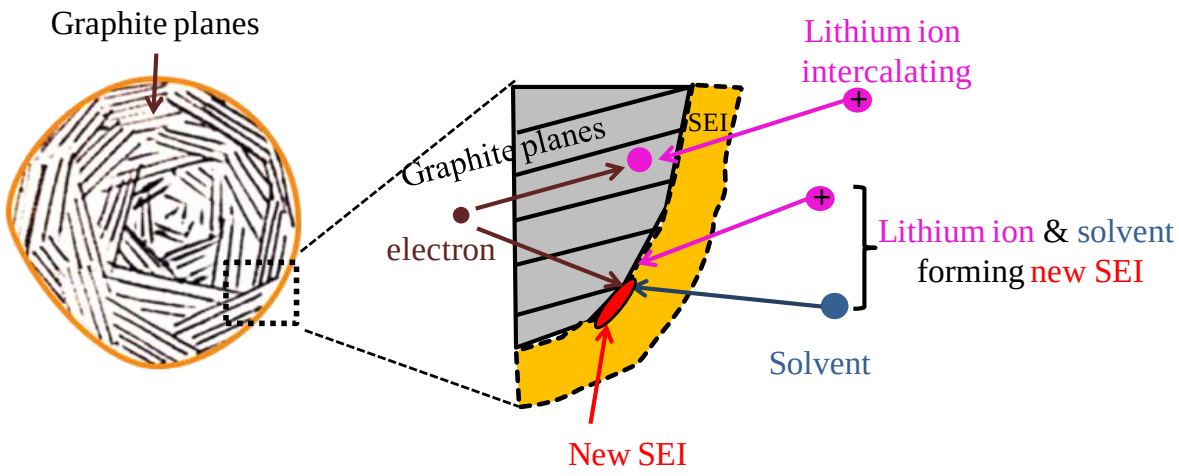

Figure 1-14: Left: graphite particle with SEI layer, Right: conceptual diagram of the formation of the SEI layer vis-à-vis intercalation, figure adapted from Pinson and Bazant[30]

Intercalation induced stress generation in electrode particles is another reason for capacity fade, which affects the capacity in two ways: 1) fracture due to stress (electrical isolation) that reduces the effective capacity of the electrode and 2) reduced electrical connectivity due to fractures.[31] When lithium is inserted into the interstitial space of host materials, local lattice spacing changes to accommodate the guest lithium. The presence of a concentration gradient causes a gradient in lattice spacing within the particle, which creates stresses in the particle (see Figure 1-15).

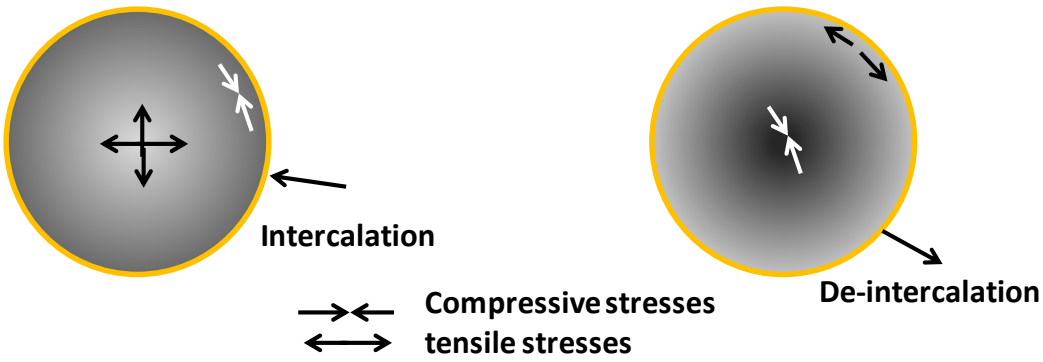

Figure 1-15: Stresses in solid particle during intercalation and deintercalation.

Intercalation induced stresses, estimated using various modeling approaches[31-35] with varying degree of sophistications, are explained later in Chapter 2. Figure 1-16 shows the anode particles after the first five cycles (SEI formation cycles) and after 100 cycles at 10 C rate at low temperature.[36]

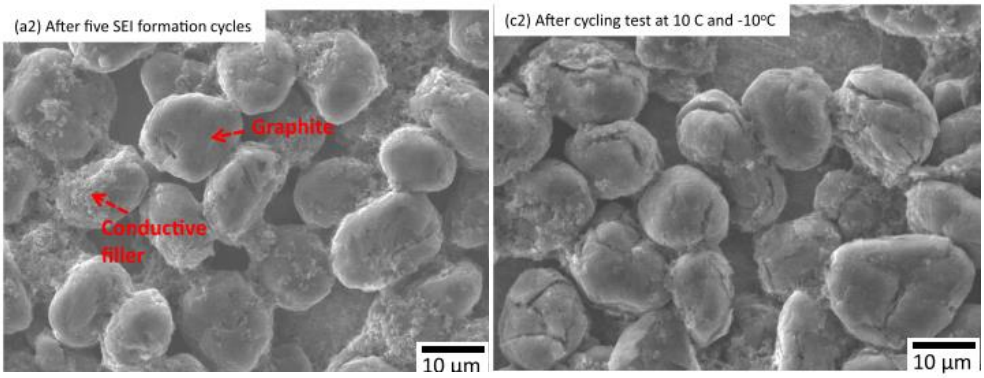

Figure 1-16: Left: anode particle after five SEI formation cycles. Right: fractured anode particles after cycling test at 10 C at -10 ºC. Reproduced by permission from Takahashi and Srinivasan,[36] (open access article).

1.7 Scope of the Dissertation

The work presented in this dissertation can broadly be categorized into two parts: optimal operation (charging/discharging) and rational design. Chapter 2 presents quantitative treatment of transport and kinetic processes associated with the lithium-ion battery along with capacity fade reactions (such as SEI layer and lithium-plating side reactions) and intercalation induced stresses. Chapter 3 presents the analytical solution for diffusion in composite materials using Fick's law

where each region has different lithium solubility and diffusivity. The analytical solutions for concentration profiles in composite materials are used to derive expressions for intercalation-induced stresses under certain simplifying assumptions.

Chapter 4, 5, and 6 focus on optimal operation for lithium-ion batteries. While Chapter 4 and 5 use a simplified battery model (single particle model), Chapter 6 uses a detailed battery model based on porous electrode theory along with concentrated solution theory (pseudo-2dimensional model).

Chapter 4 begins with the comparison of different models to quantify intercalation induced stresses in single particle under constant lithium intake boundary condition followed by an optimal charging problem formulation. The optimization problem undertaken in Chapter 4 tries to maximize charge stored in a given time in a single particle while restricting stresses to a specified bound. Chapter 5 follows the similar methodology of maximizing charge stored in a battery using single particle model while restricting overpotential for lithium-plating side reaction.

Chapter 6 uses an isothermal pseudo-2dimensional model to estimate stress distribution across the thickness of the anode to underline the importance of detailed models. The optimization problem of maximizing charge storage in a lithium-ion battery is solved numerically while restricting the peak stress values attained at the anode-separator interface.

Chapter 7—second part of the dissertation—presents the use of the isothermal pseudo-2dimensional model to investigate the effect of design parameters on battery capacity and capacity-fade mechanisms. Chapter 7 consists of two cases. Case 1 evaluates the effect of thickness-porosity combination (while maintaining constant anode capacity) on total capacity and capacity-fade mechanisms. Case 2 evaluates the effect of porosity distribution on capacity-fade mechanisms. Chapter 8 presents conclusions and future directions.

The dissertation contains three appendixes. Appendix A outlines the derivation of Butler-Volmer kinetics expression. Appendix B presents the mathematical treatment of the transport of lithium ions in electrolyte using infinitely dilute solution theory for binary salt. Appendix C derives the equations for intercalation-induced stresses using infinitesimally strain theory (for low volume expansion materials), an approach traditionally used for mathematical treatment of stresses due to thermal gradients.

Chapter 2

Continuum Models for the Lithium-ion Battery

> "The sciences do not try to explain, they hardly even try to interpret, they mainly make models. By a model is meant a mathematical construct which, with the addition of certain verbal interpretations, describes observed phenomena. The justification of such a mathematical construct is solely and precisely that it is expected to work - that is correctly to describe phenomena from a reasonably wide area. Furthermore, it must satisfy certain esthetic criteria - that is, in relation to how much it describes, it must be rather simple."
>
> **John von Neumann**

2.1 Motivations for Modeling and Simulation

There are two main aspects of the lithium-ion battery modeling and simulations with the continuum-level models. One aspect relates to the accurate estimation of usable capacity at different stages of battery life under various charging/discharging rates, temperatures, etc. Other aspect relates to rational design and operation of the lithium-ion battery to minimize system-level inefficiencies and capacity fade to ensure safe and long battery life.

Accurate estimation of battery capacity: Lithium-ion batteries require airtight seals to function safely. This requirement places significant restrictions for putting sensors to measure the variables of interest (concentration, current and potential distributions). Moreover, it is well established that using a lithium-ion battery beyond its prescribed voltage limit can degrade the battery or can cause safety issues due to side reactions such as lithium-plating or SEI growth (Figure 1-10). Unlike electrochemical double layer capacitors (EDLC) where voltage profile follows monotonic (almost linear) change with capacity, typical rechargeable batteries show a voltage plateau. The voltage

plateau makes the estimation of capacity from voltage measurement very difficult and unreliable although the plateau is desirable from the energy density point of view.

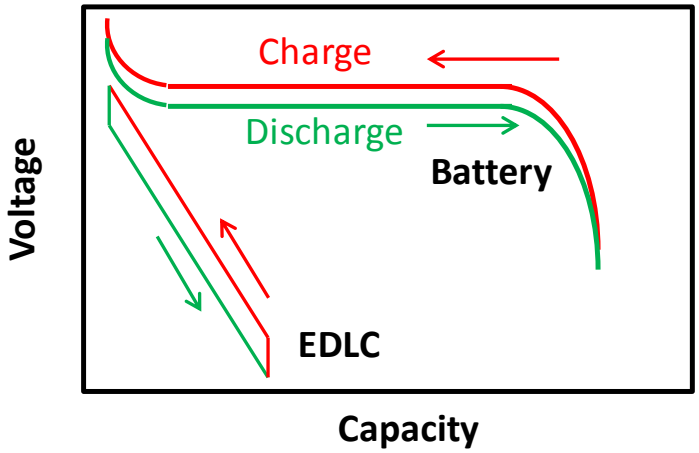

Figure 2-1: Constant current charging and discharging behavior of a battery vs. an EDLC. Note that the voltage plateau makes the estimation of battery capacity difficult solely based on voltage measurements (Figure adapted from http://en.wikipedia.org/wiki/File:Charge-Discharge-Supercap-vs-Battery.png)

Figure 2-1 shows the charge and discharge of a battery and an EDLC. The estimation of capacity is easier for an EDLC compared to a battery as there is a one-to-one correspondence between voltage and capacity for an EDLC. The situation is much worse when the charging and discharging is subject to variable current for the battery. The battery voltage behavior is highly nonlinear with respect to load current and estimation of remaining capacity based on voltage profile under variable current becomes much more difficult, and hence there is scope for detailed models to contribute.

Rational design and operation: The design variables for a lithium-ion battery are very high, as the battery consists of the anode, separator, and cathode, with the current collector and electrolyte. Large number of combinations for design parameters such as the thicknesses and porosities of different regions, concentration of lithium salt, choice of electrolyte, particle sizes of anode and cathode structure etc., make the optimization of the design parameters quite challenging. Chemical engineering based principles can be used to model the battery that can guide the design of the

lithium-ion battery. To illustrate the point, one can think about choosing the thickness-porosity combination and its effect on various capacity fade mechanics vis-à-vis energy density as given in Figure 2-2.

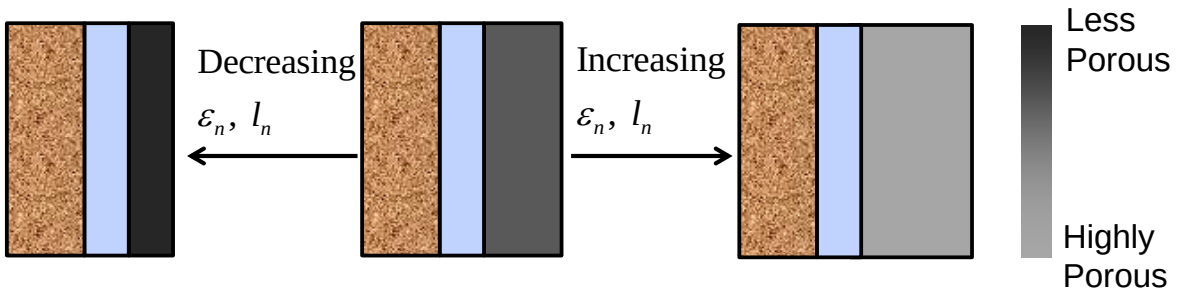

Figure 2-2: Different choices of porosities and lengths for the anode

Detailed battery models can also be used to identify parts of battery structure that are most vulnerable to capacity fade at different charging/discharging conditions. For example, it is estimated that regions near electrode-separator interfaces are most vulnerable (anode-separator interface and cathode-separator interface) to SEI layer and plating side reactions.[37] Also, at the beginning of every charge/discharge process, the battery is most vulnerable to cracking due to intercalation induced stresses.[37] These insights can be put to good use in deriving better design and charging/discharging protocols for the lithium-ion battery.

2.2 Continuum Models for the Lithium-ion Battery

The models for lithium ion batteries can be divided into three categories: equivalent circuit-based models, continuum models, and atomistic models. Atomistic models are not commonly used to simulate entire charge/discharge behavior of a battery, and their applications are limited to simulating specific physics or specific processes in the battery (Figure 2-3).

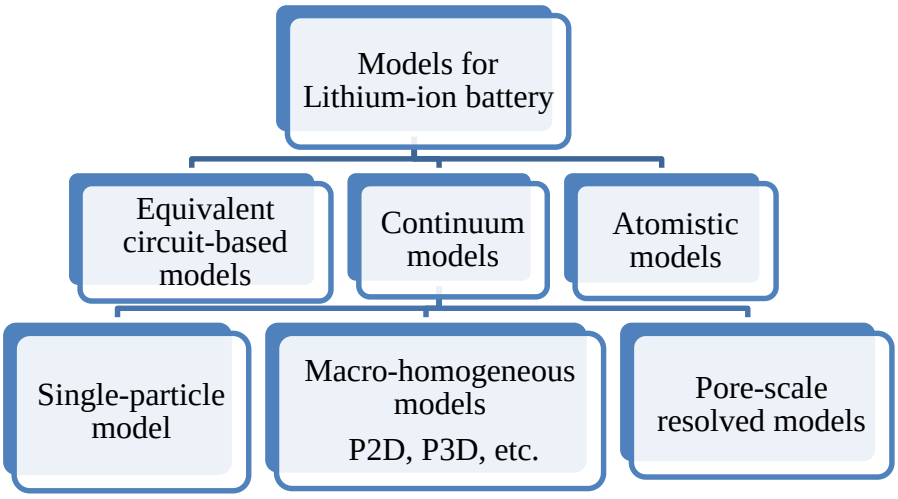

Figure 2-3: Some modeling frameworks for the lithium-ion battery

Equivalent circuit-based models fit a network of resistors and capacitors to estimate the charge/discharge behavior of a battery. These models are computationally efficient but ignore the physics of the battery hence find limited use in rational design or operation of the battery. This chapter focuses on the continuum level battery models. Lithium-ion battery involves transport in the solid phase and the electrolyte phase, along with charge transfer kinetics at the interface of the electrodes. Different models can be generated based on various approximations related to processes or structure as described in subsequent sections.

2.2.1 Single Particle Model (SPM)

The SPM assumes that the porous nature of the solid phase in the anode and the cathode can be approximated by the dynamics of a single particle in each electrode. The SPM also ignores the dynamics and variation of lithium-ion concentration in the electrolyte phase.[38,39] The flux of lithium ion at the surface of the particles is determined by the total surface area of the electrodes. The radius of this hypothetical particle is representative of the particle size distribution of the electrode material.

Figure 2-4: Schematic and processes considered in the SPM for the lithium-ion battery

The SPM for the lithium-ion battery—developed by Dr. White's group—uses Fick's law and the continuity equation for diffusion and Butler-Volmer kinetics for charge-transfer reaction (see Appendix A for the derivation of Butler-Volmer type reaction kinetics). Table 2-1 shows the Fick's second law for the diffusion of neutral lithium entity in the solid phase (equations (2.1) and (2.2)). The assumption of neutral lithium in solids may not be valid for many cathode materials (such as $LiFePO_4$[40] and $LiCoO_2$[41]) where electron prefers to be with either transition metal or oxygen compared to lithium ion.[40,41] Equation for temperature is derived based on lumped energy balance in the battery (equation (2.4)).

Table 2-1: Governing equations for the single-particle thermal model

	Governing equation	Boundary conditions	
Solid phase concentration (cathode): $c_p^s(r,t)$	$\frac{\partial c_p^s}{\partial t} = \frac{1}{r^2}\frac{\partial}{\partial r}\left[r^2 D_p^s \frac{\partial c_p^s}{\partial r}\right]$	$\left.\frac{\partial c_p^s}{\partial r}\right\|_{r=0} = 0,\ -D_p^s \left.\frac{\partial c_p^s}{\partial r}\right\|_{R_p} = \frac{I_{\text{overall}}}{a_p F}$	(2.1)
Solid phase concentration (anode): $c_n^s(r,t)$	$\frac{\partial c_n^s}{\partial t} = \frac{1}{r^2}\frac{\partial}{\partial r}\left[r^2 D_n^s \frac{\partial c_n^s}{\partial r}\right]$	$\left.\frac{\partial c_n^s}{\partial r}\right\|_{r=0} = 0,\ -D_n^s \left.\frac{\partial c_n^s}{\partial r}\right\|_{R_n} = \frac{-I_{\text{overall}}}{a_n F}$	(2.2)
Voltage $V(t)$:	$V(t) = \phi_p^s(t) - \phi_n^s(t)$		(2.3)
Temperature: $T(t)$ (Lumped energy balance)	$\frac{dT}{dt} = \frac{I_{\text{overall}}}{mC_p}\left[\left(\eta_p - \eta_n + I_{\text{overall}} R_{\text{cell}}\right) + T\left(\left.\frac{\partial U_p}{\partial T}\right\|_{surf} - \left.\frac{\partial U_n}{\partial T}\right\|_{surf}\right)\right] - \frac{hA_{HT}}{mC_p}\left(T - T_{\text{amb}}\right)$		(2.4)

Table 2-2: Additional expressions used in the SPM

Butler-Volmer kinetics (see Appendix A):	$\frac{I_{\text{overall}}}{a_p F} = 2k_p\sqrt{c_e c^s_{p,\text{surf}}\left(c^s_{\max,p} - c^s_{p,\text{surf}}\right)}\sinh\left(F\left(\phi^s_p - \phi_{e,p} - U_p\right)\Big/(2RT)\right)$	(2.5)
	$\frac{-I_{\text{overall}}}{a_n F} = 2k_n\sqrt{c_e c^s_{n,\text{surf}}\left(c^s_{\max,n} - c^s_{n,\text{surf}}\right)}\sinh\left(F\left(\phi^s_n - \phi_{e.n} - U_n\right)\Big/(2RT)\right)$	(2.6)
Specific area	$a_i = (3/R)\left(1-\varepsilon_i - \varepsilon_{f,i}\right)A_{cross}l_i,\ i = p,n$	(2.7)
Typical open circuit voltages of cathode and anode *wrt.* lithium metal (experimental fit)	$U_p = \frac{\left(-4.656 + 88.669\theta_p^2 - 401.119\theta_p^4 + 342.909\theta_p^6 - 462.471\theta_p^8 + 433.434\theta_p^{10}\right)}{\left(-1.0 + 18.933\theta_p^2 - 79.532\theta_p^4 + 37.311\theta_p^6 - 73.083\theta_p^8 + 95.96\theta_p^{10}\right)}$ $\theta_p = \frac{c^s\big\vert_{r=R_p}}{c^s_{\max,p}}$	(2.8)
	$U_n = \begin{pmatrix} 0.7222 + 0.1387\theta_n + 0.029\theta_n^{0.5} - 0.0172\theta_n^{-1} + 0.0019\theta_n^{-1.5} + \\ 0.2808\mathrm{e}^{0.9-15\theta_n} - 0.7984\mathrm{e}^{0.4465\theta_n - 0.4108} \end{pmatrix},\ \theta_n = \frac{c^s\big\vert_{r=R_n}}{c^s_{\max,n}}$	(2.9)
Solid phase diffusivity	$D_i^s = D^s_{i,\text{ref}}\exp\left(-\left(E_a^{D_i^s}/R\right)\left[1/T - 1/T_{\text{ref}}\right]\right),\ i = p,n$	(2.10)
Reaction rate constant	$k_i = k_{i,\text{ref}}\exp\left(-\left(E_a^{k_i}/R\right)\left[1/T - 1/T_{\text{ref}}\right]\right),\ i = p,n$	(2.11)

Various other models are also reported for the transport of lithium (lithium ion-electron entity) in the solid phase. Christensen *et al.*[32] presented detailed treatment of diffusion in a solid particle considering two species: lithiated substrate and empty substrate rather than lithium as guest species along with other features such as volume change, pressure-induced diffusion and non-ideal behavior. Modeling of intercalation based on Generalized Poisson-Nernst-Planck (PNP) equations where lithium ions and electrons are treated separately is considered by Lai.[22] Different thermodynamics can be incorporated in SPM framework by replacing Fick's law with valid expressions for different materials.[22] For low charging/discharging rates at normal temperatures, SPM works very well but starts to drift at higher charging/discharging rates or low temperatures.

2.2.2 Pseudo Two-dimensional (P2D) Model

A porous electrode is made of electrode particles, binders, and fillers with electrolyte in the pores. Modeling at the pore-scale accounting for the shape of individual particles is very computationally demanding. The P2D model comes under the category of macro-homogeneous models where the porous electrodes can be approximated with the help of various macroscopic parameters[28] such as porosity, tortuosity, average surface area per unit volume, volume-averaged resistivity and so forth. It must be pointed out here that these macro-homogeneous models are conceptually different from a structure with one-dimensional straight pores perpendicular to the face of the electrode, although both approaches lead to similar mathematical equations.[28,42] In P2D model, the electrode is treated as a superposition of an electrolyte phase and a solid phase at any point in space.[28] Equations for isothermal porous electrode pseudo two-dimensional (P2D) model are given in Table 2-3. Table 2-4 presents various expressions used in this model. Equations derived for lithium ion transport in electrolyte phase (equation (2.12)) consider diffusion and migration but for binary lithium salt, the electrolyte equations can be simplified by eliminating electrolyte potential from the governing equation (see Appendix B for derivation of ionic transport equation based on dilute solution theory).

The P2D model provides a very general framework to incorporate different type of physics. Equation (2.15) shows Fick's law type relation for diffusion of neutral lithium ion-electron entity in the solid host. Transport laws for different materials can be significantly different (and/or function of particle size) and can be incorporated into the P2D model framework by replacing equation (2.15) with appropriate expressions.

Table 2-3: Governing PDEs for the P2D model (see Appendix B for derivation of equation like 2.12 and 2.13)

Governing Equations	**Boundary Conditions**	
Positive Electrode		
$\varepsilon_{\mathrm{p}} \dfrac{\partial c}{\partial t} = \dfrac{\partial}{\partial x}\left[D_{\mathrm{eff,p}} \dfrac{\partial c}{\partial x} \right] + a_{\mathrm{p}} \left(1 - t_{+}\right) j_{\mathrm{p}}$	$\left.\dfrac{\partial c}{\partial x}\right\|_{x=0} = 0\ ,\ -D_{\mathrm{eff,p}} \left.\dfrac{\partial c}{\partial x}\right\|_{x=l_p^-} = -D_{\mathrm{eff,s}} \left.\dfrac{\partial c}{\partial x}\right\|_{x=l_p^+}$	(2.12)
$-\sigma_{eff,p} \dfrac{\partial \Phi_1}{\partial x}$ $-\kappa_{\mathrm{eff,p}} \dfrac{\partial \Phi_2}{\partial x} + \dfrac{2\kappa_{\mathrm{eff,p}} RT}{F}\left(1 - t_{+}\right) \dfrac{\partial \ln c}{\partial x} = I$	$\left.\dfrac{\partial \Phi_2}{\partial x}\right\|_{x=0} = 0,$ $\kappa_{\mathrm{eff,p}} \left.\dfrac{\partial \Phi_2}{\partial x}\right\|_{x=l_p^-} = \kappa_{\mathrm{eff,s}} \left.\dfrac{\partial \Phi_2}{\partial x}\right\|_{x=l_p^+}$	(2.13)
$\dfrac{\partial}{\partial x}\left[\sigma_{\mathrm{eff,p}} \dfrac{\partial \Phi_1}{\partial x} \right] = a_{\mathrm{p}} F j_{\mathrm{p}}$	$\sigma_{eff,p} \left.\dfrac{\partial \Phi_1}{\partial x}\right\|_{x=0} = -I,\ \left.\dfrac{\partial \Phi_1}{\partial x}\right\|_{x=l_p^-} = 0$	(2.14)
$\dfrac{\partial c_p^s}{\partial t} = \dfrac{1}{r^2} \dfrac{\partial}{\partial r}\left[r^2 D_p^s \dfrac{\partial c_p^s}{\partial r} \right]$	$\left.\dfrac{\partial c_p^s}{\partial r}\right\|_{r=0} = 0,\ D_p^s \left.\dfrac{\partial c_p^s}{\partial r}\right\|_{r=R_P} = -j_p$	(2.15)
Separator		
$\varepsilon_s \dfrac{\partial c}{\partial t} = \dfrac{\partial}{\partial x}\left[D_{\mathrm{eff,s}} \dfrac{\partial c}{\partial x} \right]$	$c\big\|_{x=l_p^-} = c\big\|_{x=l_p^+}\ ,\ c\big\|_{x=l_p+l_s^-} = c\big\|_{x=l_p+l_s^+}$	(2.16)
$-\kappa_{\mathrm{eff,s}} \dfrac{\partial \Phi_2}{\partial x} + \dfrac{2\kappa_{\mathrm{eff,s}} RT}{F}\left(1 - t_{+}\right) \dfrac{\partial \ln c}{\partial x} = I$	$\Phi_2\big\|_{x=l_p^-} = \Phi_2\big\|_{x=l_p^+}$ $\Phi_2\big\|_{x=l_p+l_s^-} = \Phi_2\big\|_{x=l_p+l_s^+}$	(2.17)
Negative Electrode		
$\varepsilon_n \dfrac{\partial c}{\partial t} = \dfrac{\partial}{\partial x}\left[D_{\mathrm{eff,n}} \dfrac{\partial c}{\partial x} \right] + a_n \left(1 - t_{+}\right) j_n$	$\left.\dfrac{\partial c}{\partial x}\right\|_{x=l_p+l_s+l_n} = 0$ $-D_{\mathrm{eff,s}} \left.\dfrac{\partial c}{\partial x}\right\|_{x=l_p+l_s^-} = -D_{\mathrm{eff,n}} \left.\dfrac{\partial c}{\partial x}\right\|_{x=l_p+l_s^+}$	(2.18)
$-\sigma_{\mathrm{eff,n}} \dfrac{\partial \Phi_1}{\partial x}$ $-\kappa_{\mathrm{eff,n}} \dfrac{\partial \Phi_2}{\partial x} + \dfrac{2\kappa_{\mathrm{eff,n}} RT}{F}\left(1 - t_{+}\right) \dfrac{\partial \ln c}{\partial x} = I$	$-\kappa_{\mathrm{eff,s}} \left.\dfrac{\partial \Phi_2}{\partial x}\right\|_{x=l_p+l_s^-} = -\kappa_{\mathrm{eff,p}} \left.\dfrac{\partial \Phi_2}{\partial x}\right\|_{x=l_p+l_s^+}$ $\Phi_2\big\|_{x=l_p+l_s+l_n} = 0$	(2.19)
$\dfrac{\partial}{\partial x}\left[\sigma_{\mathrm{eff,n}} \dfrac{\partial \Phi_1}{\partial x} \right] = a_n F j_n$	$\left.\dfrac{\partial \Phi_1}{\partial x}\right\|_{x=l_p+l_s^+} = 0, \sigma_{eff,n} \left.\dfrac{\partial \Phi_1}{\partial x}\right\|_{x=l_p+l_s+l_n} = -I$	(2.20)
$\dfrac{\partial c_n^s}{\partial t} = \dfrac{1}{r^2} \dfrac{\partial}{\partial r}\left[r^2 D_n^s \dfrac{\partial c_n^s}{\partial r} \right]$	$\left.\dfrac{\partial c_n^s}{\partial r}\right\|_{r=0} = 0,\ D_n^s \left.\dfrac{\partial c_n^s}{\partial r}\right\|_{r=R_P} = -j_n$	(2.21)

Table 2-4: Additional expressions used in the P2D model (see Appendix A for derivation of equation 2.22).

$j_p = 2k_p c^{0.5} c_p^s\big\|_{r=R_P}{}^{0.5} \left(c_{\max,p}^s - c_p^s\big\|_{r=R_P} \right)^{0.5} \sinh\left[\frac{F}{2RT}\left(\Phi_1 - \Phi_2 - U_p\right) \right]$	(2.22)
$j_n = 2k_n c^{0.5} c_n^s\big\|_{r=R_P}{}^{0.5} \left(c_{\max,n}^s - c_n^s\big\|_{r=R_P} \right)^{0.5} \sinh\left[\frac{F}{2RT}\left(\Phi_1 - \Phi_2 - U_n\right) \right]$	(2.23)
$\kappa_{eff,i} = \varepsilon_i^{brugg_i} \times 10^{-4} c \begin{pmatrix} -10.5 + 0.074T - 6.96\times10^{-5}T^2 + 6.68\times10^{-4}c - \\ 1.78\times10^{-5}cT + 2.8\times10^{-8}cT^2 + 4.94\times10^{-7}c^2 \\ -8.86\times10^{-10}Tc^2 \end{pmatrix}^2$ $, i = p, s, n$	(2.24)
$\sigma_{eff,i} = \sigma_i\left(1 - \varepsilon_i - \varepsilon_{f,i}\right), i = p, s, n$	(2.25)
$D_{eff,i} = D\varepsilon_i^{brugg_i}, i = p, s, n$ $D = 2.33\times10^{-4} \times 10^{-4.43 - \frac{54}{\left(T - 5\times10^{-3}c - 229\right)} - 2.2\times10^{-4}c}$	(2.26)
$a_i = \frac{3}{R_i}\left(1 - \varepsilon_i - \varepsilon_{f,i}\right), i = p, s, n$	(2.27)
$U_p = \frac{-4.656 + 88.669\theta_p{}^2 - 401.119\theta_p{}^4 + 342.909\theta_p{}^6 - 462.471\theta_p{}^8 + 433.434\theta_p{}^{10}}{-1.0 + 18.933\theta_p{}^2 - 79.532\theta_p{}^4 + 37.311\theta_p{}^6 - 73.083\theta_p{}^8 + 95.96\theta_p{}^{10}}$ $\theta_p = \frac{c_n^s\big\|_{r=R_P}}{c_{p,\max}^s}; 0.4955 \le \theta_p \le 0.99$	(2.28)
$U_n = -0.057 + 0.53\mathrm{e}^{-57\theta} - 0.184\tanh\left(20.0\theta - 21.0\right)$ $- 0.012\tanh\left(7.57\theta - 4.431\right) - 0.0304\tanh\left(18.518\theta - 3.24\right)$ $- 0.01\tanh\left(0.255\theta - 0.02653\right)$ $\theta_n = \frac{c_p^s\big\|_{r=R_P}}{c_{n,\max}^s};\ 0.01 \le \theta_n \le 0.99$	(2.29)
$D_i^s = D_{i,ref}^s \exp\left(-\frac{E_a^{D_i^s}}{R}\left(\frac{1}{T} - \frac{1}{T_{ref}} \right) \right),\ i = p, n$	(2.30)
$k_i = k_{i,ref} \exp\left(-\frac{E_a^{k_i}}{R}\left(\frac{1}{T} - \frac{1}{T_{ref}} \right) \right),\ i = p, n$	(2.31)

2.2.3 Model Reformulation

Simulation of P2D model using finite difference or finite element method tends to be computationally expensive, which has prohibited their use in the control and monitoring of internal states of battery in real time. Several simplified/reduced electrochemical models have been proposed, and control-relevant studies performed to try to address these issues.[43-48] Efforts in optimal control and nonlinear model predictive control, incorporating the SPM and other reduced order models have been published.[49,50] A mathematical reformulation method[51-54] gives rise to a computationally efficient model that can be solved in milliseconds without compromising on accuracy. These reformulation techniques consist of spectral methods (specifically orthogonal collocation) where, depending on number of collocation points in the anode, separator, and cathode, models can be generated with varying degree of accuracy. The model used in the dissertation is derived using the reformulation methodology outlined in Northrop *et al.*[51] with a change in basis (trial) functions in order to achieve better convergence properties at higher charging/discharging rates of battery operations. The change of trial functions to Chebyshev form compared to trigonometric form provides more robustness albeit at a slightly more cost.

2.3 Models for the Capacity Fade Mechanisms

The loss of capacity with time in lithium-ion batteries is attributed to many factors such as mechanical degradation or breaking of solid particles due to intercalation induced stresses, loss of active material in SEI layer growth, loss of lithium in plating side reactions, irreversible phase change in solid particles, electrolyte decomposition at high temperature, etc. In addition to these capacity fade mechanisms, there exist material-dependent fade mechanisms as well, for example, pulverization of silicon particle during lithium intercalation. The contribution of each factor will depend on cell chemistry and operating conditions. This section introduces mathematical treatment

for quantifying the effect of individual capacity fade mechanisms. How these capacity fade mechanisms collectively affect the battery is still being investigated.

2.3.1 Intercalation-induced Stresses

As briefly discussed in Chapter 1 that when lithium is inserted into interstitial space of host materials, local lattice spacing changes to accommodate the guest lithium. The presence of concentration gradient causes a gradient in lattice spacing within the particle, this gradient in lattice spacing creates stresses in the particle (see Figure 2-5). Assuming spherical symmetry, these stresses can be broken into two components: radial and tangential for the spherical particle. During intercalation, for the materials with a positive volume expansion, the radial stresses remain tensile throughout a particle (assuming zero external pressure at the surface) whereas the tangential stress becomes compressive at the surface and tensile at the center.

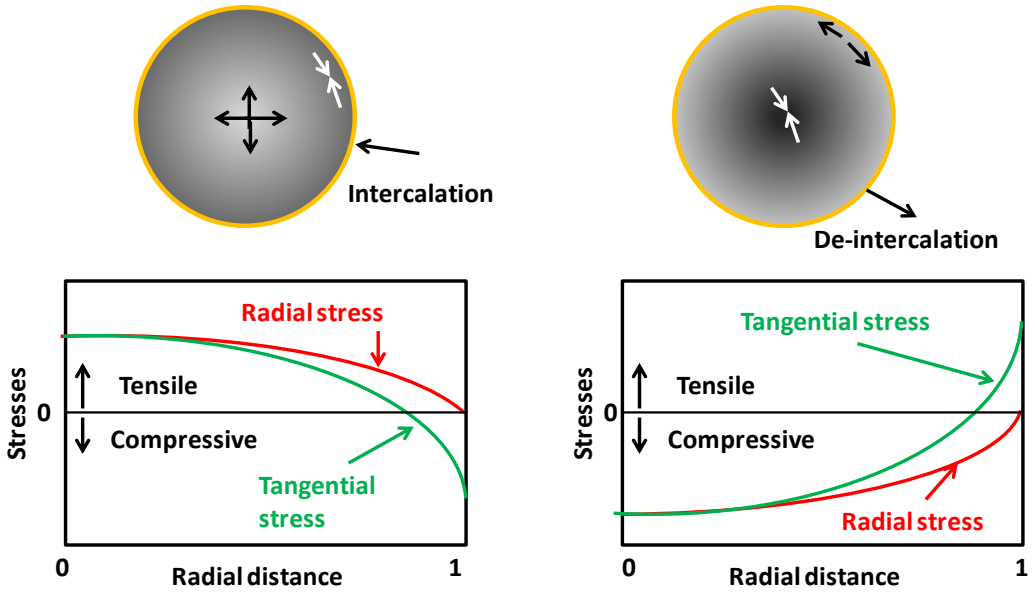

Figure 2-5: Nature of stresses during intercalation and de-intercalation

The peak (tensile) radial stress occurs at the center of the particle and peak (compressive) tangential stress occurs at the surface of the particle.[32] During deintercalation, the nature of stresses changes (i.e. tensile stresses become compressive and compressive stresses become tensile), but

the location of peak stresses remains the same for both. Therefore, the peak radial stresses at the center of the particles and peak tangential stresses at the surface of the particles are monitored in the simulations.

Review of models for intercalation induced stresses: If the stress exceeds the yield stress of a given material, the particle can break and lose contact with the matrix resulting in reduced capacity of the battery. Different models have been developed to quantify the stress developed in a particle with varying degree of sophistications. These modeling efforts can be divided into two categories: strain splitting[33-35] and stress splitting.[31,32] The theory of the strain splitting approach has been developed by Timoshenko[55] where thermal stresses have been modeled using strain splitting, with these models being called *thermal analogy models*. Here, the intercalation-induced stresses are treated in similar way as the temperature-induced stresses. On the other hand, a very detailed and rigorous model that used stress splitting was developed by Christensen *et al.*,[31,32,55] In both categories, different models can be obtained depending upon the inclusion of pressure-induced diffusion. The effect of pressure-induced diffusion (PID) becomes prominent once the concentration profile starts to develop. The inclusion of pressure-induced diffusion in the model may not have a large effect on the concentration profiles as shown by Zhang *et al.*,[34] but since the stress development depends upon the difference in concentration at different points inside the particle, the inclusion of PID does significantly affect the stress profiles. During intercalation (charging/uptake of lithium by graphite electrode), PID acts in parallel to concentration gradient-induced diffusion to make the concentration profile flatter, which relaxes the particle.[34]

In the first modeling category of strain splitting where intercalation-induced stresses are treated analogous to temperature-induced stresses (thermal analogy models), Zhang, *et al.*[34] presented a model that incorporated pressure-induced diffusion. In this model, the partial molar volume and

diffusion coefficient were assumed to be independent of the lithium concentration. Additionally, hydrostatic stress was assumed to be same as the thermodynamic pressure to simplify the pressure-induced diffusion term in the Stefan-Maxwell diffusion equation. These aforementioned assumptions enable decoupling of stress and concentration variables, resulting in a single partial differential equation for concentration. Stress profiles can then be calculated during post-processing from the lithium concentration profile. This approach makes the model very simple while capturing the basics of volume expansion in the particle within a lithium-ion battery. In this model, if pressure-induced diffusion is ignored then analytical results can be obtained for constant-current charging.[33]

Table 2-5: Governing equations for stresses given in Cheng and Verbrugge[33] (see Appendix C for derivation)

Governing Equation	
$\hat{\sigma}_r(\xi,t)=\frac{3\sigma_r(\xi,t)}{\left(\Omega_n E_n c^s_{\max,n}\right)/\left(1-\nu_n\right)}=\frac{2}{3}\left(\int_0^1 x_n(\xi,t)\xi^2 d\xi-\frac{1}{\xi^3}\int_0^\xi x_n(\xi,t)\xi^2 d\xi\right)$	(2.32)
$\hat{\sigma}_t(\xi,t)=\frac{3\sigma_t(\xi,t)}{\left(\Omega_n E_n c^s_{\max,n}\right)/\left(1-\nu_n\right)}=\left(2\int_0^1 x_n(\xi,t)\xi^2 d\xi+\frac{1}{\xi^3}\int_0^\xi x_n(\xi,t)\xi^2 d\xi-x_n(\xi,t)\right)$	(2.33)

Here σ_r is the radial stress, σ_t is the tangential stress, Ω_n is the partial molar volume of the solute, E_n is the Young's modulus, ν_n is the Poisson's ratio, $c^s_{\max,n}$ is the maximum lithium concentration in solid, ξ is the scaled radial coordinate, and x_n is the mole fraction of lithium in solid. The derivation of equations given in Table 2-5 is given in Appendix C.

In the second modeling category, the stress is divided into two components: elastic and thermodynamic. A very detailed and rigorous model had been developed by Christensen and Newman[32] to model volume expansion and contraction of lithium insertion compound that

calculates stresses due to intercalation and deintercalation of lithium. This model incorporates dependence of partial molar volume on the state of charge (SOC) as well as an experimentally measured thermodynamic factor that is again a function of the state of charge. Also, the model includes a moving boundary with non-ideal binary diffusion. Figure 2-6 compare stress profiles predicted by the different models available in the literature. The thermodynamic factor is assumed to be 1 in the model developed by Christensen and Newman[32] (that is, the open-circuit potential is purely Nernstian).

Comparison of different stress values obtained from different modeling approaches:

Numerical simulation was done for the intercalation of lithium in a carbon electrode for constant flux condition (Figure 2-6).

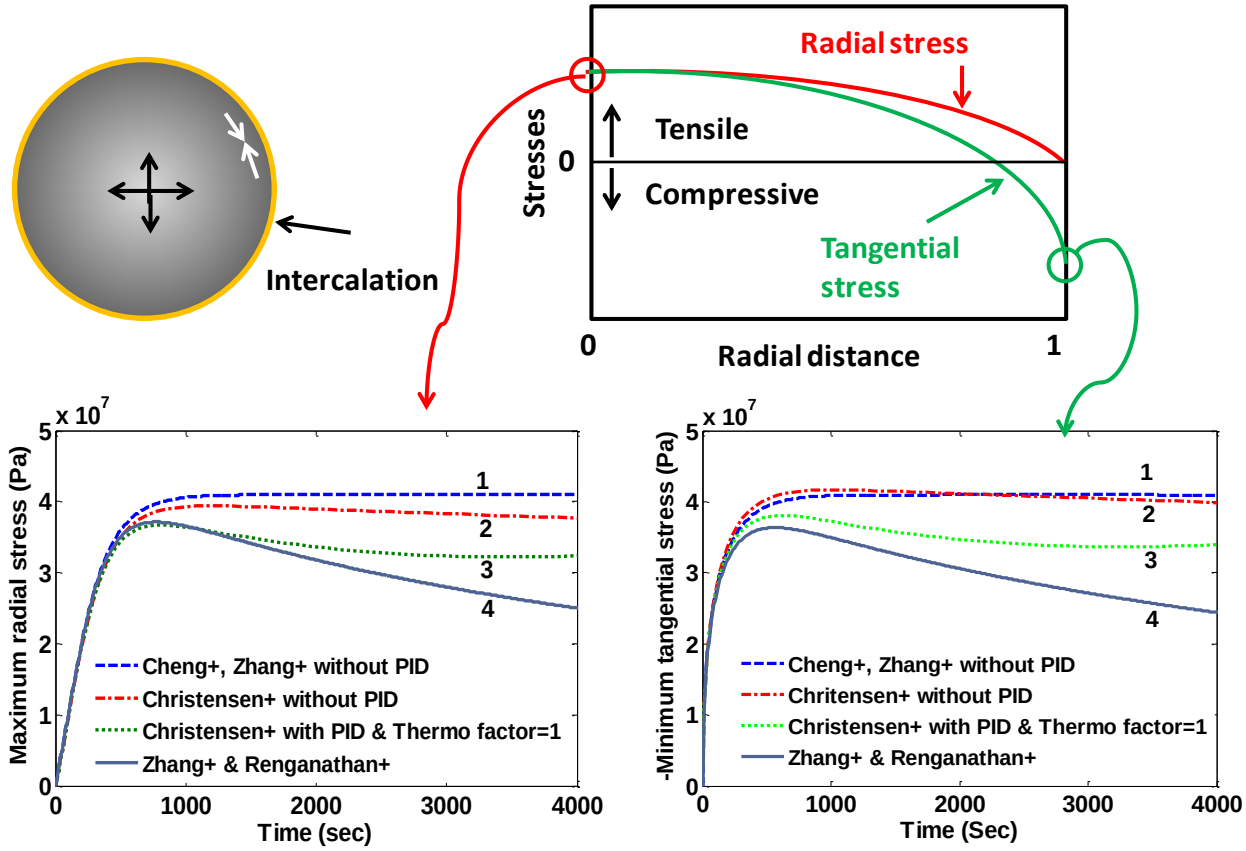

Figure 2-6: Simulation results of various models for intercalation induced stresses in a solid particle (intercalation)

Both radial and tangential stresses developed in the particle reach maxima and minima respectively

and then stay at that value when no pressure-induced diffusion is assumed in the first category of models (see blue curves in Figure 2-6). If pressure-induced diffusion is included in the model, magnitude of both stresses decrease (grey-blue curves in Figure 2-6). This decrease is due to the fact that during charging, PID works in parallel to the concentration gradient-induced diffusion and hence tries to make the concentration profile flatter, which in turn relaxes the particle. It is important to note that the peak stress occurs when the concentration at the center of the particle starts to change (that is, the concentration profile develops fully). Hence, the location of the peak will be majorly affected by the diffusion coefficient and the radius of the particle. The model developed by Christensen *et al.*[32] also shows similar results, but the difference becomes prominent as time passes. In the case of PID, magnitude of both the stresses attains extreme and then decreases but in the end the stress profiles flattens out (green curves in Figure 2-6) due to the incorporation of variable partial molar volume. In the case when PID is ignored, stress values decrease slightly after attaining maxima (red curves in Figure 2-6).

Equations shown in Table 2-5 will be used in each solid particle in P2D model to estimate the stresses at different locations of the anode and the cathode.

Due to the finite thickness of the anode, the pore wall flux becomes non-uniform except at very small rates of charging and discharging. This non-uniformity of the pore wall flux changes with time as well. In general, the pore wall flux is higher at the anode separator interface at the onset of charge/discharge of the battery; afterwards, the pore wall flux decreases at the anode-separator interface and increases at the anode-current collector interface. Due to the time-varying and thickness-dependent non-uniformity of the pore wall flux, different maximum peak stresses are observed at different times during charge/discharge. Usually, the anode-separator interface faces largest pore wall flux resulting in maximum peak stresses at that point compared to other locations

of the anode. Figure 2-7 shows the distribution of peak radial ($\hat{\sigma}_r$) and tangential stresses ($\hat{\sigma}_t$) at different locations in anode with time.

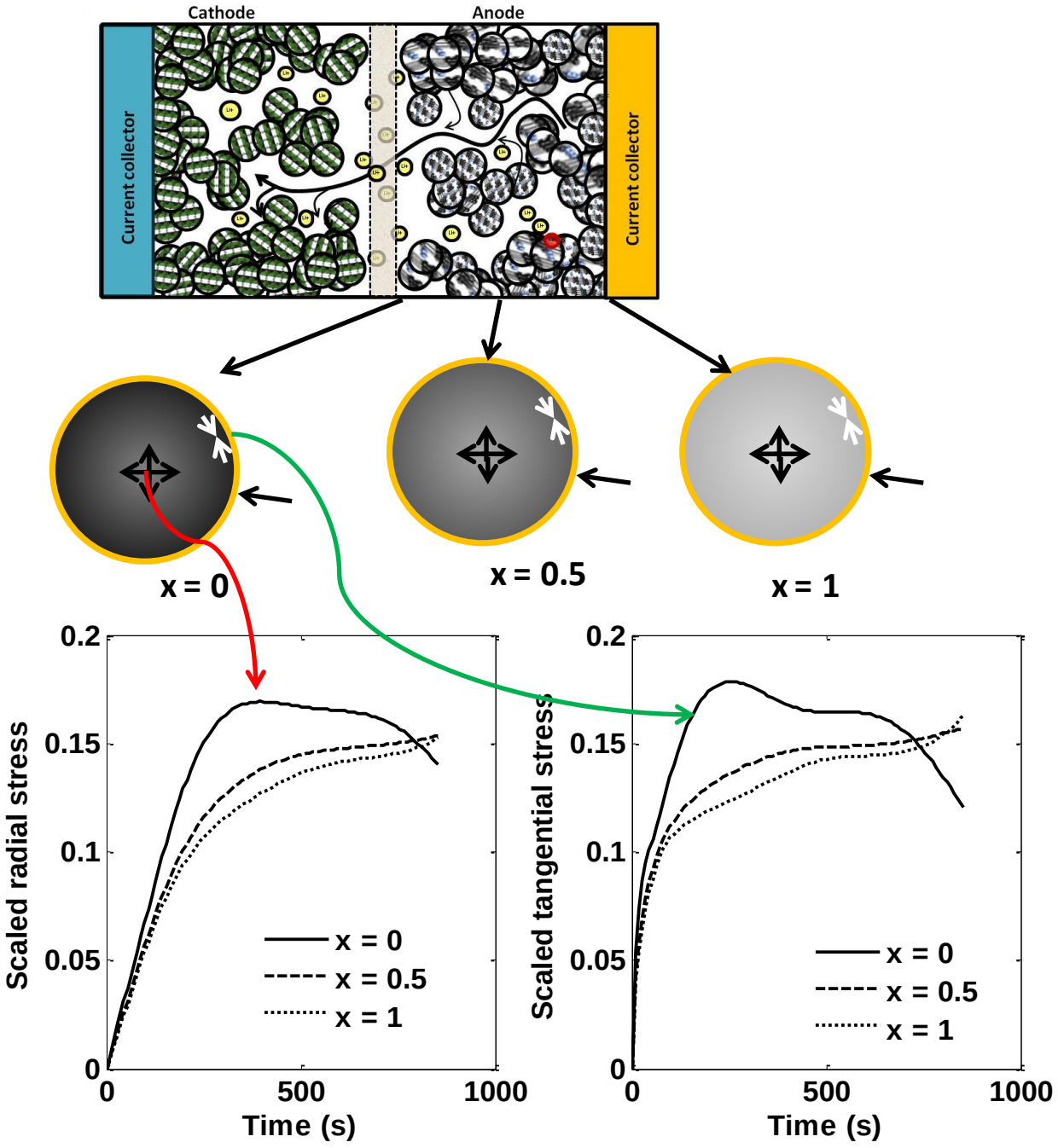

Figure 2-7: Distribution of radial and tangential stresses during charging at 4C at 25 C (x = 0 represent anode-separator interface and x = 1 represent anode-current collector interface)

It should be noted here that, when SPM is assumed, during intercalation at constant current, the

amount of lithium intake will remain same (flux will also remain same if volume expansion is ignored). Constant flux case will lead to saturation of stresses for SPM as can be seen for the case when pressure induced diffusion is ignored (Figure 2-6, dashed curves). The stress profiles in solid particles in P2D model shows variation as the flux at different points in time at different locations across the thickness of anode varies significantly. The anode-separator interface is most vulnerable to capacity fade due to stress as can be seen from Figure 2-7. Use of P2D model gives the advantage here compared to SPM model in quantifying the variation in stresses, while the SPM only gives average behavior, the P2D model quantifies the most vulnerable part of anode and cathode.

2.3.2 SEI Growth

As explained in the previous chapter (Figure 2-8), that the thermodynamic window of electrolyte is usually narrow than the anode and cathode electrochemical potentials. In that case, electrolyte (typically EC/PC/DMC with lithium salt) will decompose and form a passivating layer.

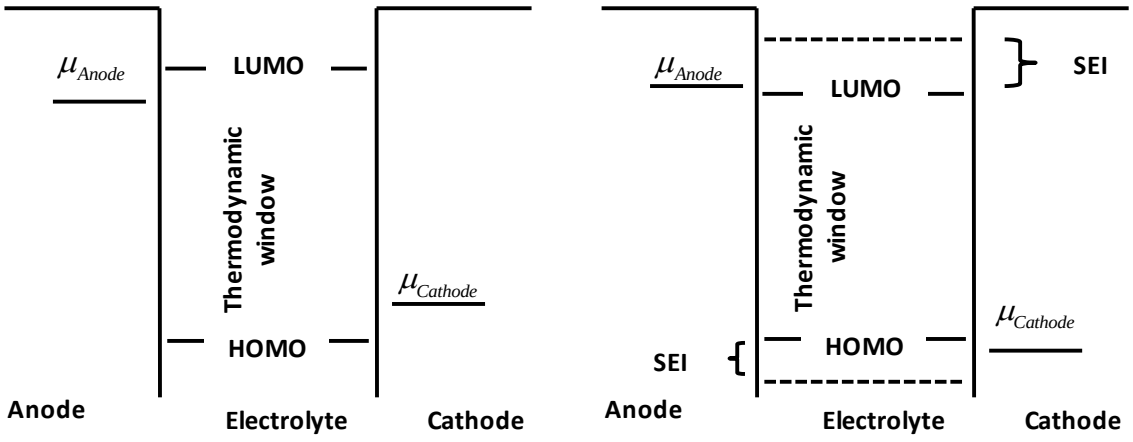

Figure 2-8: Left: ideal electrolyte having broader thermodynamic window, Right: formation of passivating layer due to smaller thermodynamic window of electrolyte (figure adapted from Goodenough and Park,[20] Copyright 2013, American Chemical Society)

The electrolyte for a typical lithium-ion battery consists of various carbonates (e.g. EC, PC, DMC, etc.). SEI formation due to the decomposition of EC by Safari *et al.*[56] is given in equations (2.34) and (2.35). The model assumes that EC molecule diffuses through the SEI layer to the SEI-

electrode interface where it may accept electron and react with lithium ion and form SEI layer. Note that the first step is only feasible when the LUMO level of EC is lower than the electrochemical potential of anode.

$$EC + e^- = EC^- \tag{2.34}$$

$$2EC^- + 2Li^+ = \left(CH_2OCO_2Li\right)_2 + C_2H_4 \tag{2.35}$$

Figure 2-9 shows the conceptual diagram of the formation of SEI layer compared to intercalation in graphite anode particle. During the first few cycles, charging and discharging of a battery is controlled to get desired SEI layer properties. As the thickness of SEI layer increases, diffusion of solvent molecules across it become more difficult, this leads to self-limiting growth in SEI layer.

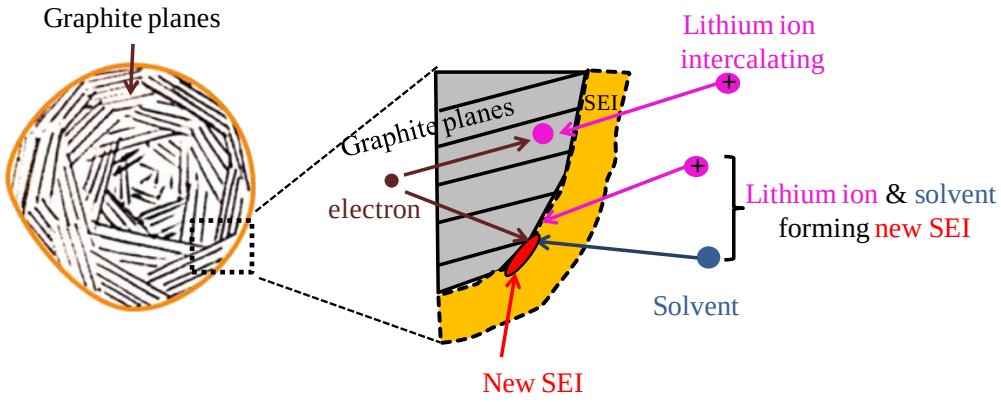

Figure 2-9: Left: graphite particle with SEI layer, Right: conceptual diagram of the formation of the SEI layer vis-à-vis intercalation, figure adapted from Pinson and Bazant[30]

Though, the growth in SEI layer is self-limiting; its magnitude is higher at higher charging rates or low charging rates at low temperatures. During the charging of a battery, the over-potential for SEI layer growth varies significantly. The variation is also predicted across the thickness of the electrodes. Similar to the case for stresses, the electrode-separator interface remains most vulnerable to SEI layer side reaction.

The overpotential for SEI reaction is given as[57]

$$\eta_{SEI}(x,t) = \phi_n^s(x,t) - \phi_e(x,t) - U_{SEI} - \left(\frac{\delta(x,t)}{\kappa_{SEI}} + \Re_{SEI}\right)\left(j_{SEI}(x,t) + j_n(x,t)\right)F\,. \quad (2.36)$$

Here, $\Re_{SEI}$ is the resistance of SEI layer formed during the initial cycles and $\delta(x,t)/\kappa_{SEI}$ refers to the increase in resistance during the fresh buildup of SEI layer, $\phi_n^s(x,t)$ is solid phase potential, $\phi_e(x,t)$ is the electrolyte phase potential, U_{SEI} is open circuit potential for SEI reaction (value ranges between 0.4 to 0.8 V), $j_{SEI}(x,t)$ is current density for SEI reaction and $j_n(x,t)$ is the current density for intercalation reaction. Various expressions are given for current density for SEI reaction.[30,56,57] Pinson and Bazant[30] gave the following expression for current density for SEI reaction on the anode side

$$j_{SEI} = -k_{SEI} c_{sol}^{0.5} c^{0.5} \exp\left(-\frac{\alpha}{FRT}\eta_{SEI}\right), \quad (2.37)$$

while Ramadass, *et al.*[57] gave expression based on kinetically limited model for anode side

$$j_{SEI} = -k_{SEI} \exp\left(-\frac{\alpha}{FRT}\eta_{SEI}\right). \quad (2.38).$$

The work presented in the dissertation shows a comparison of overpotentials wherever SEI layer is discussed. As can be seen from Figure 2-10, the overpotential for SEI reaction is higher in magnitude at $x = 0$ which is anode-separator interface, making it the most vulnerable part of anode for SEI reaction. At higher charging rate (or lower temperature) or at higher tortuosity, the variation between different points in anode is larger (see chapter 7 for more details)

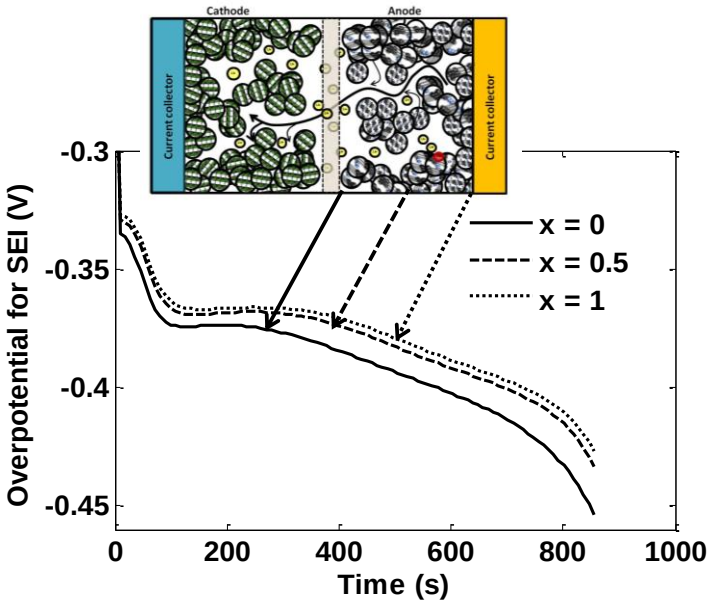

Figure 2-10: Distribution of overpotential for the SEI side reaction across the thickness of the anode during charging at 4C rate (x = 0 represents the anode-separator interface and x = 1 represents the anode-current collector interface)

2.3.3 Lithium-Plating Reaction

The lithium-plating side reaction not only causes capacity fade but also poses a significant safety issue.[11] As discussed briefly in Chapter 1 that lithium-ion batteries are inherently safer than lithium-metal batteries, as the former redueces dendrites formation during charging. The slightly more positive potential of LiC_6 compared to Li/Li^+ inherits the problem of lithium plating during charging[11] at high rates and even at low rates if the temperature is low (0.2 C at $-20\,^{\circ}\mathrm{C}$).[13,14]

The driving force for the partially irreversible[14] lithium plating side reaction at the anode can be expressed by the overpotential[58]

$$\eta_{plating}\left(x,t\right)=\phi_n^s\left(x,t\right)-\phi_e\left(x,t\right)-U_{plating,n}\,, \tag{2.39}$$

where $\eta_{plating}$ is the overpotential for lithium plating side reaction, $\phi_n^s(x,t)$ is the solid phase potential in negative electrode, $\phi_{e,n}(x,t)$ is the electrolyte-phase potential in anode, $U_{plating,n}$ is the open-circuit potential for the plating reaction which is taken to be zero, and x is the distance across

the electrode. The expression for $\eta_{plating}$ given in equation (2.39) ignores the voltage drop across the solid electrolyte interface (SEI) layer. For a uniform porosity anode, the anode-separator interface becomes most vulnerable to plating side reaction. Figure 2-11 shows the typical evolution of $\phi_n^s(x,t)-\phi_{e,n}(x,t)$ during charging.

Only when $\phi_n^s(x,t)-\phi_{e,n}(x,t)$ less than zero, the plating reaction is favored. Figure 2-11 shows that at anode-separator interface, the plating side reaction becomes feasible sooner and achieves larger magnitude compared to other parts of the anode

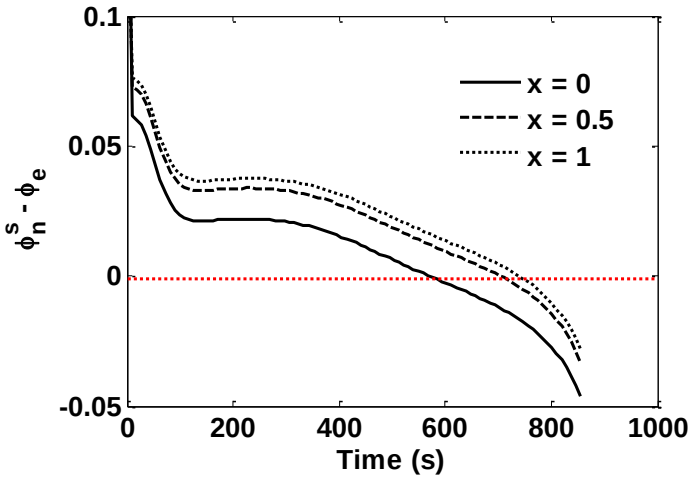

Figure 2-11: Distribution of overpotential for lithium plating side reaction across length during charging at 4C rate (x = 0 represent anode-separator interface and x = 1 represent anode-current collector interface)

2.4 Summary and Conclusions

This chapter presents the motivation for modeling and simulation efforts for the lithium-ion battery with emphasis given to chemical engineering based modeling. Two models, the SPM, and the P2D model are presented briefly with the reformulation approach to cut down on the computational burden of the P2D model. Capacity fade mechanisms based on intercalation induced stresses, SEI reaction, and plating reaction are discussed in details. Thermal degradation of the electrolyte is also a very important factor but due to lack of models in the literature, it is not presented here. The

absence of consensus over the expressions for current density for the SEI reaction is also an issue. The plating reaction is partially reversible[14] hence a reliable way to predict the buildup and depletion of plated lithium is also needed. This will require incorporating two or more competing reactions (e.g. intercalation, the SEI and the plating reaction, etc.) in the overall current density with the accurate expression for associated current densities.

List of symbols

a_i	Total surface area of electrode (m^2) in SPM and specific surface area in P2D model (m^2/m^3)
$Brugg$	Bruggeman coefficient
c_i^s	Solid-phase concentration
$c_{\max,i}^s$	Maximum solid-phase concentration
$c_{i,0}^s$	Initial solid-phase concentration
c, c_e	electrolyte concentration
c_{sol}	Solvent concentration (e.g. EC/PC/DMC)
C_p	Heat capacity
D_i^s	Solid-phase diffusivity
D	Intrinsic diffusivity of lithium ion in electrolyte
D_{eff}	Effective diffusivity of lithium ion in porous electrode
δ	Thickness of SEI layer
$E_a^{D_i^s}$	Activation energy for diffusivities
$E_a^{k_i}$	Activation energy for the reaction rate
E	Young's modulus
F	Faraday's constant
I, I_{overall}	Current (A/m^2 in P2D) and current (A, SPM) respectively
j_i	Pore wall flux ($mol/m^2/s$) in P2D and
j'	Rate of reaction ($mol/m^3/s$), Appendix A
κ	Liquid phase conductivity (intrinsic)
$k_{i,\text{ref}}$	Reference reaction rate constant
l_i	Region thickness
m	Total mass of the battery
η	Overpotential
ϕ_i^s, Φ_1	Solid-phase potential
$\phi_{e,i}$, Φ_2	Electrolyte-phase potential

$R_{P,i}$	Radius of solid particles in electrodes
R	Gas constant
R_{cell}	Effective resistance of the electrolyte
R	Radial coordinate
$\mathfrak{R}_{SEI}$	Resistance of SEI layer
σ	Solid phase intrinsic electronic conductivity
T_{ref} , T_{amb}	Reference and ambient temperature
θ	State of Charge
U	Open-circuit potential
$\varepsilon_{f,i}$	Filler fraction
ε_i	Porosity
A_{cross}	Cross-sectional area of the electrode
hA_{HT}	Heat transfer coefficient × area
Ω	Partial molar volume
ν	Poisson's ration
ξ	Scaled radial distance in anode particle $(r / R_{P,n})$

Subscripts:

eff	Effective, taking porous nature into account
e	Related to electrolyte
i	Take *n*, *p* and *s* for negative electrode, positive electrode and separator
n	Related to the negative electrode—the anode
p	Related to the positive electrode—the cathode
P	Related to particle (e.g. R_P radius of particle)
surf	Related to surface ($r = R_{P,i}$)
ref	Related to reference state
SEI	Relatead to SEI layer

List of Superscripts

s	Related to Solid Phase
+/−	Pertains to the boundary conditions from right and left side of the interface (e.g., L_p^-, L_p^+, etc.)

Chapter 3

Diffusion and Stress in Core-shell materials

> If people do not believe that mathematics is simple, it is only because they do not realize how complicated life is.
>
> **John von Neumann**

3.1 Introduction to the Core-Shell Materials

Core-shell composite structures are potential candidates for Li-ion battery electrodes as they can take advantage of materials with higher energy density and materials with higher cyclability. In order to meet energy demands and address environmental concerns, researchers are actively working on novel energy storage materials of which a significant fraction is dedicated to developing insertion materials for lithium ion batteries.[59-61] One way to achieve higher energy densities in lithium ion batteries is by replacing currently used graphite (theoretical storage capacity of 372 mAh/g) based anode with materials like silicon (theoretical storage capacity of 4200 mAh/g). While materials such as silicon and tin have high energy density compared to graphite, they suffer from high volumetric expansion (~400%) during intercalation/ deintercalation which results into pulverization and electrical isolation of the electrode materials. A change in volume of such magnitude causes delamination of the solid electrolyte interface (SEI) from the active material. Delamination and formation of new SEI layer at the exposed surface continuously consumes active materials resulting in faster capacity fade.[62] One way to take advantage of higher energy density materials is to develop core -shell composite materials where the shell materials have more favourable mechanical properties than the core. Si/C composite material in which

silicon is dispersed/coated in porous carbon has been made by several researchers.[60,62-67] To our knowledge, intercalation in core-shell materials has not been modelled and reported in the literature. Previous efforts by Subramanian and White[68] only included analysis of composite materials with two different diffusivities. However, if two different materials, such as Si/C, are used in core-shell configuration, interfacial dynamics cannot be ignored.

Subramanian and White[68] derived analytical solution under galvanostatic conditions for composite materials having concentration and flux continuity at the interface. This chapter extends the method adopted by Subramanian and White[68] for a general treatment at the interface of composite materials in order to make it useful for a wide variety of materials and configurations (e.g. core-shell configuration with flexibility of electrochemically active and inert core, hollow materials, etc.). We derive and present an analytical solution for isotropic diffusion in 1-dimension for rectangular, cylindrical and spherical core-shell particles. The results reported here can be used for Si, Ti or any core-shell or hollow material.

Section 2 gives a brief introduction to the diffusion problem in composite materials and intercalation induced stresses. Section 3 presents the solution methodology using the separation of variables approach for planar geometry and lists solutions for cylinder and sphere. Intercalation dynamics for several sets of transport parameters are presented in section 4. Section 5 illustrates the use of analytical solution for diffusion in quantifying intercalation induced stresses for spherical composite particle. Section 6 presents conclusion and future directions.

3.2 Background

Diffusion in heterogeneous media is an extensively studied problem in many branches of engineering. Heat conduction through heterogeneous media is typically studied where temperature

is continuous across interfaces.[69] Models for heat and mass transfer in biological tissues result in similar problems with discontinuous interface conditions.[70,71] Subramanian and White[68] presented analytical solution for composite material for galvanostatic boundary conditions with continuous concentration and flux at the interface. To our knowledge, none of the previous work considers the problem of diffusion in heterogeneous media with inhomogeneous boundary condition (constant flux arising from galvanostatic boundary condition at the surface where the electrochemical reaction occurs) and discontinuous interfacial concentration with associated kinetics, which is of the practical importance for novel composite battery materials. We consider the problem of diffusion in heterogeneous media composed of two different materials with different transport properties (diffusion coefficients, D_i) and associated interfacial dynamics (Figure 3-1).

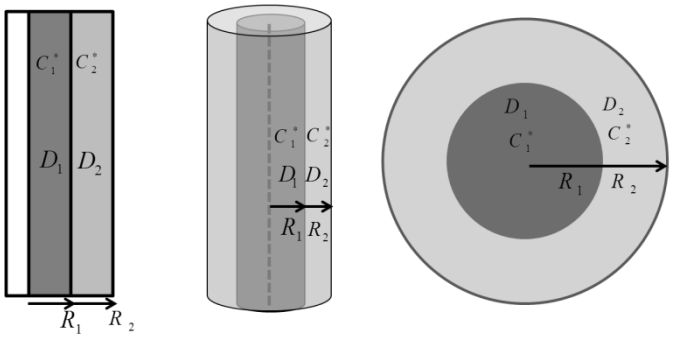

Figure 3-1: Composite geometries under consideration

Diffusion in composites with two materials can be classified into 4 possible scenarios depending on the ratio of diffusivity and equilibrium concentration (Figure 3-2). Cases A ($D_2/D_1>1$) and B ($D_2/D_1<1$) in Figure 3-2 with $c_1^*/c_2^*<1$, are very similar to the diffusion in sphere with single domain where the concentration in the inner core will always be smaller compared to the outer shell during intercalation. Interesting diffusion dynamics are observed in cases C ($D_2/D_1>1$) and

D ($D_2/D_1<1$) with $c_1^*/c_2^*>1$ which may cause the inner core of the particle to become more concentrated than the other shell.

In order to quantify the intercalation induced stresses for the four cases above, even the very basic treatment of stress will require three additional material properties: Young's modulus, Poisson's ratio and partial molar volume. Using a thermal analogy model for intercalation induced stresses assuming concentration independent material properties and ignoring volume expansion, decoupling of concentration and stress is possible.[33-35,72,73] Having all the parameters (diffusivity, equilibrium concentration, thickness, Young's modulus, Poisson's ratio, and partial molar volume) in a unified analytical framework to quantify stress will help guide the design of next generation energy storage materials.

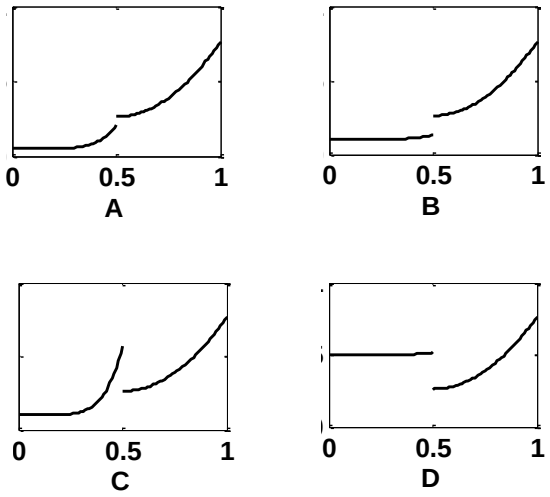

Figure 3-2: Possible diffusion dynamics in 2-region composite geometry

3.3 Model and Solution Methodology

Considering unsteady state diffusion, a material balance yields the following equation for concentration.

$$\frac{\partial c_i}{\partial t} = -\nabla \cdot N_i \tag{3.1}$$

Here i = 1 and 2 for region 1 and region 2, c_i is the concentration (mol/m^3), t is time (s) and N_i is molar flux (mol/s/m^2) which can be treated according to Fick's laws as

$$N_i = -D_i \nabla C_i \tag{3.2}$$

where D_i is diffusion coefficient (m^2/s). For simplicity, the model and method are illustrated for planar geometry. Assuming constant diffusivity and considering 1-dimensional diffusion of lithium for planar geometry, Eq. (3.1) can be written as

$$\frac{\partial c_i}{\partial t} = D_i \frac{\partial^2 c_i}{\partial r^2} \tag{3.3}$$

where r is axial distance. Transient diffusion in composite planar sheet consisting of two regions of different thicknesses and different diffusion coefficients (as described in Figure 3-1) can be described using the following equations

$$\frac{\partial}{\partial t} c_1(r,t) = D_1 \frac{\partial^2}{\partial r^2} c_1(r,t), \quad 0 < r < R_1 \tag{3.4}$$

$$\frac{\partial}{\partial t} c_2(r,t) = D_2 \frac{\partial^2}{\partial r^2} c_2(r,t), \quad R_1 < r < R_2 \tag{3.5}$$

where R_1 is the thickness of first region and $R_2 - R_1$ is the thickness of second region, D_1 and D_2 are the diffusion coefficients of the two regions. Initially both the regions are considered empty, i.e. species concentration is zero.

$$c_1(r,0)=0, \qquad c_2(r,0)=0 \text{ for all } r \tag{3.6}$$

Symmetry boundary condition (zero flux) can be used at the center

$$-D_1\frac{\partial}{\partial r}c_1(0,t)=0, \qquad t>0 \tag{3.7}$$

and galvanostatic boundary condition is considered at the surface $(r=R_2)$ where electrochemical intercalation and de-intercalation of lithium occurs.

$$-D_2\frac{\partial}{\partial r}c_2(R_2,t)=\frac{I_s}{nF}, \qquad t>0 \tag{3.8}$$

Here, I_s is the current density (A/m^2) which is a constant in case of galvanostatic charge/discharge condition, F is the Faraday's constant and n is the charge associated with the single ion of guest molecule (1 in case of lithium ion). At the interface $(r=R_1)$ between two regions, flux continuity condition is used.

$$-D_1\frac{\partial}{\partial r}c_1(R_1,t)=-D_2\frac{\partial}{\partial r}c_2(R_1,t), \quad t>0 \tag{3.9}$$

For the other boundary condition at the interface, Subramanian and White[68] considered continuity in concentration. This chapter considers a more general boundary condition which is relevant for core-shell composite materials having different capacities for lithium ions. Difference in interfacial concentration $(c_1-\kappa c_2)$ is related to local flux,[70,71] where κ is the ratio of equilibrium concentration (c_1^*/c_2^*).

$$D_1 \frac{\partial}{\partial r} c_1\left(R_1, t\right) = \ell\left[c_1\left(R_1, t\right) - \kappa c_2\left(R_1, t\right)\right], \qquad t > 0 \tag{3.10}$$

Where ℓ represents interfacial dynamics (m/s). Introducing dimensionless variables

$$x_1 = \frac{c_1}{c_0};\ x_2 = \frac{c_2}{c_0};\ X = \frac{r}{R_2};\ \tau = t \Big/ \left(\frac{R_2^2}{D_2}\right) \tag{3.11}$$

and the dimensionless parameters

$$\beta^2 = \frac{D_2}{D_1};\ \alpha = \frac{R_1}{R_2};\ \gamma = \frac{\ell R_2}{D_1};\ \delta = \frac{I_s R_2}{D_2 n F c_0} \tag{3.12}$$

The equations governing transport of lithium can be represented in the following nondimensional forms

$$\frac{\partial}{\partial \tau} x_1\left(X, \tau\right) = \frac{1}{\beta^2} \frac{\partial^2}{\partial X^2} x_1\left(X, \tau\right), \qquad 0 < X < \alpha \tag{3.13}$$

$$\frac{\partial}{\partial \tau} x_2\left(X, \tau\right) = \frac{\partial^2}{\partial X^2} x_2\left(X, \tau\right), \qquad \alpha < X < 1 \tag{3.14}$$

with initial and boundary conditions

$$x_1\left(X, 0\right) = x_2\left(X, 0\right) = 0 \text{ for all } X \tag{3.15}$$

$$\frac{\partial}{\partial X} x_1\left(0, \tau\right) = 0, \qquad \tau > 0 \tag{3.16}$$

$$\frac{\partial}{\partial X} x_2\left(1, \tau\right) = -\delta, \qquad \tau > 0 \tag{3.17}$$

$$\frac{\partial}{\partial X} x_1(\alpha,\tau) = \gamma\left(x_1(\alpha,\tau) - \kappa x_2(\alpha,\tau)\right), \qquad \tau > 0 \tag{3.18}$$

$$\frac{\partial}{\partial X} x_1(\alpha,\tau) = \beta^2 \frac{\partial}{\partial X} x_2(\alpha,\tau), \qquad \tau > 0 \tag{3.19}$$

Extending the methodology adopted by Subramanian and White[68], the following solution is proposed for this problem:

$$x_1(X,\tau) = g_1(X,\tau) + w_1(X) + v_1(\tau) \tag{3.20}$$

$$x_2(X,\tau) = g_2(X,\tau) + w_2(X) + v_2(\tau) \tag{3.21}$$

Let g_1 and g_2 satisfy the homogeneous boundary conditions and remaining terms satisfy the nonhomogeneous boundary conditions. Boundary conditions (Eqs. (3.16), (3.17), (3.18), and (3.19)) in terms of v_i, w_i and g_i can be written as

$$\frac{\partial}{\partial X} g_1(0,\tau) = 0, \text{ and } \frac{\partial}{\partial X} w_1(0) = 0, \qquad \tau > 0 \tag{3.22}$$

$$\frac{\partial}{\partial X} g_2(1,\tau) = 0 \text{ and } \frac{\partial}{\partial X} w_2(1) = -\delta, \qquad \tau > 0 \tag{3.23}$$

$$\begin{aligned} &\frac{\partial}{\partial X} g_1(\alpha,\tau) = \gamma\left(g_1(\alpha,\tau) - \kappa g_2(\alpha,\tau)\right), \text{ and} \\ &\frac{\partial}{\partial X} w_1(\alpha) = \gamma\left(w_1(\alpha) + v_1(\tau) - \kappa\left(w_2(\alpha) + v_2(\tau)\right)\right) \qquad \tau > 0 \end{aligned} \tag{3.24}$$

$$\frac{\partial}{\partial X} g_1(\alpha,\tau) = \beta^2 \frac{\partial}{\partial X} g_2(\alpha,\tau), \text{ and } \frac{\partial}{\partial X} w_1(\alpha) = \beta^2 \frac{\partial}{\partial X} w_2(\alpha), \qquad \tau > 0 \tag{3.25}$$

Substituting Eq. (3.20) into Eq. (3.13), the following equation is obtained.

$$\frac{\partial}{\partial \tau} g_1(X,\tau) + \frac{d}{d\tau} v_1(\tau) = \frac{1}{\beta^2} \frac{\partial^2}{\partial X^2} g1(X,\tau) + \frac{1}{\beta^2} \frac{d^2}{dX^2} w_1(X) \tag{3.26}$$

As g_1 satisfies the homogeneous part and, v_1 and w_1 satisfy nonhomogeneous parts, the following equations can be extracted from Eq. (3.26).

$$\frac{d}{d\tau} v_1(\tau) = \frac{1}{\beta^2} \frac{d^2}{dX^2} w_1(X) = k_1 \tag{3.27}$$

$$\frac{\partial}{\partial \tau} g_1(X,\tau) = \frac{1}{\beta^2} \frac{\partial^2}{\partial X^2} g_1(X,\tau) = -\lambda_1^2 \tag{3.28}$$

Here, k_1 and λ_1 are arbitrary constants. Solving Eq. (3.27) and (3.28) with boundary condition given by Eq. (3.22) gives the following solution

$$v_1(\tau) + w_1(X) = \frac{1}{2}\beta^2 k_1 X^2 + k_1 \tau + a_1 \tag{3.29}$$

$$g_1(X,\tau) = B_1 \cos(\lambda_1 \beta X) e^{-\lambda_1^2 \tau} \tag{3.30}$$

where a_1 and B_1 are integration constants. Similar equations can be derived for concentration in region 2 using Eq. (3.23) as boundary condition (using two arbitrary constants, λ_2 and k_2) as.

$$v_2(\tau) + w_2(X) = \frac{1}{2} k_2 X^2 - (\delta + k_2) X + k_2 \tau + a_2 \tag{3.31}$$

$$g_2(X,\tau) = B_2 \frac{\cos[\lambda_2 (X-1)]}{\sin(\lambda_2)} e^{-\lambda_2^2 \tau} \tag{3.32}$$

where a_2 and B_2 are integration constants. Eqs. (3.29), (3.30), (3.31), and (3.32) have eight constants ($a_1, a_2, k_1, k_2, \lambda_1, \lambda_2$, B_1 and B_2) to be determined using the initial condition and remaining boundary conditions at the interface ($X = \alpha$). Using expressions for w_1, w_2, v_1, v_2, g_1 and g_2 (Eqs. (3.29), (3.30), (3.31), and (3.32)) to solve for the interfacial boundary condition given by Eq. (3.24), gives rise to the following relations

$$\lambda_1 = \lambda_2 = \lambda \tag{3.33}$$

$$k_1 = \kappa k_2 \tag{3.34}$$

$$-\frac{1}{2}\gamma\kappa k_2\alpha^2 + \gamma\kappa\alpha\delta + \gamma\kappa\alpha k_2 - \gamma\kappa a_2 + \frac{1}{2}\beta^2\gamma k_1\alpha^2 + \gamma a_1 - k_1\alpha = 0 \tag{3.35}$$

$$\frac{B_1}{\cos(\alpha\lambda - \lambda)\gamma\beta\kappa} = \frac{B_2}{\sin(\lambda)\left(\beta\gamma\cos(\lambda\beta\alpha) + \lambda\sin(\lambda\beta\alpha)\right)} = A \tag{3.36}$$

The constant A is introduced to simplify the expressions. Second boundary condition at the interface (Eq.(3.25)) can be used to obtain the following relation

$$k_1 = \left(1 - \frac{1}{\alpha}\right)k_2 - \frac{\delta}{\alpha} \tag{3.37}$$

and the equation for obtaining eigenvalues (λ_n)

$$\frac{-\kappa}{\tan\phi_n} + \frac{\beta}{\tan\theta_n} + \frac{\lambda_n}{\gamma} = 0 \tag{3.38}$$

where $\theta_n = \alpha\lambda_n\beta$, $\phi_n = \lambda_n(\alpha - 1)$. The solution takes the form of infinite series

$$x_1(X,\tau)=\sum_{n=1}^{\infty}A_n\gamma\beta\kappa\cos\phi_n\cos(\lambda_n\beta X)\mathrm{e}^{-\lambda_n^2\tau}+\frac{1}{2}\beta^2k_1X^2+k_1\tau+a_1 \tag{3.39}$$

$$x_2(X,\tau)=\sum_{n=1}^{\infty}A_n(\beta\gamma\cos\theta_n+\lambda_n\sin\theta_n)\cos\left[\lambda_n(X-1)\right]\mathrm{e}^{-\lambda_n^2\tau}+\frac{1}{2}k_2X^2-(\delta+k_2)X+k_2\tau+a_2$$

(3.40)

In order to get one more equation for constants a_1 and a_2, initial conditions are used in integral form as

$$\int_0^{\alpha}x_1(X,0)dX+\int_{\alpha}^{1}x_2(X,0)dX=0 \tag{3.41}$$

which gives rise to the following equation.

$$(1-\alpha)a_2+a_1\alpha+\frac{1}{6}(\beta^2\kappa-1)k_2\alpha^3+\frac{1}{2}(k_2+\delta)\alpha^2-\frac{1}{2}\delta-\frac{1}{3}k_2=0 \tag{3.42}$$

Eqs. (3.37) and (3.34) can be used to solve for k_1 and k_2, while Eqs. (3.35) and (3.42) can be used to solve for a_1 and a_2.

$$a_1=\frac{\left[(\alpha^3\beta^2+3\alpha^3-6\alpha^2+3\alpha)(\kappa-1)+2\alpha^3(1-\beta^2)-3\alpha^2(1-\beta^2)+1\right]\kappa\delta}{6\left[\alpha(\kappa-1)+1\right]^2}+\frac{1}{\gamma}\frac{(\alpha-1)\alpha\kappa\delta}{\left[\alpha(\kappa-1)+1\right]^2}$$

(3.43)

$$a_2=\frac{\left[6\alpha^3(\kappa-1)^2-(2\alpha^3\beta^2-6\alpha^3-3\alpha)(\kappa-1)+2\alpha^3(1-\beta^2)+1\right]\delta}{6\left[\alpha(\kappa-1)+1\right]^2}+\frac{1}{\gamma}\frac{\alpha^2\kappa\delta}{\left[\alpha(\kappa-1)+1\right]^2}$$

(3.44)

$$k_1 = \kappa k_2 = -\frac{\kappa\delta}{\alpha(\kappa-1)+1} \tag{3.45}$$

For Sturm-Liouville problem of this type where the eigenfunctions are quasi-orthogonal, a constant is required to be multiplied in order to make the resultant system orthogonal. In this case κ serves the purpose.[74] The quasi-orthogonal eigenfunctions for this problem are as follows.

$$f_1(x) = \gamma\beta\kappa\cos\phi_n\cos(\lambda_n\beta X) \tag{3.46}$$

$$f_2(x) = (\beta\gamma\cos\theta_n + \lambda_n\sin\theta_n)\cos\left[\lambda_n(X-1)\right] \tag{3.47}$$

Initial conditions can be used to find the coefficients A_n using κ to make the eigenfunctions orthogonal.

$$\int_0^\alpha x_1(X,0)\,f_1(x)\,dX + \kappa\left(\int_0^\alpha x_2(X,0)\,f_2(x)\,dX\right) = 0 \tag{3.48}$$

The expression for A_n can be expressed as

$$A_n = \frac{2\beta\kappa\delta\cos\theta_n\cos\phi_n}{\chi_1^p\lambda_n\left(\chi_2^p\beta\kappa\cos^2\phi_n - \frac{1}{\gamma^2}\chi_3^p\left(\chi_4^p\right)^2\right)} \tag{3.49}$$

using the following relations

$$\chi_1^p = \kappa\gamma\cos\phi_n - \lambda_n\sin\phi_n \tag{3.50}$$

$$\chi_2^p = \cos\theta_n\sin\theta_n + \theta_n \tag{3.51}$$

$$\chi_3^p = \cos\phi_n\sin\phi_n + \phi_n \tag{3.52}$$

$$\chi_4^p = \beta\gamma\cos\theta_n + \lambda_n \sin\theta_n \tag{3.53}$$

Eqs. (3.39) and (3.40) are the analytical solution for diffusion in planar electrode where the constituents are given by equations (3.38), (3.43), (3.44), (3.45), (3.49), (3.50), (3.51), (3.52), and (3.53).

Cylindrical geometry

The governing equations for composites in non-dimensional form in cylindrical coordinates are

$$\frac{\partial}{\partial\tau}x_1(X,\tau) = \frac{1}{\beta^2}\frac{1}{X}\frac{\partial}{\partial X}\left(X\frac{\partial}{\partial X}x_1(X,\tau)\right), \qquad 0 \le X \le \alpha \tag{3.54}$$

$$\frac{\partial}{\partial\tau}x_2(X,\tau) = \frac{1}{X}\frac{\partial}{\partial X}\left(X\frac{\partial}{\partial X}x_1(X,\tau)\right), \qquad \alpha < X \le 1 \tag{3.55}$$

The initial and boundary conditions in this case can be expressed using Eqs. (3.6), (3.7), (3.8), (3.9), and (3.10). Using similar approach, the solution for cylindrical coordinate system can be represented as:

$$x_1(X,\tau) = \sum_{n=1}^{\infty} A_n \chi_2^c J_0(\beta\lambda_n X)\mathrm{e}^{-\lambda_n^2\tau} + \frac{1}{4}k_1\beta^2X^2 + k_1\tau + a_1 \qquad 0 \le X \le \alpha \tag{3.56}$$

$$x_2(X,\tau) = \sum_{n=1}^{\infty} A_n \chi_1^c \lambda_n \left[J_1(\lambda_n)Y_0(\lambda_n X) - Y_1(\lambda_n)J_0(\lambda_n X)\right]\mathrm{e}^{-\lambda_n^2 t} + \frac{k_2X^2}{4} - \left(\delta + \frac{k_2}{2}\right)\ln(X) + k_2\tau + a_2 \tag{3.57}$$

Here $J_\alpha(\bullet)$ and $Y_\alpha(\bullet)$ are the Bessel functions of first and second kind respectively. The eigenvalues are the positive roots of following equation

$$\beta^2 \chi_2^c J_0(\theta_n) + \chi_1^c \left(\beta^2 \kappa \lambda_n \left[Y_1(\lambda_n) J_0(\lambda_n \alpha) - J_1(\lambda_n) Y_0(\lambda_n \alpha) \right] + \frac{\beta \lambda \chi_2}{\gamma} \right) = 0 \tag{3.58}$$

where $\theta_n = \alpha \lambda_n \beta$. The summation coefficient is given as

$$A_n = \frac{2 J_1(\theta_n) \delta \kappa}{\lambda_n{}^2 \pi \left(\frac{\left(\chi_1^c\right)^2 \alpha^2}{2} \left[J_0^2(\theta_n) + J_1^2(\theta_n) \right] + J_1^2(\theta_n) \lambda_n{}^2 \kappa \left[\chi_2^c Y_1^2(\lambda_n) + \chi_4^c J_1(\lambda_n) Y_1(\lambda_n) + \chi_3^c J_1^2(\lambda_n) \right] \right)} \tag{3.59}$$

where

$$\chi_1^c = \beta \lambda_n \left[Y_1(\lambda_n \alpha) J_1(\lambda_n) - J_1(\lambda_n \alpha) Y_1(\lambda_n) \right] \tag{3.60}$$

$$\chi_2^c = \frac{1}{2} \left[J_0^2(\lambda_n) - \alpha^2 \left(J_1^2(\lambda_n \alpha) + J_0^2(\lambda_n \alpha) \right) \right] \tag{3.61}$$

$$\chi_3^c = \frac{1}{2} \left[Y_0^2(\lambda_n) - \alpha^2 \left(Y_1^2(\lambda_n \alpha) + Y_0^2(\lambda_n \alpha) \right) \right] \tag{3.62}$$

$$\chi_4^c = \alpha^2 \left[Y_0(\lambda_n \alpha) J_0(\lambda_n \alpha) + J_1(\lambda_n \alpha) Y_1(\lambda_n \alpha) \right] - Y_0(\lambda_n) J_0(\lambda_n) \tag{3.63}$$

and the constants are given as

$$k_1 = \kappa k_2 = \frac{-2 \kappa \delta}{\alpha^2 (\kappa - 1) + 1} \tag{3.64}$$

$$a_1 = \frac{\left[\begin{array}{l} 4\alpha^2 (1-\kappa) \ln(\alpha) - \left(\beta^2 (2-\kappa) + 1 - 2\kappa \right) \alpha^4 \\ + \left(\beta^2 - \kappa \right) 2\alpha^2 + 1 \end{array} \right] \delta \kappa}{4 \left(\alpha^2 (\kappa - 1) + 1 \right)^2} + \frac{\left(\alpha^2 - 1 \right) \alpha \delta \kappa}{\left(\alpha^2 (\kappa - 1) + 1 \right)^2 \gamma} \tag{3.65}$$

$$a_2 = \frac{a_1}{\kappa} + \frac{\delta\alpha}{2}\left[\frac{2}{\gamma\left(\alpha^2(\kappa-1)+1\right)} + \frac{\left[(\kappa-1)2\alpha\ln(\alpha)+\alpha\left(1-\beta^2\right)\right]}{\left(\alpha^2(\kappa-1)+1\right)}\right] \tag{3.66}$$

Spherical geometry

As described in detail for the rectangular core-shell, one can derive the solution for isotropic radial diffusion for spherical composite particle. For spherical system the governing equations are

$$\frac{\partial}{\partial\tau}x_1(X,\tau) = \frac{1}{\beta^2}\frac{1}{X^2}\frac{\partial}{\partial X}\left(X^2\frac{\partial}{\partial X}x_1(X,\tau)\right), \qquad 0 \le X \le \alpha \tag{3.67}$$

$$\frac{\partial}{\partial\tau}x_2(X,\tau) = \frac{1}{X^2}\frac{\partial}{\partial X}\left(X^2\frac{\partial}{\partial X}x_1(X,\tau)\right), \qquad \alpha < X \le 1 \tag{3.68}$$

The initial and boundary conditions can be expressed using Eqs (3.6), (3.7), (3.8), (3.9), and (3.10) . The solution for spherical geometry can be derived as

$$x_1(X,\tau) = \sum_{n=1}^{\infty} -A_n\frac{\chi_2^s\beta^2}{\lambda_n}\left(\frac{\sin(\lambda_n\beta X)}{X}\right)e^{-\lambda_n^2\tau} + \frac{1}{6}k_1\beta^2X^2 + k_1\tau + a_1 \tag{3.69}$$

$$\begin{aligned} x_2(X,\tau) = \sum_{n=1}^{\infty} -A_n\frac{\chi_1^s}{\lambda_n}\left(\frac{\lambda_n\cos\left[\lambda_n(X-1)\right]+\sin\left[\lambda_n(X-1)\right]}{X}\right)e^{-\lambda_n^2\tau} \\ + \frac{1}{6}k_2X^2 + \frac{1}{X}\left(\delta+\frac{1}{3}k_2\right) + k_2\tau + a_2 \end{aligned} \tag{3.70}$$

where eigenvalues are the roots of following equation (using $\theta_n = \alpha\lambda_n\beta$, and $\phi_n = \lambda_n(\alpha-1)$).

$$\left(\theta_n^2-\frac{\theta_n^2}{\lambda_n\tan\phi_n}\right)+\left(\alpha+\frac{\alpha\lambda_n}{\tan\phi_n}\right)\left(\beta^2-\kappa+\frac{\theta_n\kappa}{\tan\theta_n}\right)+\frac{1}{\gamma}\left(1-\frac{\theta_n}{\tan\theta_n}\right)\left(\alpha\lambda_n^2+1-\frac{\phi_n}{\tan\phi_n}\right)=0 \tag{3.71}$$

The summation coefficients are given as follows:

$$A_n=\frac{2\chi_1^s\delta\kappa\lambda_n}{\left[\beta^3\left(\chi_2^s\right)^2\chi_3^s-\chi_4^s\left(\chi_1^s\right)^2\kappa\right]} \tag{3.72}$$

where the constituents are given as

$$\chi_1^s=\theta_n\cos\theta_n-\sin\theta_n \tag{3.73}$$

$$\chi_2^s=\phi_n\cos\phi_n-\left(\alpha\lambda_n{}^2+1\right)\sin\phi_n \tag{3.74}$$

$$\chi_3^s=\cos\theta_n\sin\theta_n-\theta_n \tag{3.75}$$

$$\chi_4^s=\left(1-\lambda_n{}^2\right)\cos\phi_n\sin\phi_n+2\lambda_n\cos^2\phi_n-\phi_n\lambda_n{}^2-\left(\alpha+1\right)\lambda_n \tag{3.76}$$

Values of constants (a_1, a_2, k_1, and k_2) in this case turn out to be

$$k_1=\kappa k_2=\frac{-3\kappa\delta}{\alpha^3\left(\kappa-1\right)+1} \tag{3.77}$$

$$a_1=\frac{\left[\left(\left(-3\beta^2-5\right)\alpha^5+15\alpha^3-10\alpha^2\right)\left(1-\kappa\right)+\left(1-\beta^2\right)\left(2\alpha^3+5\right)\alpha^2+3\right]\delta\kappa}{10\left[\alpha^3\left(\kappa-1\right)+1\right]^2}+\frac{\left(\alpha^3-1\right)\alpha\delta\kappa}{\left[\alpha^3\left(\kappa-1\right)+1\right]^2\gamma} \tag{3.78}$$

$$a_2 = -\frac{\left[10\alpha^5(1-\kappa)^2 + \left(\left(-2\beta^2+10\right)\alpha^5 - 15\alpha^3\right)(1-\kappa) - \left(1-\beta^2\right)2\alpha^5 - 3\right]\delta}{10\left[\alpha^3(\kappa-1)+1\right]^2} + \frac{\kappa\alpha^4\delta}{\left[\alpha^3(\kappa-1)+1\right]^2\gamma} \tag{3.79}$$

3.4 Results and Discussion

This section presents transient concentration profiles for spherical core-shell particle. Though the solution is general enough to describe slower interfacial dynamics, for illustration purposes, only cases with very fast interfacial kinetics ($\gamma \gg 1$) are discussed. Three different sets of parameter values are chosen to visualize the diffusion dynamics that resemble to cases B, C and D in Figure 3-2.

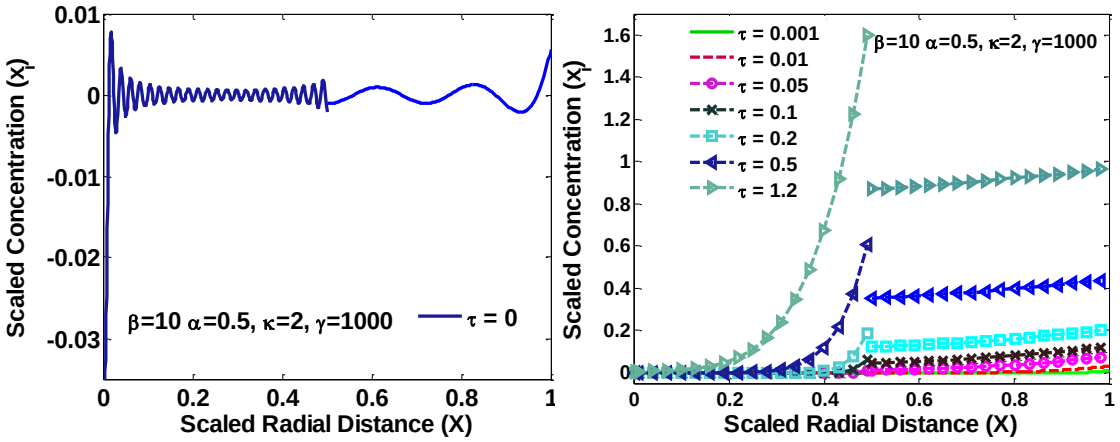

Figure 3-3: (Left) concentration at t = 0, (Right) concentration profiles during intercalation

Figure 3-3 presents concentration profiles for β >1 and κ >1 (equivalent to case C in Figure 3-2). For κ =2, the interfacial concentration in the core will be twice compared to the interfacial concentration in the shell. Moreover two orders of magnitude difference in diffusivity ($\beta^2 = D_2/D_1 = 100$) will create steep concentration gradients in the core which will lead to

significant stress development in the particle. The initial concentration at t =0 (Gibb's Phenomena), is also shown in following Figs. 3-8.

Figure 3-4 describes the concentration profiles for β =1 and κ >1 (close to case D in Figure 3-2). The choice of above parameters leads to interesting situation of having the inner core more concentrated than the shell. This situation can never occur in single domain spherical charging with nonnegative current. One interesting difference in the current case versus the previous case is that despite having κ greater than one, the average concentration in inner core is smaller than the shell for the previous case. This phenomenon will alter the stress dynamics discussed in the following section.

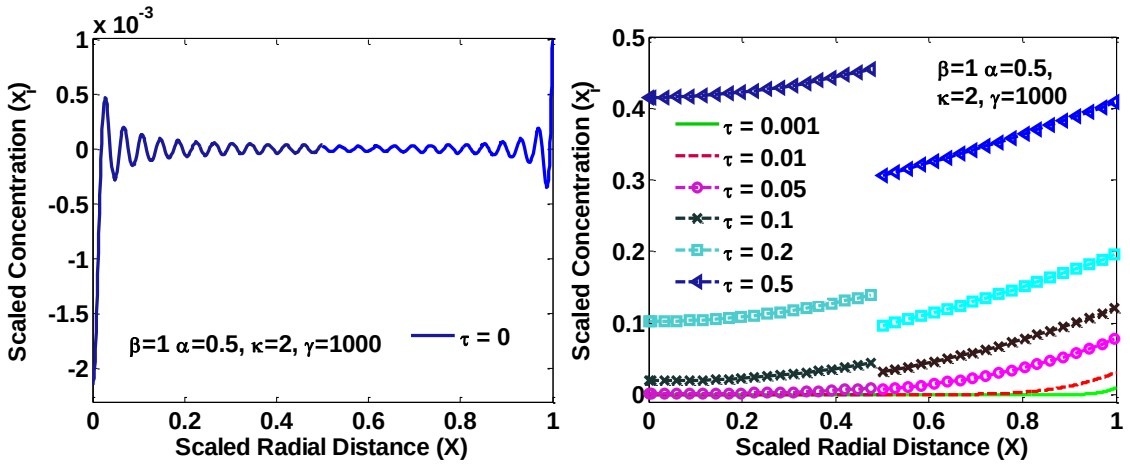

Figure 3-4: (Left) concentration at t = 0, (Right) concentration profiles during intercalation at different time

Figure 3-5 describes the concentration profiles for β <1 and κ <1 (equivalent to case B in Figure 3-2). As the inner core has higher diffusion coefficient than the outer shell, a flat concentration profile is expected in the inner core.

Cases with $\kappa < 1$ are similar to diffusion in a sphere with single domain as the inner core will always have lower concnetration than the outer core. But interesting stress profiles can be seen in

these cases depending on the values of partial molar volume (Ω). For example, three cases can be visualized for $\Omega_{core}/\Omega_{shell} < \kappa$, $\Omega_{core}/\Omega_{shell} = \kappa$, $\Omega_{core}/\Omega_{shell} > \kappa$ that will generate different stress profiles.

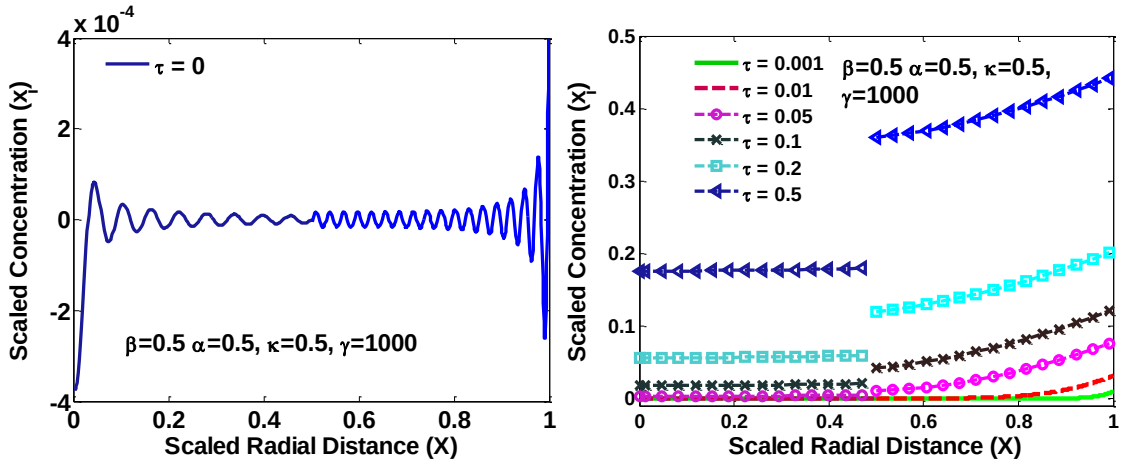

Figure 3-5: (Left) concentration at t = 0, (Right) concentration profiles during intercalation at different time

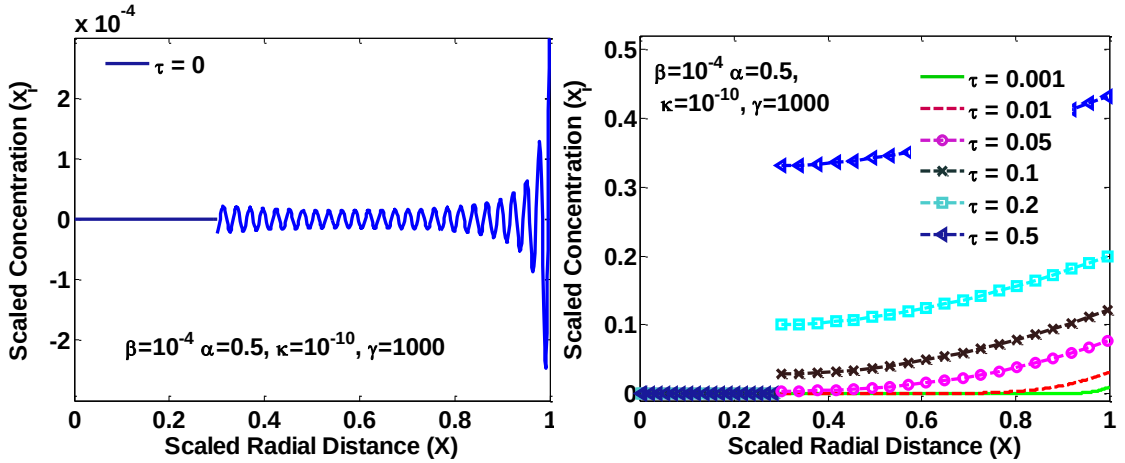

Figure 3-6: (Left) concentration profiles at t = 0, (Right) concentration profiles during intercalation at different time in a hollow sphere (inert core)

Next, we demonstrate the use of derived solution to describe transport in special cases. For example, choice of $\kappa \ll 1$ can mimic the transport of lithium in hollow spherical particle or particle with inert core, Figure 3-6 shows the concentration profiles in a hollow sphere using $\kappa = 10^{-10}$, and $\beta = 10^{-4}$.

Similarly, using $\kappa = 2$, $\beta = 1$, $\gamma \gg 1$, the solution derived by Subramanian and White[68] can be constructed (Figure 3-7) suggesting the validity and flexibility of the model developed. Lastly, using $\kappa = 1$, $\beta = 1$, and $\gamma \gg 1$, solution for diffusion in a sphere with single domain can be obtained (Figure 3-8). The model developed shows that while very little changes may be observed in the charge discharge curves (qualitatively), situation deep inside the core shell material can be very different from the spherical particle case with the same material.

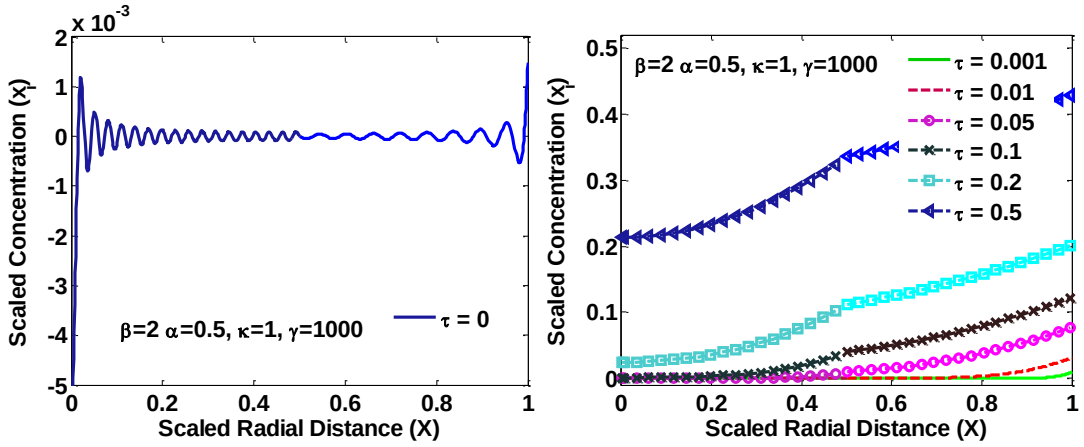

Figure 3-7: (Left) concentration at t = 0, (Right) concentration profiles during intercalation at different time in sphere with continuous concentration at the interface

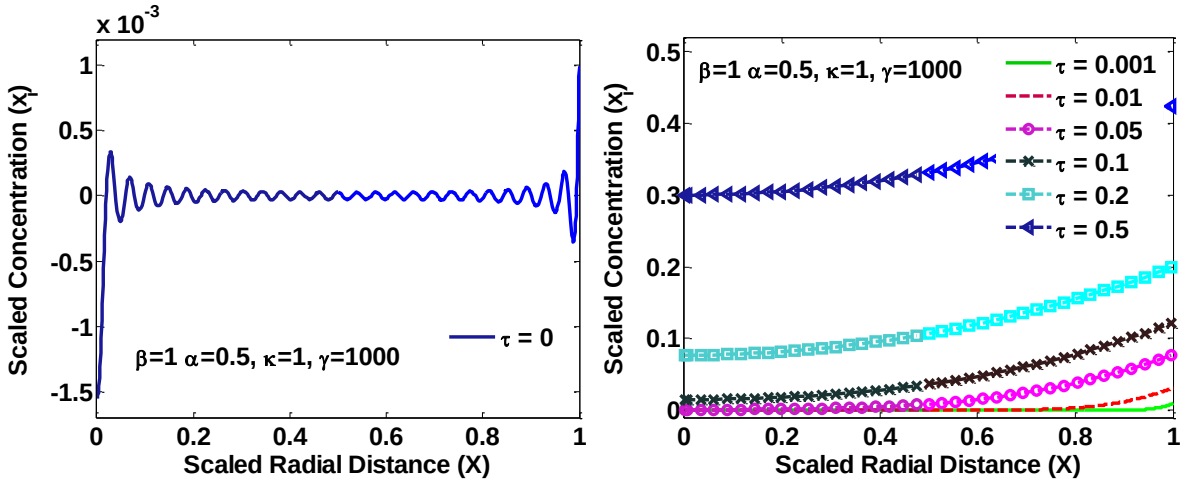

Figure 3-8: (Left) concentration at t = 0, (Right) concentration profiles during intercalation at different time with core and shell having exact same material properties

3.5 Stress Estimation in Core-Shell Composite Particles

One of the reasons for designing core-shell type composite electrode materials is to circumvent the pulverization of high energy materials with high volumetric expansion. Intercalation induced stress generation is one of the main reasons for capacity fade. Models to quantify intercalation-induced stress can be divided into two categories: strain splitting[33-35,73] and stress splitting.[31,32] The theory of the strain splitting approach has been developed by Timoshenko[75] where thermal stresses have been modeled using strain splitting, with these models being called *thermal analogy models*. Here, the intercalation-induced stresses are treated in similar way as the temperature-induced stresses. A very detailed model that used stress splitting was developed by Christensen *et al.*,[31,32] which was shown to be equivalent to the former approach (strain splitting) by Timoshenko.[75] In both categories, different models can be obtained depending upon the inclusion of pressure-induced diffusion. Inclusion of pressure induced diffusion results in nonlinear partial differential equations (PDEs). It is very difficult to apply analytical treatment to such PDEs, hence this chapter focuses on stress calculation ignoring pressure induced diffusion and using strain splitting method. Detailed description of strain-splitting method to model intercalation induced stresses in spherical geometry with isotropic radial diffusion can be found in literature.[33-35,73] Deshpande *et al.*[73] presented analytical expressions for the intercalation-induced stresses developed in a spherical particle with moving phase boundary assuming lithium concentration independent material properties (Young's modulus (E), partial molar volume (Ω), Poisson's ratio (ν) and neglecting volume expansion. These assumptions may not give accurate description for systems with high volume expansion (e.g. Silicon), but they allow analytical treatment of the problem and decouple concentration and stresses. Expressions are listed in dimensionless form for radial (σ_r) and

tangential stresses (σ_t) in both regions of the isotropic spherical particle with only radial diffusion, derivation of these equations can be found in Deshpande *et al.*[73] Defining following expressions

$$Q_1(X) = \int_0^X \xi^2 x_1(\xi)\, d\xi \tag{3.80}$$

$$Q_2(X) = \int_\alpha^X \xi^2 x_2(\xi)\, d\xi \tag{3.81}$$

where ξ is a dummy integration variable, $x_i = c_i / c_0$ and introducing the dimensionless variables

$$\hat{\sigma}_{r_i} = \frac{\sigma_{r_i}}{\Xi};\ \hat{\sigma}_{t_i} = \frac{\sigma_{t_i}}{\Xi} \tag{3.82}$$

where $\Xi = c_0 \Omega_2 E_2$ and the dimensionless parameters

$$\Theta = \frac{E_1}{E_2};\ \Pi = \frac{\Omega_1}{\Omega_2} \tag{3.83}$$

the dimensionless radial and tangential stress can be expressed as

$$\sigma_{r_1}(X) = \frac{2}{3}\frac{\Pi\Theta}{(1-\nu_1)}\left(\frac{\Delta_2}{\alpha^3\Delta_1} Q_1(\alpha) - \frac{1}{X^3} Q_1(X) - \frac{3(1-\nu_1)}{\Delta_1\Pi} Q_2(1) \right), 0 < X < \alpha \tag{3.84}$$

$$\sigma_{t_1}(X) = \frac{2}{3}\frac{\Pi\Theta}{(1-\nu_1)}\left(\frac{\Delta_2}{\alpha^3\Delta_1} Q_1(\alpha) - \frac{3(1-\nu_1)}{\Pi\Delta_1} Q_2(1) + \frac{1}{2}\frac{Q_1(X)}{X^3} - \frac{1}{2} x_1(X) \right), 0 < X < \alpha \tag{3.85}$$

$$\sigma_{r_2}(X) = \frac{2}{3(1-\nu_2)}\left(\begin{array}{l} \dfrac{3\Theta\Pi(1-X^3)(1-\nu_2)}{\Delta_1 X^3} Q_1(\alpha) \\ + \left(\dfrac{2\alpha^3\Delta_3}{\Delta_1 X^3} - \dfrac{\Delta_4}{\Delta_1} \right) Q_2(1) - \dfrac{Q_2(X)}{X^3} \end{array} \right), \alpha < X < 1 \tag{3.86}$$

$$\sigma_{t_2}(X)=\frac{1}{(1-\nu_2)}\left(\begin{array}{l}\dfrac{Q_2(X)}{3X^3}-\dfrac{x_2(X)}{3}-\dfrac{\Theta\Pi(1-\nu_2)}{\Delta_1}\left(2+\dfrac{1}{X^3}\right)Q_1(\alpha)\\ -\left(\Delta_4+\dfrac{\Delta_3\alpha^3}{X^3}\right)\dfrac{2Q_2(1)}{3\Delta_1}\end{array}\right),\alpha<X<1 \tag{3.87}$$

where

$$\Delta_0=\left[2(2\nu_2-1)\alpha^3-(1+\nu_2)\right]\Theta,\qquad \Delta_1=\Delta_0+2(1-\alpha^3)(2\nu_1-1),\qquad \Delta_2=\Delta_0+(1-\alpha^3)(1+\nu_1),$$

$\Delta_3=(2\nu_2-1)\Theta+1-2\nu_1$, and $\Delta_4=(1+\nu_2)\Theta+2(1-2\nu_1)$

Three scenarios are discussed using $\delta=-0.25$ (intercalation). First, a core-shell particle with continuous concentration profiles using $\kappa=1$, and $\gamma\gg1$ is considered (Figure 3-7 and 3-8). Then, stress generation in core-shell particles with discontinuous concentration (specifically $\kappa>1$) are presented (Figure 3-3 and Figure 3-4) followed by hollow sphere (Figure 3-6)

Core-shell sphere with continuous concentration at the interface ($\kappa=1,\ \gamma\gg1$):

If transport and mechanical properties of both the regions are assumed to be equal with fast interfacial dynamics (i.e. $\kappa=1,\ \beta=1,\ \Pi=1,\ \Theta=1$, and $\nu_1=\nu_2$), the resultant configuration will denote diffusion and stress generated in a sphere with single domain. Figure 3-8 shows the concentration distribution and Figure 3-9 shows the radial and tangential stresses. Such a simplification gives rise to the basic understanding of intercalation induced stresses in a particle. The radial and tangential stresses are mainly dependent on some representation of the gradient of concentration profiles (difference between average concentration up to the point of interest and total average concentration). As the short time dynamics start to fade out (around τ =0.2 in Figure 3-8), the stress profiles start to saturate reaching a maxima (Figure 3-9), which is expected as the steepness of profiles remains constant afterwards. Positive values of stress represent tensile stress

and negative values denote compressive stress. The concentration profiles make the outer layers expand more compared to inner layers resulting in tensile radial stress during intercalation at every point in *X*. Tangential stresses on the other hand are compressive at the surface and tensile at the center. The peak compressive stress occurs at the surface and peak tensile stress at the center of the particle and the locations for peak stresses do not change during intercalation.

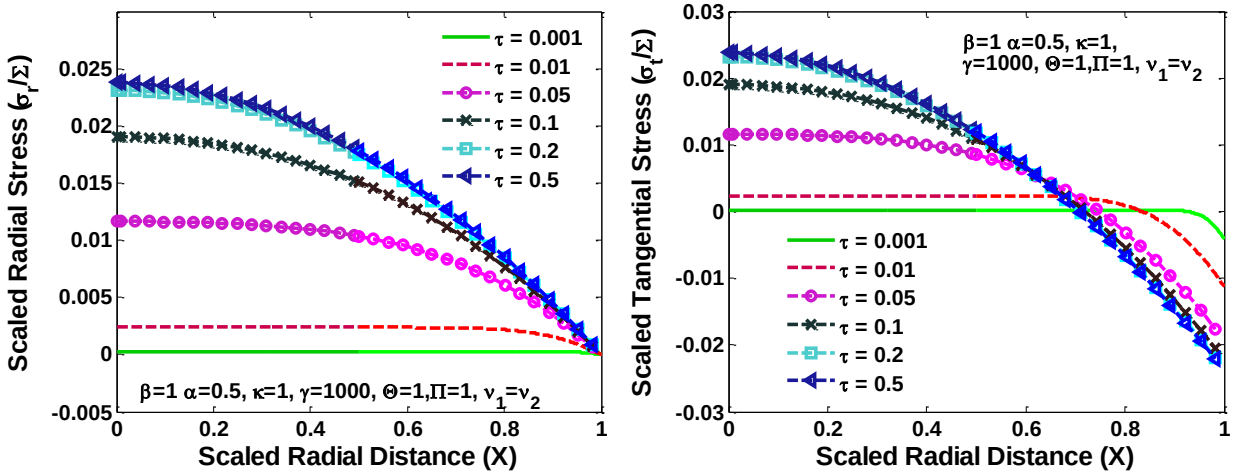

Figure 3-9: Radial and tangential stresses during galvanostatic intercalation in spherical particle of single domain

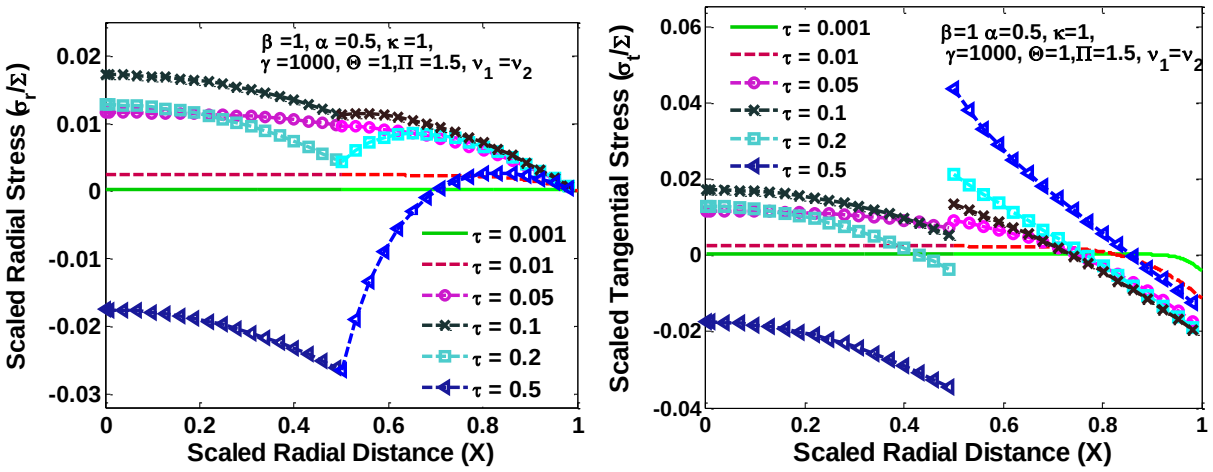

Figure 3-10: Radial and tangential stresses during galvanostatic intercalation in spherical particle with higher partial molar volume for the core

Saturation of stresses to a maximum value is due to uniform partial molar volume for both materials. If partial molar volume of the inner core is assumed to be larger than the outer shell (i.e. $\Pi > 1$) keeping other parameters same, the stress profiles will change drastically even though the concentration profiles will remain the same. After the short time dynamics die out, the inner core will have to face more expansion due to higher partial molar volume facing resistance from the shell while expanding, which will result in compressive nature of radial and tangential stresses at the center. As can be seen from Figure 3-10, the peak radial and tangential stresses at the center go through a maxima and then change from tensile to compressive. Location and nature of peak stresses for the inner core also changes from the center to the interface and from tensile to compressive.

Similarly, if the partial molar volume of the core is small compared to the shell (i.e. $\Pi < 1$), the radial stress will remain positive (tensile stress) at every point in *X* and keep increasing. Tangential stress in the core will also remain positive but at the interface, it will go through a maxima and then change from tensile to compressive.

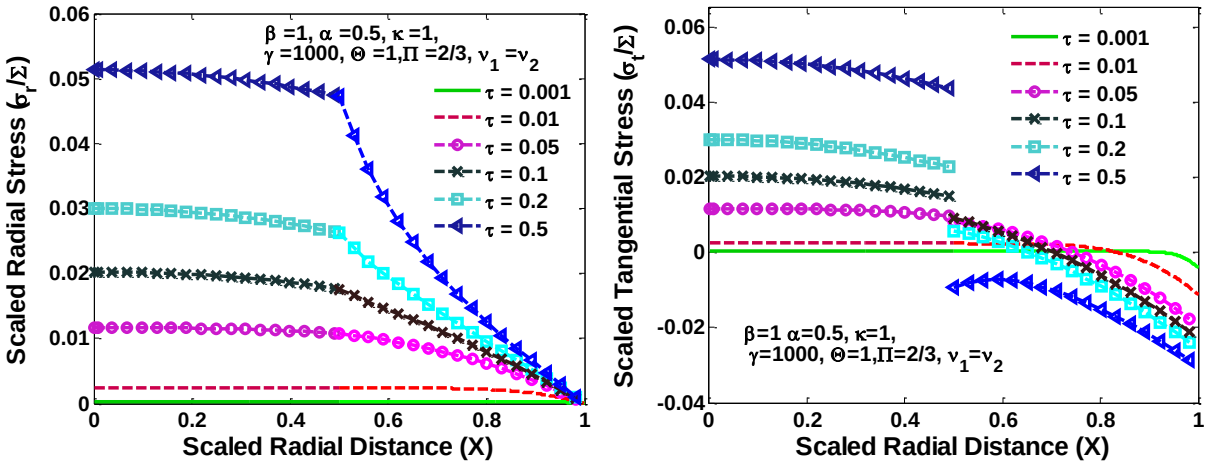

Figure 3-11: Radial and tangential stresses during galvanostatic intercalation in spherical particle with lower partial molar volume for the core

Though having different values of diffusivity in both regions ($\beta \neq 1$) will affect the magnitude of stress developed as steepness of concentration profiles is affected by the values of β (Figure 3-7), the shape of underlying profiles remains more or less similar.

Core-shell sphere with discontinuous concentration at the interface ($\kappa \neq 1$, $\gamma \gg 1$):

The parameters in this section are chosen to represent the core-shell behavior of Si/C type core-shell material with Si/Sn as the core and graphite as the shell to illustrate the utility of the model for newer generation materials. It is beyond the scope of this chapter to include volume changes and plasticity, however in our opinion the importance of interface dynamics needs to be addressed for the newer materials and hence this analysis is included. The diffusion coefficient of the inner core (Si) is assumed to be two orders of magnitude smaller than that of the outer shell ($\beta^2 = D_2/D_1 = 100$) and Young's modulus of the core is assumed to be one order of magnitude larger than the shell ($\Theta = \Omega_1/\Omega_2 = 10$). κ and Π are also chosen to approximately represent the mechanical properties of these materials ($\kappa = 2$ and $\Pi = 1.5$). As the inner core has higher magnitudes of stresses compared to the outer shell, a different kind of scaling ($\mathrm{sgn}[(\cdot)]|(\cdot)|^{1/4}$, here sgn is a signum function) is done to represent the stresses in Figure 3-12. This scaling takes care of both positive and negative values and maintains continuity of radial stresses (also the reason for the amplification in the Gibb's phenomenon). As the diffusivity of the core is very small compared to the shell, more time is required for transient behavior to fade out hence stress profiles are plotted up to $\tau = 1.2$.

In this configuration, the radial and tangential stresses at the center keep rising and remain tensile for all time. This is due to very small diffusion coefficient in the core compared to the shell which,

in effect, restricts the core to have enough concentration that can swell the core despite higher partial molar volume and higher interfacial concentration. Even though the concentration in the core is small compared to the shell, the interface on the core side will have double the concentration and partial molar volume compared to the interface on the shell side. This causes the core side interface to swell significantly compared to its nearby region, developing compressive stress at the interface ($\tau = 1.2$ in Figure 3-12).

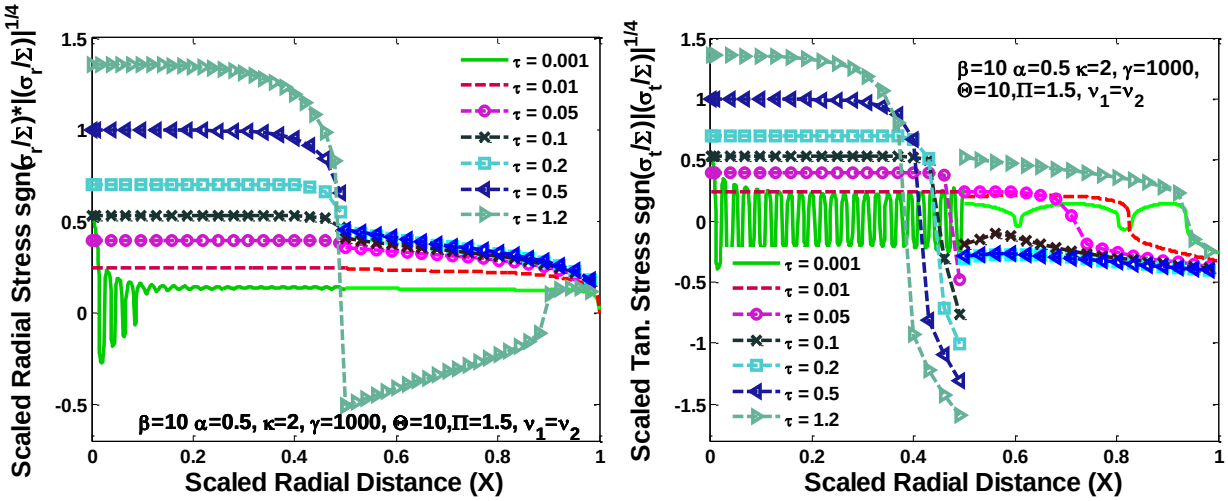

Figure 3-12: Radial and tangential stresses during galvanostatic intercalation in Si/C type core-shell particle; oscillations are amplified due to scaling

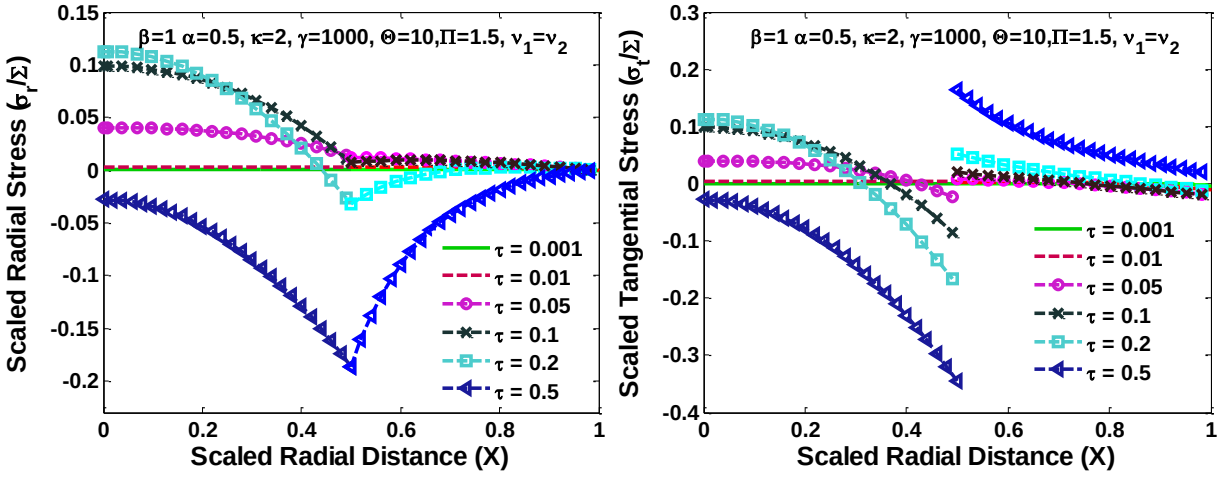

Figure 3-13: Radial and tangential stresses during galvanostatic intercalation in Si/C type core-shell particle for equal diffusivities

If the ratio of diffusivity (β^2) is changed to 1 keeping other parameters constant, that will make the core more concentrated than the shell (after the short time transient dies out, Figure 3-4), in that case expansion of the core aided with higher partial molar volume will lead to compressive radial and tangential stresses in the core (Figure 3-13).

The magnitude of peak stresses in the particle also depends on the ratio of core and shell thicknesses (α). For Si/C type core-shell configuration, as the thickness of the core (silicon type material) is decreased, stress generated will be smaller due to flatter concentration profiles in the core (less diffusion resistance). This situation conflicts with the objective of having increased energy density compared to graphite particle. On the other hand, if the value of α is chosen close to 1, the stress generated will be significantly higher, which may lead to breaking of the outer shell. Hence a careful selection of material properties is needed in order to deliver efficient energy storage material. As seen earlier, changes in one or two parameters can drastically change the stress behavior which gives an opportunity to carefully tune the transport parameters for better material properties to address issues relating to capacity fade. Our future efforts will address optimization of these design parameters based on the model reported here.

Hollow Sphere or Sphere with Inert Core:

As discussed earlier (Figure 3-6), solution derived in this chapter can be used to mimic the transport behavior of a hollow spherical particle or a particle with inert core. Stress profile for the same is plotted in Figure 3-14. Absence of the inner core will result in the absence of radial stresses at the inner surface of the particle. This can equivalently be represented as very small Young's modulus for the core ($\Theta = 10^{-10}$) with equal partial molar volume ($\Pi = 1$). Following plots were obtained by choosing $\alpha = 0.3$, $\delta = -0.25$, $\nu_1 = 0.3$, and $\nu_2 = 0.3$. As the radial stress is zero on

both the surfaces, the radial stress in the particle goes through a maxima for $\alpha < X < 1$. Moreover, the peak radial stress and tangential stress saturate to a maximum value for large τ. Figure 3-14 also shows that the location of peak radial stress shifts towards the center from surface under these charging conditions.

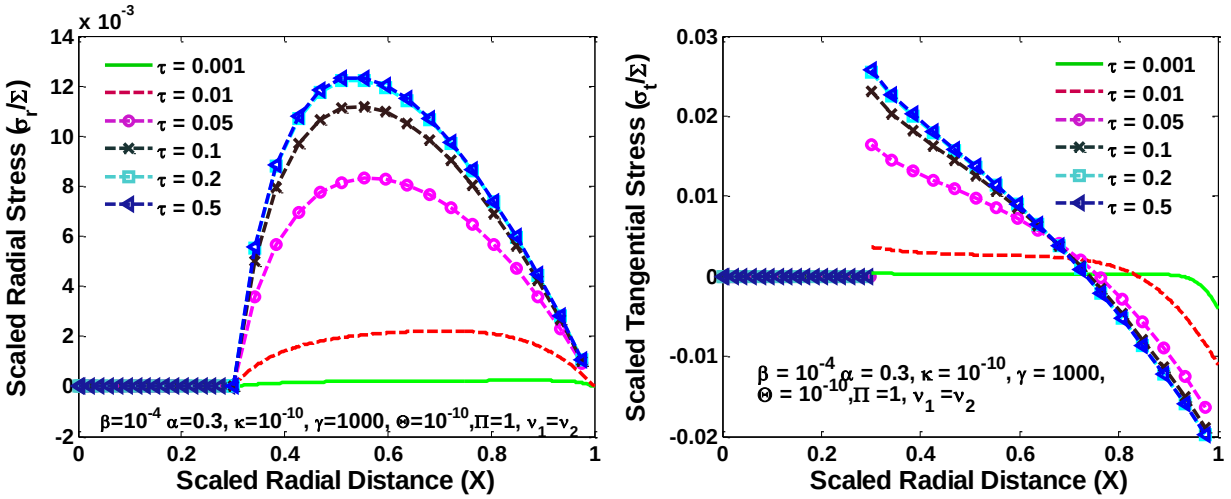

Figure 3-14:Radial and tangential stresses for hollow sphere

Similar stress calculations can be performed for radial isotropic diffusion in core-shell and hollow cylindrical geometry. The above analysis does not incorporate volume expansion, pressure induced diffusion and concentration dependent material properties. As there can exist a significant stress difference at the interface (Figure 3-10, Figure 3-11, Figure 3-12, and Figure 3-13), pressure induced diffusion may play a significant role and alter the dynamics.

3.6 Conclusions

Intercalation of lithium in core-shell material is modeled with a very general treatment at the interface including interfacial dynamics. The model is solved using a modified separation of variables method developed earlier. It was shown that diffusion in core-shell particles can be modeled using 3 important parameters (ratio of diffusivities, ratio of equilibrium concentrations, and interface dynamics). Cases studied in this chapter assumes very fast interfacial dynamics but

slower interfacial dynamics do play a role in concentration profiles and stress behavior specially at short times.

List of symbols

A_n	Coefficients in infinite series
a_i, k_i	Constants used to represent solution
α	Fractional coverage of region 1 (R_1/R_2)
B_i	Constants
β^2	Ratio of diffusivity (D_2/D_1)
c_i^*	Equilibrium concentration, mol/m3
c_i	Concentration, mol/m3
χ_m^j	Eigenvalues dependent constants
D_i	Diffusion coefficient, m^2/s
Δ_i	Dimensionless groups to represent stress in compact form
δ	Dimensionless current density
E	Young's modulus, Pa
F	Faraday's constant, 96487 C/g equivalent
$f_i(x)$	Eigenfunctions
ϕ_n, θ_n	Eigenvalues dependent constants
g_i	Variable to present Homogeneous solution
s	Dimensionless interfacial kinetics
I_s	Current density, A/m^2
κ	Ratio of equilibrium concentration
ℓ	Interfacial dynamics, m/s
λ_i	Constant
λ_n	Eigenvalues
N_i	Molar flux, $mol/s/m^2$
n	Charge associated with the single ion of guest molecule
Π	Ratio of partial molar volume
Θ	Ratio of Young's Modulus

r	Axial distance/radial distance, m
R_1	Thickness of first region, m
R_2	Total thickness of the geometry, m
σ_{r_i}	Radial stress, Pa
σ_{t_i}	Tangential stress, Pa
$\hat{\sigma}_{r_i}$	Dimensionless radial stress
$\hat{\sigma}_{t_i}$	Dimensionless tangential stress
t	Time, sec
τ	Dimensionless time
ν	Poisson's ratio
w_i , v_i ,	Variables to present nonhomogeneous solution
x_i	Dimensionless concentration
X	Dimensionless axial/radial distance
Ω	Partial molar volume, m^3/mol

Subscripts used in list of symbols

i	i = 1 or 2, for region 1 ($0 < r < R_1$) and region 2 ($R_1 < r < R_2$)
n	n=1.. ∞ , positive eigenvalues
m	Constants used to make the expression compact (used in χ_m^j)

List of superscript

p, c, s	Denote planar, cylinder and sphere respectively (used in χ_m^j)

Chapter 4
Optimal Charging using the SPM: Stress Effects

With four parameters I can fit an elephant, and with five I can make him wiggle his trunk.
John von Neumann

4.1 Motivation

As discussed in previous chapters (chapters 1 and 2), intercalation-induced stress generation in electrode particles is one of the main reasons for capacity fade, which affect the capacity in two ways; fracture due to stress (electrical isolation) that reduces the capacity and the effect of loss in the connectivity of the particles.[31] To the best of our knowledge, none of the optimal charging profile reported in the literature includes the intercalation-induced stresses while deriving optimal charging profiles. The progress made in understanding the capacity fade mechanisms[32,76-80] has paved the way for inclusion of that knowledge in deriving optimal controls. In this chapter, we have incorporated the particle-level stress-strain effect with a single-particle model to derive an optimal charging profile that restricts the peak stresses inside a particle. This chapter illustrates that almost the maximum possible amount of charge can be stored within a given time (one hour), if the current profile is optimally derived, with significantly lower stress being developed within the particle. Section 2 reviews various stress models reported in the literature for battery models (detailed discussion is presented in chapter 2). Section 3 provides a brief description of the model used to perform the optimization. Section 4 defines the optimal control problem. Section 5 presents results and discussion, which are followed by conclusions and future directions.

4.2 Review of Stress Models

Although, a detailed review of stress models in single particle is presented in chapter 2 along with framework to incorporate it with P2D model, a brief review is presented here for the sake of completeness of this chapter. Readers who are familiar with stress models can skip this section and may directly go the next section.

During intercalation of lithium into a graphite particle, significant stress is developed inside the particle. In particular, higher rates of charging yield to higher stress. If the stress exceeds the yield stress of a given material, the particle can break and lose contact with the matrix resulting in reduced capacity of the battery. Different models have been developed to quantify the stress developed in a particle with varying degree of sophistications. These modeling efforts can be divided into two categories: strain splitting[33-35] and stress splitting.[31,32] The theory of the strain splitting approach has been developed by Timoshenko[75] where thermal stresses have been modeled using strain splitting, with these models being called *thermal analogy models*. Here, the intercalation-induced stresses are treated in similar way as the temperature-induced stresses. A very detailed and rigorous model that used stress splitting was developed by Christensen *et al.*,[31,32] which was shown to be equivalent to the former approach (strain splitting) by Timoshenko.[75] In both categories, different models can be obtained depending upon the inclusion of pressure-induced diffusion. The effect of pressure-induced diffusion (PID) becomes prominent once the concentration profile starts to develop. The inclusion of pressure-induced diffusion in the model may not have a large effect on the concentration profiles, but since the stress development depends upon the difference in concentration at different points inside the particle, the inclusion of PID does significantly affect the stress profiles. During intercalation (charging/uptake of lithium by

graphite electrode), PID acts in parallel to concentration gradient-induced diffusion to make the concentration profile flatter, which relaxes the particle.

In the first modeling category of strain splitting where intercalation-induced stresses is treated analogous to temperature-induced stresses (thermal analogy models), Zhang *et al.*[34] presented a model that incorporated pressure-induced diffusion. In this model, the partial molar volume and diffusion coefficient were assumed to be independent of the lithium concentration. Additionally, hydrostatic stress was assumed to be same as the thermodynamic pressure to simplify the pressure-induced diffusion term in the Stefan-Maxwell diffusion equation. These aforementioned assumptions enable decoupling of stress and concentration variables, resulting in a single partial differential equation for concentration. Stress profiles can then be calculated during post-processing from the lithium concentration profile. This approach makes the model very simple while capturing the basics of volume expansion in the particle within a lithium-ion battery. In this model, if pressure-induced diffusion is ignored then analytical results can be obtained for constant-current charging.[33] The same model formulation was implemented in a pseudo-2D model of a dual porous insertion electrode cell sandwich comprising lithium cobalt oxide and carbon electrode, where a moving boundary formulation was used to address two phases involved inside the lithium cobalt oxide electrode by Renganathan *et al.*[35]

In the second modeling category, the stress is divided into two components: elastic and thermodynamic. A very detailed and rigorous model had been developed by Christensen *et al.*[32] to model volume expansion and contraction of lithium insertion compound that calculates stresses due to intercalation and de-intercalation of lithium. This model incorporates dependence of partial molar volume on the state of charge (SOC) as well as an experimentally measured thermodynamic factor that is again a function of the state of charge. Also, the model includes a moving boundary

with non-ideal diffusion. Figure 4-1 and Figure 4-2 compare stress profiles predicted by the different models available in the literature. The thermodynamic factor is assumed to be 1 in the model developed by Christensen *et al.*[32] (that is, the open-circuit potential is purely Nernstian).

Comparison of different stress values obtained from different modeling approaches

For the current study, we have focused our attention on single particle representation of the electrode[81]. In this modeling approach, the behavior of entire porous electrode is simplified by replacing it with a solid spherical particle. The current density that goes inside this particle is determined by the total surface area of the electrode. The radius of this hypothetical particle is representative of the particle size distribution of the electrode material. This representation of lithium ion battery simulates the behavior of real battery with reasonable accuracy at lower rates of charge and discharge. For the present case, we have not incorporated state of charge dependent diffusivity and thermodynamic factor. Including these will make the following analysis material specific. Moreover, in order to handle such a large variation in diffusion coefficient with SOC (2 order of magnitude), different numerical discretization schemes may be needed for efficient simulation and optimization.[52,82,83] Numerical simulation was done for intercalation of lithium in a carbon electrode (charging) for the parameter values presented in Table 1. Both radial and tangential stresses developed in the particle reach maxima and minima respectively and then stay at that value when no pressure-induced diffusion is assumed in the first category of models (see dashed curves in Figure 4-1 and Figure 4-2). If pressure-induced diffusion is included in the model, magnitudes of both stresses decrease (solid curves in Figure 4-1 and Figure 4-2).

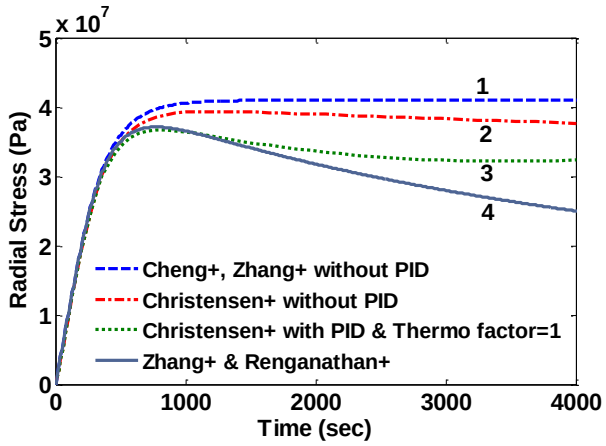

Figure 4-1: Radial stresses during intercalation

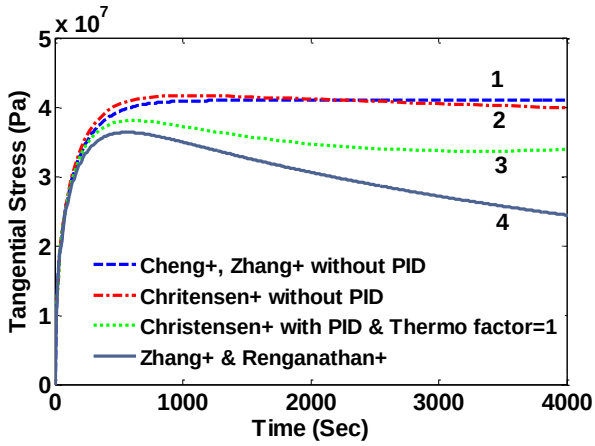

Figure 4-2: Tangential stress during intercalation

Table 4-1: Parameters and dimensionless groups used to generate simulation results

Parameter	Symbol and dimensions	Value
Radius of particle	R_n	12.5×10^{-6} m
Stoichiometric Maximum concentration	$C_n^{\max}$	31833 mol/m^3 [b]
Total surface area of anode	S_n	0.7824 m^2
Diffusion coefficient	D_n	3.9×10^{-14} m^2/s
Faraday's constant	F	96487 C/mol
Young's Modulus	E_n	15×10^{9} Pa[a]
Poison's ratio	ν_n	0.3[a]
Molecular weight	Mw_n	78.64 g/mol[b]
Density	ρ_n	2.1×10^{6} g/cc[a]
Partial Molar volume	Ω_n	4.08×10^{-6}
Applied current	i_{app}	1.656 A (1C)
Time scaling	τ	3600 sec
$\theta = \frac{2}{9}\frac{\Omega_n^2 E_n}{RT(1-\nu_n)}$		3.202×10^{-5} m^3/mol
$\theta = \frac{2}{9}\frac{\Omega_n^2 E_n c_n^{max}}{RT(1-\nu_n)}$		1.019214

[a] values obtained from Christensen *et al.*[32] [b] Values obtained from Renganathan *et al.*[35]

This decrease is due to the fact that during intercalation PID works in parallel to the concentration gradient-induced diffusion and hence tries to make the concentration profile flatter, which in turn relaxes the particle. It is important to note that the peak stress occurs when the concentration at the

center of the particle starts to change (that is, the concentration profile develops fully). Hence the location of peak will be majorly affected by the diffusion coefficient, and the radius of the particle. The model developed by Christensen *et al.*[32] also shows similar results but the difference becomes prominent as time passes. In the case of PID, magnitude of both the stresses attains extreme and then decreases but in the end the stress profiles flattens out (dotted curves in Figure 4-1 and Figure 4-2) due to the incorporation of variable partial molar volume. In the case when PID is ignored, stress values decrease slightly after attaining maxima (dash-dotted curves in Figure 4-1 and Figure 4-2).

While the difference between the predicted stress values becomes prominent with time, the initial development of stress profiles is similar in all the cases. Also, the time at which peak stress occurs does not vary too much between all the models. In the following optimization study, we have used two variants of the model developed by Zhang *et al.*[34] to derive at the optimal charging profile. The first variant includes pressure-induced diffusion and the second version does not. In our opinion, this captures both the worst case and the best case. In addition, the moving boundary model involves index-2 Differential Algebraic equations (DAE) and is computationally challenging to use for optimization.

4.3 Model Description

The detailed description and derivation of the model equations were given by Zhang *et al.*[34] The final equations are summarized here. The mole fraction is governed by a single partial differential equation that is decoupled from the stress equations,

$$\frac{\partial}{\partial t} x_n(x,t) = \frac{\tau D_n}{x^2 R_n^{\,2}} \frac{\partial}{\partial x}\left(x_n^{\,2} N(x,t)\right) \tag{4.1}$$

where $x_n(x,t)$ is the mole fraction of lithium in the LiC_6 electrode, x is dimensionless length, t is dimensionless time, and

$$N(x,t) = \left(1+\theta x_n(x,t)\right)\frac{\partial}{\partial x}x_n(x,t)$$

is the dimensionless flux. The description of parameters, their values and units are given in Table 4-1. The boundary conditions are

$$N(x,t)\big|_{x=1} = \left(1+\theta x_n(x,t)\right)\frac{\partial}{\partial x}x_n(x,t)\bigg|_{x=1} = \frac{R_n I_{app}}{c_{nmax} D_n F S_n} \tag{4.2}$$

$$\frac{\partial}{\partial x}x_n(x,t)\bigg|_{x=0} = 0 \tag{4.3}$$

with initial condition of uniform mole fraction:

$$x_n(x,0) = 0.0078 \tag{4.4}$$

The pressure-induced diffusion effect can be ignored by setting the value of θ to be 0. Radial stress ($\sigma_r(x,t)$), tangential stresses ($\sigma_t(x,t)$), and hydrostatic stress ($\sigma_h(x,t)$) are given by

$$\sigma_r(x,t) = \frac{2\Omega_n E_n c_n^{\max}}{3(1-\nu_n)}\left(\int_0^1 x_n(x,t)x^2dx - \frac{1}{x^3}\int_0^x x_n(x,t)x^2dx\right) \tag{4.5}$$

$$\sigma_t(x,t) = \frac{\Omega_n E_n c_n^{\max}}{3(1-\nu_n)}\left(2\int_0^1 x_n(x,t)x^2dx + \frac{1}{x^3}\int_0^x x_n(x,t)x^2dx - x_n(x,t)\right) \tag{4.6}$$

$$\sigma_h(x,t) = \frac{1}{3}\left(\sigma_r(x,t) + 2\sigma_t(x,t)\right) \tag{4.7}$$

Radial stress at the surface of the particle is equal to the external pressure, which is assumed to be zero. From equation **Error! Reference source not found.** it is clear that maximum radial stress will occur at the center while charging, so a bound on the stress at the center can ensure the bounds hold at all the points in the particle. Similar logic can be extended to equation (4.6) so that stress at the surface of the particle will be considered for bounds on the tangential stress. From Figure 4-1 and Figure 4-2 it is clear that stress development occurs at very short times, which poses a very interesting challenge since most of the reformulation and global polynomial approximations performed to make the simulation faster are not accurate at very short times.[52,85] Initially, while the battery is at rest, the concentration profile in the particle is flat. This kind of behavior is difficult to capture with lower order polynomials. Hence in this work, no solid-phase reformulation is performed to carry out the optimization. The finite difference method is applied to discretize the governing partial differential equation along the radius of the particle x. A fourth-order accurate $O(h^4)$ finite difference scheme was implemented at the internal node points with second-order finite difference schemes at the boundaries. Maximum percentage relative error for 40 and 60 node points compared to 100 node points in spatial dimension was found to be 1.4% and 0.6% at $t = 0$, this error goes to order of 0.001 very fast (before the stress hits the maxima). 40 internal node points were used to discretize in the spatial dimension. In the finite difference form, the index i goes from 1 to $N + 2$:

$$\frac{\partial^2}{\partial x^2} x_n(x,t) = \frac{1}{12\Delta x^2}\left(-x_{n_{i-2}}(t) + 16x_{n_{i-1}}(t) - 30x_{n_i}(t) + 16x_{n_{i+1}}(t) - x_{n_{i+2}}(t)\right), \; i = 3 \text{ to } N \quad (4.8)$$

$$\frac{\partial}{\partial x} x_n(x,t) = \frac{1}{12\Delta x}\left(x_{n_{i-2}}(t) - 8x_{n_{i-1}}(t) + 8x_{n_{i+1}}(t) - x_{n_{i+2}}(t)\right), \; i = 3 \text{ to } N, \quad (4.9)$$

Points adjacent to boundaries:

$$\frac{\partial^2}{\partial x^2} x_n(x,t) = \frac{x_{n_{i-1}}(t) + x_{n_{i+1}}(t) - 2x_{n_{i+1}}(t)}{\Delta x^2},\ i = 2 \text{ and } N+1, \tag{4.10}$$

$$\frac{\partial}{\partial x} x_n(x,t) = \frac{1}{2}\left(\frac{x_{n_{i+1}}(t) - x_{n_{i-1}}(t)}{\Delta x} \right),\ i = 2 \text{ and } N+1, \tag{4.11}$$

The left boundary condition is approximated using 3-point forward difference for the derivative:

$$\frac{\partial}{\partial x} x_n(x,t) = \frac{1}{2}\left(\frac{-3x_{n_i}(t) + 4x_{n_{i+1}}(t) - x_{n_{i+2}}(t)}{\Delta x} \right),\ i = 1. \tag{4.12}$$

The right boundary condition is approximated using 3-point backward difference for the derivative:

$$\frac{\partial}{\partial x} x_n(x,t) = \frac{1}{2}\left(\frac{x_{n_{i-2}}(t) - 4x_{n_{i-1}}(t) + 3x_{n_i}(t)}{\Delta x} \right),\ i = N+2. \tag{4.13}$$

After discretization in *x*, the resultant set of equations was discretized using the third-order Euler backward difference formula (BDF) in time. A total of 100 node points in time were used with a fixed final time of 1 hour. The complete discretization resulted in a system of [(2 boundary condition + 40 equations for internal node points) + (1 equation for average mole fraction + 1 equation for radial stress at the center + 1 equation for tangential stress at surface)] × 100 (node points in time) = 4500 algebraic equations.

4.4 Problem Formulation

The maximization of charge transferred is equivalent to maximization of the average mole fraction (*Q*) in a limited time with voltage, surface mole fraction, and stress constraints considered with a single-particle model. Numerous methods are available for solving constrained dynamic optimization problems, including (*i*) variational calculus, (*ii*) Pontryagin's maximum principle,

(*iii*) control vector iteration, (*iv*) control vector parameterization, and (*v*) simultaneous nonlinear programming.[86-88] Control vector parameterization (CVP) and simultaneous nonlinear programming are commonly used strategies that employ nonlinear programming (NLP) solvers. This paper uses the simultaneous nonlinear programming approach. The optimal control problem under consideration is:

$$\max_{i_{app}(t)} Q = \int_0^1 i dt = \int_0^1 \frac{i_{app}(t) R_n}{c_{nmax} D_n F S_n} dt \tag{4.14}$$

subject to: PDE model, BCs, and IC (4.1) to (4.6) with constraints:

$$0 \le i_{app}(t) \le 2\,\mathrm{C} \tag{4.15}$$

$$0 \le x_n(1,t) \le 0.6 \tag{4.16}$$

$$\sigma_r(x,t) \le \sigma_r^{\max} \tag{4.17}$$

$$\sigma_t(x,t) \le \sigma_t^{\max} \tag{4.18}$$

where i is the dimensionless current, i_{app} is the applied current (A), Q is the average mole fraction, $\sigma_r^{\max}$ and $\sigma_t^{\max}$ can take the values of yield stress of the material, and $x_n(1,t)$ is the mole fraction at the surface, which should not exceed the value of 0.6, as this value determines the voltage of the lithium-ion battery.

The discretized form of this problem statement takes the form

$$\max_{i_{app}(k)} Q = \sum_{k=1}^{n} \frac{i(k)}{n} \tag{4.19}$$

such that

$$F_k\left(z(k+1), z(k), y(k), i_{app}(k)\right) = 0 \tag{4.20}$$

$$G_k\left(z(k), y(k), i_{app}(k)\right) = 0 \tag{4.21}$$

initial conditions: $z(k=1) = z_0$ and bounds:

$$\begin{aligned} & i_{\min} \le i_{app}(k) \le i_{\max}, \\ & y_{\min} \le y(k) \le y_{\max}, \\ & z_{\min} \le z(k) \le z_{\max} \end{aligned} \tag{4.22}$$

where F_k represents differential equation constraints (converted to algebraic form using BDF), G_k represents algebraic equation constraints, n represents the number of discretization points in time, z represents differential states, and y represents algebraic states with an applied current of i_{app}. The differential state constraints include physically meaningful bounds on the solid-phase lithium. A bound was placed on the mole fraction at any point in the particle as well as on the maximum radial and the minimum tangential stresses at the center and the surface respectively.

In simultaneous nonlinear programming,[86-88] both the control variables and state variables are discretized, which results in a large set of nonlinear equations to be solved simultaneously for obtaining the optimum profile. The resultant system had 4600 variables (4500 states variables with 100 control variables) and hence 100 degrees of freedom. The nonlinear system of 4500 equations was solved using the nonlinear programming (NLP) solver IPOPT[89] with constraints on the control variables (2C rate), mole fraction (0.6), radial stress at the center, and tangential stress at the surface.

4.5 Results and Discussion

Case 1: Charging for one hour

The yield stress for LiC_6 is 30 MPa; however, a slightly more relaxed bound on the stress (37.5 MPa) was placed with maximum allowable current of 2C (3.312 A in this case). Below are the results from the optimization study.

The charging profile starts at the maximum allowable C rate. Very soon the tangential stress hits its bound, and from that point onwards, the charging current starts to decrease (see Figure 4-3). In the case of regular diffusion (with no PID), the current takes a value around 1C which ensures proper bounds on the stress. In the case of PID, the value of the current ramps up slowly until the surface mole fraction reaches the value of 0.6 (see Figure 4-3). This behavior is observed since pressure-induced diffusion helps the particle relax during intercalation and optimized charging profile utilizes this phenomenon to enable an aggressive storage policy. In both the cases, as soon as the surface mole fraction reaches the value of 0.6 (the upper bound on mole fraction at the surface of particle), the current starts decreasing to make sure this bound is not violated. This part is similar to constant voltage charging.

In the case of pressure-induced diffusion during intercalation, the optimized current profile takes advantage of the relaxation of the profiles inside the particle and can enable more charge to be stored. Figure 4-4 shows that the average concentration stored in the particle at the end of charging is more when PID is taken into account in the optimization.

Figure 4-5 shows profiles for the tangential stresses. From Figure 4-5 it is clear that tangential stress hits its maximum sooner than the radial stress. Hence it will act first as active constraints. It can be noted that the maximum tangential stress is negative (compressive stress) at the surface of

the particle. Figure 4-6 shows the radial stress profiles at the center (which in case of charging is the maximum radial stress). The notch in the current profile in Figure 4-3 after which it starts to ramp up is attributed to the radial stress bounds becoming active at that time (see Figure 4-6).

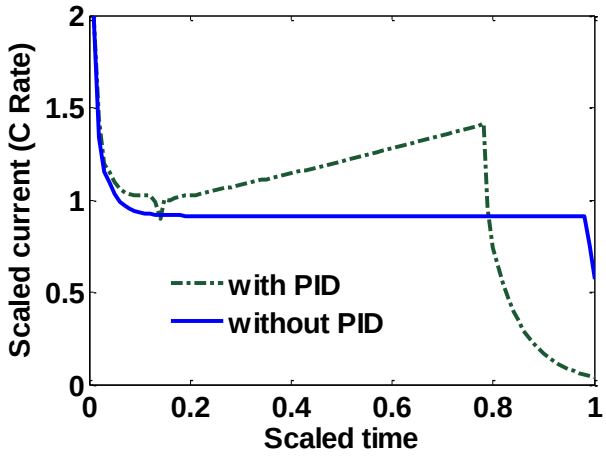

Figure 4-3: Optimal charging profile

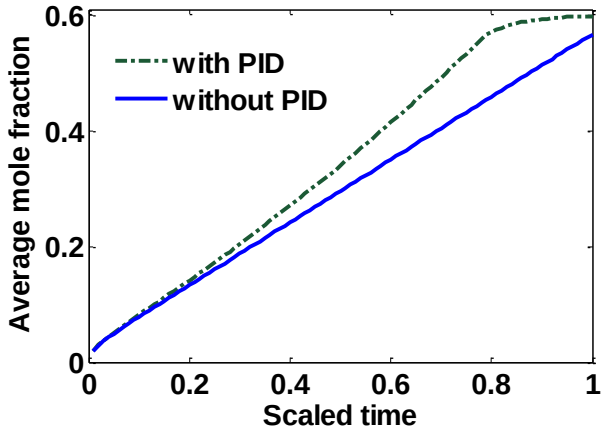

Figure 4-4: Average mole fraction with PID and without PID

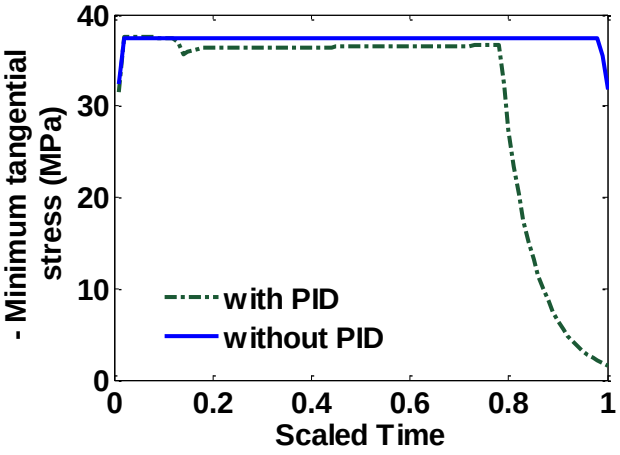

Figure 4-5: Negative minimum tangential stress (at the particle surface)

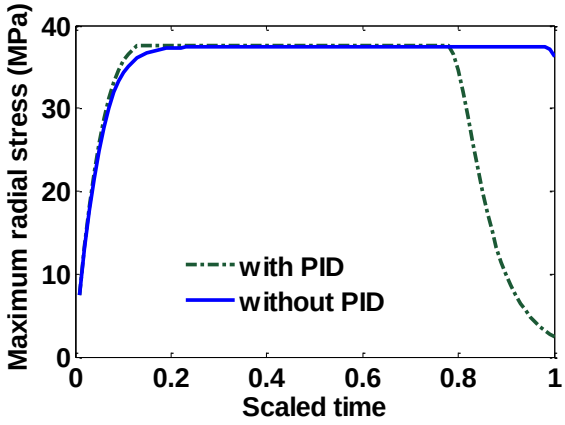

Figure 4-6: Maximum radial stress (at center)

Table 4-2 shows the computational matrix for both cases, with the objective function being the average mole fraction that has the maximum value of 0.6. Since the problem without PID is a linear problem, the time taken to solve that is lesser compared to the case with PID.

Table 4-2: Computational matrix

	Without PID	With PID
Final time (t_f)	1 h	1 h
Objective value (average mole fraction)	5.65782	0.59833
Total CPU sec in IPOPT (*w/o* function evaluations)	8.560	11.698
Total CPU sec in NLP function evaluations	0.021	0.083
IPOPT tolerance	1×10^{-7}	1×10^{-7}

Case 2: Charging for one hour with varying bounds on the maximum stress

The optimum profile for an unconstrained charge maximization problem mimics the traditionally used constant current followed by constant voltage (CC-CV), (though the value of constant current is optimized and not 1C). The addition of stress-based constraints will limit the charge stored in a given period of time compared to the CC-CV. The rate of increase of SOC decreases in the later part of the CC-CV profile (while maintaining constant voltage) and that is when the optimized profile can compensate for the charge not stored due to the constraints. In this study, we have enforced the constraints on the radial and tangential stresses while optimizing for charge stored in a given time. Depending on the value of the permitted peak stress the optimal charging profile changes. As the stress constraints are relaxed, the SOC stored gets closer to the SOC stored during CC-CV protocol. To obtain a Pareto-optimal curve between peak stress and SOC stored, the peak stress allowed was varied from 22.5 MPa to 85 MPa.

Figure 4-7 is the Pareto-optimal profile, which indicates that an optimum charging profile can significantly reduce the stress generation with very little or no compromise on the amount of charge stored. For the case in which pressure-induced diffusion is incorporated, the compromise in SOC stored is even smaller. Since the model that we have considered represents the most conservative (without PID) and most aggressive (with PID) cases, all of the Pareto efficiency curves derived by using different models should lie between the two Pareto optimality curves obtained. Table 4-3 shows values of the objective function (average mole fraction at the end of one hour) with corresponding values of bounds on the stress in both cases. From the table, it is clear that if we strictly follow the 30 MPa stress limit (which is the yield stress for a carbon-based electrode), the optimized profile can only give up to 0.456 average mole fraction (0.573 for the PID model).

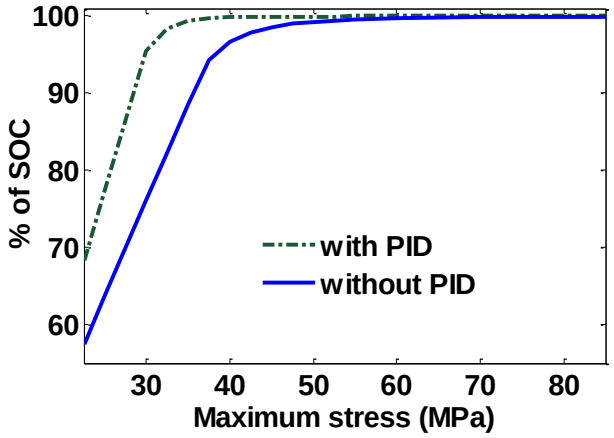

Figure 4-7: Pareto efficiency of optimized charging current

Relaxing this constraint to 40 MPa gives much better results (more that 99% of the maximum possible SOC for PID and more than 96.6% for without PID). If the constraints on the radial and tangential stress are relaxed then the gain in the objective function is marginal whereas the stress values grow significantly.

In this paper, the same constraints on both stresses are used. The bounds on radial and tangential stress need not be same in general. In addition, limits on the two stresses may not be the same for practical applications. The maximum radial stress at the center of the particle is tensile and the minimum tangential stress at the surface is compressive while charging. If any external compressive stresses are present at the surface of particle (stress during packing of material), the radial stress profile will shift lower by the same amount.

Figure 4-8 shows the average mole fraction at the end of charging with different values of maximum allowable stress. The arrow indicates the direction of the relaxed bounds. Conventionally used experimental charging profiles can be viewed as an optimal profile for the problem with unbounded values for the stress limits, which roughly corresponds to the topmost curve in which the average concentration reaches closest to 0.6 in one hour.

The optimal profile with constraints performed in this simulation suggest that, for more than 99% of the SOC in one hour, the 6^{th} and 12^{th} curves from the bottom in case of PID and without PID, respectively, are well suited. These curves correspond to 35 MPa (with PID) and 50 MPa (without PID) peak stress development in both cases.

Figure 4-9 represents the optimized charging profiles for both cases. As the bounds are relaxed, the optimized charging current takes the shape of constant current followed by constant voltage profile (CC-CV) for both models. The optimized charging profile for the model with PID shows an interesting trend where the current values drop from the 2C rate and then again reaches the 2C rate. As explained earlier, the positive slope in the charging current is proportional to the pressure-induced diffusion effect. Figure 4-11 shows the minimum tangential and maximum radial stress profiles for both cases. The dynamics of the minimum tangential stress and maximum radial stress will determine the active stress constraints with time. When PID is included, the tangential stress hits its extremum before the radial stress but the extremum attained by the radial stress has a higher magnitude than for the tangential stress (see Figure 4-10). When PID is not modeled, the tangential and radial stresses reach the same maximum magnitude but the tangential stress reaches the extremum faster.

In the case of PID, it is clear from Figure 4-10 that tangential stress acts as an active constraint initially (until the dimensionless time goes to about 0.15, perfectly flat tangential stress values are observed in Figure 4-11) and later the radial stress governs the maximum possible value of the current (the flat portion of the stress in Figure 4-12 after the dimensionless time of about 0.15). In the case without PID, the tangential stress act as an active constraint for the entire time of charging (Figure 4-11).

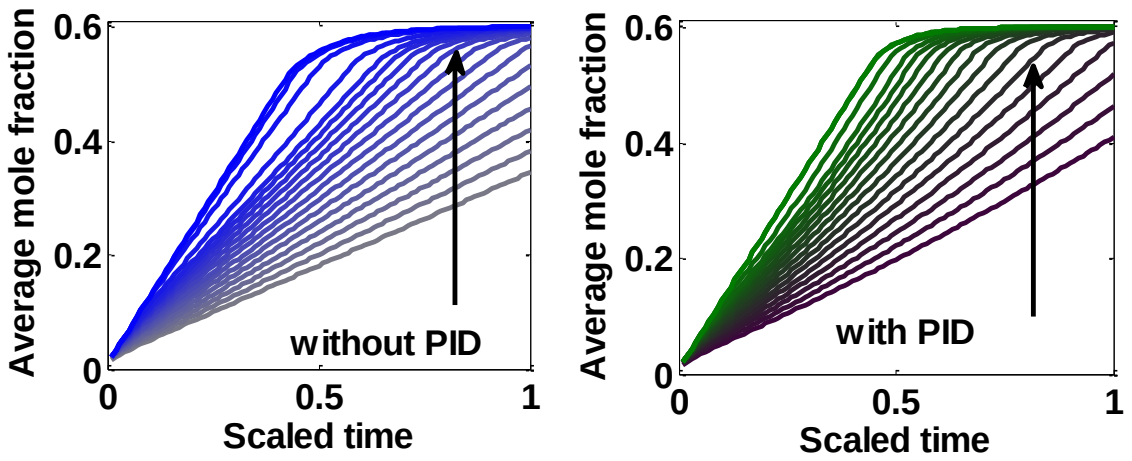

Figure 4-8: SOC stored vs. time (arrows indicate relaxed stress constraints)

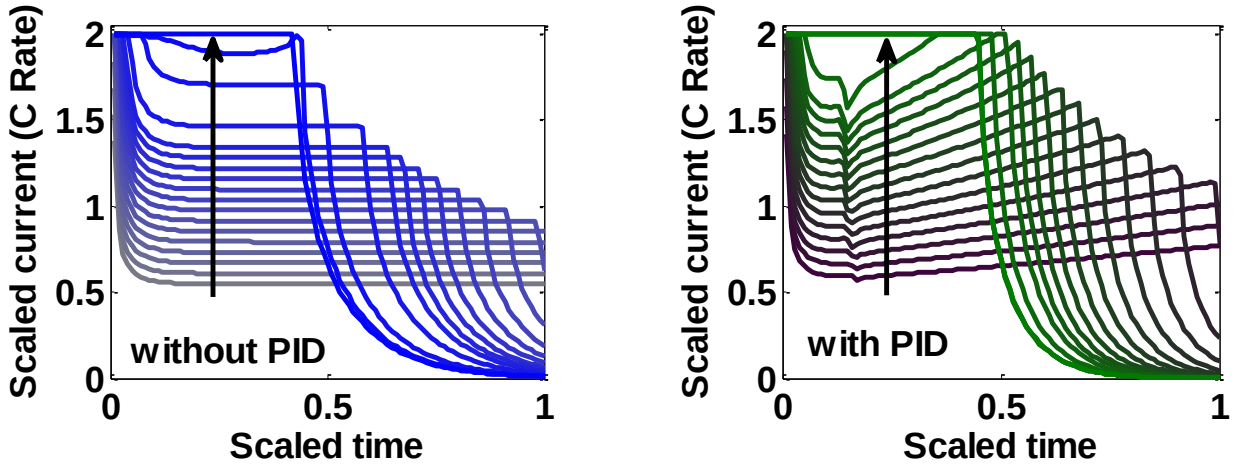

Figure 4-9: Optimal charging profile (arrows indicate relaxed stress constraints)

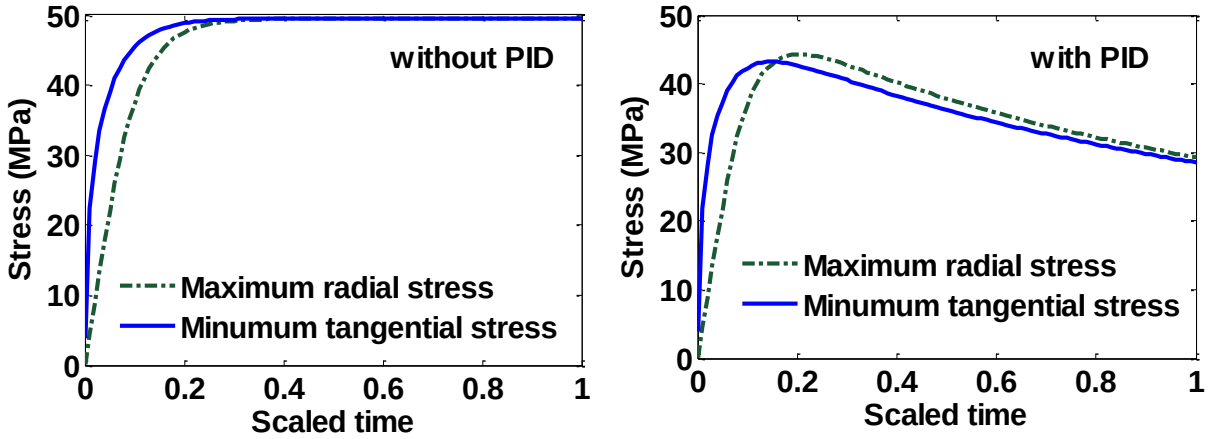

Figure 4-10: Maximum radial and negative of minimum tangential stress in both cases with constant charging current of 1C

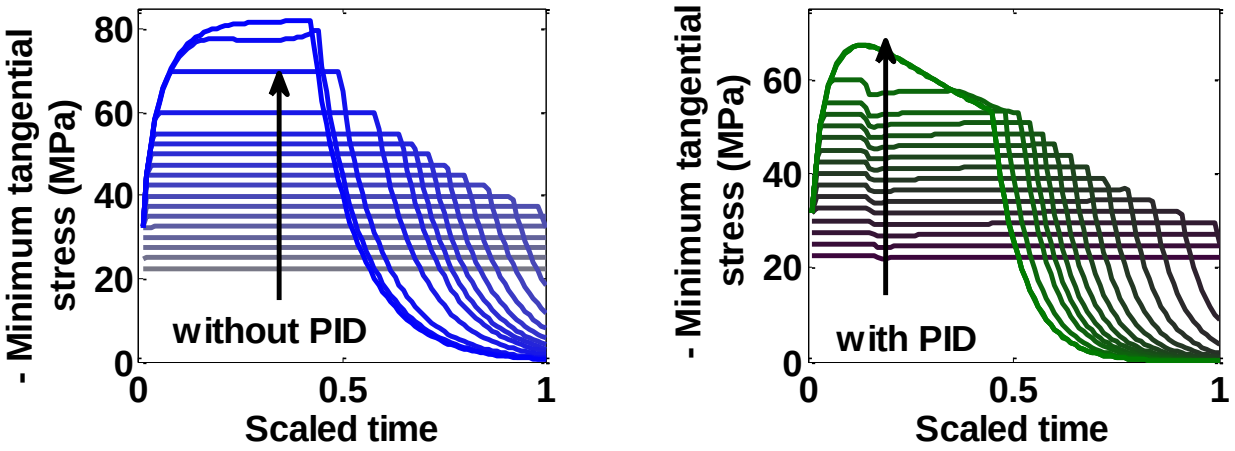

Figure 4-11: Negative maximum tangential stress (arrows indicates relaxed stress constraints)

From the above analysis, it is clear that pressure-induced diffusion helps relax the particle during intercalation. This effect can be exploited to achieve higher SOC during a fixed time. Some discussion on PID is warranted as this effect will do the exact opposite to the other particle (in this case, deintercalation in the cathode material). As intercalation progresses in the anode, PID helps the particle to relax, but on the other hand PID causes steeper concentration gradient, which will increase stress as de-intercalation from the cathode takes place. In that case, the value of the stress will keep rising. These effects can be ignored for some cathode materials (with equal radius as LiC_6 at the anode) like $LiMnO_2$ which has high yield stress (around 100 MPa) and smaller Young's modulus (10 GPa) compared to LiC_6.

Since the peak stress during de-intercalation does not occur at short times for the cathode material, this will not affect the charging profiles derived here. However, for different sets of parameters (for different materials, chemistry, or design), stress developed in both the particles may act as active constraints in the optimization (e.g., smaller radius of carbon material and lower diffusivity of the cathode material).

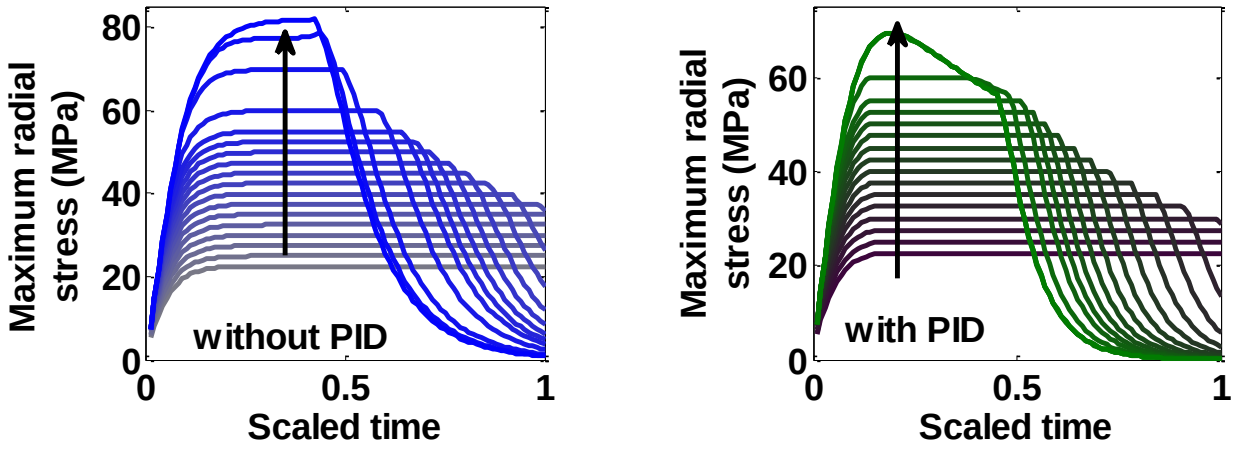

Figure 4-12:Maximum radial stress (arrow indicates relaxed stress constraints)

Table 4-3: Bound on stress and values of objective function

Sr. No.	Bound on Stress	Without PID	With PID	Sr. No.	Bound on Stress	Without PID	With PID
1	22.5	0.344316	0.409451	10	45.0	0.591480	0.599635
2	25.0	0.381707	0.462722	11	47.5	0.593965	0.599763
3	27.5	0.419097	0.517975	12	50.0	0.595556	0.599839
4	30.0	0.456486	0.573022	13	52.5	0.596630	0.599886
5	32.5	0.493878	0.590486	14	55.0	0.597362	0.599916
6	35.0	0.530926	0.595931	15	60.0	0.598267	0.599947
7	37.5	0.565492	0.598041	16	70.0	0.599061	0.599965
8	40.0	0.580106	0.598962	17	80.0	0.599310	0.599964
9	42.5	0.587358	0.599406	18	85.0	0.599388	0.599964

Most of the existing charging profiles (e.g. CC-CV) depend completely on the experimentally measurable variables (e.g. voltage) which make their implementation simple. The optimal charging profiles derived from dynamic optimization schemes depend on the internal states and other model parameters. Hence implementation of these charging protocols requires state

estimation algorithms to be used for predicting these internal states. Future work includes developing semi-empirical laws based on observed states to mimic optimal profiles obtained through offline optimization or developing model predictive control schemes.[90-92]

4.6 Conclusion and Future Directions

The stress-strain effect (mechanical fracture) is a dominant mechanism in capacity fade, in particular for new high capacity materials like germanium and silicon. The need to have safe and smarter use of batteries requires us to incorporate capacity fade mechanisms so that appropriate charging strategies can be devised that can reduce capacity fade. Various models developed to quantify the effect of capacity fade due to mechanical stress-strain effects were reviewed. Two models were chosen that represent the extremes of the stress effect in this particular case. The most conservative (with PID) and most aggressive stress profiles (without PID) lead to different charging protocols and different Pareto efficiency curves. Since the chosen models represent the extremes of the available stress models, the Pareto efficiency curve derived by other models should lie between them. The optimal charging profile was derived for varying the limit of the peak allowable stress generated in the particle. It was found that the optimal charging profile in both cases were able to reduce the stress developed significantly with very little compromise on the charge stored. The compromise on the charge stored was lesser in the case when PID was modeled. The CPU time reported in this study also suggests that real-time control schemes can be developed that utilize sensors for pressure and strain measurement to arrive at improved charging schemes.

The results reported in this chapter are based on a single particle model for mechanical-electrochemical behavior without volume expansion. However, the method of deriving optimal profiles based on robust optimization approaches that can handle nonlinear state and path

constraints can be used to satisfy any relevant objective (e.g. minimizing capacity fade, efficient utilization of electrode) given a physically meaningful model that can quantify those effects.

For example, possible extensions of the proposed approach include

- SOC dependent diffusion coefficient: Use of diffusion coefficient varying with SOC has been reported in the literature[93] which suggests around 2 orders of magnitude change with change in SOC. The model addressed here solves nonlinear spherical diffusion and hence can adapt to this change very easily. When diffusion coefficient exhibit strong dependency on SOC, additional number of node points or more efficient algorithms for spatial discretization may be needed.[82]
- Volume expansion: To address significant volume expansion, SPM should be modified to accommodate moving boundaries. Such systems after spatial discretization results in an index-2 DAE system. Special numerical schemes are being studied to simulate these models efficiently.[84]
- Porous Electrode: SPM needs to be integrated with pseudo 2D model in order to model the porous electrode and obtain non-uniform current distribution and reaction rate.[94] This will then enable us to accommodate other capacity fade mechanisms (e.g. side reaction).
- The changing properties (degradation) of the battery material with time make the electrode more vulnerable to mechanical failure. Use of degradation as an internal state which can be propagated in time will help improve the accuracy in predicting the health of a battery. Inclusion of different physical mechanisms to get close to real system requires more advances in modeling, simulation and optimization. Many researchers are pursuing dynamic optimization framework to derive smart operating protocols.[50,95-98] Continued research in fundamental understanding of underlying physics (e.g. fracture, capacity fade, hot spot

formation), with parallel efforts in efficient simulation and reformulation of these detailed models will help define and solve a more realistic optimization problem to guide the way for model based designs for the next generation of energy storage devices.[99] Note that, providing a robust software framework that can work for detailed nonlinear models is very difficult. This chapter provides a first step towards the same.

Chapter 5

Optimal Charging using the SPM: Li-Plating

> No amount of experimentation can ever prove me right; a single experiment can prove me wrong.
>
> **Albert Einstein**

5.1 Introduction

A lithium-plating side reaction at the lithiated graphite (LiC_6) anode leads to poor safety of the lithium-ion battery. Faster charging at normal temperature may lead to a plating side reaction during the end of charging at the anode-separator interface. At lower temperature, the lithium-plating side reaction may become thermodynamically favorable during almost the entire charging period, even at low rates. This chapter presents an approach using an electrochemical engineering model and dynamic optimization framework to derive charging profiles to minimize lithium plating at low temperatures. Transport parameters for lithium-ion battery are very sensitive at low temperatures. This chapter shows the derivation of the optimal charging profile considering strict lower bounds on the plating reaction depending on various thermal insulation conditions (adiabatic, isothermal, and normal heat transfer coefficient) surrounding the battery.

Lithium-plating side reaction not only causes capacity fade but also poses a significant safety issue.[11] Though lithium-ion batteries are inherently safer than lithium-metal batteries, because the former avoids dendrite formation during charging, the slightly more positive potential of LiC_6 compared to Li/Li^+ inherits the problem of lithium plating during charging[11] at high rates[13] and

even for low rates at low temperature. The driving force for the lithium-plating side reaction at the anode can be expressed by the overpotential:[58]

$$\eta_{plating} = \phi_n^s(x,t) - \phi_{e,n}(x,t) - U_s \tag{5.1}$$

Where $\eta_{plating}$ is the plating overpotential, $\phi_n^s(x,t)$ is the solid-phase potential which is defined for the porous electrode, $\phi_{e,n}(x,t)$ is the electrolyte-phase potential, U_s is the open-circuit potential for the plating reaction which is taken to be zero, and *x* is the distance across the electrode. The expression for $\eta_{plating}$ in (5.1) ignores the voltage drop across the solid-electrolyte interface (SEI) layer. The lithium-plating side reaction becomes feasible only when $\eta_{plating}$ is negative as the plating reaction is irreversible in nature. Detailed electrochemical engineering-based models incorporating concentrated solution theory and porous electrode theory that can simulate the potential distribution inside porous structures are available.[27,94,100-102]

A single-particle model[38,39] (SPM) is used to derive the optimal charging profiles. The SPM ignores the distribution of concentration and potential across the thicknesses of the electrodes and separator. At low temperature, $\eta_{plating}$ (the *x* dependency does not appear in the SPM) shifts down due to increased temperature-dependent transport resistance and may become negative even for the beginning of charging, which makes the battery vulnerable to lithium plating even at low charging rate for these temperatures.

Section 2 discusses the SPM along with its equations and presents simulation results for charging a battery at low temperature (268 K). Section 3 discusses the optimal charging problem

formulation. The results and discussion are in Section 4 and the conclusions and future directions are in Section 5.

5.2 Model Description

Detailed models that incorporate electrochemical, transport, and thermodynamic processes along with the geometry of the underlying system can be used to monitor and control the internal states of a battery.[27,94,100-102] Simplifications of these models have been proposed that preserve the important features of detailed models. The SPM assumes that the porous nature of the solid phase in the anode and cathode can be approximated by the dynamics of a single particle. The SPM also ignores the dynamics and variation of lithium-ion concentration in the electrolyte phase.

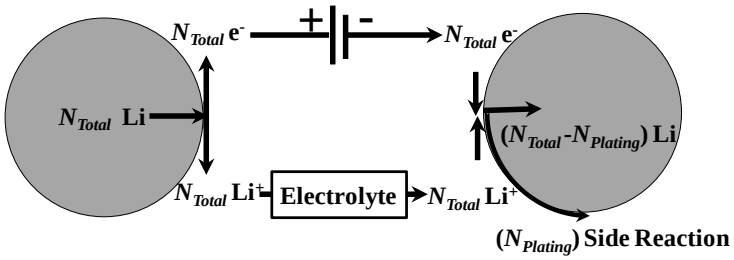

Figure 5-1: Conceptual diagram of the plating side reaction.

Figure 5-1 is a conceptual diagram of the plating side reaction in the SPM framework. Table 5-1 shows the governing equations for the SPM,[38,39] which models Fickian diffusion in the solid particle, where $c_i^s(r,t)$ is the solid-phase lithium concentration ($i = n$ and p for anode and cathode respectively) which has radial and time dependence, V is the voltage across the battery, T is the temperature of the battery, and ϕ_i^s refers to the potential of the solid particles. The equation for the temperature is derived from the general energy balance. A simplified energy balance equation ignoring the reversible heat caused by the reaction entropy change is used in this study. These simplifications may lead to less accurate prediction of the variables at the cell level. The solid-

phase diffusivities (D_i) of both anode and cathode particles are assumed to follow an Arrhenius-type relationship, as shown in Table 5-2, which also shows the additional expressions used in the SPM. A list of parameters and their values used in this chapter are in given in Table 5-3 and Table 5-4.

Table 5-1: Governing equations for the single-particle thermal model

	Governing equation	Boundary conditions	
Solid phase conc. (cathode): $c_p^s(r,t)$	$\frac{\partial c_p^s}{\partial t} = \frac{1}{r^2}\frac{\partial}{\partial r}\left[r^2 D_p^s \frac{\partial c_p^s}{\partial r} \right]$	$\left.\frac{\partial c_p^s}{\partial r}\right\|_{r=0} = 0,\ -D_p^s \left.\frac{\partial c_p^s}{\partial r}\right\|_{R_p} = \frac{I_{\text{overall}}}{a_p F}$	(5.2)
Solid phase conc. (anode): $c_n^s(r,t)$	$\frac{\partial c_n^s}{\partial t} = \frac{1}{r^2}\frac{\partial}{\partial r}\left[r^2 D_n^s \frac{\partial c_n^s}{\partial r} \right]$	$\left.\frac{\partial c_n^s}{\partial r}\right\|_{r=0} = 0,\ -D_n^s \left.\frac{\partial c_n^s}{\partial r}\right\|_{R_n} = \frac{-I_{\text{overall}}}{a_n F}$	(5.3)
Voltage $V(t)$:	$V(t) = \phi_p^s(t) - \phi_n^s(t)$		(5.4)
Temperature: $T(t)$ (Energy balance)	$\frac{dT}{dt} = \frac{I_{\text{overall}}}{mC_p}\left[\left(\eta_p - \eta_n + I_{\text{overall}} R_{\text{cell}}\right) + T\left(\left.\frac{\partial U_p}{\partial T}\right\|_{surf} - \left.\frac{\partial U_n}{\partial T}\right\|_{surf} \right) \right] - \frac{hA_{HT}}{mC_p}\left(T - T_{\text{amb}}\right)$		(5.5)

Table 5-2: Additional expressions used in the SPM

Butler-Volmer kinetics:	$\frac{I_{\text{overall}}}{a_p F} = 2k_p \sqrt{c_e c_{p,\text{surf}}^s \left(c_{\text{max},p}^s - c_{p,\text{surf}}^s\right)} \sinh\left(F\left(\phi_p^s - \phi_{e,p} - U_p\right) \Big/ (2RT) \right)$	(5.6)
	$\frac{-I_{\text{overall}}}{a_n F} = 2k_n \sqrt{c_e c_{n,\text{surf}}^s \left(c_{\text{max},n}^s - c_{n,\text{surf}}^s\right)} \sinh\left(F\left(\phi_n^s - \phi_{e.n} - U_n\right) \Big/ (2RT) \right)$	(5.7)
Specific area	$a_i = \left(3/R\right)\left(1 - \varepsilon_i - \varepsilon_{f,i}\right) A_{cross} l_i,\ i = p,n$	(5.8)
Typical open circuit voltages of cathode and anode *wrt.* lithium metal (experimental fit)	$U_p = \frac{\left(-4.656 + 88.669\theta_p^2 - 401.119\theta_p^4 + 342.909\theta_p^6 - 462.471\theta_p^8 + 433.434\theta_p^{10}\right)}{\left(-1.0 + 18.933\theta_p^2 - 79.532\theta_p^4 + 37.311\theta_p^6 - 73.083\theta_p^8 + 95.96\theta_p^{10}\right)}$ $\theta_p = \frac{c^s\|_{r=R_p}}{c_{\text{max},p}^s}$	(5.9)
	$U_n = \begin{pmatrix} 0.7222 + 0.1387\theta_n + 0.029\theta_n^{0.5} - 0.0172\theta_n^{-1} + 0.0019\theta_n^{-1.5} + \\ 0.2808\mathrm{e}^{0.9-15\theta_n} - 0.7984\mathrm{e}^{0.4465\theta_n - 0.4108} \end{pmatrix},\ \theta_n = \frac{c^s\|_{r=R_n}}{c_{\text{max},n}^s}$	(5.10)

Solid phase diffusivity	$D_i^s = D_{i,\text{ref}}^s \exp\left(-\left(E_a^{D_i^s}/R\right)\left[1/T - 1/T_{\text{ref}}\right]\right),\ i = p,n$	(5.11)
Reaction rate constant	$k_i = k_{i,\text{ref}} \exp\left(-\left(E_a^{k_i}/R\right)\left[1/T - 1/T_{\text{ref}}\right]\right),\ i = p,n$	(5.12)

Before considering an optimal control formulation, it is useful to evaluate the potential for lithium plating at low temperatures. Three different cases (isothermal, h = 25 W/m^2-K and adiabatic) are considered to understand the internal state evolution during charging at 268 K. Figure 5-2 shows the simulation results (current, voltage, plating overpotential, and temperature profiles) with the SPM at three different heat transfer coefficients for a 1.5 C rate of constant current charging followed by constant potential charging (CC-CV). This type of charging is considered the traditional charging protocol. The time evolution of plating overpotential at room temperature follows similar trends but the values remains around 0.03 to 0.1 V at 2C rate with a normal heat transfer coefficient.[13]

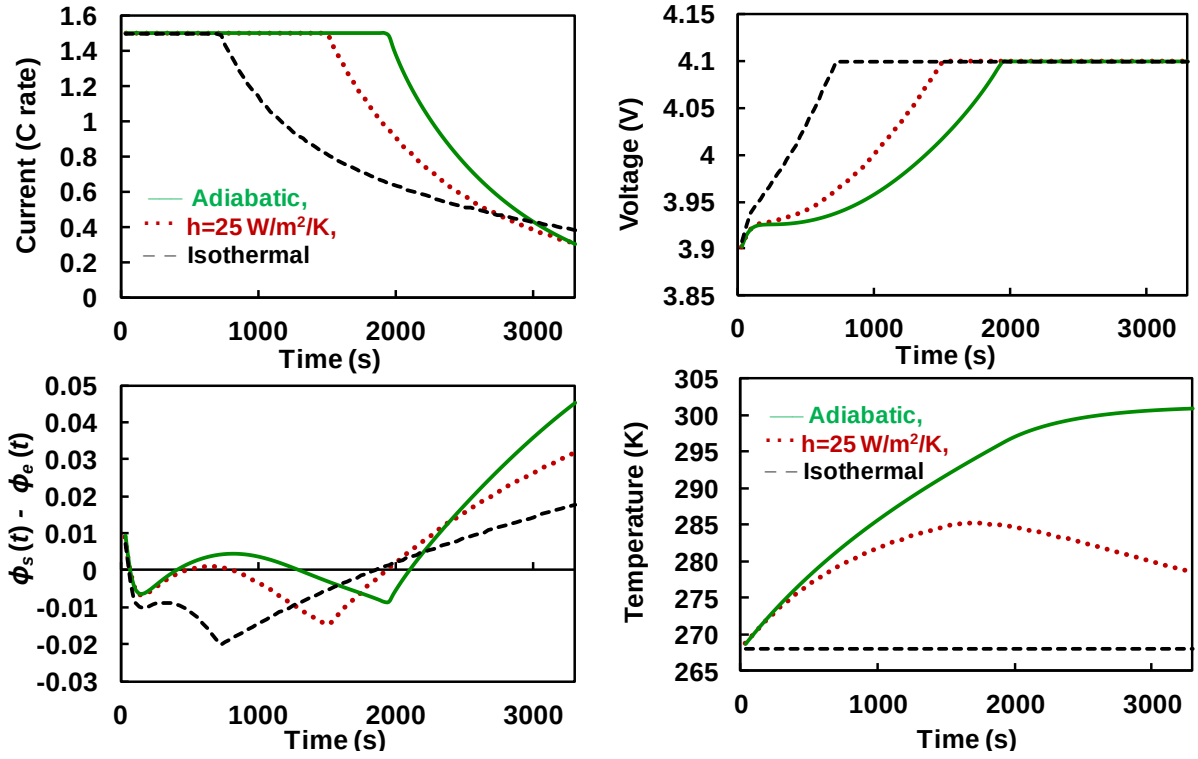

Figure 5-2: SPM simulation at different heat transfer coefficients with CC-CV at 1.5 C at 268 K.

For the adiabatic case, the battery temperature increases faster leading to reduced transport resistance (diffusion and kinetic), which will lead to a lower observed voltage across the battery during charging. The battery in this case is less vulnerable to the plating side reaction with the plating side reaction being feasible $\left(\phi_n^s(t)-\phi_{e,n}^s(t)<0\right)$ only for small and intermediate times (see Figure 5-2, solid green curves). Isothermal charging (dashed black curves in Figure 5-2) is the worst-case scenario, with the plating reaction being feasible for a longer period of time. For a normal heat transfer coefficient (dotted red curves in Figure 5-2), the situation is in between the two cases (isothermal and adiabatic charging). In the next section, the optimal charging problem is formulated to obtain charging profiles that restrict the overpotential for plating at 0 V.

5.3 Optimal Control Formulation

This chapter considers the maximization of charge transferred in a limited time with constraints placed on current, voltage, and plating overpotential using the SPM. Previous efforts in this direction include the derivation of optimal charging profiles considering other capacity fade mechanics (side reaction during charging,[50] thermal degradation,[95] and intercalation-induced stress using SPM[103]). Numerous methods are available for solving constrained dynamic optimization problems, including (*i*) variational calculus, (*ii*) Pontryagin's maximum principle, (*iii*) control vector iteration, (*iv*) control vector parameterization, and (*v*) simultaneous nonlinear programming.[86-88] Control vector parameterization (CVP) and simultaneous nonlinear programming are commonly used strategies that employ nonlinear programming (NLP) solvers. IPOPT, which implements an interior point primal-dual method is used in this work.[89]

Consider the optimal charging profile with fixed final time (3300 s) and with the objective of maximizing stored charge. The optimal control problem of interest can be formulated as (in discretized version):

$$
\begin{aligned}
&\max_{I_{\text{overall}}(k)} \textstyle\sum_{k=1}^{N} I_{\text{overall}}(k); \\
&\text{such that:} \\
&F_k(z(k+1), z(k), y(k), I_{\text{overall}}(k)) = 0 \\
&G_k(z(k), y(k), i_{\text{applied}}(k)) = 0 \\
&\text{initial conditions } z(k=1) = z_0 \text{ and bounds} \\
&0 \le I_{\text{overall}}(k) \le I_{\max}, \;\; y_{\min} \le y(k) \le y_{\max}, \\
&z_{\min} \le z(k) \le z_{\max},
\end{aligned}
\tag{5.13}
$$

with F_k differential equation constraints, G_k algebraic equation constraints, N time discretizations, z differential states, y algebraic states, and an applied current of $I_{\text{overall}}(k)$. The differential state constraints include physically meaningful bounds on the solid-phase lithium concentration in the anode and cathode solid particle. Meaningful bounds are also provided for the algebraic states (e.g., $2.8 \le V(k) \le 4.1$, $0 \le \eta_{plating}(k)$) and the control variable ($0 \le I_{\text{overall}}(k) \le I_{\max}$).

5.4 Results and Discussion

A fourth-order accurate finite difference method (third-order accurate at the boundaries) is used to discretize the diffusion equation in the solid particles in the radial direction to generate system of differential algebraic equations (DAEs). The discretized version of the partial differential equation (5.2) at the κ th internal node point in the radial direction in the solid particles of the anode and cathode (κ starts at 2) is

$$\frac{dc_{i,\kappa}^{s}(t)}{dt}=\frac{D_i^s}{(dr)^2}\left(\begin{array}{l}\dfrac{\left(c_{i,\kappa-2}^{s}(t)-8c_{i,\kappa-1}^{s}(t)+8c_{i,\kappa+1}^{s}(t)-c_{i,\kappa+2}^{s}(t)\right)}{6(\kappa-1)}\\ +\dfrac{1}{12}\left(-c_{i,\kappa-2}^{s}(t)+16c_{i,\kappa-1}^{s}(t)-30c_{i,\kappa}^{s}(t)+16c_{i,\kappa+1}^{s}(t)-c_{i,\kappa+2}^{s}(t)\right)\end{array}\right) \quad (5.14)$$

A similar discretization was performed to convert the PDE (2.2) to a set of ordinary differential equations (ODEs). These ODEs along with the equation for temperature (an ODE), voltage (an algebraic equation), and boundary conditions for the solid particles (algebraic equations) lead to a system of DAEs. The first-order Euler backward scheme was used to discretize the resulting system of DAEs into algebraic equations. The nonlinear program was solved using IPOPT.[89]

Figure 5-3 shows the optimization results for $I_{\max}$ set to 1.5C. For isothermal charging (black dashed curves), the charging profile is mostly governed by the plating overpotential and overall voltage. During isothermal charging, the temperature-dependent transport parameters do not vary and the stored charge in a given time is lowest compared to the other cases where the transport resistance decreases.

Charging in the adiabatic and normal cases (heat transfer coefficient = 25 W/m^2-K) show very interesting profiles. In both cases, the charging profiles are controlled by different active constraints at different times. The optimal charging current consists of five segments, each being governed/ controlled by an active constraint. Initially, the maximum charging current ($I_{\max}$) acts as the active constraints for a very small time followed by the plating overpotential ($\eta_{plating}$) constraint. Later, the dynamics of $\phi_n^s(t)-\phi_{e,n}^s(t)$ play a significant role in determining the shape of the optimal charging profile. As $\eta_{plating}$ recovers $\left(\phi_n^s(t)-\phi_{e,n}^s(t)>0\right)$, the current takes the

maximum value followed by $\eta_{plating}$ becoming the active constraint. The end of charging is then controlled by the voltage drop (V) across of the battery.

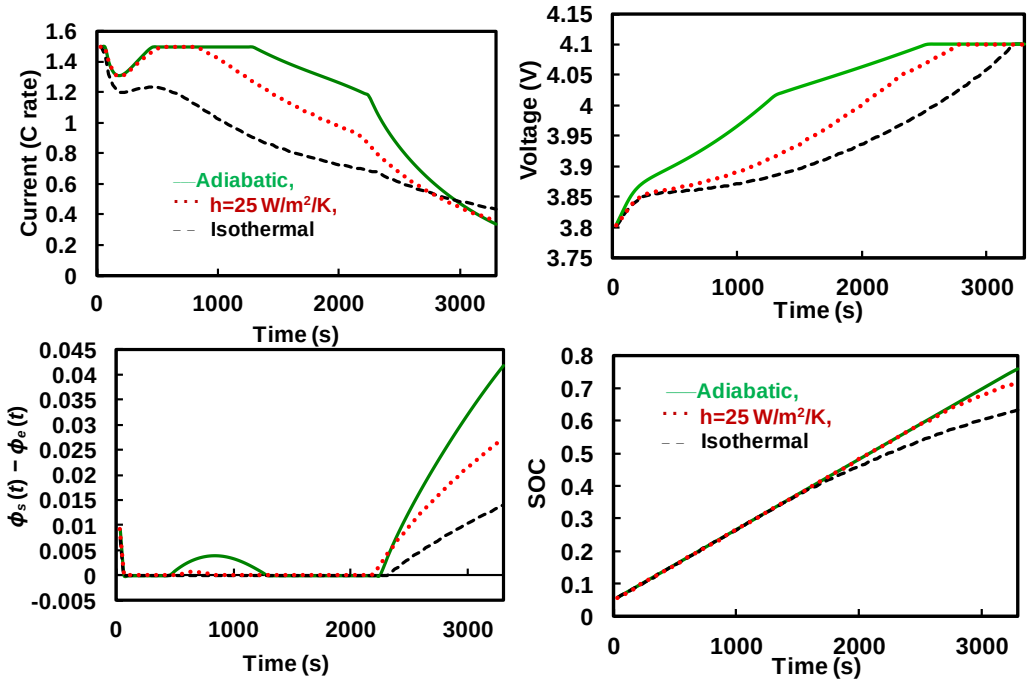

Figure 5-3: Optimization results at 268 K at I_{max} = 1.5C with minimum bound on $\eta_{plating}$ (SOC refers to state of charge).

The optimal charging profiles for different values of I_{max} can be generated in a similar fashion. As can be seen from Figure 5-4 for I_{max} = 1C, the charge stored or state of charge (SOC) in adiabatic charging is significantly higher compared to other cases. In the case of adiabatic charging, $\phi_n^s(t) - \phi_{e,n}^s(t)$ remains positive throughout charging, hence $\eta_{plating}$ never becomes an active constraint, which gives rise to the traditional CC-CV charging profile (green solid curves in Figure 5-4). For a normal heat transfer coefficient and isothermal charging, $\eta_{plating}$ becomes the active path constraint during the charging process.

It is clear from the two cases that, at lower temperature, even the 1C rate of CC-CV charging is not the best charging protocol when $\eta_{plating}$ is considered. The dynamics of $\eta_{plating}$ dominates the charging profile and hence model-based optimal charging profiles are advised when charging batteries at lower temperatures. Use of electrochemical engineering model-based charging profiles requires robust estimation of transport parameters and their temperature dependence.

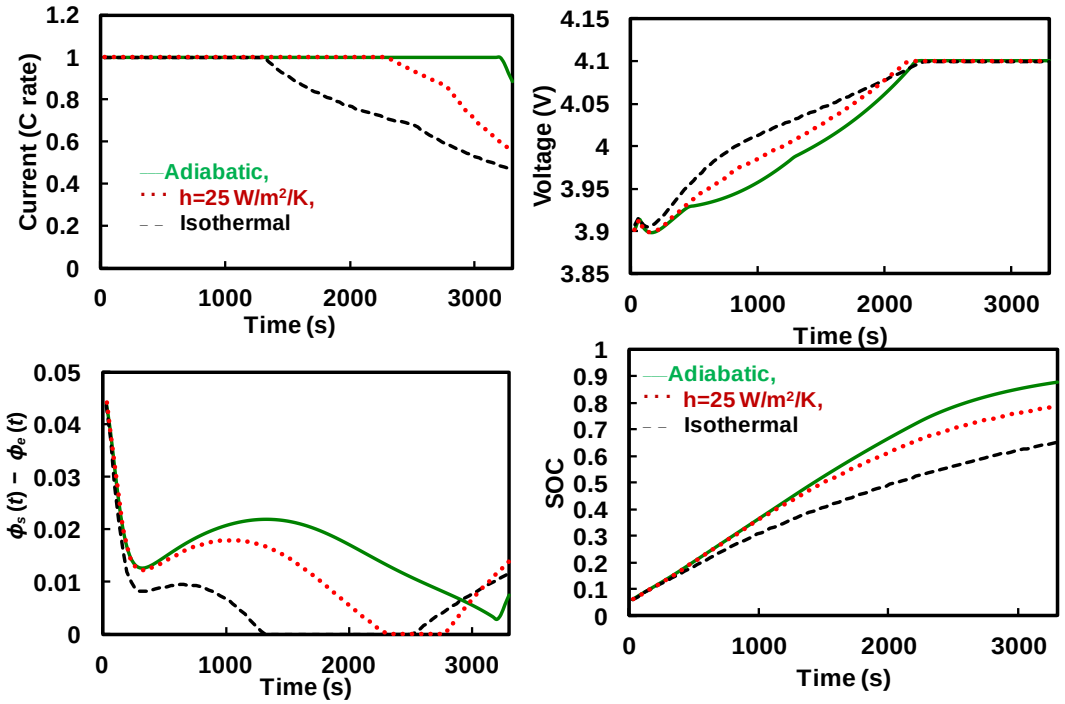

Figure 5-4: Optimization results at 268 K at I_{max} = 1C with minimum bound on $\eta_{plating}$.

These optimization studies performed using the SPM may not be very accurate at lower temperature. Use of a porous pseudo-two dimensional (P2D) model will be pursued for identifying the charging protocol because of the expected non-uniform current density.

5.5 Conclusions

This chapter addresses lithium plating during charging at low temperature, which is closely related to the safe operation of a lithium-ion battery. A single-particle model, which makes significant

simplification in transport processes, is used with a general energy balance equation with additional simplification. Although this model has some limits on its applicability for prediction of the internal variables when used at the cell level, the optimal control problem formulated here places a lower bound on $\eta_{plating}$ in addition to voltage and current bounds. The dynamic optimization framework is used to quickly predict the optimal charging profiles for different environmental conditions and bounds. Accurate prediction as well as a P2D model for modeling spatial variation of $\eta_{plating}$ can be used to further refine the charging protocol, which will be performed in the future. The proposed framework offers an alternative of calculating real-time optimal charging profiles, provided that temperature-dependent transport parameters are known.

Table 5-3: List of parameters and values

	Cathode[a]	Separator[a]	Anode[a]	Units
$\frac{a_i}{A_{\text{cross}} l_i}$	354000		144720	m^2/m^3
$c_{i,\max}^s$	51554		30555	mol/m^3
$c_{i,0}^s$	48976.3		3208.27	mol/m^3
c_e		1000		mol/m^3
C_p		823		J/kg-K
$D_{i,\text{ref}}^s$	1×10^{-14}		3.9×10^{-14}	m^2/s
$E_a^{D_i^s}$	29000 [b]		35000 [b]	J/mol
$E_a^{k_i}$	58000 [b]		20000 [b]	J/mol
F		96487		C/mol
$k_{i,0}$	2.33×10^{-11}		5×10^{-10}	$m^{2.5}/(mol^{0.5}s)$
l_i	80×10^{-6}	25×10^{-6}	88×10^{-6}	m
m		44×10^{-3}		kg
$R_{p,i}$	5×10^{-6} [b]		10×10^{-6} [b]	m
R		8.314		J/mol-K
T_{ref}		298.15		K
$\varepsilon_{f,i}$	0.025		0.0326	

ε_i	0.385	0.724	0.485	
hA_{HT}		0.02		W/K

[a] Unless otherwise noted, all parameters used for the electrodes and separator are from Subramanian *et al.*[53]
[b] Assumed value

Table 5-4: List of variables

a_i	Total surface area of electrode (m^2)	N	Time discretizations
c_i^s	Solid-phase concentration	N_{Total}	Total intercalated lithium
$c_{i,\max}^s$	Maximum solid-phase concentration	N_{Plating}	Lithium lost in the plating reaction
$c_{i,0}^s$	Initial solid-phase concentration	η	Overpotential
c_e	electrolyte concentration	ϕ_i^s	Solid-phase potential
C_p	Heat capacity	$\phi_{e,i}$	Electrolyte-phase potential
$D_{i,\text{ref}}^s$	Solid-phase diffusivity	$R_{p,i}$	Particle radius
$E_a^{D_i^s}$	Activation energy for diffusivities	R	Gas constant
$E_a^{k_i}$	Activation energy for the reaction rate	R_{cell}	Effective resistance of the electrolyte
F	Faraday's constant	R	Radial coordinate
I_{overall}	Current (A)	T_{ref}, T_{amb}	Reference and ambient temperature
$k_{i,\text{ref}}$	Reference reaction rate constant	U	Open-circuit potential
k	Discretization index in time domain	$\varepsilon_{f,i}$	Filler fraction
κ	Discretization index in radial direction	ε_i	Porosity
l_i	Region thickness	A_{cross}	Cross-sectional area of the electrode
m	Total mass of the battery	hA_{HT}	Heat transfer coefficient × area

Chapter 6

Optimal Charging using the P2D Model: Intercalation Induced Stresses

If I have been able to see further, it was only because I stood on the shoulders of giants
Isaac Newton

6.1 Introduction

This chapter illustrates the application of dynamic optimization in obtaining the optimal current profile for charging a lithium-ion battery by restricting the intercalation-induced stresses to a pre-determined limit estimated using a pseudo two-dimensional (P2D) model. This chapter focuses on the problem of maximizing the charge stored in a given time while restricting capacity fade due to intercalation-induced stress. Conventional charging profiles for lithium-ion batteries (e.g., constant current followed by constant voltage or CC-CV) are not derived by considering capacity fade mechanisms, which are not only inefficient in terms of lifetime usage of the batteries but are also slower by not taking into account the changing dynamics of the system.

The use of physically meaningful models in deriving these strategies has received attention. Methekar *et al.*[98] looked at the problem of energy maximization for a set time with constraints on voltage using Control Vector Parametrization (CVP). Klein *et al.*[49] considered the minimum-time charging problem while including constraints on temperature rise and side reactions. Rahimian *et al.*[50] calculated the optimal charging current as a function of cycle number for a lithium-ion battery experiencing capacity fade using a single-particle model (SPM).[38] Hoke *et al.*[97] used a lithium-ion battery lifetime model to reduce battery degradation in a variable electricity cost environment

using the SPM. Previous efforts included the derivation of optimal charging profiles considering various phenomena that account for capacity fade separately (plating overpotential at the anode,[5] side reaction during charging,[6] thermal degradation,[95] intercalation-induced stress using SPM,[103] etc.). Fracture of solid electrode particles due to intercalation induced stresses is one of the dominant capacity fade mechanics which affect the battery capacity in two ways[80]: (1) It leads to loss of solid phase due to isolation from the electronically conducting matrix of electrode. (2) It also increases the surface area, which lead to SEI layer formation at the newly exposed area resulting in capacity fade. In addition, past efforts to minimize capacity fade using SEI layer or other mechanisms are reported elsewhere.[13,50] Work done in Suthar *et al.*[103] used the single-particle representation for a porous electrode to derive an optimal charging profile considering intercalation-induced stresses. This chapter extends that work for higher charge/discharge rates by determining optimal charging profiles using the *isothermal pseudo 2-dimensional model with stress-strain effect*.

Section 2 gives a brief introduction to the pseudo two-dimensional (P2D) model and model reformulation. Section 3 describes the stress-related problems associated with high rate charging. The optimal control problem is formulated in Section 4. Section 5 discusses two scenarios of optimal charging profiles derived by placing constraints on the stresses developed. Section 6 presents conclusions and future directions.

6.2 Model Description

Detailed models that incorporate electrochemical, transport, and thermodynamic processes along with the geometry of the underlying system can be used to monitor and control the internal states of a battery.[27,94,100-102] The isothermal porous electrode P2D model is one such model which is given in Table 6-1. Various expressions used in the model are presented in Table 6-2.

Table 6-1: Governing PDEs for the P2D model

Governing Equations	**Boundary Conditions**	
Positive Electrode		
$\varepsilon_{\mathrm{p}} \dfrac{\partial c}{\partial t} = \dfrac{\partial}{\partial x}\left[D_{\mathrm{eff,p}} \dfrac{\partial c}{\partial x} \right] + a_{\mathrm{p}} \left(1 - t_{+}\right) j_{\mathrm{p}}$	$\left.\dfrac{\partial c}{\partial x}\right\|_{x=0} = 0\ ,\ -D_{\mathrm{eff,p}} \left.\dfrac{\partial c}{\partial x}\right\|_{x=l_p^-} = -D_{\mathrm{eff,s}} \left.\dfrac{\partial c}{\partial x}\right\|_{x=l_p^+}$	(6.1)
$-\sigma_{eff,p} \dfrac{\partial \Phi_1}{\partial x}$ $-\kappa_{\mathrm{eff,p}} \dfrac{\partial \Phi_2}{\partial x} + \dfrac{2\kappa_{\mathrm{eff,p}} RT}{F}\left(1 - t_{+}\right) \dfrac{\partial \ln c}{\partial x} = I$	$\left.\dfrac{\partial \Phi_2}{\partial x}\right\|_{x=0} = 0,$ $\kappa_{\mathrm{eff,p}} \left.\dfrac{\partial \Phi_2}{\partial x}\right\|_{x=l_p^-} = \kappa_{\mathrm{eff,s}} \left.\dfrac{\partial \Phi_2}{\partial x}\right\|_{x=l_p^+}$	(6.2)
$\dfrac{\partial}{\partial x}\left[\sigma_{\mathrm{eff,p}} \dfrac{\partial \Phi_1}{\partial x} \right] = a_{\mathrm{p}} F j_{\mathrm{p}}$	$\sigma_{eff,p} \left.\dfrac{\partial \Phi_1}{\partial x}\right\|_{x=0} = -I,\ \left.\dfrac{\partial \Phi_1}{\partial x}\right\|_{x=l_p^-} = 0$	(6.3)
$\dfrac{\partial c_p^s}{\partial t} = \dfrac{1}{r^2} \dfrac{\partial}{\partial r}\left[r^2 D_p^s \dfrac{\partial c_p^s}{\partial r} \right]$	$\left.\dfrac{\partial c_p^s}{\partial r}\right\|_{r=0} = 0,\ D_p^s \left.\dfrac{\partial c_p^s}{\partial r}\right\|_{r=R_P} = -j_p$	(6.4)
Separator		
$\varepsilon_s \dfrac{\partial c}{\partial t} = \dfrac{\partial}{\partial x}\left[D_{\mathrm{eff,s}} \dfrac{\partial c}{\partial x} \right]$	$c\big\|_{x=l_p^-} = c\big\|_{x=l_p^+}\ ,\ c\big\|_{x=l_p+l_s^-} = c\big\|_{x=l_p+l_s^+}$	(6.5)
$-\kappa_{\mathrm{eff,s}} \dfrac{\partial \Phi_2}{\partial x} + \dfrac{2\kappa_{\mathrm{eff,s}} RT}{F}\left(1 - t_{+}\right) \dfrac{\partial \ln c}{\partial x} = I$	$\Phi_2\big\|_{x=l_p^-} = \Phi_2\big\|_{x=l_p^+}$ $\Phi_2\big\|_{x=l_p+l_s^-} = \Phi_2\big\|_{x=l_p+l_s^+}$	(6.6)
Negative Electrode		
$\varepsilon_n \dfrac{\partial c}{\partial t} = \dfrac{\partial}{\partial x}\left[D_{\mathrm{eff,n}} \dfrac{\partial c}{\partial x} \right] + a_n \left(1 - t_{+}\right) j_n$	$\left.\dfrac{\partial c}{\partial x}\right\|_{x=l_p+l_s+l_n} = 0$ $-D_{\mathrm{eff,s}} \left.\dfrac{\partial c}{\partial x}\right\|_{x=l_p+l_s^-} = -D_{\mathrm{eff,n}} \left.\dfrac{\partial c}{\partial x}\right\|_{x=l_p+l_s^+}$	(6.7)
$-\sigma_{\mathrm{eff,n}} \dfrac{\partial \Phi_1}{\partial x}$ $-\kappa_{\mathrm{eff,n}} \dfrac{\partial \Phi_2}{\partial x} + \dfrac{2\kappa_{\mathrm{eff,n}} RT}{F}\left(1 - t_{+}\right) \dfrac{\partial \ln c}{\partial x} = I$	$-\kappa_{\mathrm{eff,s}} \left.\dfrac{\partial \Phi_2}{\partial x}\right\|_{x=l_p+l_s^-} = -\kappa_{\mathrm{eff,p}} \left.\dfrac{\partial \Phi_2}{\partial x}\right\|_{x=l_p+l_s^+}$ $\Phi_2\big\|_{x=l_p+l_s+l_n} = 0$	(6.8)
$\dfrac{\partial}{\partial x}\left[\sigma_{\mathrm{eff,n}} \dfrac{\partial \Phi_1}{\partial x} \right] = a_n F j_n$	$\left.\dfrac{\partial \Phi_1}{\partial x}\right\|_{x=l_p+l_s^+} = 0,\ \sigma_{eff,n} \left.\dfrac{\partial \Phi_1}{\partial x}\right\|_{x=l_p+l_s+l_n} = -I$	(6.9)
$\dfrac{\partial c_n^s}{\partial t} = \dfrac{1}{r^2} \dfrac{\partial}{\partial r}\left[r^2 D_n^s \dfrac{\partial c_n^s}{\partial r} \right]$	$\left.\dfrac{\partial c_n^s}{\partial r}\right\|_{r=0} = 0,\ D_n^s \left.\dfrac{\partial c_n^s}{\partial r}\right\|_{r=R_P} = -j_n$	(6.10)

Table 6-2: Additional expressions used in the P2D model

$j_p = 2k_p c^{0.5} c_p^s\big\vert_{r=R_P}{}^{0.5} \left(c_{\max,p}^s - c_p^s\big\vert_{r=R_P} \right)^{0.5} \sinh\left[\frac{F}{2RT}\left(\Phi_1 - \Phi_2 - U_p\right) \right]$	(6.11)
$j_n = 2k_n c^{0.5} c_n^s\big\vert_{r=R_P}{}^{0.5} \left(c_{\max,n}^s - c_n^s\big\vert_{r=R_P} \right)^{0.5} \sinh\left[\frac{F}{2RT}\left(\Phi_1 - \Phi_2 - U_n\right) \right]$	(6.12)
$\kappa_{eff,i} = \varepsilon_i^{brugg_i} \begin{pmatrix} 4.1253\times10^{-2} + 5.007\times10^{-4} c - 4.7212\times10^{-7} c^2 \\ +1.5094\times10^{-10} c^3 - 1.6018\times10^{-14} c^4 \end{pmatrix}, i = p,s,n$	(6.13)
$\sigma_{eff,i} = \sigma_i \left(1 - \varepsilon_i - \varepsilon_{f,i}\right), i = p,s,n$	(6.14)
$D_{eff,i} = D\varepsilon_i^{brugg_i}, i = p,s,n$	(6.15)
$a_i = \frac{3}{R_i}\left(1 - \varepsilon_i - \varepsilon_{f,i}\right), i = p,s,n$	(6.16)
$U_p = \frac{-4.656 + 88.669\theta_p{}^2 - 401.119\theta_p{}^4 + 342.909\theta_p{}^6 - 462.471\theta_p{}^8 + 433.434\theta_p{}^{10}}{-1.0 + 18.933\theta_p{}^2 - 79.532\theta_p{}^4 + 37.311\theta_p{}^6 - 73.083\theta_p{}^8 + 95.96\theta_p{}^{10}}$ $\theta_p = \frac{c_p^s\big\vert_{r=R_P}}{c_{\max,p}^s}$	(6.17)
$U_n = 0.7222 + 0.1387\theta_n + 0.029\theta_n{}^{0.5} - 0.0172\theta_n{}^{-1} + 0.0019\theta_n{}^{-1.5}$ $+ 0.2808\mathrm{e}^{0.9-15\theta_n} - 0.7984\mathrm{e}^{0.4465\theta_n - 0.4108}$ $\theta_n = \frac{c_n^s\big\vert_{r=R_P}}{c_{\max,n}^s}$	(6.18)

These electrochemical models tend to be computationally expensive, which has prohibited their use in the control and monitoring of internal states in real time. Several simplified/reduced electrochemical models have been proposed and control-relevant studies performed to try to address these issues.[43-48] Efforts in optimal control and nonlinear model predictive control, incorporating a SPM and other reduced order models have been published.[49,50] A mathematical reformulation method[51-54] gives rise to a computationally efficient model that can be solved in milliseconds without compromising on accuracy. These reformulation techniques consist of spectral methods (specifically orthogonal collocation) where, depending on number of collocation

points in the anode, separator, and cathode, models can be generated with varying degree of accuracy. The model used in the present study is derived using the reformulation methodology outlined in Northrop *et al.*[51] with a change in basis (trial) functions in order to achieve better convergence properties at higher charging/discharging rates of battery operations. The change of trial functions to Chebyshev form provides more robustness albeit at a slightly more cost. This study uses a reformulated model derived based on Chebyshev polynomials[104] as trial functions with 4 collocation points in both the anode and cathode, 2 collocation points in the separator, and 4 collocation points in the radial direction inside the solid particles (see Figure 6-1).

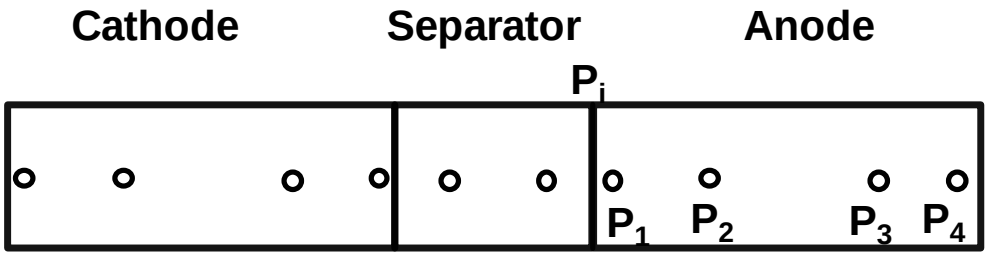

Figure 6-1: Collocation points across the electrodes (zeroes of Chebyshev-Gauss-Lobatto (CGL) polynomials, locations (approximate) in anode and cathode: 0.038, 0.309, 0.691, 0.962 and in separator: 0.146, 0.853).

The resulting system of equations, along with equations to represent radial and tangential stresses in solid particles of the anode, consists of 88 differential algebraic equations (DAEs). This system of DAEs is developed by discretizing the spatial derivatives using orthogonal collocation to ensure the time remains as the only independent variable. This allows for optimized time stepping algorithms to be used and results in 50 ordinary differential equations (ODEs) and 38 algebraic equations. Variables involved in the current study are summarized in Table 6-3. These variables (other than peak radial and peak tangential stresses) also act as coefficients of the polynomials that express the profiles across *x* and radial directions.

Table 6-3: Summary of variables involved in this present study (P_i refers to separator-anode interface)

Variable	**Collocation points**				**No. of**
ODE	Anode	Separator	Cathode	Radial	**Equations**
Solid Phase concentration	4	N/A	4	4	32
Average solid phase concentration	4	N/A	4	N/A	8
Electrolyte concentration	4	2	4	N/A	10
Algebraic					
Voltage across battery					1
Electrolyte potential	4	2	4		10
Solid phase potential	4	N/A	4		8
Local pore wall flux	4	N/A	4		8
Radial stress	4+1(P_i)				5
Tangential stress	4+1(P_i)				5
Plating overpotential	1 (P_i)				1
Total Equations					**88**

Various models, varying in their sophistication, have been proposed to quantify the intercalation-induced stresses in the solid particles. These models are divided in two categories: stress splitting[31,32] and strain splitting.[33-35] In this chapter, a model presented by Cheng and Verbrugge[33] is used. This stress model does not incorporate a moving boundary formulation and ignores thermodynamic factors and pressure-induced diffusion. These simplifications restrict its use to materials with very low volumetric expansion. The resulting equations describing radial stress (σ_r) and tangential stress (σ_t) generated in spherical particles are given in Table 6-4. The tensile stress is taken as positive and compressive stress is taken as negative.

Table 6-4: Governing equations for intercalation-induced stress

Governing Equation	
$\hat{\sigma}_r(\xi,t)=\dfrac{3\sigma_r(\xi,t)}{\Omega_n E_n c_n^{\max}/(1-\nu_n)}=\dfrac{2}{3}\left(\int_0^1 x_n(\xi,t)\xi^2 d\xi-\dfrac{1}{\xi^3}\int_0^{\xi} x_n(\xi,t)\xi^2 d\xi\right)$	(6.19)
$\hat{\sigma}_t(\xi,t)=\dfrac{3\sigma_t(\xi,t)}{\Omega_n E_n c_n^{\max}/(1-\nu_n)}=\left(2\int_0^1 x_n(\xi,t)\xi^2 d\xi+\dfrac{1}{\xi^3}\int_0^{\xi} x_n(\xi,t)\xi^2 d\xi-x_n(\xi,t)\right)$	(6.20)

Here Ω_n is the partial molar volume of the solute, E_n is the Young's modulus, and ν_n is the Poisson's ratio. Parameters values used in this study are listed in Table 6-5.

Table 6-5: List of parameters

Symbol	Parameter	Positive Electrode[a]	Separator[a]	Negative Electrode[a]	Units
a_i	Particle Surface Area to Volume	354000		144720	m^2/m^3
Brugg	Bruggeman Coefficient	1.5 [b]	1.5 [b]	1.5 [b]	
$c_{i,\max}^s$	Maximum solid phase concentration	51554		30555	mol/m^3
$c_{i,0}^s$	Initial solid phase concentration	48976.3		3208.3	mol/m^3
c_0	Initial electrolyte concentration	1000	1000	1000	mol/m^3
D	Electrolyte diffusivity	7.5×10^{-10}	7.5×10^{-10}	7.5×10^{-10}	m^2/s
D_i^s	Solid Phase Diffusivity	1×10^{-14}		3.9×10^{-14}	m^2/s
F	Faraday's Constant		96487		C/mol
k_i	Reaction Rate constant	2.33×10^{-11}		5×10^{-10}	$m^{2.5}/(mol^{0.5}$ s)
l_i	Region thickness	80×10^{-6}	25×10^{-6}	88×10^{-6}	m
$R_{p,i}$	Particle Radius	5×10^{-6} [b]		10×10^{-6} [b]	m
R	Gas Constant		8.314		J/mol/ K
T_{ref}	Temperature		298.15		K
t_+	Transference number		0.364		
$\varepsilon_{f,i}$	Filler fraction	0.025		0.0326	
ε_i	Porosity	0.385	0.724	0.485	
σ_i	Solid phase electronic conductivity	59		48.24	S/m
Ω	Partial molar volume	4.0815×10^{-6} [c]			m^3/mol
E	Young's modulus	15×10^{9} [d]			Pa
ν	Poisson's ratio	0.3 [d]			

[a] Unless otherwise noted, all parameters used for the electrodes and separator are from Subramanian *et al.*[53]
[b] Assumed value
[c] Values obtained from Renganathan *et al.*[35]
[d] Values obtained from Christensen *et al.*[80]

6.3 Stress-related Problems with High Charging Rate

Factors that may cause capacity fade include thermal degradation, side reactions (lithium plating, etc.), and mechanical degradation due to intercalation-induced stresses. This chapter focuses on addressing the capacity fade associated with high anode stresses. Simulation results (voltage, current and radial and tangential stresses) of CC-CV charging with three different maximum charging rates (2C, 3C and 4C) are plotted in Figures 6-2, 6-3 and 6-4.

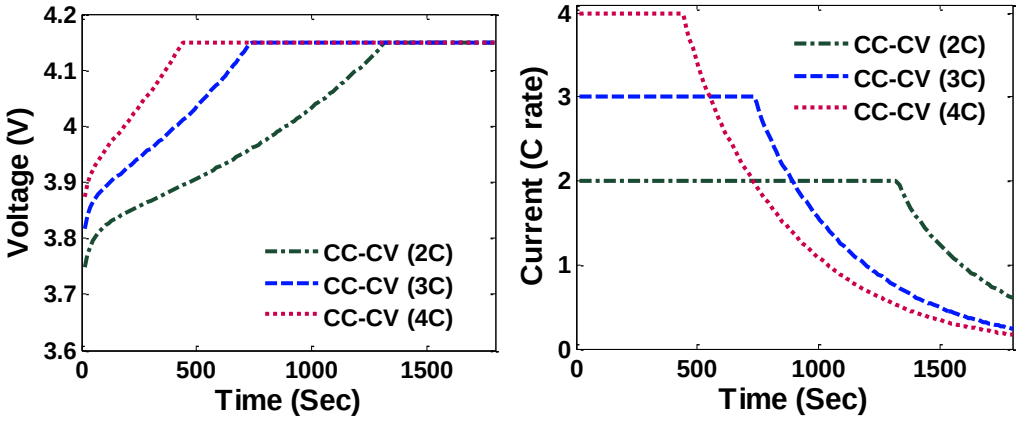

Figure 6-2: Voltage and current profiles during CC-CV charging with different C rate.

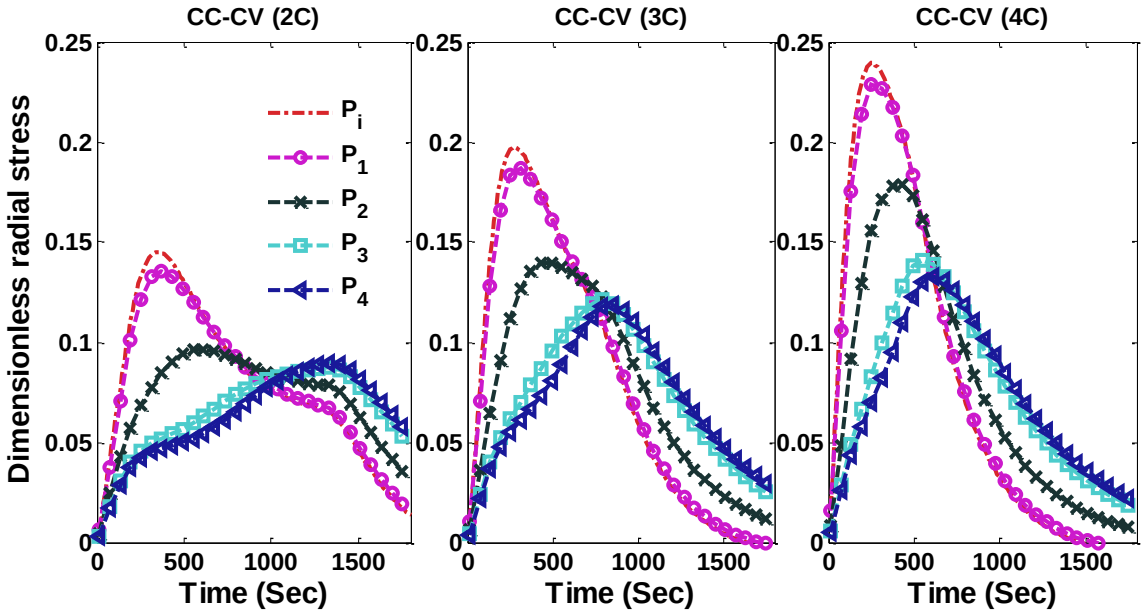

Figure 6-3: Radial stresses (tensile) at the center of the particles at the separator anode interface (P_i) and 4 collocation points are plotted for CC-CV charging at 2C, 3C, and 4C.

During intercalation, for the materials with positive volume expansion, radial stresses remain tensile throughout a particle (assuming zero external pressure at the surface) whereas tangential stress becomes compressive at the surface and tensile at the center. The peak (tensile) radial stress occurs at the center of the particle and peak (compressive) tangential stress occurs at the surface of the particle,[32] hence peak (tensile) radial stresses at the center of the particles and peak (compressive) tangential stresses at the surface of the particles are monitored and controlled. As shown by Christensen and Newman[32] and also clear from the formulas given in Table 6-4 that the peak (tensile) tangential stresses and the peak (tensile) radial stresses are same at the center of the particles, hence controlling and monitoring one of them will be sufficient. Figure 6-2 shows the voltage and current profile for CC-CV charging with three different maximum currents.

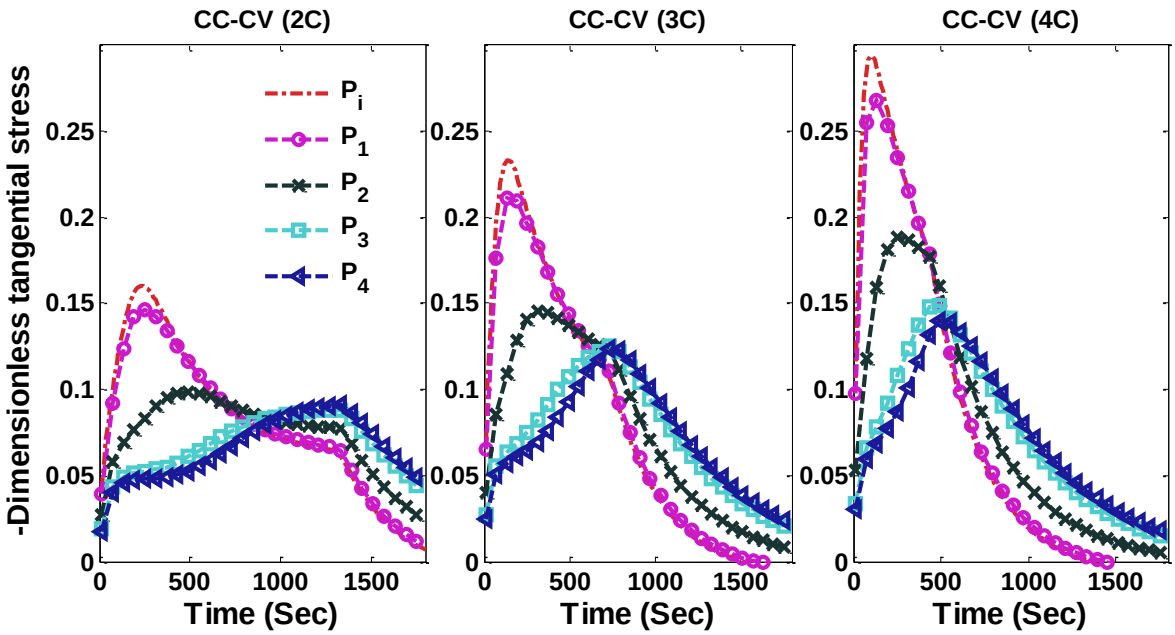

Figure 6-4: Tangential stresses (compressive) at the surface of the particles at the separator-anode interface (P_i) and 4 collocation points are plotted CC-CV charging at 2C, 3C, and 4C.

Figure 6-3 shows the peak (tensile) radial stress at the center of the anode particles for different CC-CV protocols. Each graph in Figures 6-3 and 6-4 consists of five curves representing separator-anode interface (P_i) and 4 collocation points (P_1, P_2, P_3, and P_4, see Figure 6-1 for the location of

collocation points). Peak tangential stress at the surface of the particle has a compressive nature (the negative of tangential stress is plotted). Figure 6-4 shows the peak (compressive) tangential stresses at the surface of the particles in three different CC-CV protocols at different points in the anode (separator-anode interface and 4 collocation points).

The stress profiles predicted using the P2D model differs significantly from the stress profiles predicted using a SPM. For the set of parameters used in the current study, the separator-anode interface achieves maximum current density at the beginning of charging. Figure 6-5 shows the distribution of pore wall flux across the anode at different points in time during CC-CV charging with maximum current of 2C. As charging proceeds, the intake from at the separator-anode interface reduces and other parts of the anode start to contribute more. This decrease in flux gives rise to relaxation of stress at the anode-separator interface at a later time. This relaxation is due to a decrease in the pore wall flux and not due to pressure-induced diffusion.

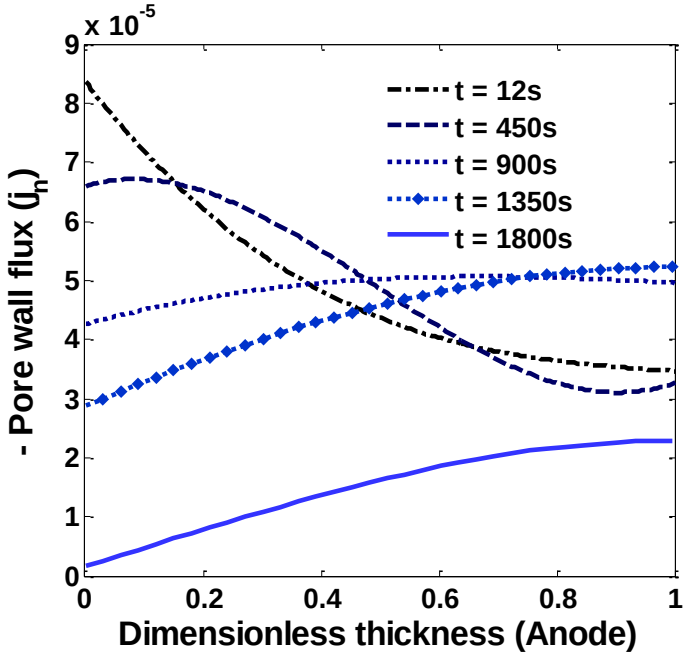

Figure 6-5: Pore wall flux for CC-CV charging with 2C. The separator-anode interface is at 0 on the horizontal axis.

It is clear from the above simulation that the peak radial stresses at the center of the particles and peak tangential stresses at the surface of the particles goes through extrema in time. The extremum values of these stresses occur at the anode-separator interface. This study focuses on restricting the extremum value of peak radial stresses and tangential stresses. Also, the tangential stresses at the surface of the particle show faster dynamics compared to radial stresses at the center.

6.4 Problem Formulation

This chapter focuses on the maximization of charge transferred in a limited time with constraints placed on current, voltage, and stresses predicted with the reformulated P2D model. Numerous methods are available for solving constrained dynamic optimization problems, including (*i*) variational calculus, (*ii*) Pontryagin's maximum principle, (*iii*) control vector iteration, (*iv*) control vector parameterization, and (*v*) simultaneous nonlinear programming.[86-88] Control vector parameterization (CVP) and simultaneous nonlinear programming are commonly used strategies that employ nonlinear programming (NLP) solvers. This study uses the simultaneous nonlinear programming approach.

Consider the optimal charging profile with fixed final time under the objective of maximization of the charge stored (Q). The optimal control problem of interest can be formulated as:

$$\max_{i_{app}(t)} Q = \int_0^{t_f} i_{app}(t)dt \tag{6.21}$$

subject to:

$$\text{PDE model, BCs, and ICs} \tag{6.22}$$

$$
\begin{aligned}
&0 \le i_{app}(t) \le 4C \\
&2.8 \le V(t) \le 4.15 \\
&\hat{\sigma}_r(x,r,t) \le \hat{\sigma}_r^{\max} \\
&-\hat{\sigma}_t(x,r,t) \le \hat{\sigma}_t^{\max}
\end{aligned}
\tag{6.23}
$$

Where i_{app} is the applied current (A), t_f is the final time (s), $V(t)$ is voltage across the battery (V), $\hat{\sigma}_r(x,r,t)$ and $\hat{\sigma}_t(x,r,t)$ are radial and tangential stresses (dimensionless), and $\hat{\sigma}_r^{\max}$ and $\hat{\sigma}_t^{\max}$ are restrictions on the extremum stress. Using mathematical reformulation techniques, the PDE model is converted to a system of DAEs which is then converted to a system of nonlinear algebraic equations by performing temporal discretization. An Euler backward discretization scheme is used to convert the reformulated P2D model into a system of nonlinear algebraic equations. Moreover, bounds on only the peak radial stresses at the center and peak tangential stresses at the surface of the particles are placed. The discretized form of this problem statement takes the form

$$
\max_{i_{app}(k)} Q = \frac{1}{n}\sum_{k=1}^{n} i_{app}(k) \tag{6.24}
$$

such that:

$$
F_k\left(z(k+1), z(k), y(k), i_{app}(k)\right) = 0 \tag{6.25}
$$

$$
G_k\left(z(k), y(k), i_{app}(k)\right) = 0 \tag{6.26}
$$

$$
\text{initial conditions: } z(k=1) = z_0 \tag{6.27}
$$

bounds:

$$
\begin{aligned}
&i_{\min} \le i_{applied}(k) \le i_{\max} \\
&y_{\min} \le y(k) \le y_{\max} \\
&z_{\min} \le z(k) \le z_{\max}
\end{aligned}
\tag{6.28}
$$

where F_k represents differential equation constraints, G_k represents algebraic equation constraints, N represents the number of discretization points in time, z represents differential states, and y represents algebraic states with an applied current of i_{app}. The differential state constraints include physically meaningful bounds on the solid-phase lithium.

In simultaneous nonlinear programming,[86-88] both the control variables and state variables are discretized, which results in a large set of nonlinear equations to be solved simultaneously for obtaining the optimum profile. 150 steps are used for time discretization resulting in a nonlinear system of $13200\left(88\times150\right)$ equations. The nonlinear program was solved using the nonlinear programming solver IPOPT.[89]

6.5 Results and Discussion

In this study, different upper bounds on the radial and lower bounds on tangential stresses are placed and optimal charging profiles are derived. As mentioned before, during charging, the peak (compressive) tangential stress occurs at the surface of the particle and peak (tensile) radial stress occurs at the center of the particle. For graphite-based anode material, the fracture threshold for the tensile stress is much lower compared to compressive stress.[80] Two scenarios are considered: (1) charging a fully discharged (0% SOC) battery for 1800 s, (2) charging a half-discharged (50% SOC) battery for 900 s.

6.5.1 Charging a Fully Discharged Battery for 1800 s

Figure 6-2 shows the voltage and current profiles of charging a fully discharged battery for 1800 s using CC-CV with three different maximum charging rates. Figure 6-3 shows the peak radial stress in three cases of CC-CV where the maximum values attained by peak radial stresses (dimensionless) are 0.24, 0.199, and 0.146 (4C, 3C, and 2C respectively).

Two cases are considered initially. In Case 1, the upper bound on peak (tensile) radial stresses (at anode-separator interface and 4 collocation points) is restricted to the maximum value of the peak radial stresses obtained during CC-CV charging with 3C ($\sigma_r^{\max}$ = 0.199). Similarly, Case 2 corresponds to maximum value of peak radial stresses in case of CC-CV charging with 2C ($\sigma_r^{\max}$ = 0.146). Figure 6-6 shows the results of optimal charging problem. The green (dash dot) curve represents optimal charging profile and voltage for Case 1 and the blue (dash) curve represents Case 2.

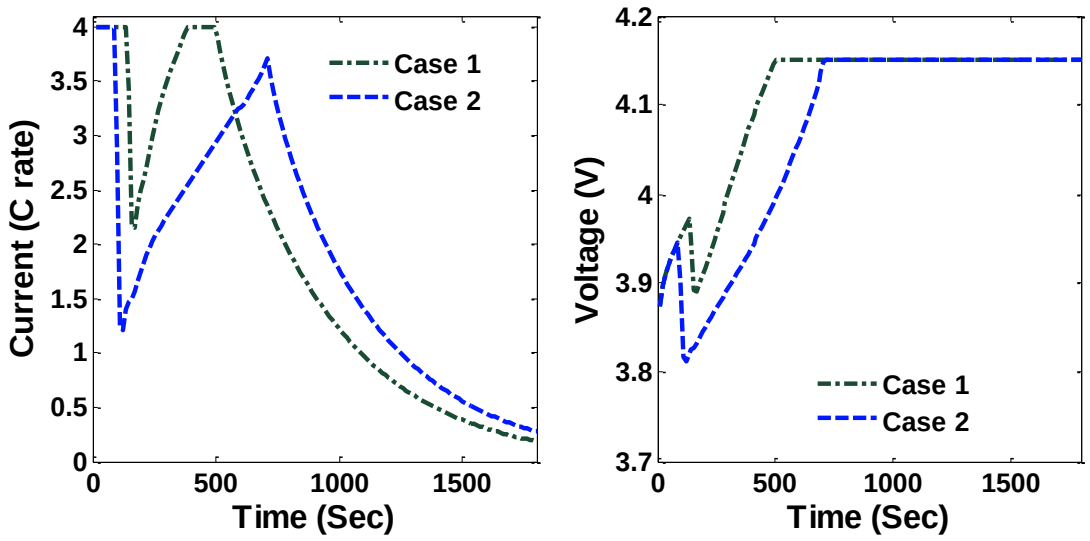

Figure 6-6: Optimal charging profiles and corresponding cell voltage for Cases 1 and 2 (upper bounds on peak radial stresses corresponds to CC-CV with 3C and 2C).

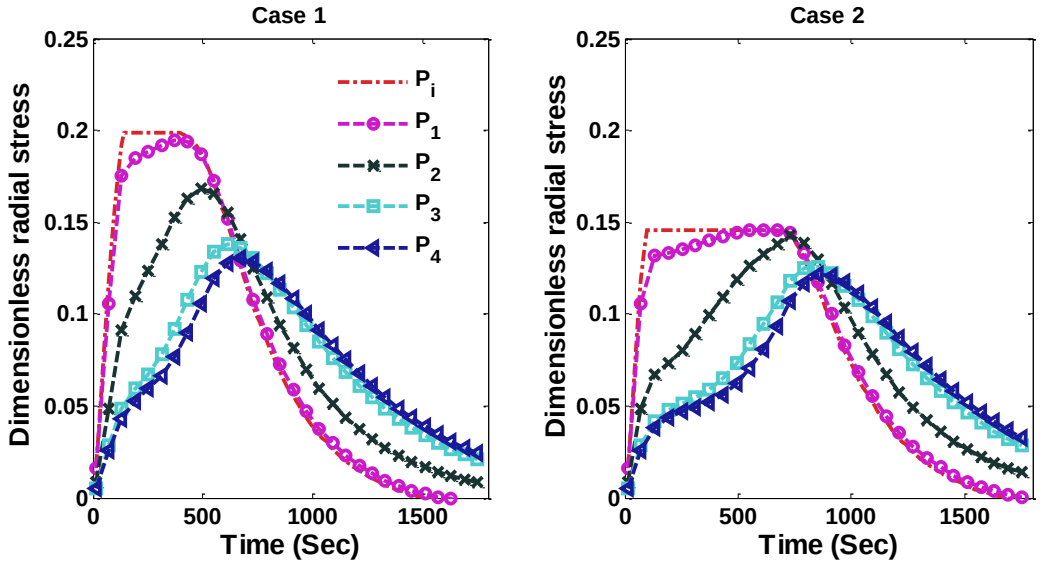

Figure 6-7: Peak radial stresses corresponding to optimal charging profiles for Cases 1 and 2 (Scenario 1).

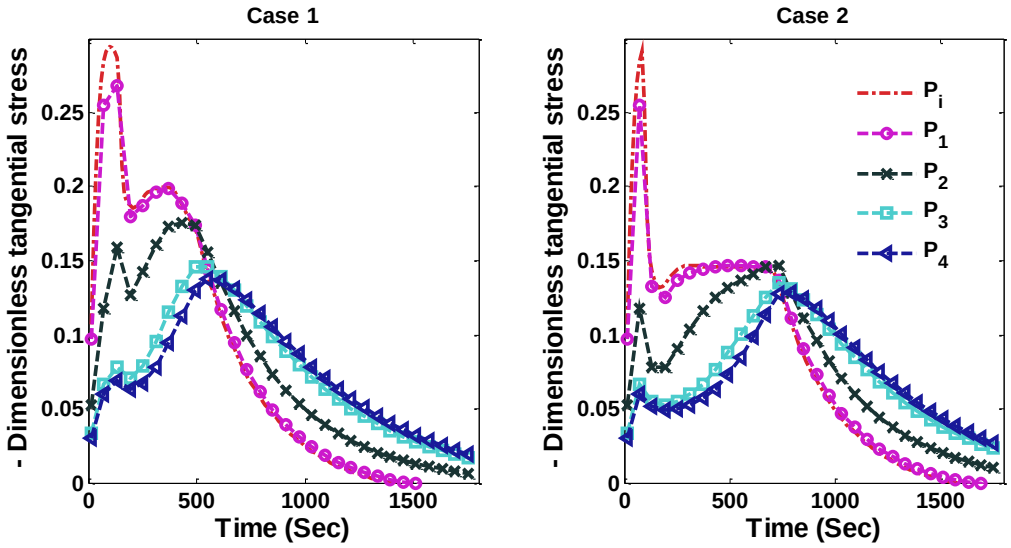

Figure 6-8: Peak tangential stresses corresponding to optimal charging profiles for Cases 1 and 2 (Scenario 1).

The optimal charging profiles derived for Cases 1 and 2 compromise very little on the charge stored compared to CC-CV with 4C but provide stress profiles that are as good as CC-CV with 3C and 2C for stress-induced capacity fade (since fracture during intercalation is mainly due to tensile stress for graphite-type materials[80]). Figure 6-7 shows radial stresses corresponding to Cases 1 and 2. It is clear from Figure 6-7 that optimal charging profiles restrict the peak radial stresses at the desired level. Figure 6-8 shows the peak tangential stresses for Cases 1 and 2 at five points in

the anode. Due to the faster dynamics of the tangential stresses, the maximum peak tangential stresses near the anode-separator interface do not see much decrease in the new charging profiles (see Figure 6-8).

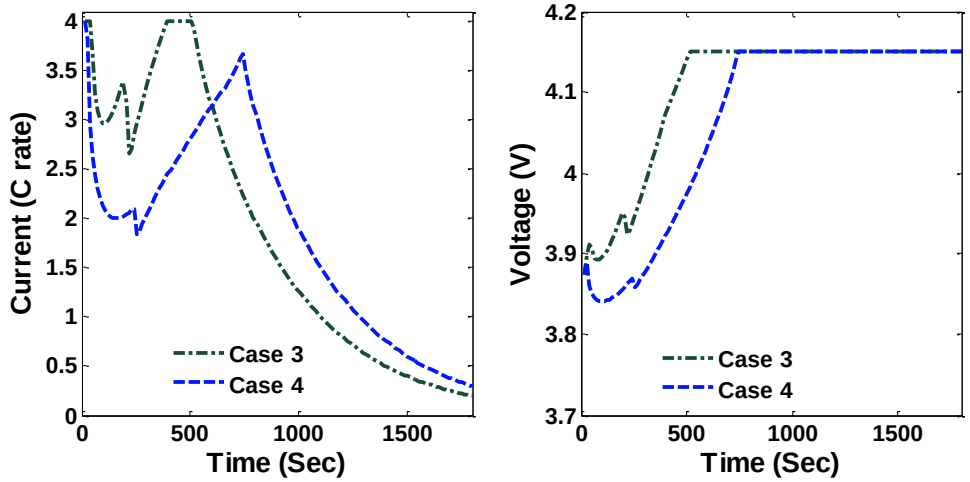

Figure 6-9: Optimal charging profiles and corresponding cell voltage for Cases 3 and 4 (Scenario 1).

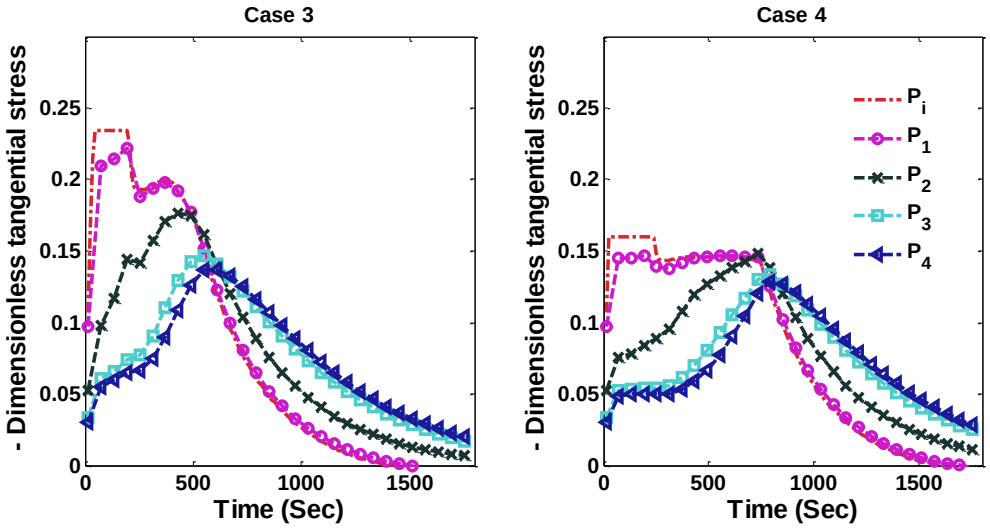

Figure 6-10: Peak tangential stresses corresponding to optimal charging profiles for Cases 3 and 4 (Scenario 1).

Since the fracture threshold can vary between materials, it may be important to put bounds on the peak (compressive) tangential stresses for some materials. Additional bounds can be placed on peak (compressive) tangential stresses and optimal charging profiles can be derived. The minimum values attained by peak tangential stresses at the surface of the particles during charging with CC-

CV at 4C, 3C, and 2C are −0.296, −0.234, and −0.16 (dimensionless), respectively (see Figure 6-3). Cases 3 and 4 (considered below) have upper bounds on peak radial stress and lower bound on peak tangential stress that corresponds to extreme values of stresses during CC-CV at 3C ($\sigma_r^{\max} = 0.199,\ \sigma_t^{\max} = 0.234$) and 2C ($\sigma_r^{\max} = 0.146,\ \sigma_t^{\max} = 0.16$) respectively. Figure 6-9 shows the optimal charging profiles for Cases 3 and 4. The specific shape of the optimal charging profile is created because different constraints become active at different points in time during the charging: maximum current followed by tangential stresses, followed by radial stresses, and finally maximum voltage.

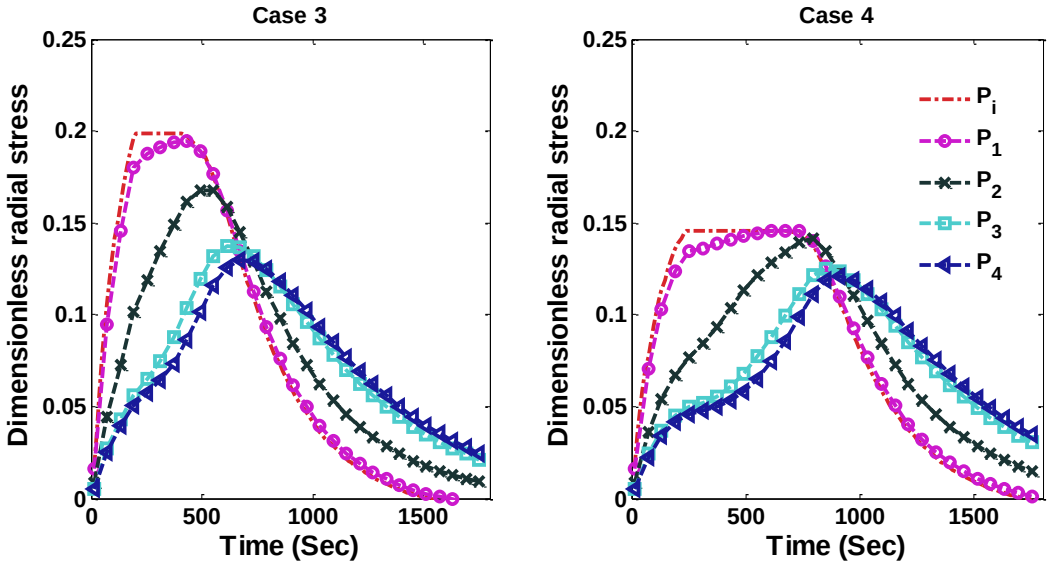

Figure 6-11: Peak radial stresses corresponding to optimal charging profiles for Cases 3 and 4 (Scenario 1).

Figures 6-10 and 6-11 show the corresponding tangential stresses and radial stresses.

The results are summarized in Table 6-6 based on charge stored during CC-CV at 4C. The optimization results show a very small compromise in charge stored compared to CC-CV at 4C can give rise to charging profiles that are as safe as CC-CV with 2C (considering only mechanical

degradation). Moreover, the percentage of SOC compromise strongly depends on the final time chosen for optimization scheme.

Table 6-6: Summary of results for Scenario 1

Cases	Maximum peak radial stress	Minimum peak tangential stress	Charge stored (compared to CC-CV at 4C)
CC-CV (4C)	0.24	−0.296	-
Case 1	0.199	-	99.73%
Case 3	0.199	−0.234	99.61%
CC-CV (3C)	0.199	−0.234	99.00%
Case 2	0.146	-	98.65%
Case 4	0.146	−0.16	98.34%
CC-CV (2C)	0.146	−0.16	94.55%

6.5.2 Charging a Battery at Different SOC

In this scenario, optimal charging of a half-discharged battery is considered for 900 s. CC-CV charging with three different rates (2C, 3C, and 4C) results in different voltage, current, and stress profiles. Simulation results of CC-CV charging with different charging current are plotted in Figure 6-12 (voltage and current), Figure 6-13 (peak radial stresses), and Figure 6-14 (peak tangential stresses).

Similar to the previous scenario, four cases are considered here:

1. $\sigma_r^{\max} = 0.1452$ (corresponds to maximum peak radial stress of CC-CV with 3C)
2. $\sigma_r^{\max} = 0.109$ (corresponds to maximum peak radial stress of CC-CV with 2C)

3. $\sigma_r^{\max} = 0.1452$, $\sigma_t^{\max} = 0.173$ (corresponds to maximum peak radial and tangential stress of CC-CV with 3C)

4. $\sigma_r^{\max} = 0.109$, $\sigma_t^{\max} = 0.123$ (corresponds to maximum peak radial and tangential stress of CC-CV with 2C)

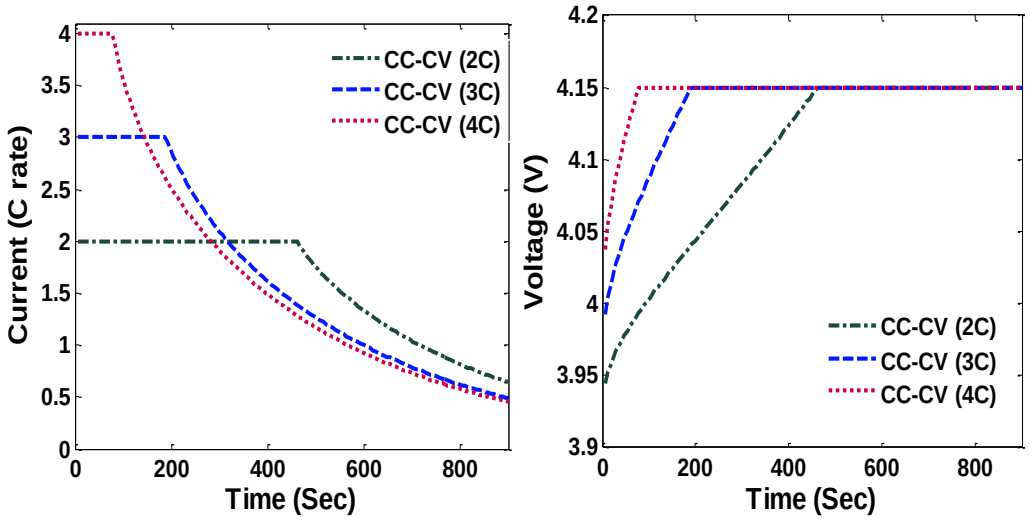

Figure 6-12: Voltage and current profiles during CC-CV charging with different C rate.

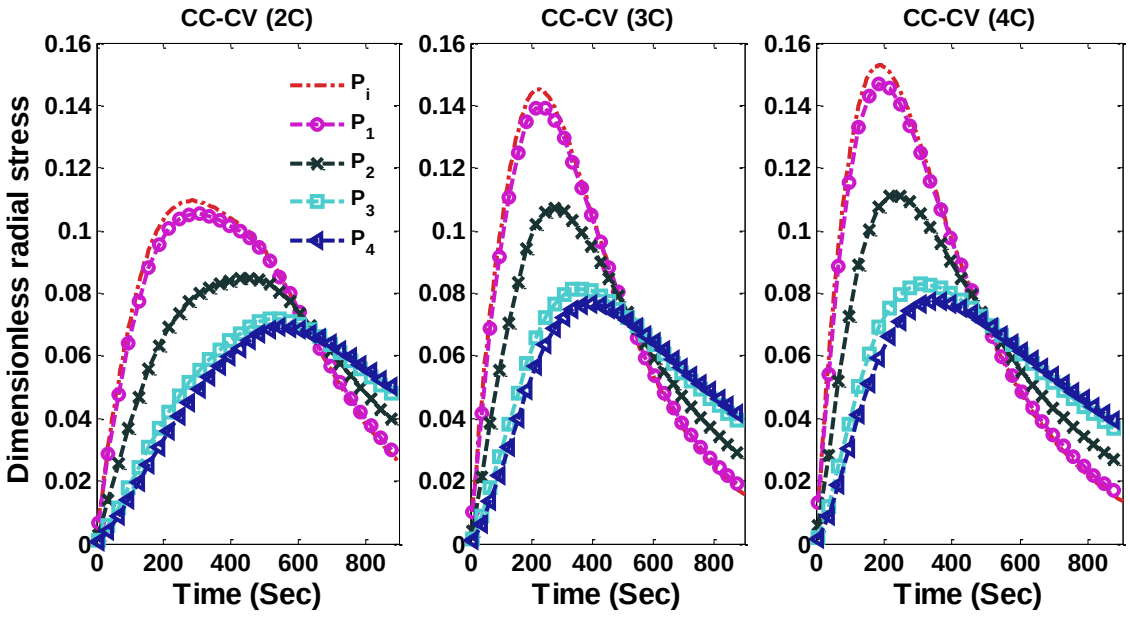

Figure 6-13: Radial stresses (tensile) at the center of the particles at the separator-anode interface (P_i) and 4 collocation points are plotted for CC-CV charging at 2C, 3C, and 4C.

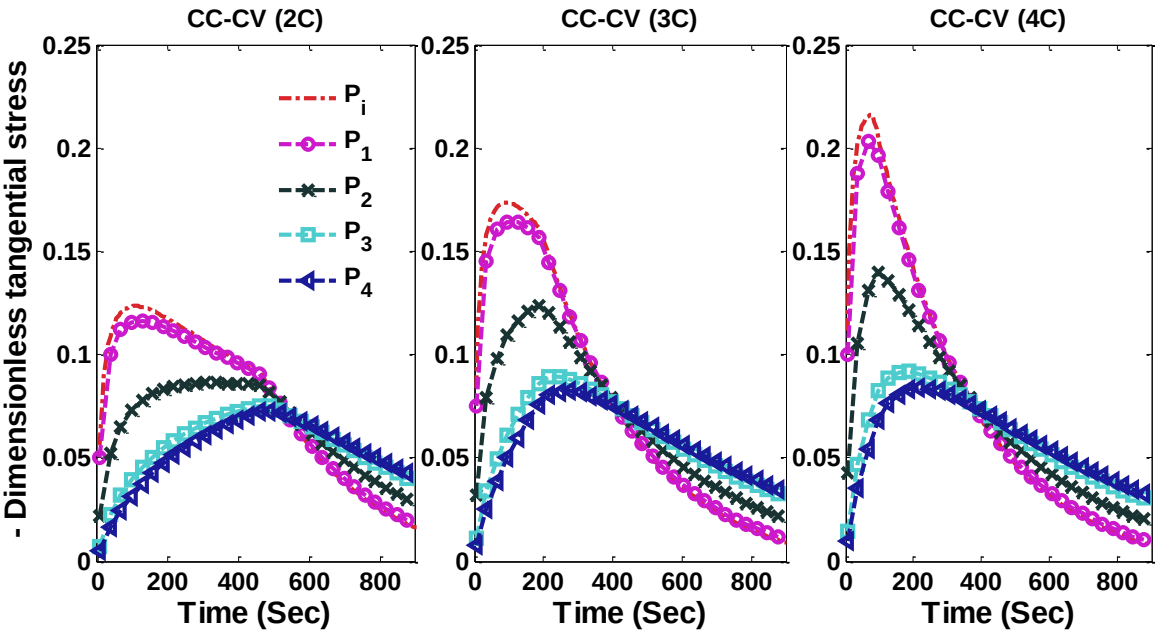

Figure 6-14: Tangential stresses (compressive) at the surface of the particles at the separator-anode interface (P_i) and 4 collocation points are plotted CC-CV charging at 2C, 3C, and 4C.

The optimal charging profile for Cases 1 and 2 are plotted in Figure 6-15, which restricts the peak (tensile) radial stresses that develop in the anode.

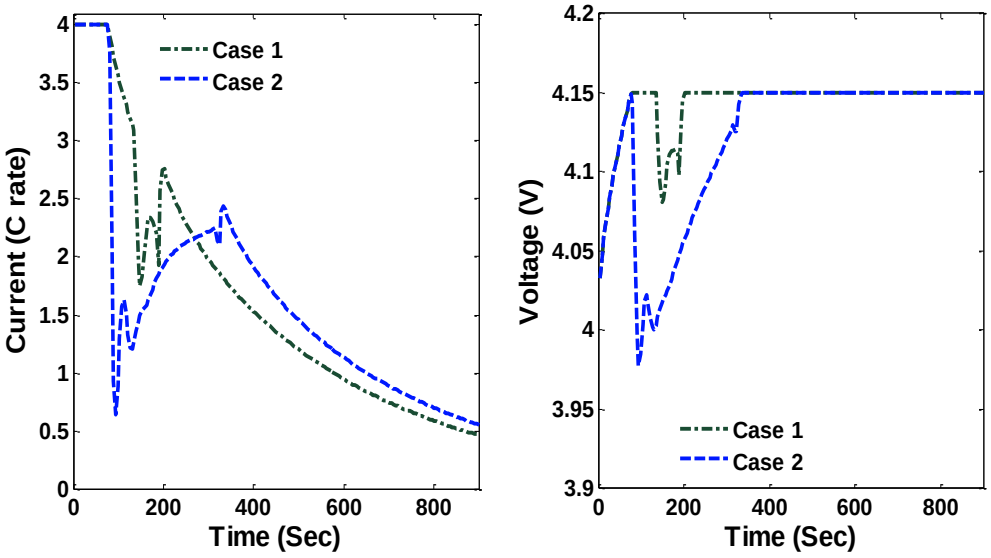

Figure 6-15: Optimal charging profiles and corresponding cell voltage for Cases 1 and 2 (Scenario 2).

Stress profiles corresponding to optimal charging profiles for Cases 1 and 2 are plotted in Figures 6-16 and 6-17. Results for Cases 3 and 4, which restrict both radial and tangential stresses, are

plotted in Figure 6-18 and corresponding peak radial and tangential stresses are plotted in Figures 6-19 and 6-20. Table 6-7 summarizes the results associated with Scenario 2 which again suggest that a very small compromise on the SOC stored can yield improved charging profiles.

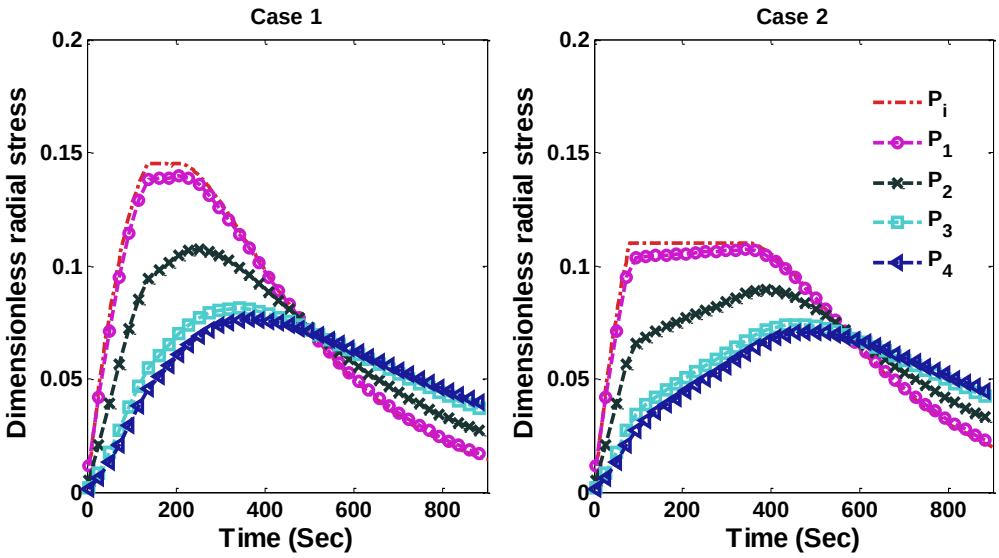

Figure 6-16: Peak radial stresses corresponding to optimal charging profiles for Cases 1 and 2 (Scenario 2).

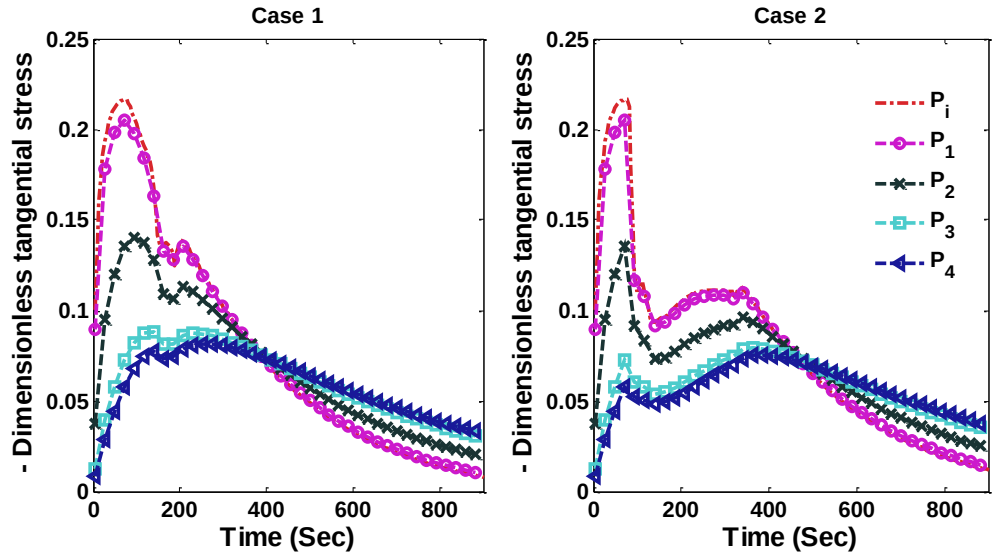

Figure 6-17: Peak tangential stresses corresponding to optimal charging profiles for Cases 1 and 2 (Scenario 2).

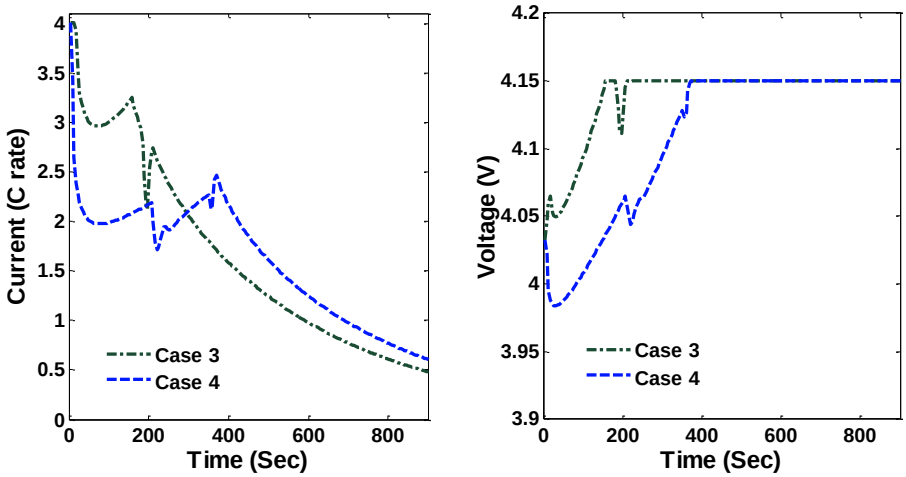

Figure 6-18: Optimal charging profiles and corresponding cell voltage for Cases 3 and 4 (Scenario 2).

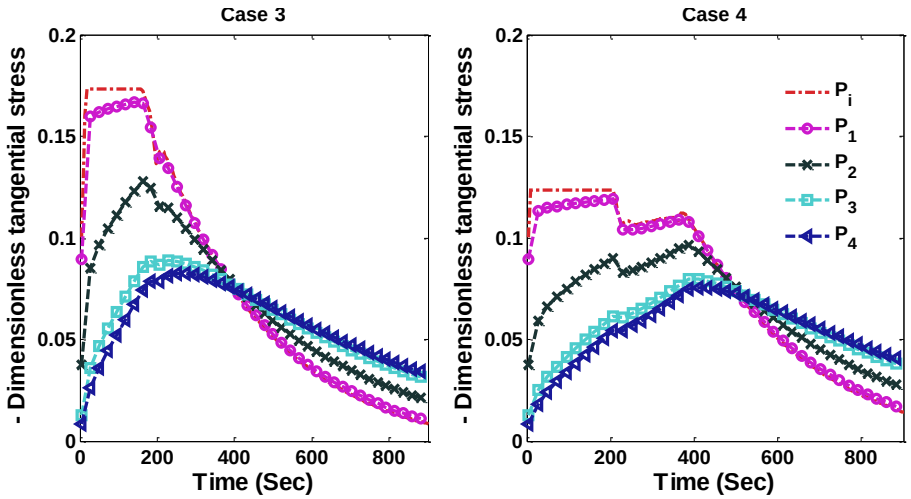

Figure 6-19: Peak tangential stresses corresponding to optimal charging profiles for Cases 3 and 4 (Scenario 2).

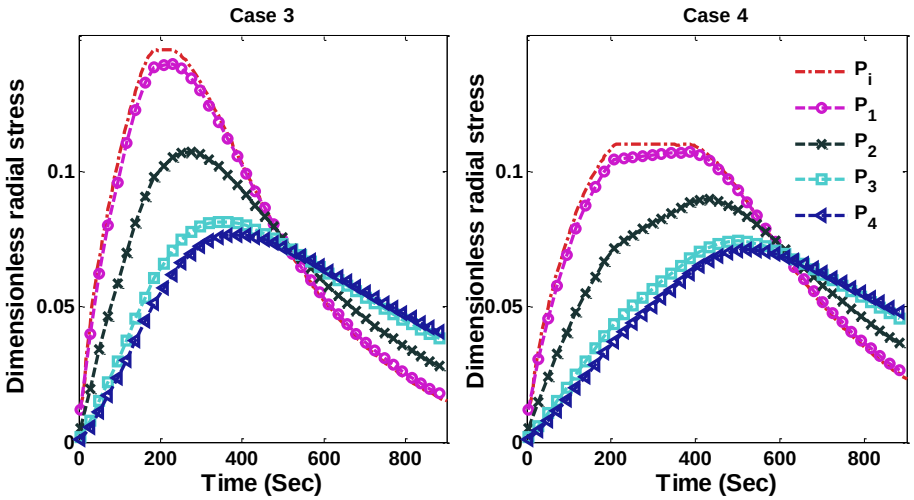

Figure 6-20: Peak radial stresses corresponding to optimal charging profiles for Cases 3 and 4 (Scenario 2).

Table 6-7: Summary of results for Scenario 2

Cases	Maximum peak radial stress	Minimum peak tangential stress	Charge stored (compared to CC-CV at 4C)
CC-CV (4C)	0.153	−0.215	-
Case 1	0.145	-	99.73%
Case 3	0.145	−0.173	99.21%
CC-CV (3C)	0.145	−0.173	99.0%
Case 2	0.109	-	97.3%
Case 4	0.109	−0.123	95.8%
CC-CV (2C)	0.109	−0.123	94.8%

6.6 Conclusions and Future Directions

This chapter shows the use of a dynamic optimization framework to derive optimal charging profiles using a reformulated P2D model considering intercalation-induced stresses. It is very clear from the analysis that the local pore wall flux varies significantly from the average current density, hence a P2D model is necessary to correctly capture the peak radial and tangential stresses. Since the anode-separator interface faces more stress compared to the rest of the anode (see Figure 6-5), smarter charging profiles can be derived which can reduce the mechanical damage due to stress. It should be noted here that single particle model accounts for the average behavior and hence gives lower values for intercalation-induced stresses (Chapter 4).

A limitation of this study is its use of an isothermal model. A thermal model may be used to broaden the scope of this work. It should be noted that the nonlinear thermal dependencies of material properties make the optimization problem more difficult to solve. Moreover, at higher rates, for certain chemistries and parameter values, the plating side reaction becomes possible near the anode-separator interface which can also be handled using a dynamic optimization framework.[13] The model used to represent intercalation induced stresses in this study is applicable

only for materials with small volumetric expansion (up to 10%) and ignores any thermodynamic factor. Efforts will be made in the future to incorporate additional capacity fade mechanics (thermal degradation, plating side reaction, etc.) into a single optimization framework and to use better models to describe intercalation-induced stresses. Use of a reformulated P2D model can also help place physically meaningful voltage constraints. In this study, 4.15 V is chosen as the upper bound for voltage, which can be replaced by some meaningful constraints that minimizes side reactions and electrolyte decomposition.

List of Variables and Parameters

a	Surface area per volume of electrode
Brugg	Bruggeman Coefficient
c	Electrolyte concentration
c^s	Solid Phase Concentration
D	Electrolyte phase Diffusion coefficient
D_{eff}	Effective Diffusion coefficient
D^s	Solid phase diffusion coefficient
E	Young's modulus
F	Faraday's Constant
I	Applied Current
j	Pore wall flux
k	Reaction rate constant
l	Length of region
R_p	Particle Radius
R	Gas Constant
T_{ref}	Reference Temperature
t_+	Transference number
T	Temperature
U	Open Circuit Potential
ν	Poisson's ratio
ε	Porosity
ε_f	Filling fraction
θ	State of Charge
κ	Liquid phase conductivity

σ	Solid Phase Conductivity
Φ_1	Solid Phase Potential
Φ_2	Liquid Phase Potential
Ω	Partial molar volume
x_n	solid phase concentration in anode particle /Maximum solid phase concentration in anode ($c_n^s / c_{n,\max}^s$)
ξ	Scaled radial distance in anode particle $(r / R_{p,n})$

List of Subscripts

eff	Effective, as for diffusivity or conductivity
n	Related to the negative electrode—the anode
P	Related to the positive electrode—the cathode
S	Related to the separator

List of Superscripts

s	Related to Solid Phase
$+/-$	Pertains to the boundary conditions from right and left side of the interface (e.g. L_p^-, L_p^+, etc.)

Chapter 7

Effect of Porosity, Thickness and Tortuosity on Capacity Fade of Anode

> The fewer moving parts, the better. Exactly. No truer words were ever spoken in the context of engineering.
>
> **Christian Cantrell**

7.1 Introduction

The graphite anode in lithium-ion batteries is vulnerable to capacity fade due to several mechanisms. Advancement in understanding of such capacity fade mechanisms has paved the way for selecting design parameters that consider these effects. Present chapter shows the effect of porosity, thickness, and tortuosity of the anode on capacity fade mechanisms. Three main capacity fade mechanisms are analyzed in this chapter: (1) solid electrolyte interface (SEI) side reaction, (2) lithium plating side reaction and (3) mechanical degradation due to intercalation induced stresses. Moreover, for a given thickness and porosity of anode, the effect of porosity variation on capacity fade mechanisms is also presented.

Research on various fronts is underway to address the issues mentioned above. While finding better materials and improving their properties is one approach, the use of system level approach to reach better efficiency in existing and emerging systems is another approach. The true potential of battery materials cannot be realized due to system level inefficiencies, especially where transport effects become limiting (e.g. higher rates of charging/discharging at normal temperature or low temperatures operations).

One of the many problems that can be addressed by continuum level modeling approaches is finding the thicknesses and porosities of anode and cathode materials while keeping various processes and objectives in mind. These objectives may be discharge capacities at higher rates, charging time, mechanical degradation due to intercalation induced stresses, loss of active lithium due to parasitic side reaction (SEI layer and lithium plating), safety, etc. While one would like to maximize energy density by packing the solid phase material compactly with larger thickness; rate capacity, safety and capacity fade may cause such an approach to be impractical.

How should one choose the porosity and length of anode and cathode is an interesting research problem. Design optimization (porosity and thickness) for lithium-ion battery can be traced back to the work done by Prof. Newman using the reaction zone model[105] and with the pseudo two dimensional model.[94] Work on determining the optimal porosity distribution by considering the ohmic drop has been done by Ramadesigan *et al*.[106] Effect of low temperature and porosity on the performance of lithium-ion batteries is also studied by Ji *et al.*[107] While these works are based on maximizing the energy/power density of lithium-ion batteries by choosing optimal design parameters, no work has been done in quantifying the effect of design parameters on capacity fade mechanisms. With the advances made in understanding capacity fade reactions and intercalation induced stresses in intercalation materials, proper treatment can be given in selection of the porosity and the thicknesses of electrode materials based on detailed electrochemical engineering models augmented with capacity fade mechanisms.

One of the practical problems that can be addressed by continuum level models can be summarized in a question: "*How should one choose the design parameters (thicknesses, porosities, area etc) so that high rate capacity and energy density can be achieved considering the effect of capacity fade mechanisms?"* Although this is a problem of practical importance, the large number of design

parameters prevent a full understanding to be developed here. Rather, we choose a simpler problem of selecting the porosity and thickness of the anode and their effect on capacity fade mechanisms, while maintaining all other parameters constant.

Section 2 briefly introduces the continuum level model used to simulate battery charge/discharge behavior and explains intercalation induced stress and overpotentials for parasitic side reactions. Section 3 describes the problem statement of selecting design parameters for improved battery design. Section 4 discusses simulation results which highlight the effect of porosity and length of the anode as well as porosity variation in anode on capacity fade and cell capacities, followed by conclusion.

7.2 Model description

Detailed models that incorporate electrochemical, transport, and thermodynamic processes along with the geometry of the underlying system can be used to monitor and control the internal states of a battery.[27] The isothermal porous electrode pseudo-two dimensional (P2D) model is one such model which is given in Table 6-1.

Table 6-2 presents various expressions used in this model. The P2D model is general enough to incorporate various capacity fade mechanisms. This chapter focuses on three main sources of capacity fade and safety issues in batteries: intercalation induced stresses, SEI layer side reaction and lithium plating side reaction.

Table 7-1: Governing PDEs for the P2D model

Governing Equations	**Boundary Conditions**	
Positive Electrode		
$\varepsilon_{\mathrm{p}} \dfrac{\partial c}{\partial t} = \dfrac{\partial}{\partial x}\left[D_{\mathrm{eff,p}} \dfrac{\partial c}{\partial x} \right] + a_{\mathrm{p}} \left(1 - t_{+}\right) j_{\mathrm{p}}$	$\left.\dfrac{\partial c}{\partial x}\right\|_{x=0} = 0\ ,\ -D_{\mathrm{eff,p}} \left.\dfrac{\partial c}{\partial x}\right\|_{x=l_p^-} = -D_{\mathrm{eff,s}} \left.\dfrac{\partial c}{\partial x}\right\|_{x=l_p^+}$	(7.1)
$-\sigma_{eff,p} \dfrac{\partial \Phi_1}{\partial x}$ $-\kappa_{\mathrm{eff,p}} \dfrac{\partial \Phi_2}{\partial x} + \dfrac{2\kappa_{\mathrm{eff,p}} RT}{F}\left(1 - t_{+}\right) \dfrac{\partial \ln c}{\partial x} = I$	$\left.\dfrac{\partial \Phi_2}{\partial x}\right\|_{x=0} = 0,\ \kappa_{\mathrm{eff,p}} \left.\dfrac{\partial \Phi_2}{\partial x}\right\|_{x=l_p^-} = \kappa_{\mathrm{eff,s}} \left.\dfrac{\partial \Phi_2}{\partial x}\right\|_{x=l_p^+}$	(7.2)
$\dfrac{\partial}{\partial x}\left[\sigma_{\mathrm{eff,p}} \dfrac{\partial \Phi_1}{\partial x} \right] = a_{\mathrm{p}} F j_{\mathrm{p}}$	$\sigma_{eff,p} \left.\dfrac{\partial \Phi_1}{\partial x}\right\|_{x=0} = -I,\ \left.\dfrac{\partial \Phi_1}{\partial x}\right\|_{x=l_p^-} = 0$	(7.3)
$\dfrac{\partial c_p^s}{\partial t} = \dfrac{1}{r^2} \dfrac{\partial}{\partial r}\left[r^2 D_p^s \dfrac{\partial c_p^s}{\partial r} \right]$	$\left.\dfrac{\partial c_p^s}{\partial r}\right\|_{r=0} = 0,\ D_p^s \left.\dfrac{\partial c_p^s}{\partial r}\right\|_{r=R_P} = -j_p$	(7.4)
Separator		
$\varepsilon_s \dfrac{\partial c}{\partial t} = \dfrac{\partial}{\partial x}\left[D_{\mathrm{eff,s}} \dfrac{\partial c}{\partial x} \right]$	$c\|_{x=l_p^-} = c\|_{x=l_p^+}\ ,\ c\|_{x=l_p+l_s^-} = c\|_{x=l_p+l_s^+}$	(7.5)
$-\kappa_{\mathrm{eff,s}} \dfrac{\partial \Phi_2}{\partial x} + \dfrac{2\kappa_{\mathrm{eff,s}} RT}{F}\left(1 - t_{+}\right) \dfrac{\partial \ln c}{\partial x} = I$	$\Phi_2\|_{x=l_p^-} = \Phi_2\|_{x=l_p^+}$ $\Phi_2\|_{x=l_p+l_s^-} = \Phi_2\|_{x=l_p+l_s^+}$	(7.6)
Negative Electrode		
$\varepsilon_n \dfrac{\partial c}{\partial t} = \dfrac{\partial}{\partial x}\left[D_{\mathrm{eff,n}} \dfrac{\partial c}{\partial x} \right] + a_n \left(1 - t_{+}\right) j_n$	$\left.\dfrac{\partial c}{\partial x}\right\|_{x=l_p+l_s+l_n} = 0$ $-D_{\mathrm{eff,s}} \left.\dfrac{\partial c}{\partial x}\right\|_{x=l_p+l_s^-} = -D_{\mathrm{eff,n}} \left.\dfrac{\partial c}{\partial x}\right\|_{x=l_p+l_s^+}$	(7.7)
$-\sigma_{\mathrm{eff,n}} \dfrac{\partial \Phi_1}{\partial x}$ $-\kappa_{\mathrm{eff,n}} \dfrac{\partial \Phi_2}{\partial x} + \dfrac{2\kappa_{\mathrm{eff,n}} RT}{F}\left(1 - t_{+}\right) \dfrac{\partial \ln c}{\partial x} = I$	$-\kappa_{\mathrm{eff,s}} \left.\dfrac{\partial \Phi_2}{\partial x}\right\|_{x=l_p+l_s^-} = -\kappa_{\mathrm{eff,p}} \left.\dfrac{\partial \Phi_2}{\partial x}\right\|_{x=l_p+l_s^+}$ $\Phi_2\|_{x=l_p+l_s+l_n} = 0$	(7.8)
$\dfrac{\partial}{\partial x}\left[\sigma_{\mathrm{eff,n}} \dfrac{\partial \Phi_1}{\partial x} \right] = a_n F j_n$	$\left.\dfrac{\partial \Phi_1}{\partial x}\right\|_{x=l_p+l_s^+} = 0,\ \sigma_{eff,n} \left.\dfrac{\partial \Phi_1}{\partial x}\right\|_{x=l_p+l_s+l_n} = -I$	(7.9)

$\frac{\partial c_n^s}{\partial t} = \frac{1}{r^2}\frac{\partial}{\partial r}\left[r^2 D_n^s \frac{\partial c_n^s}{\partial r} \right]$	$\left.\frac{\partial c_n^s}{\partial r}\right\|_{r=0} = 0,\ D_n^s \left.\frac{\partial c_n^s}{\partial r}\right\|_{r=R_P} = -j_n$	(7.10)

Table 7-2: Additional expressions used in the P2D model

$j_p = 2k_p c^{0.5} \left. c_p^s \right\|_{r=R_P}^{0.5} \left(c_{\max,p}^s - \left. c_p^s \right\|_{r=R_P} \right)^{0.5} \sinh\left[\frac{F}{2RT}\left(\Phi_1 - \Phi_2 - U_p \right) \right]$	(7.11)
$j_n = 2k_n c^{0.5} \left. c_n^s \right\|_{r=R_P}^{0.5} \left(c_{\max,n}^s - \left. c_n^s \right\|_{r=R_P} \right)^{0.5} \sinh\left[\frac{F}{2RT}\left(\Phi_1 - \Phi_2 - U_n \right) \right]$	(7.12)
$\kappa_{eff,i} = \varepsilon_i^{brugg_i} \times 10^{-4} c \left(\begin{matrix} -10.5 + 0.074T - 6.96\times10^{-5}T^2 + 6.68\times10^{-4}c - \\ 1.78\times10^{-5}cT + 2.8\times10^{-8}cT^2 + 4.94\times10^{-7}c^2 - 8.86\times10^{-10}Tc^2 \end{matrix} \right)^2$ $, i = p, s, n$	(7.13)
$\sigma_{eff,i} = \sigma_i \left(1 - \varepsilon_i - \varepsilon_{f,i} \right), i = p, s, n$	(7.14)
$D_{eff,i} = D\varepsilon_i^{brugg_i}, i = p, s, n$ $D = 2.33\times10^{-4} \times 10^{-4.43 - \frac{54}{\left(T - 5\times10^{-3}c - 229\right)} - 2.2\times10^{-4}c}$	(7.15)
$a_i = \frac{3}{R_i}\left(1 - \varepsilon_i - \varepsilon_{f,i} \right), i = p, s, n$	(7.16)
$U_p = \frac{-4.656 + 88.669\theta_p^{\,2} - 401.119\theta_p^{\,4} + 342.909\theta_p^{\,6} - 462.471\theta_p^{\,8} + 433.434\theta_p^{\,10}}{-1.0 + 18.933\theta_p^{\,2} - 79.532\theta_p^{\,4} + 37.311\theta_p^{\,6} - 73.083\theta_p^{\,8} + 95.96\theta_p^{\,10}}$ $\theta_p = \frac{c^s\|_{r=R_{P,n}}}{c_{\max,p}^s}; 0.4955 \le \theta_p \le 0.99$	(7.17)
$U_n = -0.057 + 0.53\mathrm{e}^{-57\theta} - 0.184\tanh\left(20.0\theta - 21.0\right) - 0.012\tanh\left(7.57\theta - 4.431\right)$ $- 0.0304\tanh\left(18.518\theta - 3.24\right) - 0.01\tanh\left(0.255\theta - 0.02653\right)$ $\theta_n = \frac{c^s\|_{r=R_{P,n}}}{c_{\max,n}^s} 0.01 \le \theta_n \le 0.99$	(7.18)
$D_i^s = D_{i,ref}^s \exp\left(-\frac{E_a^{D_i^s}}{R}\left(\frac{1}{T} - \frac{1}{T_{ref}} \right) \right),\ i = p, n$	(7.19)
$k_i = k_{i,ref} \exp\left(-\frac{E_a^{k_i}}{R}\left(\frac{1}{T} - \frac{1}{T_{ref}} \right) \right),\ i = p, n$	(7.20)

7.2.1 Intercalation induced stresses

Various models, varying in their sophistication, have been proposed to quantify the intercalation-induced stresses in the solid particles. These models are divided in two categories: stress splitting[31,32] and strain splitting.[33-35] In this chapter, a model presented by Cheng and Verbrugge[33] is used. This stress model does not incorporate a moving boundary formulation and ignores thermodynamic factors and pressure-induced diffusion. These simplifications restrict its use to materials with very low volumetric expansion. The resulting equations describing radial stress (σ_r) and tangential stress (σ_t) generated in spherical particles are given in Table 6-4. In this study, tensile stress is taken as positive and compressive stress is taken as negative. Here Ω_n is the partial molar volume of the solute, E_n is the Young's modulus, and ν_n is the Poisson's ratio. Parameters values used in this study are listed in Table 7-4.

Table 7-3: Governing equations for intercalation-induced stress

Governing Equation	
$\overline{\sigma_r}(\xi,t)=\dfrac{3\sigma_r(\xi,t)}{\left(\dfrac{\Omega_n E_n c^s_{n,\max}}{1-\nu_n}\right)}=\dfrac{2}{3}\left(\int_0^1 \dfrac{c_n^s(\xi,t)}{c^s_{n,\max}}\xi^2 d\xi-\dfrac{1}{\xi^3}\int_0^{\xi}\dfrac{c_n^s(\xi,t)}{c^s_{n,\max}}\xi^2 d\xi\right)$	(7.21)
$\overline{\sigma_t}(\xi,t)=\dfrac{3\sigma_t(\xi,t)}{\left(\dfrac{\Omega_n E_n c^s_{n,\max}}{1-\nu_n}\right)}=\left(2\int_0^1 \dfrac{c_n^s(\xi,t)}{c^s_{n,\max}}\xi^2 d\xi+\dfrac{1}{\xi^3}\int_0^{\xi}\dfrac{c_n^s(\xi,t)}{c^s_{n,\max}}\xi^2 d\xi-\dfrac{c_n^s(\xi,t)}{c^s_{n,\max}}\right)$	(7.22)

Table 7-4: List and values of parameters

Symbol	Parameter	Positive Electrode[a]	Separator[a]	Negative Electrode[a]	Units
Brugg	Bruggeman coefficient	1.5 /2.5	1.5 [b]	1.5 [b]	
$c_{i,\max}^{s}$	Maximum solid phase concentration	51554		30555	mol/m^3
c_0	Initial electrolyte concentration	1000	1000	1000	mol/m^3
$D_{i,o}^{s}$	Reference solid phase diffusivity	1×10^{-14}		3.9×10^{-14}	m^2/s
$E_i^{D^s}$	Activation energy for diffusivity	5000 [b]		5000 [b]	J/mol
E_i^{k}	Activation energy for reaction rate	5000 [b]		5000 [b]	J/mol
F	Faraday's constant		96487		C/mol
$k_{i,o}$	Reference reaction rate constant	2.33×10^{-11}		5.03×10^{-11}	m$^{2.5}$/(mol$^{0.5}$ s)
l_i	Region thickness	80×10^{-6}	25×10^{-6}	88×10^{-6}	m
$R_{p,i}$	Particle radius	2×10^{-6} [b]		10×10^{-6} [b]	m
R	Gas constant		8.314		J/mol/ K
T_{ref}	Temperature		298.15		K
t_+	Transference number		0.364		
$\varepsilon_{f,i}$	Filler fraction	0.025		0.0326	
ε_i	Porosity	0.385	0.724	0.485	
ρ	Density	2500	1100	2500	kg/m^3
σ_i	Solid phase electronic conductivity	59		48.24	S/m
Ω	Partial molar volume	4.0815×10^{-6} [c]			m^3/mol
E	Young's modulus	15×10^{9} [d]			Pa
ν	Poisson's ratio	0.3 [d]			
$\Re_{SEI}$	Resistance	0.00215 [b]			Ω
ρ_e	Density of electrolyte	2000 [b]			kg/m^3

[a] Unless otherwise noted, all parameters used for the electrodes and separator are from Subramanian *et al.*[53] Porosity, length, surface area for anode is given for base case.
[b] Assumed value
[c] Values obtained from Renganathan *et al.*[35]
[d] Values obtained from Christensen *et al.*[80]

During intercalation, for the materials with a positive volume expansion, the radial stresses remain tensile throughout a particle (assuming zero external pressure at the surface) whereas the tangential stress becomes compressive at the surface and tensile at the center. The peak (tensile) radial stress occurs at the center of the particle and peak (compressive) tangential stress occurs at the surface of the particle.[32] During deintercalation, the nature of stresses changes (i.e. tensile stresses become compressive and compressive stresses become tensile), but the location of peak stresses remains the same for both. Therefore, the peak radial stresses at the center of the particles and peak tangential stresses at the surface of the particles are monitored. As shown by Christensen and Newman[32] and also clear from the equations given in Table 6-4, the peak tangential stresses and the peak radial stresses are same at the center of the particles, and so monitoring one of the either stresses would be sufficient for our analysis.

Due to the finite thickness of the anode, the pore wall flux becomes non-uniform except at very small rates of charging and discharging. This non uniformity of the pore wall flux changes with time as well. In general, the pore wall flux is higher at the anode separator interface at the onset of charge/discharge of the battery; afterwards, the pore wall flux decreases at the anode-separator interface and increases at the anode-current collector interface. Due to the time-varying and thickness-dependent non-uniformity of the pore wall flux, different maximum peak stresses are observed at different times during charge/discharge. Usually, the anode-separator interface faces largest pore wall flux resulting in maximum peak stresses at that point compared to other locations of the anode. Figure 7-1 shows the distribution of peak radial ($\overline{\sigma_r}$) and tangential stresses ($\overline{\sigma_t}$) at different locations in anode with time. In this study, we will focus on peak stresses and their maximum values in the solid particle at the anode-separator interface (solid curves in Figure 7-1).

One more thing to note here is that the dynamics of peak tangential stresses (which occurs at the surface) is faster compared to peak radial stresses (which occurs at the center).

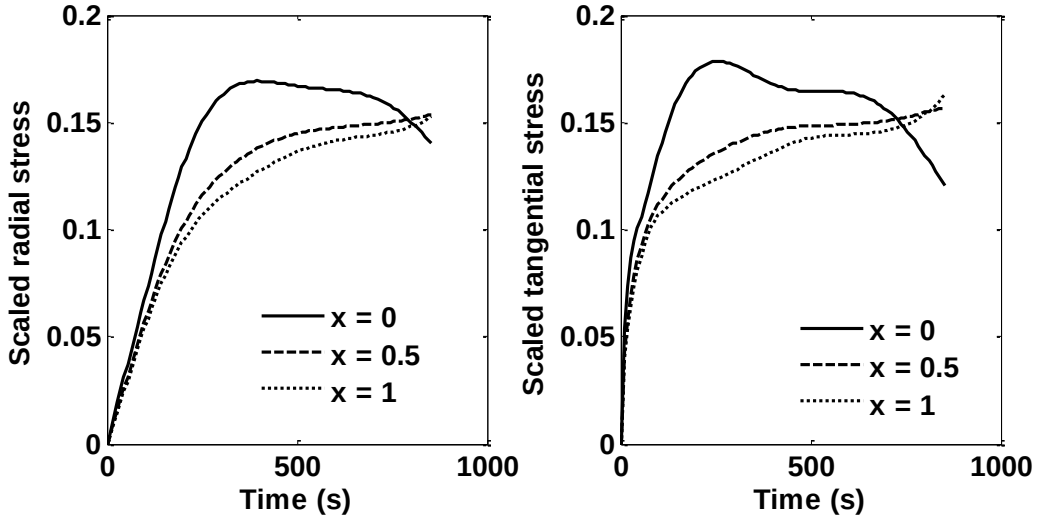

Figure 7-1: Distribution of radial and tangential stresses during charging at 4C at 25 C (x = 0 represent anode-separator interface and x = 1 represent anode-current collector interface)

7.2.2 Lithium plating side reaction

As mentioned earlier, lithium plating side reaction not only causes capacity fade but also poses a significant safety issue.[11] Though lithium-ion batteries are inherently safer than lithium-metal batteries, as the former avoids dendrite formation during charging, the slightly more positive potential of LiC_6 compared to Li/Li^+, inherits the problem of lithium plating during charging[11] at high rates and even low rates at low temperature (0.2 C at $-20\,^{\circ}\mathrm{C}$).[13,14]

The driving force for the partially irreversible[14] lithium plating side reaction at the anode can be expressed by the overpotential:[58]

$$\eta_{plating}\left(x,t\right)=\phi_n^s\left(x,t\right)-\phi_e\left(x,t\right)-U_{plating,n} \tag{7.23}$$

where $\eta_{plating}$ is the overpotential for lithium plating side reaction, $\phi_n^s\left(x,t\right)$ is the solid phase potential in negative electrode, $\phi_{e,n}\left(x,t\right)$ is the electrolyte-phase potential in anode, $U_{plating,n}$ is the

open-circuit potential for the plating reaction which is taken to be zero, and x is the distance across the electrode. The expression for $\eta_{plating}$ given in (7.23) ignores the voltage drop across the solid electrolyte interface (SEI) layer. For a uniform porosity anode, the anode-separator interface becomes most vulnerable to plating side reaction. Figure 7-2 shows the typical evolution of $\phi_n^s(x,t)-\phi_{e,n}(x,t)$ during charging.

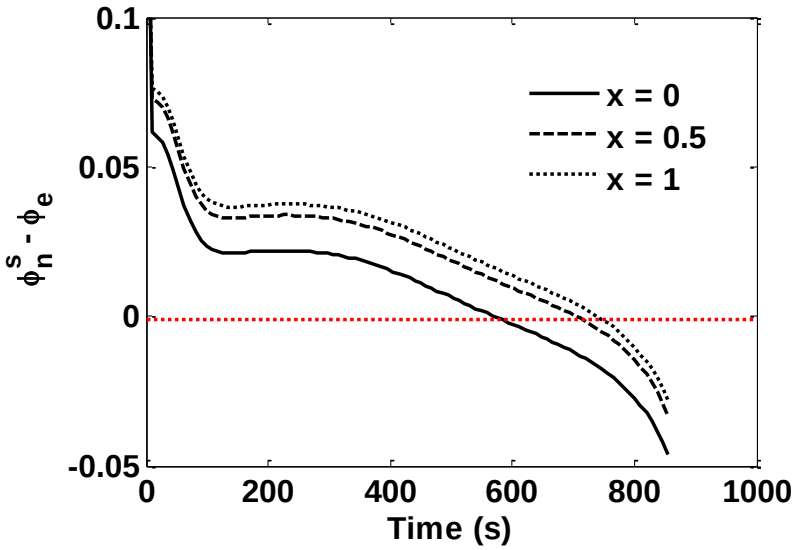

Figure 7-2: Distribution of overpotential for lithium plating side reaction across length during charging at 4C rate (x = 0 represent anode-separator interface and x = 1 represent anode-current collector interface)

Only when $\phi_n^s(x,t)-\phi_{e,n}(x,t)$ less than zero, the plating reaction is favored. Figure 7-2 shows that at anode-separator interface, the plating side reaction becomes feasible sooner and achieves larger magnitude compared to other parts of the anode.

7.2.3 Overpotential for SEI Layer

In this simulation the voltage drop across the SEI layer is not modeled in rigorous sense as given in equation (7.24),[57]

$$\eta_{SEI}(x,t)=\phi_n^s(x,t)-\phi_e(x,t)-U_{SEI}-\left(\frac{\delta(x,t)}{\kappa_{SEI}}+\Re_{SEI}\right)\left(j_{SEI}(x,t)+j_n(x,t)\right)F \qquad (7.24)$$

Here, $\Re_{SEI}$ is the resistance of SEI layer formed during the initial cycles and $\delta(x,t)/\kappa_{SEI}$ refers to the increase in resistance during the fresh buildup of SEI layer. Simplified expression given in equation (7.25) is used to approximate the overpotential for SEI layer assuming that the increase in SEI layer thickness is very small per cycle. In our opinion this is justified as the magnitude of voltage drop across the SEI layer and current density associated with SEI layer ($j_{SEI}(x,t)$) are small, hence equation (7.25) should give a good approximation to equation (7.24) for any reasonable operation.

$$\eta_{SEI}(x,t) = \phi_n^S(x,t) - \phi_e(x,t) - U_{SEI} - \Re_{SEI} j_n(x,t) F \tag{7.25}$$

Figure 7-3 shows the evolution of overpotential for SEI layer as approximated by equation (7.25) . The magnitude is larger for anode-separator interface for this case as well and hence will be the focus of this study.

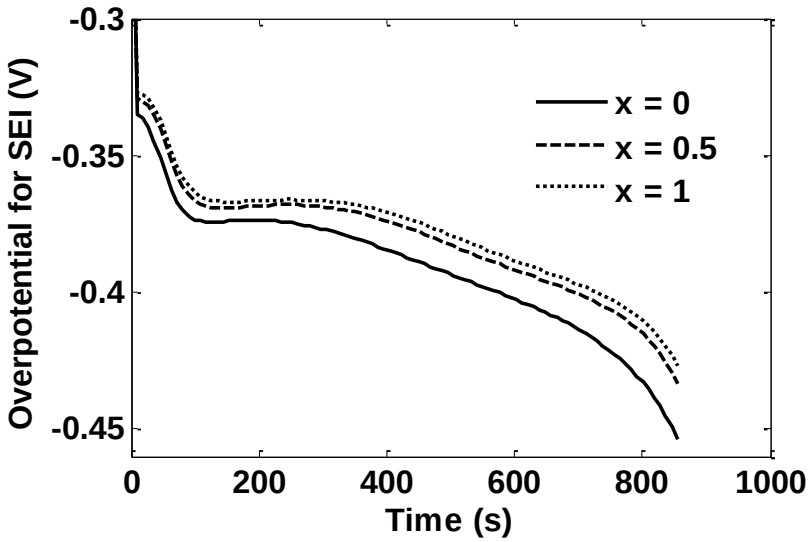

Figure 7-3: Distribution of overpotential for SEI side reaction across length during charging at 4C rate (x = 0 represent anode-separator interface and x = 1 represent anode-current collector interface)

7.3 Problem Statement

While various factors (thickness of electrode and current collector, particle radius, filler fractions, porosity, etc.) can be varied to get the optimal battery design, here we focus on the porosity and length of anode and its effect on battery performance. The porous solid phase structure in the anode and cathode consists of networks of interconnected and irregular pores or channels. Usually the electrode materials are designed as porous structures made up of solid particles. One way to reduce the complexity of these structures and avoid pore scale modeling is to use macro homogeneous models[27] where tortuosity is used to obtain effective transport properties.[108,109] A Bruggeman relationship is often used to relate tortuosity τ with porosity as $\varepsilon^{1-brugg_n}$ where $brugg_n$ is the Bruggeman coefficient. Effective conductivity and diffusivity in the porous anode can be expressed as follows:

$$\kappa_{eff,n} = \frac{\kappa\varepsilon_n}{\tau} = \varepsilon_n^{brugg_n}\kappa \tag{7.26}$$

$$D_{eff,n} = \frac{D\varepsilon_n}{\tau} = D\varepsilon_n^{brugg_n} \tag{7.27}$$

Here κ (S/m) and D (m^2/s) are intrinsic conductivity and diffusivity of the electrolyte, and both are function of lithium-ion concentration and temperature, whereas $\kappa_{eff,n}$ and $D_{eff,n}$ are the effective conductivity and diffusivity taking the porous nature into account. The increase in porosity would improve the conductivity and diffusivity of lithium-ions in the electrolyte. The solid phase conductivity is given in equation (7.28), which denotes the porosity correction of the intrinsic conductivity of solid phase material.

$$\sigma_{eff,n} = \sigma_n\left(1-\varepsilon_n-\varepsilon_{f,n}\right) \tag{7.28}$$

here σ_n and $\sigma_{eff,n}$ are the intrinsic electronic conductivity (S/m) and the effective electronic conductivity of solid phase of anode respectively. As porosity increases, the electronic conductivity will decrease as less volume is available for charge transport in the solid phase. Assuming spherical shape and uniform particle size, the specific area can also be written as follows:

$$a_n = \frac{3}{R_{P,n}}\left(1-\varepsilon_n-\varepsilon_{f,n}\right) \tag{7.29}$$

a_n is the specific area (m^2/m^3) and, $R_{p,n}$ is radius of anode particles and $\varepsilon_{f,n}$ is filler fraction. An increase in porosity will lead to decrease in area. In this study, two scenarios are analyzed with respect to discharge capacity and effect on capacity fade mechanisms during both charge and discharge.

- Varying porosity and length with fixed total capacity
- Varying porosity across thickness for fixed length and average porosity

7.3.1 Varying porosity and length with fixed total capacity

As mentioned before, the problem treated in this work assumes a given loading of the anode and cathode material. We allow the variation of length and porosity such that the total capacity of anode remains constant. In other words, choice of low porosity will lead to smaller thickness of anode and high porosity will lead to larger thickness of anode. Figure 2-2 illustrate the same.

Table 7-5 shows the capacity of cathode and anode as well as initial concentration for discharge simulation. For safety and capacity fade related issues, the anode is not allowed to be completely discharged or completely charged.

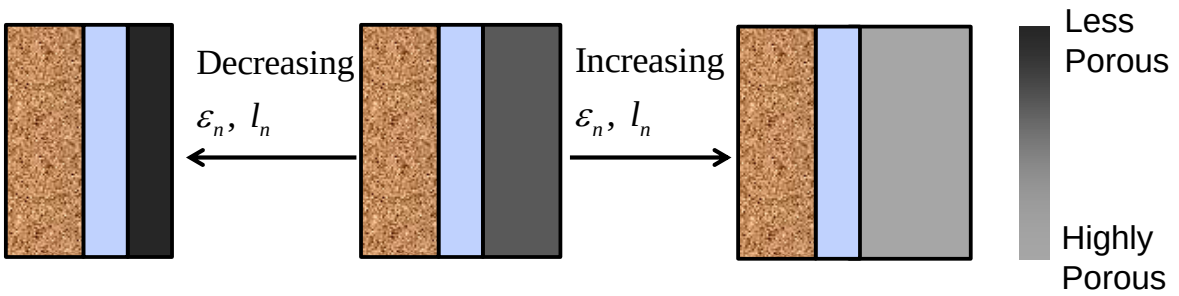

Figure 7-4**:** Different choices of porosities and lengths for fixed anode capacity

Table 7-5: Capacities and initial concentration (charged condition) of both electrodes

Electrode	Initial concentration	Capacity of electrodes	
Cathode	$c_{p,0}^s = 0.5c_{p,\max}^s$	$\left(1-\varepsilon_p-\varepsilon_{fp}\right)l_p\left(c_{p,0}^s-c_{p,\min}^s\right)$	1.217 mol/m^2
Anode	$c_{n,0}^s = 0.95c_{n,\max}^s$	$\left(1-\varepsilon_n-\varepsilon_{fn}\right)l_n\left(c_{n,\max}^s-c_{n,0}^s\right)$	1.232 mol/m^2

The problem at hand is to vary porosity and length such that the material loading in anode remains the same, i.e.,

$$\left(1-\varepsilon_{n,new}-\varepsilon_{fn}\right)l_{n,new}=\left(1-\varepsilon_n-\varepsilon_{fn}\right)l_n \tag{7.30}$$

Base values of anode length $\left(l_n\right)$ and porosity $\left(\varepsilon_n\right)$ are taken as 88×10^{-6} m and 0.485 respectively which corresponds to anode capacity given in Table 7-5. Different thicknesses $\left(l_{n,new}\right)$ and porosities ($\varepsilon_{n,new}$) will be chosen based on the constraint given by equation (7.30).

The maximum theoretical capacity of the battery will be determined by the smaller of the capacities of two electrodes. Depending on the initial lithium concentration in anode and cathode, the maximum theoretical capacity of battery will differ. Initial concentration and corresponding capacities of the base case undertaken are listed in Table 7-5. List of porosities and corresponding lengths constrained by equation (7.30) used in this study are given in Table 7-6. Note that some of the porosity values may not be experimentally feasible due to negligible mechanical strength of

highly porous electrode (i.e. porosity 0.55). Filler fraction is also assumed to be the same for all the porosity and length combination. The electrodes with smaller porosity and thickness are referred to as *thinner, less-porous* electrode and electrode with larger porosity and thickness are referred as *thicker, more-porous* electrode.

Table 7-6: List of porosities and lengths used

Length $l_{n,new}$ (m)	59.5×10^{-6}	63.9×10^{-6}	69×10^{-6}	75×10^{-6}	88×10^{-6}	101.4×10^{-6}
Porosity $\varepsilon_{n,new}$	0.25	0.30	0.35	0.40	0.485	0.55

7.3.2 Varying porosity across thickness for fixed average porosity and length

The second scenario considered in this study tries to quantify the effect of inhomogeneity of porosity in a given electrode. It has been shown by Chen *et al.*[111] that electrodes are not uniform in porosity distribution and contain patches of small and large porosities due to manufacturing limitations. In this scenario, one such example of varying porosity and its effect on capacity fade mechanics is studied. The problem statement is simplified by taking a linearly varying porosity distribution of the form given in equation (7.31).

$$\varepsilon_n(x) = \varepsilon_{avg,n} + s\left(x - \frac{1}{2}\right) \tag{7.31}$$

Here $\varepsilon_{avg,n}$ is the average porosity of the anode, s is the slope of porosity distribution, and x represents the scaled thickness of the anode which goes from 0 (anode-separator interface) to 1 (anode-current collector interface). This form of porosity variation across anode will make sure that the average porosity remains the same which in turn will ensure that the material loading does not vary when the porosity distribution is changed (see Figure 7-5). To see the effect of local

porosity variation on side reactions, we choose the anode thickness to be 63.9×10^{-6} m and average porosity to be $\varepsilon_{avg,n} = 0.30$.

For the case when *s* is negative, the anode-separator interface has maximum porosity and anode-current collector has least porosity. On the other hand when *s* is positive, the reverse is true. Then case when *s* is positive could be understood by assuming a patch of low porosity at the anode-separator interface.

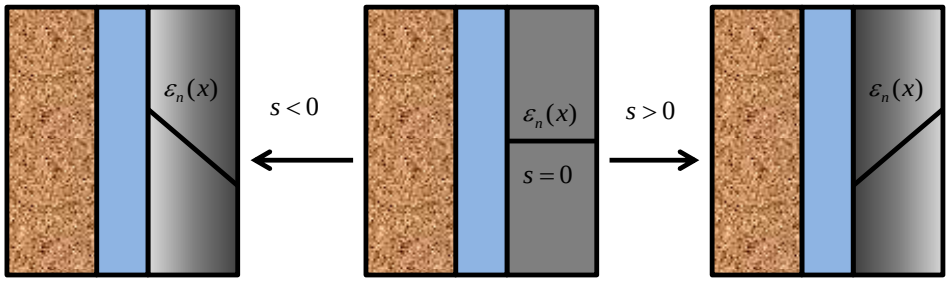

Figure 7-5: Linear porosity distribution in anode

7.4 Result and Discussion

Battery charge and discharge are simulated at isothermal conditions. A voltage cutoff of 2.8 V is used for discharging and 4.2 V is used for charging. The following definitions of energy and average power density are used.

Energy density $\equiv 1/m_{cell}\int_0^{t_f} V(t)I_{app}dt$

Average power density $\equiv 1/(t_f m_{cell})\int_0^{t_f} V(t)I_{app}dt$

where m_{cell} is the mass of the cell sandwich per unit area (only accounts for the mass of the electrodes, electrolyte and separator; mass of the current collectors and other accessories are not used in this calculation). t_f is the final time when the cell reaches 2.8 V while discharge, and I_{app} is

the applied current (A/m^2). Since the energy density and power density used here excludes the contribution from current collector and other accessories, a factor of 0.33 is used to estimate the capacity of entire cell.[94] For scenarios mentioned previously, different values of Bruggeman coefficient and temperature are used, resulting in three cases: 1) $brugg^n$ 1.5, T 298 K, 2) $brugg^n$ 2.5, T 298 K, 3) $brugg^n$ 1.5, Low temperature (288 K for discharge and 278 K for Charge). The Ragone plots are generated with discharge current up to 14C rate. Higher discharge current and lower temperature leads to very high electrolyte concentration in *thinner, less-porous* electrode configurations ($>4000\,mol/m^3$) for which the expression for concentration dependent intrinsic conductivity and diffusivity are not applicable. This is why during discharge a temperature of 288 K is used for simulation but during charging (where only 4C rate is considered), a relatively lower temperature of 278 K is used.

7.4.1 Varying porosity and length with fixed total capacity

During discharging, the effect of length-porosity is analyzed for battery capacities (Ragone plots) and intercalation-induced stresses. The effect of length-porosity on parasitic side reactions (plating and SEI reactions) in the anode is only relevant during charging hence their effect is studied during charging alone.

Discharging: Ragone plots and intercalation-induced stresses

For the given initial conditions and cell parameters, the discharge curves were simulated at different rates and Ragone plots were generated for all six combination of length-porosity given in Table 7-6 (Figure 7-6). It is to be noted that difference in energy density at lower power density is strictly due to the change in the weight of the electrolyte in the anode as the weight of the solid phase of the anode is constant for every choice of length and porosity. The time to reach 2.8 V (t_f) at low rate of discharge is almost equal for all porosity-length choices (which is expected).

The simulated points in Figure 7-6 show the effect of length and porosity on battery performance. For a smaller Bruggeman coefficient ($brugg^n$ = 1.5) the *thinner, less-porous* electrodes give rise to higher energy density even at low temperature of 278 K due to less electrolyte weight (left and right subplots of Figure 7-6). At very high rates of discharge, the final time $\left(t_f\right)$ starts to shrink down for *thinner, less-porous* electrodes compared to *thicker, more-porous* electrodes but less electrolyte weight in *thinner, less-porous* still dominates the energy density.

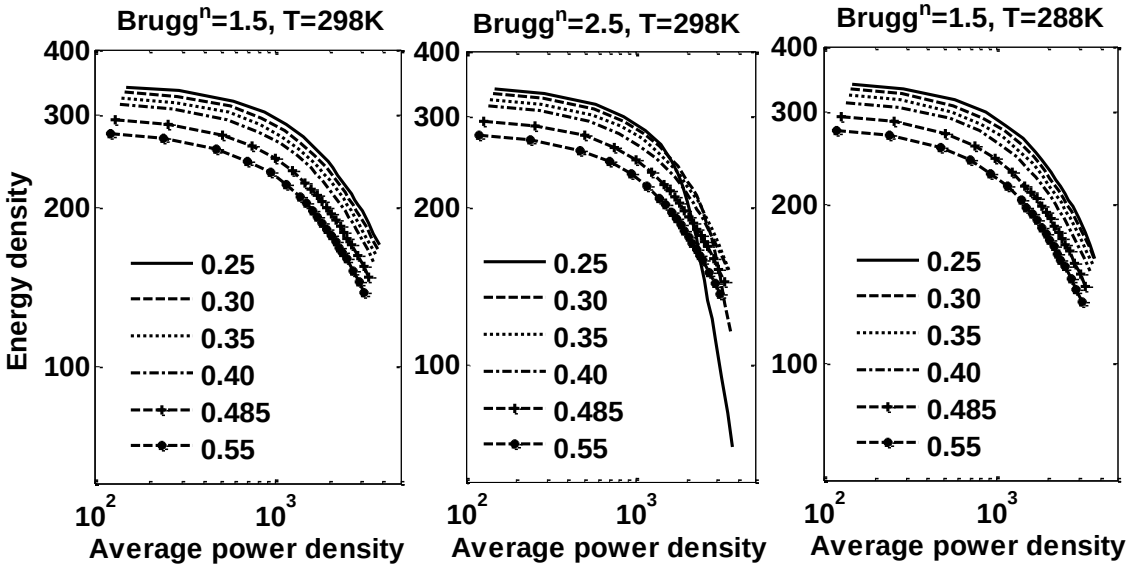

Figure 7-6: Simulated Ragone plot for different thicknesses of anode

The Bruggeman coefficient value is usually taken as 1.5 for porous structures made by uniform size spherical particles.[108,112] For other shapes and variation in particle size, higher values of Bruggeman coefficient can be used. As can be seen from Figure 7-6 (middle subplot), the discharge capacity for thinner electrodes at high power density decreases significantly when the Bruggeman coefficient is higher. In other words, t_f for *thinner, less-porous* electrodes is very short at higher discharge rates as compared to *thicker, more-porous* electrodes.

During deintercalation, the peak radial stresses are compressive at the center and peak tangential stresses are tensile at the surface. Figure 7-7 and Figure 7-8 show the extremum values obtained for peak tangential stresses (surface of the particle) and peak radial stresses (center of the particle) in the solid particle at the anode-separator interface during the discharge period. As mentioned before, the anode-separator interface is most likely to face the largest magnitude of stresses during charging/discharging (Figure 7-1).

For case 1 (*brugg*^{n} 1.5, room temperature, left subplots of Figure 7-7 and Figure 7-8) maxima for each type of peak stresses increases monotonically with the discharge rate. For thinner electrodes, the maximum values for both radial and tangential stresses are higher compared to thicker electrodes. At low temperature (case 3, right subplots), the maximum value of peak tangential stresses reaches higher values compared to room temperature case. On the other hand, the maximum values achieved by radial stresses seem to decrease at higher discharge rates. This apparent decrease happens simply because the cell does not last long enough for radial stresses to reach their maximum (as mentioned earlier, the peak radial stresses have slower dynamics, see Figure 7-1).

For higher Bruggeman coefficients, *thinner, less-porous* electrodes lead to significant increase in maximum values of both peak tangential stresses and peak radial stresses. For *thinner, less-porous* electrode, the maximum value of peak radial stresses decreases at higher rate of discharge because the t_f is not long enough for radial stresses to reach their maximum. It is clear that the thinner electrodes with smaller porosities lead to higher stresses in the particle and the stress effect becomes critical if the anode tortuosity is higher. It is worth mentioning here that for few cases for *thinner, less-porous* electrodes with high Bruggeman coefficients, the electrolyte concentration at the very end of discharge shoots up to as high as 5 molar (note that the diffusivity and conductivity

expressions used here may not be very accurate). This is the reason why temperature lower than 288 K is not used for discharge simulation.

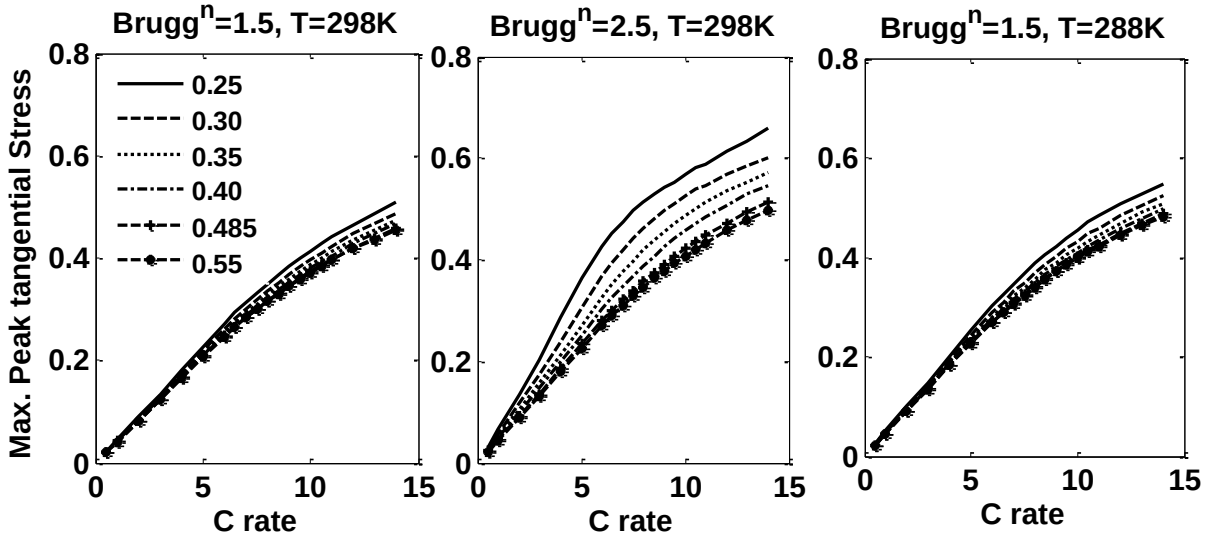

Figure 7-7: Maximum peak tangential stresses during discharging at different C rates

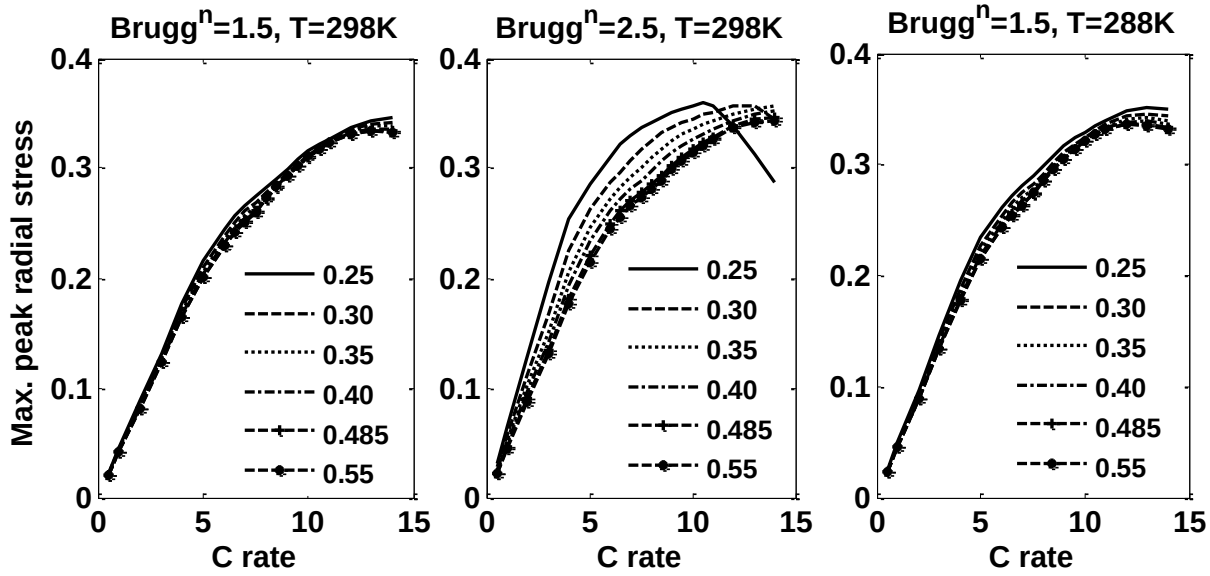

Figure 7-8: Maximum peak radial stresses during discharging at different C rates

Charging: intercalation-induced stresses

The anode is vulnerable to parasitic side reactions (SEI layer and plating side reaction) during charging. The intercalation induced stresses during charging are also studied here although

Takahashi and Srinivasan[36] suggest that fracture during lithiation is not likely. Initial anode concentration 961 mol/m^3 and initial cathode concentration 51022 mol/m^3 is used to simulate the battery charging.

Here, a charging rate of 4C is used to analyze the battery performance. The effective resistance during charging and discharging are different due to the asymmetrical nature of open circuit potentials of anode and cathode. Unlike the case for discharge, here we focus on only 4C rate of charging to illustrate the capacity fade mechanics during charging. During discharging, the final time to reach 2.8 V at 4C rate is almost same for all the cases (around 10 s difference between *thinner, less-porous* and *thicker, more-porous* electrodes for *brugg*^{n} 2.5 and *T* 298 K), but during charging, the time to reach 4.2 V is significantly different especially for higher Bruggeman coefficient (a difference of 200 s for *brugg*^{n} 2.5 and *T* 298 K).

For the charging rate of 4C for different cases, Figure 7-9 shows voltage profile and effect of length-porosity combination on final time to reach 4.2 V. For *thinner, less-porous* anodes, the charging capacity drops down significantly for the higher Bruggeman coefficient.

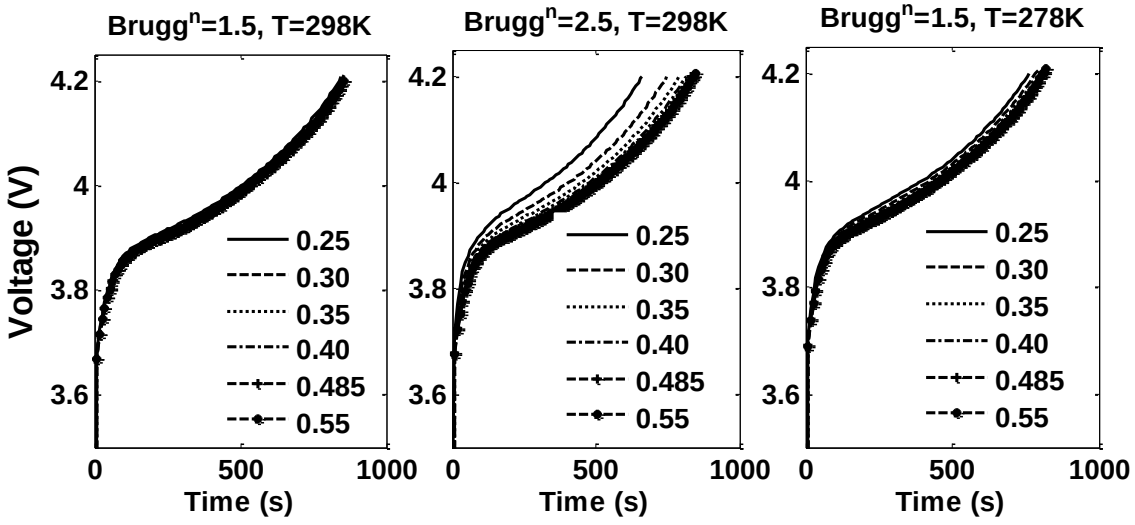

Figure 7-9: Voltage profiles during charging at 4C rate for different anode thicknesses

During charging, the effect of porosity-length combination on the peak radial and peak tangential stresses is shown in Figure 7-10 and Figure 7-11. Peak tangential stress (at the surface of the solid particle) is now compressive and peak radial stress (at the center of the particle) is tensile. Figure 7-10 shows the peak tangential stress at the surface of the solid particle at anode-separator interface. Since, only a single charging rate is used here (4C rate), time evolution of stress profiles are plotted for different thickness-porosity combinations unlike the discharging case (Figure 7-7 and Figure 7-8) where only the maximum values of these peak stresses are plotted. Figure 7-11 show peak radial stresses and at the anode-separator interface. Both peak radial and peak tangential stresses at anode-separator interface go through maxima during charging at 4C. The porosity-length combination has significant effect on the extremum values reached by peak radial and tangential stresses. For *thicker, more-porous* anode, the stress values remain similar as can be seen from Figure 7-10 and Figure 7-11 (curves for *thicker, more-porous* electrodes are virtually indistinguishable), but for *thinner, less-porous* anode peak stresses are significantly higher at higher Bruggeman coefficient (around 50% increase in the stress!).

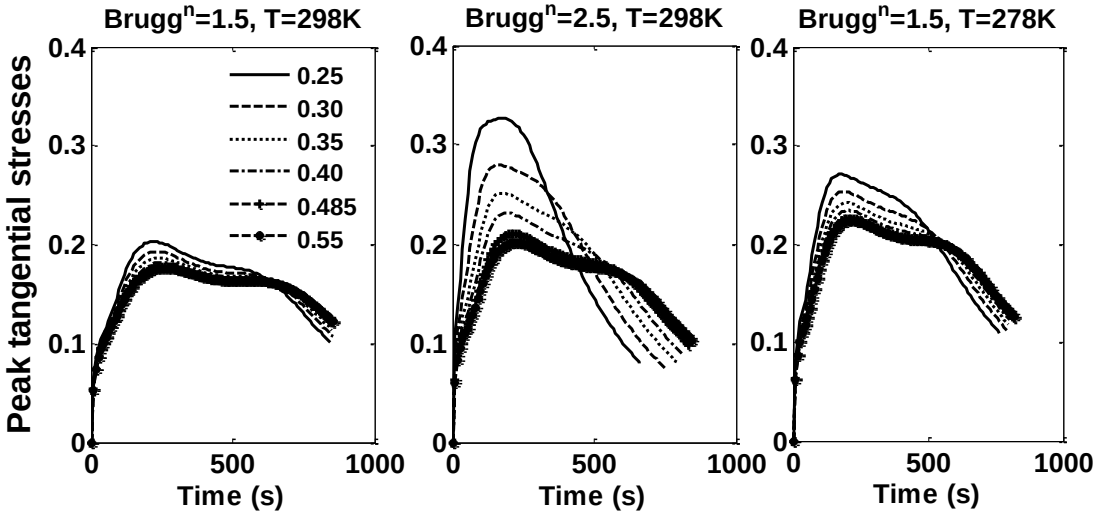

Figure 7-10: Peak tangential stresses (compressive) at anode-separator interface during charging at 4C rate

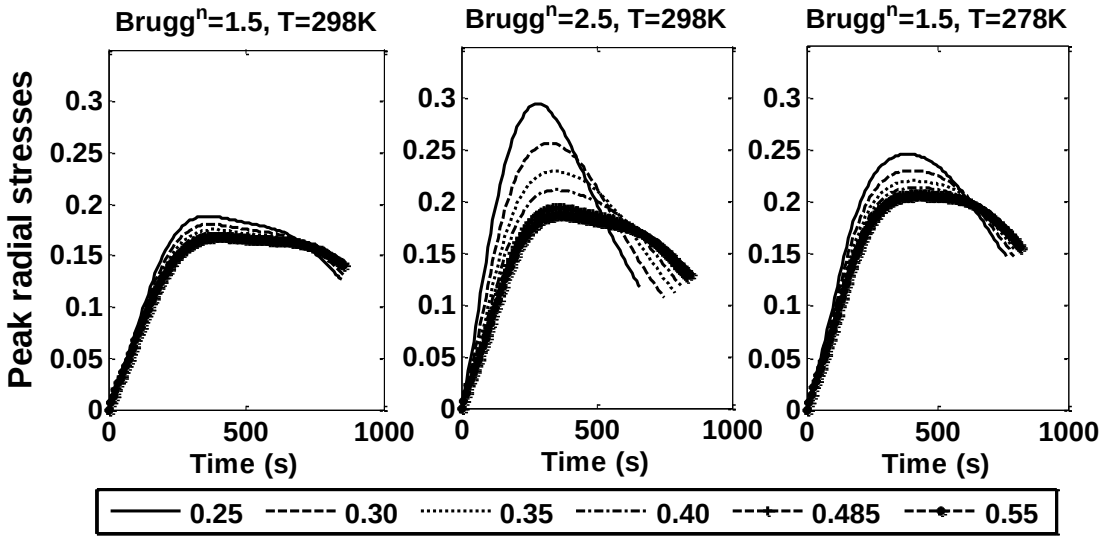

Figure 7-11**:**Peak radial stresses (tensile) at anode-separator interface during charging at 4C rate

Charging: parasitic reactions

The anode-separator interface remains the most vulnerable part of the battery with respect to parasitic side reactions (see Figure 7-2 for distribution of overpotential with anode thickness), Figure 7-12 shows the overpotential for plating at anode-separator interface. As mentioned earlier, the plating side reaction becomes feasible only when the overpotential is negative. Similar to previous cases, the overpotential for plating reaction is higher for *thinner*, *less-porous* electrode irrespective of the Bruggeman coefficient and temperature. The effect is more severe with a higher Bruggeman coefficient (middle subplot, Figure 7-12). Lower temperature with smaller Bruggeman coefficient (i.e. 1.5) does lead to higher driving force for plating side reaction.

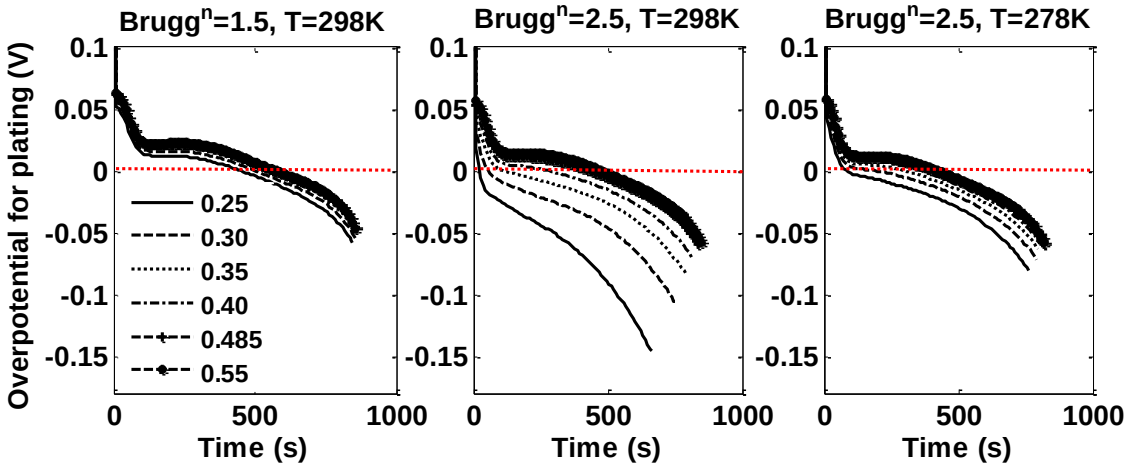

Figure 7-12: Overpotential for plating side reaction during charging at 4C rate (note that plating reaction in feasible only when overpotential is negative)

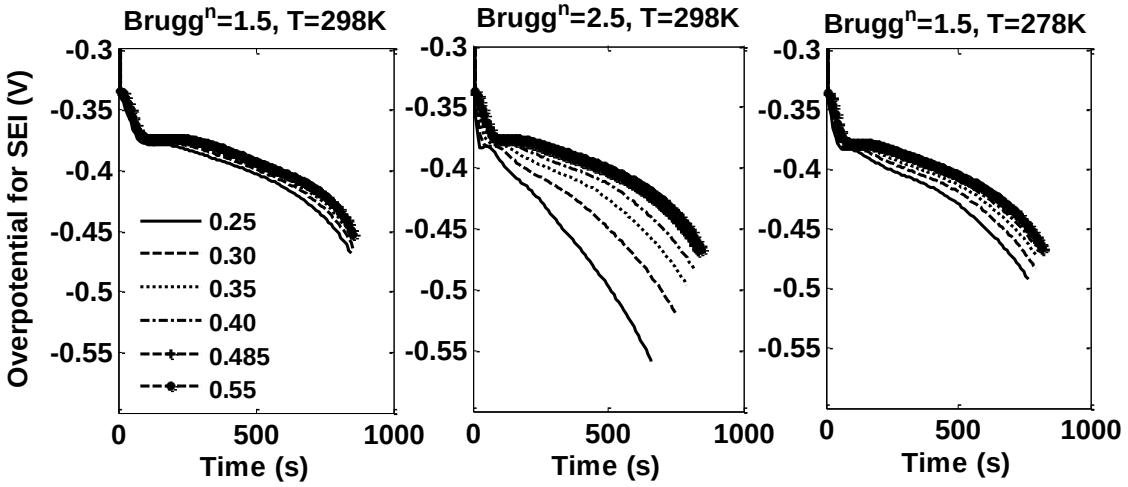

Figure 7-13: Overpotential for SEI side-reaction during charging at 4C rate

Similarly, the overpotential for the SEI side reaction is plotted in Figure 7-13. The SEI side reaction is irreversible and becomes feasible only during intercalation in anode. The overpotential for SEI reaction follows the similar trends as overpotential for plating side reactions. For *thinner, less-porous* anode, overpotential for SEI side reactions is higher compared to other cases, and for higher Bruggeman coefficient, the effect is more pronounced. It should be mentioned here that the current density for both the SEI side reaction and the lithium plating reaction has exponential dependence on the overpotentials.

7.4.2 Varying porosity across thickness for fixed average porosity and length

Due to manufacturing limitations, the electrode structure may not have a uniform porosity distribution. In order to mimic the inhomogeneity of porosity in simplest fashion, a linear varying porosity is assumed. Three values of slopes (0.2, 0 and −0.2) are used to carry out simulation with average porosity ($\varepsilon_{avg,n}$) of 0.30 and thickness of 63.9×10^{-6} m (Table 7-6, case 2). Steeper porosity distribution ($|s| > 0.2$) leads to very small porosities at either end or causes electrolyte concentration to shoot up significantly above 4 molar during the end of charge/discharge.

Discharging: Ragone plots and intercalation-induced stresses

Figure 7-14 shows the simulate Ragone plot for different porosity gradients. Since the average porosity is constant ($\varepsilon_{avg,n} = 0.30$) for all the cases, the energy and power densities are identical at very small rate of discharge. Even at higher rates of discharge, a smaller Brugemann coefficient ($brugg^n$ = 1.5) does not lead to much change in energy density. On the other hand, higher Bruggeman coefficient with positive slope of 0.2 (less porousity at the anode-separator interface) leads to significant reduction in discharge capacity. Though the discharge capacities are not much affected by the porosity gradients for a smaller Bruggeman coefficient, the maximum peak tangential stresses (tensile during deintercalation) at the anode-separator interface are influenced by the gradients (see Figure 7-15). Maximum peak radial stresses also follow trends similar to the maximum peak tangential stresses, except at the high discharge rates for higher Bruggeman coefficient where battery voltage drops below 2.8 V before the peak radial stresses could reach their maxima (middle subplot of Figure 7-16). A slope of -0.2 (more porosity at anode-separator interface) gives rise to better capacity and less stresses compared to zero and positive porosity gradient. Similarly, to the previous scenario of discharging, the electrolyte concentration shoots

above 5 molar concentration near the end of discharge for a very few cases for higher Bruggeman coefficient.

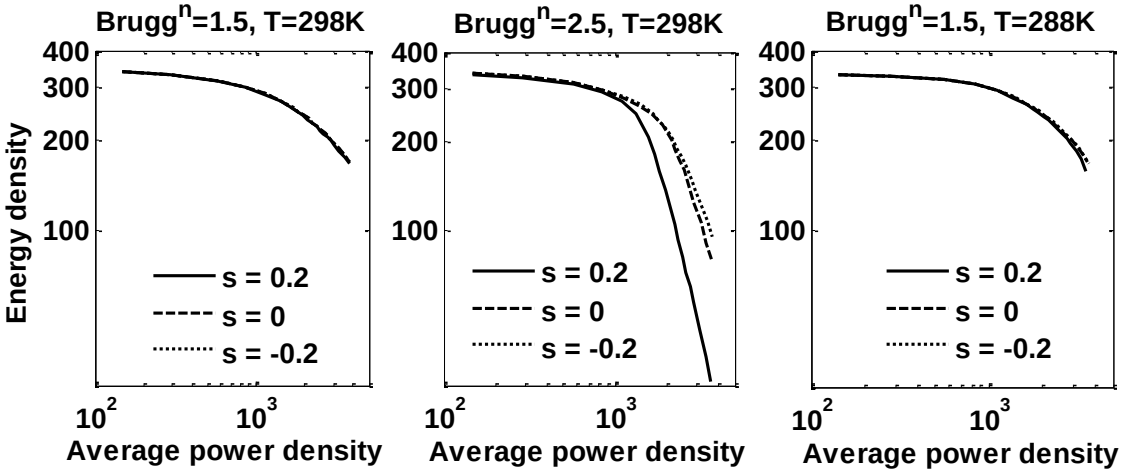

Figure 7-14:Simulated Ragone plot for different porosity gradient of anode

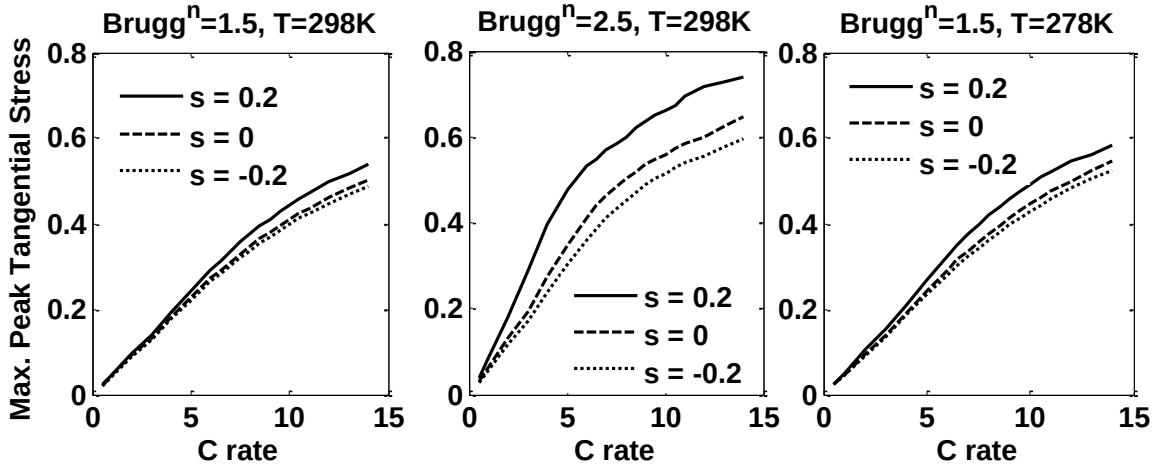

Figure 7-15:Maximum peak tangential stresses during discharging at different C rates

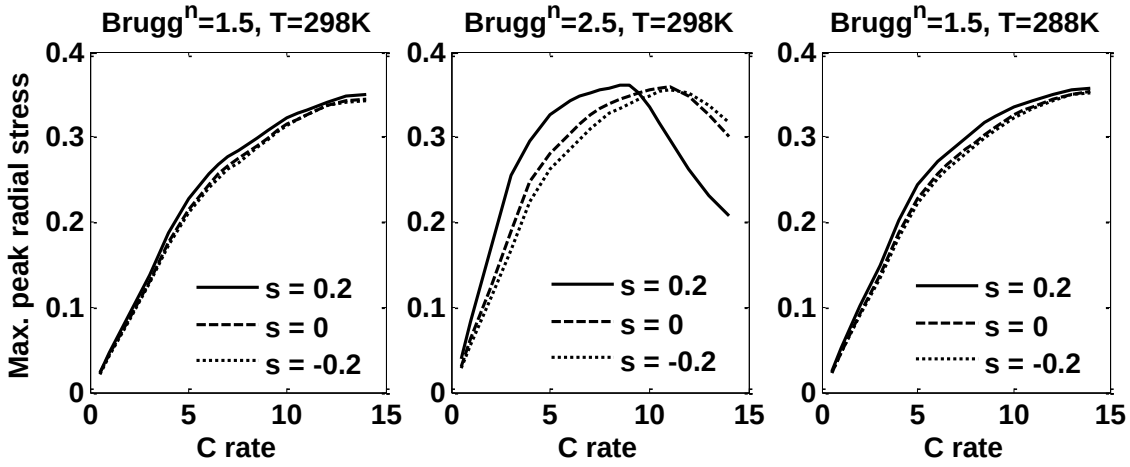

Figure 7-16: Maximum peak radial stresses during discharging at different C rates

Charging: intercalation-induced stresses

Figure 7-17 shows the charging profiles with porosity gradient. In each case the voltage rise is faster when slope is positive. Here also, in each case, negative porosity gradient (more porosity at anode-separator interface) gives favorable capacity fade behavior compared to zero and positive slope. Positive porosity gradient turns out to be very critical for higher Bruggeman coefficient (middle subplots).

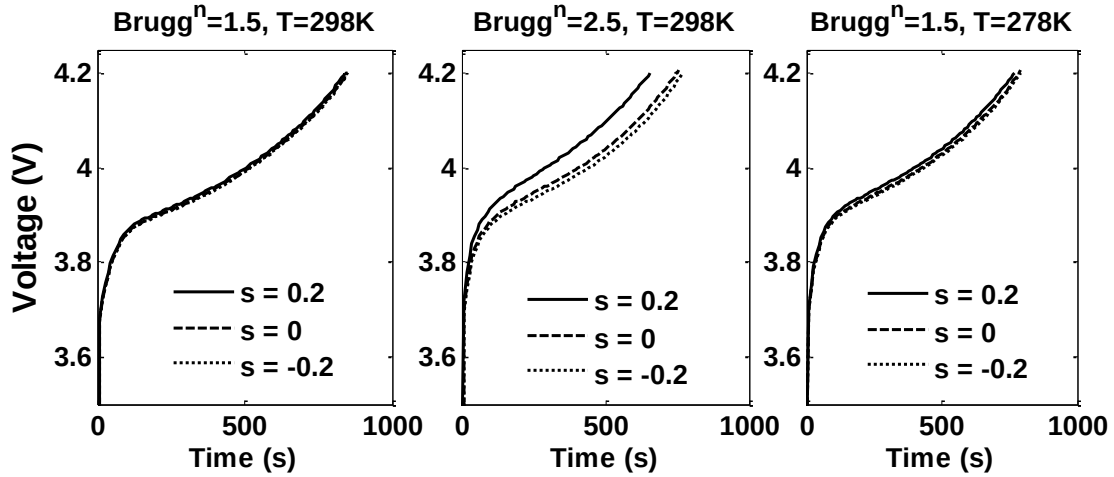

Figure 7-17: Voltage profiles during charging at 4C rate corresponding to different porosity gradient

Figure 7-18 and Figure 7-19 shows the peak radial (tensile) and peak tangential (compressive) stresses respectively.

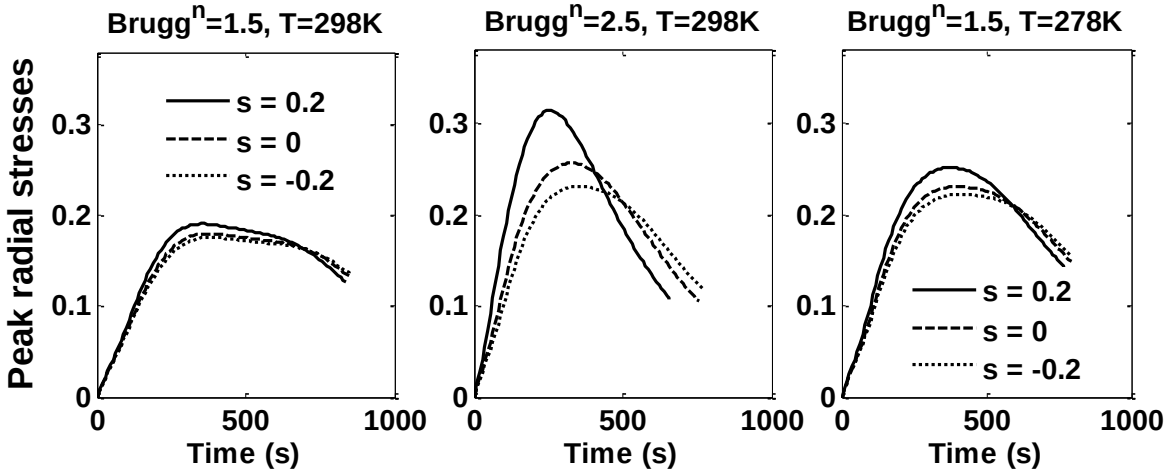

Figure 7-18: Peak radial stresses during charging at 4C rate at anode-separator interface

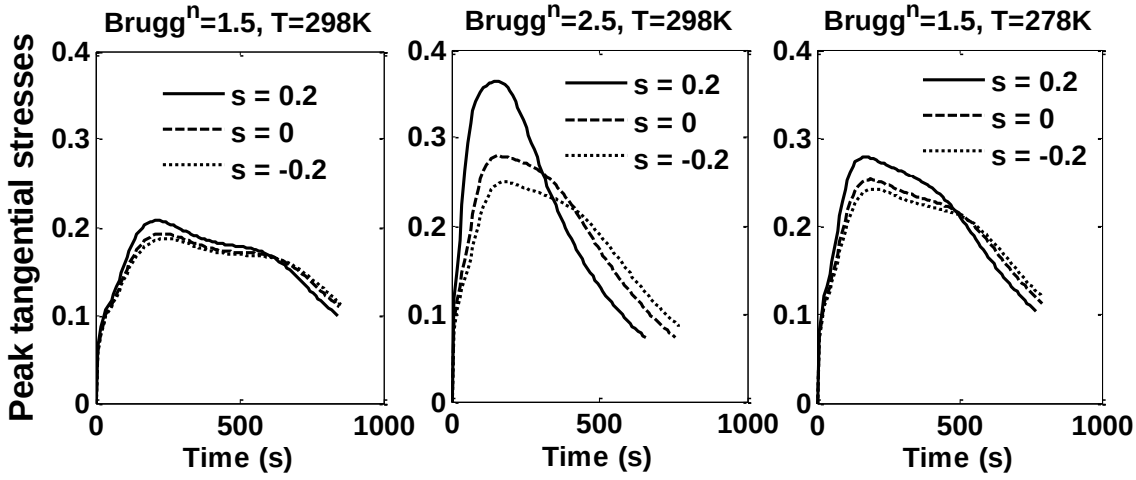

Figure 7-19: Peak tangential stresses during charging at 4C rate at anode-separator interface

Charging: Parasitic reactions

Figure 7-20 and Figure 7-21 shows the overpotential for SEI and plating side reactions. These curves also follow similar trends in which positive slopes lead to higher magnitude of overpotential and negative slope give rise to smaller overpotential for capacity fade.

The common theme that arises from this study is that the discharge capacity is not a strong function of the length-porosity combination or porosity variation across anode for less tortuous anode at room temperature (for the specified material loading). But, for a more tortuous anode, the capacity decreases significantly at higher discharge rates. In every case, *thinner, less-porous* electrodes and

electrode with less porosity at anode-separator interface leads to higher magnitude of stresses and overpotential for parasitic side reactions. For the parameters values used in the current simulation and the base case anode (0.485 porosity with 88×10^{-6} m thick electrode), the *thinner, less-porous* electrode generate larger variation in current density across anode thickness compared to *thicker, more-porous* electrodes. While the trends of Overpotential for SEI side reaction and plating side reaction are similar, SEI side reaction remain feasible for entire charging process, which is not the case for plating side reaction during charging.

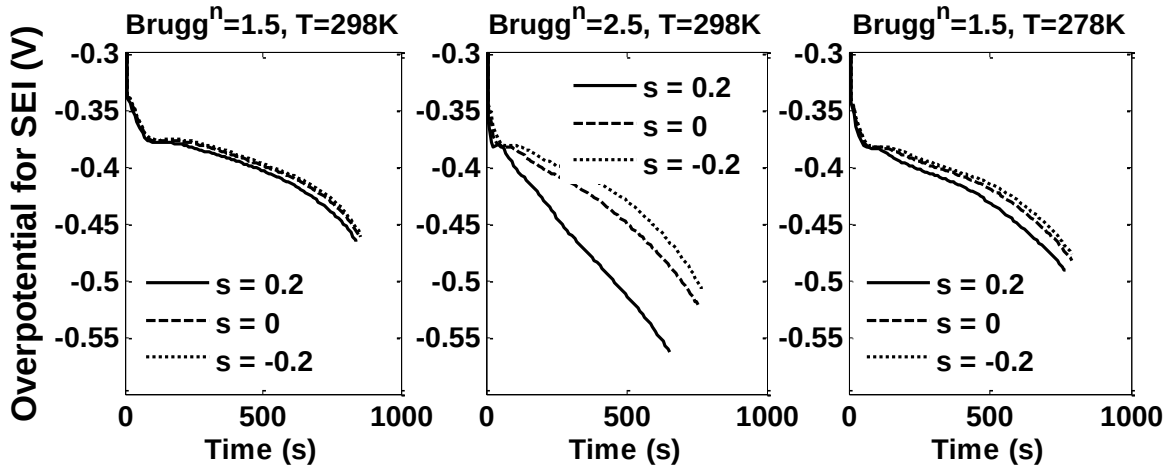

Figure 7-20: Overpotential for SEI side reaction during charging at 4C rate

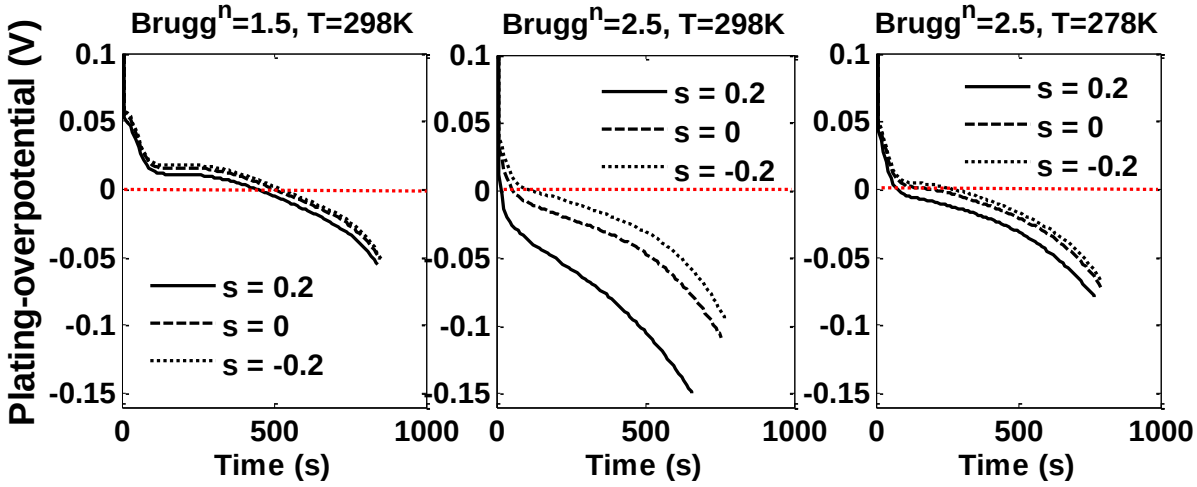

Figure 7-21: Overpotential for plating during charging at 4C rate

The model used in the current study has certain limitations and shortcomings which are summarized below.

- The concentration dependence of the factor $\left(1+d\ln f_{\pm}/d\ln c\right)$ is not taken into account.
- The stress model used to estimate intercalation induced stresses is valid only for materials with small volume expansion.
- Overpotentials for parasitic side reactions and lithium plating reactions are approximate but this approximation should be good enough, as the magnitude of current density due to parasitic side reactions are usually very small.
- For very few cases (especially with higher Bruggeman coefficient and *thinner*, *less-porous* electrode), the electrolyte concentration shoots beyond the validity of the expressions for conductivity and diffusivity at the very end of discharge. Charging simulation has no such issues as the charging current is small (4C) compared to discharging currents. This effect is mainly due to concentration dependent diffusivity for lithium-ion concentration in electrolyte. Such high concentration of lithium-ion is not observed if concentration dependence of lithium-ion in electrolyte phase is dropped.

7.5 Conclusions and Future Directions

The problem of porosity-length optimization for lithium-ion batteries is examined from a different perspective where the porosity and length are varied with a constraint of fixed theoretical capacity. First, *thinner, less-porous* and *thicker, more-porous* electrode are compared for discharge capacity, peak stresses and overpotentials for parasitic side reactions at different temperature and different Bruggeman coefficients. Low temperature charge and discharge follow trends very similar to room

temperature, except for the fact that all the capacity fade effects are more pronounced and reduction in discharge capacity is more drastic at low temperature.

The Bruggeman coefficient has a significant effect on every aspect of the capacity and capacity-fade mechanisms. Smaller porosity with a larger tortuosity give rise to a significant reduction in discharge capacity despite having smaller thickness and the cell becomes more susceptible to all capacity fade mechanisms discussed here.

The manufacturing difficulty of forming a uniform porosity anode is considered in a simple way where porosity is varied linearly in the anode, keeping the average porosity constant. The discharge capacity of less tortuous anode is not much affected by the porosity gradients but the capacity fade mechanics are. For the more tortuous anode ($burgg^n = 2.5$), the discharge capacities as well as capacity fade mechanisms are severely affected by a positive porosity gradient (less porosity at anode-separator interface). Interestingly a negative porosity gradient (more porosity at anode-separator interface) leads to better discharge capacity and smaller driving force for capacity fade mechanisms in all the cases. This suggests that *thinner, less-porous* electrodes may give rise to better discharge capacity and acceptable capacity fade behavior if the tortuosity is near unity (columnar electrodes).

In this study, for a fixed value of anode and cathode loading, the effect of porosity, thickness is observed at different charging/discharging conditions. The complete problem would be to derive design parameters (length, porosity and porosity distribution) for a fixed ratio of anode to cathode loading (instead of fixed value) in order to get good rate-capacities and favorable capacity fade behavior. Such problem statement will require use of an optimization framework, as the possible design combinations are large, and will be the focus of future work.

List of Variables and Parameters

a	Surface area per volume of electrode
$brugg$	Bruggeman coefficient
c	Electrolyte concentration
c^s	Solid phase concentration
δ	Thickness of SEI layer
D	Intrinsic diffusivity of lithium ion in electrolyte
D_{eff}	Effective diffusivity of lithium ion in porous electrode
D^s	Solid phase diffusion coefficient
$E_i^{D^s}, E_i^k$	Activation energy (for diffusivity and reaction rate)
E	Young's modulus
F	Faraday's constant
I	Applied current
j	Pore wall flux
κ	Liquid phase conductivity (intrinsic)
k	Reaction rate constant
l	Length of region
$\Re$	SEI layer resistance
R_p	Particle radius
R	Gas constant
T_{ref}	Temperature
t_+	Transference number
T_{ref}	Reference temperature (298.16 K)
T	Temperature
U	Open circuit potential
ν	Poisson's ratio
ε	Porosity
ε_f	Filling fraction
θ	State of Charge
σ	Solid phase conductivity
ρ	Density
Φ_1	Solid phase potential
Φ_2	Liquid phase potential
Ω	Partial molar volume
ξ	Scaled radial distance in anode particle $r / R_{P,n}$

List of Subscripts

eff	Effective, as for diffusivity or conductivity
e	Related to electrolyte
n	Related to the negative electrode—the anode
p	Related to the positive electrode—the cathode
P	Related to particle (e.g. R_P radius of particle)
s	Related to the separator
SEI	Related to SEI

List of Superscripts

s	Related to Solid Phase
+/–	Pertains to the boundary conditions from right and left side of the interface (e.g. L_p^-, L_p^+, etc.)

Chapter 8

Conclusions and Future Directions

> Engineers like to solve problems. If there are no problems handily available, they will create their own problem.
>
> **Scott Adams**

8.1 On the Lithium-Insertion Mechanism

The P2D model is a very general framework that can incorporate various solid phase insertion mechanisms. Traditionally, Fick's law is used to model the transport of lithium as electro-neutral entity inside the solid phase.[27] For some materials, Fick's law may give reasonable results, most materials do not follow homogeneous insertion. Materials such as $LiFePO_4$, TiO_2, etc. show strong phase separation behavior depending on particle size hence they require different modeling approach.[7] The reaction site for such materials is also under debate.[40] Chapter 1 (Figure 1-11) shows the staging phenomena in graphite anode, but such details are missing in the existing P2D model. Adopting material specific intercalation mechanism in P2D framework is very critical in order to accurately model the physical processes inside lithium-ion battery so that the P2D model can be extended to model the capacity fade mechanisms accurately.

8.2 On the Capacity Fade Mechanisms

The P2D model is capable of incorporating various capacity-fade mechanisms such as:

- SEI layer formation at the electrode surfaces
- Plating side reactions at the graphite anode
- High volumetric expansion in Si and Sn (around 400%)

- Mechanical degradation due to intercalation-induced stresses
- Thermal degradation of electrolyte at high temperature.

However, expressions to quantify the effect of each capacity-fade mechanism are not well understood. For example, Plating reaction on graphite anode is mentioned as an irreversible reaction in the literature (Perkins *et al.*[58]). Recently Zinth *et al.*[14] suggested lithium-plating as partially reversible reaction based on experimental evidence. It is also suggested that the plated-lithium intercalate in the graphite anode when the battery is allowed to rest for a sufficient time. Such slow dynamics makes the estimation of the state of charge (SOC) and the state of health (SOH) very difficult.

Similarly, various expressions for SEI layer current density have been proposed depending on the assumptions of diffusion-limited growth vs. reaction rate-limited growth. Experimental determination of rate laws for SEI layer formation is also very difficult.

Intercalation-induced stresses also pose a challenge in quantifying the effect of stress on particle cracking. Particle cracking require probabilistic treatment dependent on the magnitude of stress. The probabilistic nature of mechanical degradation causes additional challenges in quantifying the capacity fade. What are the criteria and probability of particle cracking at a certain level of stress? How long is the crack? How much area is created when the particle cracks facilitating the formation of fresh SEI layer? All these questions require quantitative treatment in order to predict the capacity fade.

Experimentally validated expressions for above-mentioned capacity-fade mechanisms is critical in order to derive optimal charge/discharge profiles or derive design parameters for long lasting lithium-ion battery.

8.3 On the Optimization Algorithm and Problem Definition

The derivation of optimal charging/discharging profiles is based on simultaneous optimization approach[86] where the battery model and associated constraints are discretized in time and space to generate a large system of algebraic equations (see Figure 8-1). In most cases, Euler Backward (EB) method and higher order backward difference formulas are used to discretize the battery model in time. Although, EB discretization performs reasonably well and is robust, the accuracy offered by EB discretization is not satisfactory (at most 1st order accurate). Implicit Runge-Kutta (IRK) based discretization schemes give rise to computationally efficient optimization problem,[87] and will be the focus of future research.

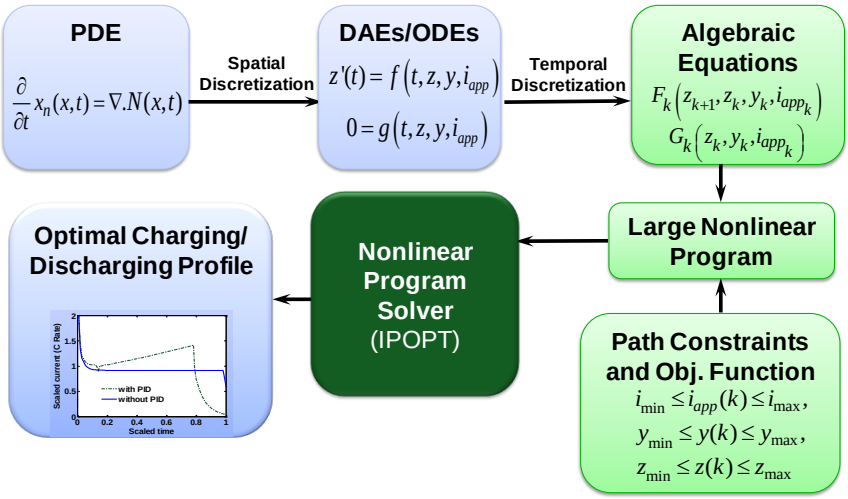

Figure 8-1: Schematic of simultaneous optimization approach

The optimization problem considered in Chapters 5 places lower bounds on plating over-potentials. A better problem (also more physically meaningful) formulation would be to minimize the amount of plated lithium, rather than to restrict the plating over-potential. It is to be noted here that the SEI layer growth depends on both exchange current density (a function of lithium and electrolyte concentrations) and plating over-potential. The lack of confidence in expressions for plating reaction prevents such analysis.

The optimization problem of practical importance will be to derive charging/discharging profiles such that the life of the battery is maximized. To address this problem, all capacity-fade mechanisms need to be incorporated and solved with thermal P2D model. Such optimization problems are poorly scaled problems as time scale of capacity-fade mechanisms is very large compared to the time scale of some of the variables such as potentials. Solving such optimization problem is numerically challenging and will be pursued in future.

8.4 On the Model Driven Battery Design

Chapter 7 presents the problem of porosity-length optimization for lithium-ion batteries where the porosity and length are varied with a constraint of fixed theoretical capacity. *Thinner, less-porous* and *thicker, more-porous* electrodes are compared for discharge capacity, peak stresses and overpotentials for parasitic side reactions at different temperature and different Bruggeman coefficients. The manufacturing difficulty of forming a uniform porosity anode is considered in a simple way where porosity is varied linearly in the anode, keeping the average porosity constant.

As mentioned in Chapter 7, the complete problem would be to derive design parameters (length, porosity and porosity distribution, see Figure 8-2) for a fixed ratio of anode to cathode loading (instead of fixed value) for good rate capacities and favorable capacity fade behavior. The equation (8.1) shows the constraint to be obeyed by the design variables.

$$\frac{\int_0^{l_n}\left(1-\varepsilon_n(x)-\varepsilon_{fn}\right)\left(c^s_{\max,n}-{}^s_{\min,n}\right)dx}{\int_0^{l_p}\left(1-\varepsilon_p(x)-\varepsilon_{fp}\right)\left(c^s_{\max,p}-{}^s_{\min,p}\right)dx}=\text{Constant} \tag{8.1}$$

Here $\varepsilon_n(x)$, $\varepsilon_p(x)$, (porosity distributions in anode and cathode respectively), l_n and l_p (thicknesses of anode and cathode respectively) are the design variables.

Such problem statement will require the use of an optimization framework, as the possible design combinations are large, and will be the focus of future work.

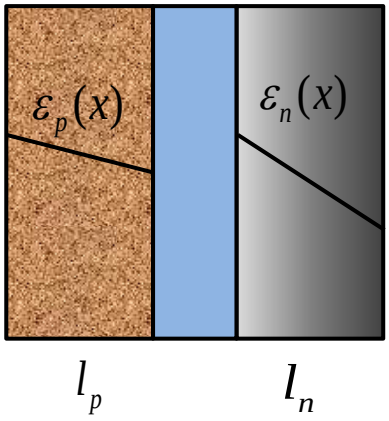

Figure 8-2: Design variables considering both anode and cathode

Work done in Chapter 7 involves isothermal P2D model. Usually, the charging/discharging of lithium-ion battery at high rates (up to 14C rate) will have a significant temperature rise due to limited heat transfer. Thermal model with a normal range of the heat transfer coefficient should be considered in order to derive the design parameters which assure good battery capacity and minimize capacity fade.

For the battery architecture discussed in chapter 1 and 2 (Anode, separator and cathode sandwich), usually the electrode-separator interfaces turn out to be the most vulnerable to capacity fade mechanisms compared to other parts of electrodes. As shown in Chapters 6 and 7, the effects of three capacity-fade mechanisms considered are most severe at the electrode-separator interface. Multiple active materials can be used[113,114] to design electrodes with variation in relative loading across the thickness of anode and cathode. Such variation in relative loading of multiple active materials may be useful in providing uniform capacity fade across the thickness of electrodes.

References

1. T. Nguyen and R. F. Savinell, *Electrochem. Soc. Interface*, **19**, 54 (2010).
2. P. Simon, Y. Gogotsi and B. Dunn, *Science*, **343**, 1210 (2014).
3. V. Pop, H. J. Bergveld, D. Danilov, P. P. L. Regtien and P. H. L. Notten, *Battery management systems: accurate state-of-charge indication for battery powered applications*, Springer Verlag (2008).
4. M. M. Thackeray, C. Wolverton and E. D. Isaacs, *Energy & Environmental Science*, **5**, 7854 (2012).
5. M. Winter, J. O. Besenhard, M. E. Spahr and P. Novák, *Advanced Materials*, **10**, 725 (1998).
6. M. Z. Bazant, *Accounts of chemical research*, **46**, 1144 (2013).
7. P. Bai, D. A. Cogswell and M. Z. Bazant, *Nano Letters*, **11**, 4890 (2011).
8. J.-Y. Shin, D. Samuelis and J. Maier, *Advanced Functional Materials*, **21**, 3464 (2011).
9. M. R. Palacin, *Chemical Society Reviews*, **38**, 2565 (2009).
10. J. B. Goodenough and Y. Kim, *Chemistry of Materials*, **22**, 587 (2010).
11. J.-M. Tarascon and M. Armand, *Nature*, **414**, 359 (2001).
12. Z. Ogumi and M. Inaba, *Bulletin of the Chemical Society of Japan*, **71**, 521 (1998).
13. P. W. C. Northrop, B. Suthar, V. Ramadesigan, S. Santhanagopalan, R. D. Braatz and V. R. Subramanian, *J. Electrochem. Soc.*, **161**, E3149 (2014).
14. V. Zinth, C. von Lüders, M. Hofmann, J. Hattendorff, I. Buchberger, S. Erhard, J. Rebelo-Kornmeier, A. Jossen and R. Gilles, *J. Power Sources*, **271**, 152 (2014).
15. S. Y. Huang, L. Kavan, I. Exnar and M. Grätzel, *J. Electrochem. Soc.*, **142**, L142 (1995).
16. K. Xu, *Chemical reviews*, **104**, 4303 (2004).
17. M. Wissler, *J. Power Sources*, **156**, 142 (2006).
18. A. K. Padhi, K. S. Nanjundaswamy and J. B. Goodenough, *J. Electrochem. Soc.*, **144**, 1188 (1997).
19. S. P. Ong, W. D. Richards, A. Jain, G. Hautier, M. Kocher, S. Cholia, D. Gunter, V. L. Chevrier, K. A. Persson and G. Ceder, *Computational Materials Science*, **68**, 314 (2013).
20. J. B. Goodenough and K.-S. Park, *Journal of the American Chemical Society*, **135**, 1167 (2013).
21. J. O. Besenhard, *Handbook of Battery Materials, by JO Besenhard (Editor), pp. 648. ISBN 3-527-29469-4. Wiley-VCH, April 1999.*, **1** (1999).
22. W. Lai, *J. Power Sources*, **196**, 6534 (2011).
23. A. Van der Ven, M. K. Aydinol, G. Ceder, G. Kresse and J. Hafner, *Phys Rev B*, **58**, 2975 (1998).
24. V. Srinivasan and J. Newman, *J. Electrochem. Soc.*, **151**, A1517 (2004).
25. G. K. Singh, G. Ceder and M. Z. Bazant, *Electrochim. Acta*, **53**, 7599 (2008).
26. K. West, T. Jacobsen and S. Atlung, *J. Electrochem. Soc.*, **129**, 1480 (1982).
27. M. Doyle, T. F. Fuller and J. Newman, *J. Electrochem. Soc.*, **140**, 1526 (1993).
28. J. Newman and K. E. Thomas-Alyea, *Electrochemical systems*, John Wiley & Sons (2012).
29. T. M. Bandhauer, S. Garimella and T. F. Fuller, *J. Electrochem. Soc.*, **158**, R1 (2011).
30. M. B. Pinson and M. Z. Bazant, *J. Electrochem. Soc.*, **160**, A243 (2013).
31. J. Christensen and J. Newman, *J. Electrochem. Soc.*, **153**, A1019 (2006).
32. J. Christensen and J. Newman, *J Solid State Electr*, **10**, 293 (2006).

33. Y.-T. Cheng and M. W. Verbrugge, *J. Power Sources*, **190**, 453 (2009).
34. X. Zhang, W. Shyy and A. Marie Sastry, *J. Electrochem. Soc.*, **154**, A910 (2007).
35. S. Renganathan, G. Sikha, S. Santhanagopalan and R. E. White, *J. Electrochem. Soc.*, **157**, A155 (2010).
36. K. Takahashi and V. Srinivasan, *J. Electrochem. Soc.*, **162**, A635 (2015).
37. B. Suthar, P. W. C. Northrop, R. D. Braatz and V. R. Subramanian, *J. Electrochem. Soc.*, **161**, F3144 (2014).
38. M. Guo, G. Sikha and R. E. White, *J. Electrochem. Soc.*, **158**, A122 (2011).
39. S. Santhanagopalan, Q. Guo, P. Ramadass and R. E. White, *J. Power Sources*, **156**, 620 (2006).
40. P. Bai and M. Z. Bazant, *Nat Commun*, **5** (2014).
41. G. Ceder, A. V. d. Ven, C. Marianetti and D. Morgan, *Modelling and Simulation in Materials Science and Engineering*, **8**, 311 (2000).
42. R. De Levie, *Advances in electrochemistry and electrochemical engineering*, **6**, 329 (1967).
43. S. Santhanagopalan and R. E. White, *J. Power Sources*, **161**, 1346 (2006).
44. K. A. Smith, C. D. Rahn and C. Y. Wang, *Energ. Convers. Manage*, **48**, 2565 (2007).
45. N. A. Chaturvedi, R. Klein, J. Christensen, J. Ahmed and A. Kojic, Modeling, estimation, and control challenges for lithium-ion batteries, in *Proceedings of the American Control Conference*, p. 1997 (2010).
46. D. Di Domenico, G. Fiengo and A. Stefanopoulou, Lithium-ion battery state of charge estimation with a Kalman filter based on a electrochemical model, in *IEEE International Conference on Control Applications*, p. 702 (2008).
47. D. Di Domenico, A. Stefanopoulou and G. Fiengo, *Journal of Dynamic Systems, Measurement, and Control*, **132**, 061302 (2010).
48. S. J. Moura, N. A. Chaturvedi and M. Krstic, PDE estimation techniques for advanced battery management systems-part I: SoC estimation, in *Proceedings of the American Control Conference* (2012).
49. R. Klein, N. A. Chaturvedi, J. Christensen, J. Ahmed, R. Findeisen and A. Kojic, Optimal charging strategies in lithium-ion battery, in *Proceedings of the American Control Conference*, p. 382 (2011).
50. S. K. Rahimian, S. C. Rayman and R. E. White, *J. Electrochem. Soc.*, **157**, A1302 (2010).
51. P. W. C. Northrop, V. Ramadesigan, S. De and V. R. Subramanian, *J. Electrochem. Soc.*, **158**, A1461 (2011).
52. V. Ramadesigan, V. Boovaragavan, J. C. Pirkle and V. R. Subramanian, *J. Electrochem. Soc.*, **157**, A854 (2010).
53. V. R. Subramanian, V. Boovaragavan, V. Ramadesigan and M. Arabandi, *J. Electrochem. Soc.*, **156**, A260 (2009).
54. V. Ramadesigan, V. Boovaragavan, M. Arabandi, K. Chen, H. Tsukamoto, R. Braatz and V. Subramanian, *ECS Transactions*, **19**, 11 (2009).
55. S. Timoshenko, Theory of elasticity, section 107, in, ONTI (1934).
56. M. Safari, M. Morcrette, A. Teyssot and C. Delacourt, *J. Electrochem. Soc.*, **156**, A145 (2009).
57. P. Ramadass, B. Haran, P. M. Gomadam, R. White and B. N. Popov, *J. Electrochem. Soc.*, **151**, A196 (2004).
58. R. D. Perkins, A. V. Randall, X. Zhang and G. L. Plett, *J. Power Sources*, **209**, 318 (2012).

59. M. M. Ren, Z. Zhou, X. P. Gao, W. X. Peng and J. P. Wei, *The Journal of Physical Chemistry C*, **112**, 5689 (2008).
60. A. M. Wilson and J. R. Dahn, *J. Electrochem. Soc.*, **142**, 326 (1995).
61. A. S. Arico, P. Bruce, B. Scrosati, J.-M. Tarascon and W. van Schalkwijk, *Nat Mater*, **4**, 366 (2005).
62. F. M. Hassan, V. Chabot, A. R. Elsayed, X. Xiao and Z. Chen, *Nano Letters* (2013).
63. U. Kasavajjula, C. Wang and A. J. Appleby, *J. Power Sources*, **163**, 1003 (2007).
64. Y.-S. Hu, R. Demir-Cakan, M.-M. Titirici, J.-O. Müller, R. Schlögl, M. Antonietti and J. Maier, *Angewandte Chemie International Edition*, **47**, 1645 (2008).
65. S.-H. Ng, J. Wang, D. Wexler, K. Konstantinov, Z.-P. Guo and H.-K. Liu, *Angewandte Chemie International Edition*, **45**, 6896 (2006).
66. R. Demir Cakan, M.-M. Titirici, M. Antonietti, G. Cui, J. Maier and Y.-S. Hu, *Chemical Communications*, 3759 (2008).
67. L. Su, Y. Jing and Z. Zhou, *Nanoscale*, **3**, 3967 (2011).
68. V. R. Subramanian and R. E. White, *J. Power Sources*, **96**, 385 (2001).
69. H. Carslaw and J. Jaeger, *Conduction of Heat in Solids*, Oxford University Press, London (1973).
70. G. Pontrelli and F. de Monte, *International Journal of Heat and Mass Transfer*, **50**, 3658 (2007).
71. G. Pontrelli and F. de Monte, *International Journal of Heat and Mass Transfer*, **53**, 3629 (2010).
72. R. Deshpande, Y.-T. Cheng and M. W. Verbrugge, *J. Power Sources*, **195**, 5081 (2010).
73. R. Deshpande, Y.-T. Cheng, M. W. Verbrugge and A. Timmons, *J. Electrochem. Soc.*, **158**, A718 (2011).
74. C. W. Tittle, *J Appl Phys*, **36**, 1486 (1965).
75. S. Timoshenko, *Theory of elasticity, section 107*, McGraw Hill Book Company, New York (1934).
76. C. R. Yang, Y. Y. Wang and C. C. Wan, *J. Power Sources*, **72**, 66 (1998).
77. P. Arora, M. Doyle and R. E. White, *J. Electrochem. Soc.*, **146**, 3543 (1999).
78. R. Deshpande, M. Verbrugge, Y.-T. Cheng, J. Wang and P. Liu, *J. Electrochem. Soc.*, **159**, A1730 (2012).
79. P. Arora, R. E. White and M. Doyle, *J. Electrochem. Soc.*, **145**, 3647 (1998).
80. J. Christensen, *J. Electrochem. Soc.*, **157**, A366 (2010).
81. G. Ning and B. N. Popov, *J. Electrochem. Soc.*, **151**, A1584 (2004).
82. Y. Zeng, P. Albertus, R. Klein, N. Chaturvedi, A. Kojic, M. Z. Bazant and J. Christensen, *J. Electrochem. Soc.*, **160**, A1565 (2013).
83. J. C. Forman, S. Bashash, J. L. Stein and H. K. Fathy, *J. Electrochem. Soc.*, **158**, A93 (2011).
84. S. De, B. Suthar, D. Rife, G. Sikha and V. R. Subramanian, *J. Electrochem. Soc.*, **160**, A1675 (2013).
85. K. Smith and C. Y. Wang, *J. Power Sources*, **161**, 628 (2006).
86. L. T. Biegler, *Chemical Engineering and Processing: Process Intensification*, **46**, 1043 (2007).
87. S. Kameswaran and L. T. Biegler, *Comput Chem Eng*, **30**, 1560 (2006).
88. M. D. Canon, C. D. Cullum, Jr. and E. Polak, *Theory of Optimal Control and Mathematical Programming*, McGraw-Hill, New York (1970).

89. A. Wächter and L. T. Biegler, *Mathematical Programming*, **106**, 25 (2006).
90. V. M. Zavala and L. T. Biegler, *Comput Chem Eng*, **33**, 1735 (2009).
91. D. Q. Mayne, J. B. Rawlings, C. V. Rao and P. O. M. Scokaert, *Automatica*, **36**, 789 (2000).
92. M. Morari and J. H. Lee, *Comput Chem Eng*, **23**, 667 (1999).
93. S.-L. Wu, W. Zhang, X. Song, A. K. Shukla, G. Liu, V. Battaglia and V. Srinivasan, *J. Electrochem. Soc.*, **159**, A438 (2012).
94. T. F. Fuller, M. Doyle and J. Newman, *J. Electrochem. Soc.*, **141**, 1 (1994).
95. B. Suthar, V. Ramadesigan, P. W. C. Northrop, B. Gopaluni, S. Santhanagopalan, R. D. Braatz and V. R. Subramanian, in *American Control Conference (ACC), 2013*, p. 5350.
96. R. Klein, N. A. Chaturvedi, J. Christensen, J. Ahmed, R. Findeisen and A. Kojic, in, p. 382.
97. A. Hoke, A. Brissette, D. Maksimovic, A. Pratt and K. Smith, in *Vehicle Power and Propulsion Conference (VPPC), 2011 IEEE*, p. 1.
98. R. Methekar, V. Ramadesigan, R. D. Braatz and V. R. Subramanian, *ECS Transactions*, **25**, 139 (2010).
99. V. Ramadesigan, P. W. C. Northrop, S. De, S. Santhanagopalan, R. D. Braatz and V. R. Subramanian, *J. Electrochem. Soc.*, **159**, R31 (2012).
100. P. Arora, M. Doyle and R. E. White, *J. Electrochem. Soc.*, **146**, 3543 (1999).
101. M. Doyle and J. Newman, *Electrochim. Acta*, **40**, 2191 (1995).
102. P. M. Gomadam, J. W. Weidner, R. A. Dougal and R. E. White, *J. Power Sources*, **110**, 267 (2002).
103. B. Suthar, V. Ramadesigan, S. De, R. D. Braatz and V. R. Subramanian, *Phys. Chem. Chem. Phys.*, **16**, 277 (2014).
104. P. W. C. Northrop, B. Suthar and V. R. Subramanian, *Improved Reformulation for the Simulation of Lithium-Ion Battery Operation Using Chebyshev Based Spectral Methods*, Manuscript under review.
105. J. Newman, *J. Electrochem. Soc.*, **142**, 97 (1995).
106. V. Ramadesigan, R. N. Methekar, F. Latinwo, R. D. Braatz and V. R. Subramanian, *J. Electrochem. Soc.*, **157**, A1328 (2010).
107. Y. Ji, Y. Zhang and C.-Y. Wang, *J. Electrochem. Soc.*, **160**, A636 (2013).
108. I. V. Thorat, D. E. Stephenson, N. A. Zacharias, K. Zaghib, J. N. Harb and D. R. Wheeler, *J. Power Sources*, **188**, 592 (2009).
109. B. Vijayaraghavan, D. R. Ely, Y.-M. Chiang, R. García-García and R. E. García, *J. Electrochem. Soc.*, **159**, A548 (2012).
110. D. Antartis, S. Dillon and I. Chasiotis, *Journal of Composite Materials* (2015).
111. Y. H. Chen, C. W. Wang, X. Zhang and A. M. Sastry, *J. Power Sources*, **195**, 2851 (2010).
112. N. A. Zacharias, D. R. Nevers, C. Skelton, K. Knackstedt, D. E. Stephenson and D. R. Wheeler, *J. Electrochem. Soc.*, **160**, A306 (2013).
113. P. Albertus, J. Christensen and J. Newman, *J. Electrochem. Soc.*, **156**, A606 (2009).
114. P. M. Gomadam, D. R. Merritt, E. R. Scott, C. L. Schmidt, P. M. Skarstad and J. W. Weidner, *J. Electrochem. Soc.*, **154**, A1058 (2007).
115. A. J. Bard and L. R. Faulkner, *Electrochemical methods: fundamentals and applications*, Wiley New York (1980).
116. A. Ramos and C. Please, *arXiv preprint arXiv:1503.05912* (2015).
117. S. Prussin, *J Appl Phys*, **32**, 1876 (1961).

Appendix A

Butler-Volmer Kinetics

Sketch of derivation for Butler-Volmer kinetics is adapted from Bard and Faulkener[115] and Newman and Thomas-Alyea.[28]

One electron transfer reaction with species O and R can be expressed as

$$O + e \underset{\leftarrow \text{backward } (k_b)}{\overset{\text{forward } (k_f) \rightarrow}{=}} R . \tag{A.1}$$

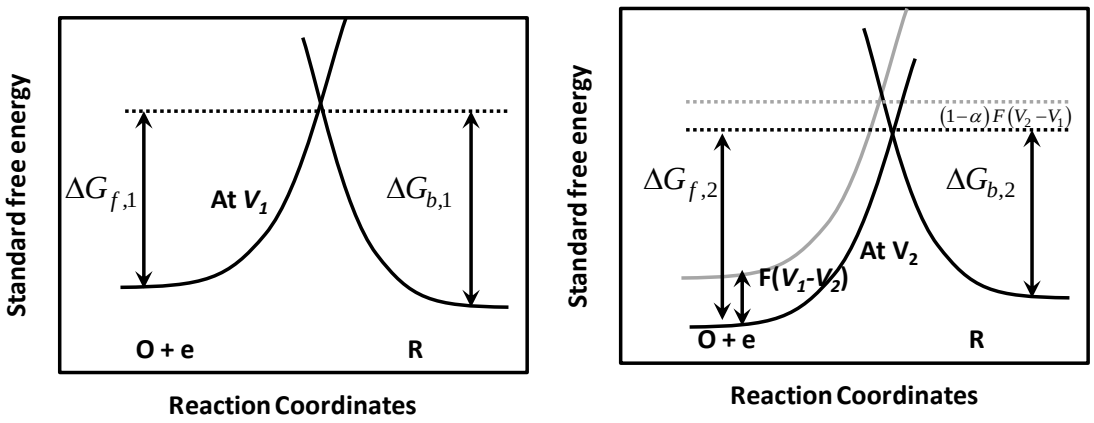

Figure A-1: Change in standard free energy of forward and backward reaction due to potential change

Left plot of Figure A-1 shows the standard free energy vs. reaction coordinates at some reference potential V_1, and the right plot shows the standard free energy curve at some other potential V_2.

From Figure A-1, the standard free energy at V_2 ($\Delta G_{f,2}$ and $\Delta G_{b,2}$) can be written in terms of standard free energy at V_1 ($\Delta G_{f,1}$ and $\Delta G_{b,1}$) using a factor of α as follows:

$$\Delta G_{f,2} = \Delta G_{f,1} + \alpha F\left(V_2 - V_1\right) \tag{A.2}$$

$$\Delta G_{b,2} = \Delta G_{b,1} - (1-\alpha) F (V_2 - V_1) \tag{A.3}$$

Assuming rate constant for forward and backward reaction follows Arrhenius form given by following equations:

$$k_f = A_f \exp\left(\frac{-\Delta G_f}{RT}\right), \tag{A.4}$$

$$k_b = A_b \exp\left(\frac{-\Delta G_b}{RT}\right). \tag{A.5}$$

Here A_f and A_b are frequency factors and ΔG_f and ΔG_b are activation barrier for forward and backward rate of reaction. The net rate of reaction at some voltage V_2 *wrt.* some reference potential V_1 can be written as:

$$r = \frac{i}{nF} = k_f c_O - k_b c_R \tag{A.6}$$

Using equations (A.2) and (A.3), the expression for net rate of reaction can be expanded as

$$r = \frac{i}{nF} = A_f c_O \exp\left(\frac{-\left(\Delta G_{f,1} + \alpha F (V_2 - V_1)\right)}{RT}\right) - A_b c_R \exp\left(\frac{-\left(\Delta G_{b,1} - (1-\alpha) F (V_2 - V_1)\right)}{RT}\right). \tag{A.7}$$

The potential dependence of rate constant can be separated as follows:

$$r = \frac{i}{nF} = k_{f^*} c_O \exp\left(-\frac{\alpha F (V_2 - V_1)}{RT}\right) - k_{b^*} c_R \exp\left(\frac{(1-\alpha) F (V_2 - V_1)}{RT}\right). \tag{A.8}$$

At some potential U, there will be zero net rate of reaction leading (i.e. equilibrium).

$$r = \frac{i}{nF} = k_{f^*} c_O \exp\left(-\frac{\alpha F \left(U - V_1\right)}{RT} \right) - k_{b^*} c_R \exp\left(\frac{\left(1-\alpha\right) F \left(U - V_1\right)}{RT} \right) = 0 \qquad \text{(A.9)}$$

Solving equation (A.9) gives

$$U - V_1 = -\frac{RT}{F} \ln\left(\frac{k_{b^*} c_R}{k_{f^*} c_O} \right) \qquad \text{(A.10)}$$

The potential difference between V_2 and V_1 can be expressed in terms of surface over-potential ($\eta = V - U$) as follows:

$$V_2 - V_1 = \left(V_2 - U\right) + \left(U - V_1\right) = \eta + \left(U - V_1\right) \qquad \text{(A.11)}$$

Using equation (A.11), equation (A.8) can be rewritten as:

$$r = \frac{i}{nF} = k_{f^*} c_O \exp\left(-\frac{\alpha F \left(\eta + \left(U - V_1\right)\right)}{RT} \right) - k_{b^*} c_R \exp\left(\frac{\left(1-\alpha\right) F \left(\eta + \left(U - V_1\right)\right)}{RT} \right) \qquad \text{(A.12)}$$

$$r = \frac{i}{nF} = k_{f^*} c_O \exp\left(-\frac{\alpha F \eta}{RT} - \frac{\alpha F \left(U - V_1\right)}{RT} \right) - k_{b^*} c_R \exp\left(\frac{\left(1-\alpha\right) F \eta}{RT} + \frac{\left(1-\alpha\right) F \left(U - V_1\right)}{RT} \right)$$

(A.13)

Using equation (A.10), this can be rewritten as:

$$r = \frac{i}{nF} = k_{f^*} c_O \exp\left(-\frac{\alpha F \eta}{RT} \right) \left(\frac{k_{b^*} c_R}{k_{f^*} c_O} \right)^{\alpha} - k_{b^*} c_R \exp\left(\frac{\left(1-\alpha\right) F \eta}{RT} \right) \left(\frac{k_{b^*} c_R}{k_{f^*} c_O} \right)^{-(1-\alpha)} \qquad \text{(A.14)}$$

$$r = \frac{i}{nF} = k_{f^*}^{1-\alpha} c_O^{1-\alpha} k_{b^*}^{\alpha} c_R^{\alpha} \left(\exp\left(-\frac{\alpha F \eta}{RT} \right) - \exp\left(\frac{\left(1-\alpha\right) F \eta}{RT} \right) \right) \qquad \text{(A.15)}$$

$$r = \frac{i}{nF} = i_o \left(\exp\left(-\frac{\alpha F \eta}{RT} \right) - \exp\left(\frac{(1-\alpha) F \eta}{RT} \right) \right), \text{ where } i_o = k_{f^*}^{1-\alpha} c_O^{1-\alpha} k_{b^*}^{\alpha} c_R^{\alpha} \qquad \text{(A.16)}$$

The equation (A.16) is also known as Butler-Volmer equation.

Appendix B

Dilute Solution Theory for Ionic Transport in Electrolyte

The following derivation is adapted from Newman and Thomas-Alyea[28] and Ramos and Please.[116] The continuity equation in any infinitesimal region can be written as for positively or negatively charged species of concentration c_i

$$\underset{\text{Accumulation}}{\frac{d}{dt}c_i} = \underset{\text{net input}}{-\nabla.N_i} + \underset{\text{Reaction}}{R_i} . \tag{B.1}$$

Here, N_i is the flux of species and R_i the rate of formation/depletion of i^{th} species. Electroneutrality will give rise to the following equation with z_i are number of charges carried by a cation or an anion:

$$\sum_i z_i c_i = 0 \tag{B.2}$$

Assuming that dissociation of one molecule leads to υ_+ and υ_- number of anions and cations:

$$\sum_i z_i \upsilon_i = 0 \tag{B.3}$$

One can define electrolyte concentration as for binary salt as

$$c = \frac{c_+}{\upsilon_+} = \frac{c_-}{\upsilon_-} . \tag{B.4}$$

Assuming dilute solution theory and ignoring convective transport, the flux expression takes the following form

$$N_i = -z_i u_i F c_i \nabla\Phi - D_i \nabla c_i . \tag{B.5}$$

u_i is mobility (average velocity of species in a solution when force 1N/mol is applied), F is Faraday's constant, Φ is electrostatic potential (V), c_i is concentration (mol/m^3), D_i is diffusion coefficient (m^2/s). For Binary salt (i = + and −), following equations can be obtained for cation and anion concentrations.

$$\frac{d}{dt} c_- = z_- u_- F \nabla.\left(c_- \nabla\Phi\right) + \nabla.\left(D_- \nabla c_-\right) + R_- \tag{B.6}$$

$$\frac{d}{dt} c_+ = z_+ u_+ F \nabla.\left(c_+ \nabla\Phi\right) + \nabla.\left(D_+ \nabla c_+\right) + R_+ \tag{B.7}$$

Using, equation (B.4), equations (B.6) and (B.7) can be expressed in electrolyte concentration.

$$\frac{d}{dt} c = z_- u_- F \nabla.\left(c \nabla\Phi\right) + \nabla.\left(D_- \nabla c\right) + \frac{R_-}{\upsilon_-} \tag{B.8}$$

$$\frac{d}{dt} c = z_+ u_+ F \nabla.\left(c \nabla\Phi\right) + \nabla.\left(D_+ \nabla c\right) + \frac{R_+}{\upsilon_+} \tag{B.9}$$

Difference of above equations will yield

$$\left(z_+ u_+ - z_- u_-\right) F \nabla.\left(c \nabla\Phi\right) + \nabla.\left(\left(D_+ - D_-\right) \nabla c\right) + \frac{R_+}{\upsilon_+} - \frac{R_-}{\upsilon_-} = 0 \tag{B.10}$$

using which, the potential variable can be eliminated from equation (B.8) resulting in

$$\frac{d}{dt}c = \nabla.\left(D'\nabla c\right) + R', \tag{B.11}$$

here

$$D' = \frac{z_+u_+D_- - z_-u_-D_+}{z_+u_+ - z_-u_-} \tag{B.12}$$

and

$$R' = \frac{z_+u_+\dfrac{R_-}{\upsilon_-} - z_-u_-\dfrac{R_+}{\upsilon_+}}{z_+u_+ - z_-u_-}. \tag{B.13}$$

Current density (A/m^2) flowing in the electrolyte is due to ions transport only; hence the net current can be expressed in terms of fluxes:

$$i_e = F\sum_i z_iN_i = F\left(z_+N_+ + z_-N_-\right) \tag{B.14}$$

Using flux expressions (equation (B.5)), equation (B.14) can be expanded as

$$i_e = -F^2\left(z_-^2u_-c_- + z_+^2u_+c_+\right)\nabla\Phi - F\left[z_+D_+\nabla c_+ + z_-D_-\nabla c_-\right]. \tag{B.15}$$

Using ionic conductivity $\kappa = F^2\left(z_-^2u_-c_- + z_+^2u_+c_+\right)$ and Nernst-Einstein relationship ($D_i = RTu_i$), equation (B.15) can be rewritten as

$$i_e = -\kappa\nabla\Phi - RTF\left[z_+u_+\upsilon_+ + z_-u_-\upsilon_-\right]\nabla c. \tag{B.16}$$

Using the definition of conductivity and transference number $\left(t_+ = z_+u_+/\left(z_+u_+ - z_-u_-\right)\right)$ for positive and negative ions, the mobility for positive and negative ions (u_+ and u_- respectively) can

be replaced from equation (B.16) to generate equation (B.22) via a number of simplification steps described below.

Using equation (B.3) ($z\_\upsilon\_ + z_+\upsilon_+ = 0$), equation (B.16) can be rearranged as

$$i_e = -\kappa\nabla\Phi - RTFz_+\upsilon_+\left[u_+ - u\_\right]\nabla c \tag{B.17}$$

or
$$i_e = -\kappa\nabla\Phi - RTFz_+\upsilon_+\left[u_+ - u\_\right]\left(\frac{\left(z\_^2u\_c\_ + z_+^2u_+c_+\right)}{\left(z\_^2u\_c\_ + z_+^2u_+c_+\right)}\right)\nabla c \tag{B.18}$$

or
$$i_e = -\kappa\nabla\Phi - \frac{RT\kappa}{F}\left[u_+ - u\_\right]\left(\frac{z_+\upsilon_+}{\left(z\_^2u\_c\_ + z_+^2u_+c_+\right)}\right)\nabla c \tag{B.19}$$

or
$$i_e = -\kappa\nabla\Phi - \frac{RT\kappa}{F}\left[u_+ - u\_\right]\left(\frac{z_+\upsilon_+}{\left(z\_^2u\_\upsilon\_ + z_+^2u_+\upsilon_+\right)}\right)\frac{\nabla c}{c} \tag{B.20}$$

or
$$i_e = -\kappa\nabla\Phi - \frac{RT\kappa}{F}\frac{\left(z_+\upsilon_+u_+ - z_+\upsilon_+u\_\right)}{\left(z\_^2u\_\upsilon\_ + z_+^2u_+\upsilon_+\right)}\frac{\nabla c}{c} \tag{B.21}$$

or
$$i_e = -\kappa\nabla\Phi - \frac{RT\kappa}{F}\left(\frac{t_+}{z_+} + \frac{t\_}{z\_}\right)\nabla \ln c \tag{B.22}$$

here

$$t_+ = \frac{z_+u_+}{\left(z_+u_+ - z\_u\_\right)} = 1 - t\_ \tag{B.23}$$

Charge balance will yield the following equation

$$-\frac{\nabla.i_e}{z_+\upsilon_+F}=\frac{R_+}{\upsilon_+}-\frac{R_-}{\upsilon_-} \tag{B.24}$$

Using equation (B.22) for expression for i_e, following equation can be obtained

$$-\nabla\left(\kappa\nabla\Phi\right)-\frac{RT}{F}\left(\frac{t_+}{z_+}+\frac{t_-}{z_-}\right)\nabla.\left(\kappa\nabla\ln c\right)=z_+\upsilon_+F\left(\frac{R_+}{\upsilon_+}-\frac{R_-}{\upsilon_-}\right) \tag{B.25}$$

For typical lithium salt ($LiPF_6$), $z_+=+1$, $z_-=-1$, $\upsilon_+=+1$, $\upsilon_-=-1$ and the fact that anion does not take part in reaction following simplified expressions can be obtained:

$$\frac{d}{dt}c=\nabla.\left(D'\nabla c\right)+\frac{1-t_+}{F}j' \tag{B.26}$$

$$-\nabla\left(\kappa\nabla\Phi\right)-\frac{RT}{F}\left(2t_+-1\right)\nabla.\left(\kappa\nabla\ln c\right)=j'. \tag{B.27}$$

Here $j'=FR_+=\nabla.i_e=\partial i_e/\partial x$ (for one dimensional case) has unit of $A/m^3/s$ and different from pore wall flux j_i ($mol/m^2/s$).

Note that these equations are given for ionic transport in electrolyte only, in porous structure current is carried by both solid phase and electrolyte phase. The total current will be given by following equation

$$i_e+i_s=I. \tag{B.28}$$

Where i_s is current in the solid phase (see (2.13)).

Appendix C

Derivation of Equations for Stresses

(adapted from Timoshenko,[75] Prussin,[117] and Cheng and Verbrugge[33])

Hook's law establishes relationship between stress (σ) and strain (ε) in one direction namely

$$\varepsilon_r = \frac{\sigma_r}{E}. \tag{C.1}$$

Where *E* is the Young's modulus. Extension in radial direction due to radial stresses is accompanied by contractions in lateral directions, i.e.

$$\varepsilon_\theta = -\nu\frac{\sigma_r}{E},\ \varepsilon_\phi = -\nu\frac{\sigma_r}{E}. \tag{C.2}$$

Here *v* is the Poisson's ratio. Similarly, stresses in other direction (σ_θ and σ_ϕ) will also create strain in all directions. As long as the strains are small enough, they can be superimposed to calculate net strain due to all stresses as follows:

$$\varepsilon_r = \frac{1}{E}\left(\sigma_r - \nu\sigma_\theta - \nu\sigma_\phi\right) \tag{C.3}$$

$$\varepsilon_\theta = \frac{1}{E}\left(\sigma_\theta - \nu\sigma_r - \nu\sigma_\phi\right) \tag{C.4}$$

$$\varepsilon_\phi = \frac{1}{E}\left(\sigma_\phi - \nu\sigma_r - \nu\sigma_\theta\right) \tag{C.5}$$

Assuming spherical symmetry ($\sigma_\theta = \sigma_\phi$ and $\varepsilon_\theta = \varepsilon_\phi$), we have the following equations:

$$\varepsilon_r = \frac{1}{E}\left(\sigma_r - 2\nu\sigma_\theta\right) \tag{C.6}$$

$$\varepsilon_\theta = \frac{1}{E}\left((1-\nu)\sigma_\theta - \nu\sigma_r\right) \tag{C.7}$$

In the presence of the guest molecule, the composition dependent strain can be modeled in a similar fashion as temperature induced stresses.[75]

$$\varepsilon_r = \frac{1}{E}\left(\sigma_r - 2\nu\sigma_\theta\right) + \frac{\Omega c}{3} \tag{C.8}$$

$$\varepsilon_\theta = \frac{1}{E}\left((1-\nu)\sigma_\theta - \nu\sigma_r\right) + \frac{\Omega c}{3} \tag{C.9}$$

Here Ω is partial molar volume and *c* is the solute concentration (lithium, in case of lithium-ion battery).

Infinitesimal strain theory can be used to derive the relationship between local displacement *u* and strain in radial and tangential direction assuming spherical symmetry. (i.e. $\varepsilon_r = \partial u/\partial r$ and $\varepsilon_\theta = u/r$)

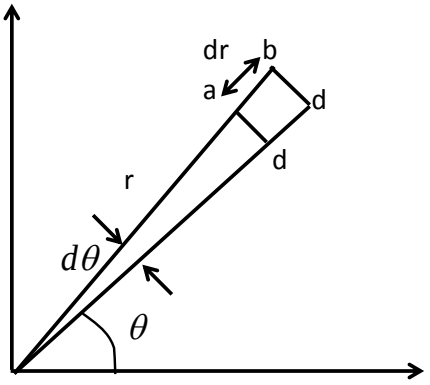

Figure C-1: Infinitesimal element method for relation between displacement and strain

Consider the *ad* branch of *abcd* loop (Figure C-1). The radial displacement of *ad* branch is $u(r)$, whereas for *bd* it is $u+\left(\partial u/\partial r\right)dr$. Hence radial strain can be calculated as:

$$\varepsilon_r = \frac{\left[u+\left(\partial u/\partial r\right)dr\right]-u}{dr} = \frac{\partial u}{\partial r} \tag{C.10}$$

Similarly, *ad* branch can be considered to calculate tangential strain. The original length of *ad* branch is $rd\theta$, after displacement u in the radial direction it is $\left(r+u\right)d\theta$. Hence the tangential strain is

$$\varepsilon_\theta = \frac{\left[\left(r+u\right)d\theta\right]-\left[rd\theta\right]}{rd\theta} = \frac{u}{r} \tag{C.11}$$

The condition of mechanical equilibrium without the presence of any body force is considered for polar coordinates in Figure C-2 (for spherical coordinates, the final form will differ by a factor of 2), for simplicity, only normal stresses are considered here.

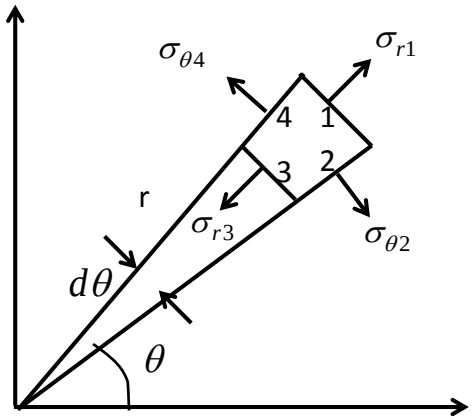

Figure C-2: Mechanical equilibrium without body force in polar coordinates

In the radial direction the mechanical balance will give rise to the following equation:

$$\sigma_{r_1} r_1 d\theta - \sigma_{r_3} r_3 d\theta - \left(\sigma_{\theta_2} (r_1 - r_3) \frac{d\theta}{2} + \sigma_{\theta_4} (r_1 - r_3) \frac{d\theta}{2} \right) = 0 \tag{C.12}$$

Assuming infinitesimally small element, the equation will simplify to

$$\frac{(\sigma r)_1 \, d\theta - (\sigma r)_3 \, d\theta - \left(\sigma_{\theta_2} dr \frac{d\theta}{2} - \sigma_{\theta_4} dr \frac{d\theta}{2} \right)}{dr d\theta} = 0 \tag{C.13}$$

$$\frac{\partial (\sigma_r r)}{\partial r} - \sigma_\theta = 0 \tag{C.14}$$

$$\frac{\partial \sigma_r}{\partial r} + \frac{(\sigma_r - \sigma_\theta)}{r} = 0 \tag{C.15}$$

For spherical coordinates, the equation is

$$\frac{\partial \sigma_r}{\partial r} + 2\frac{(\sigma_r - \sigma_\theta)}{r} = 0 \, . \tag{C.16}$$

Equation (C.8), (C.9), (C.10), (C.11), and (C.16) constitute second order differential equation in *u* (given by equation (C.17)) which can be solved by posing two boundary conditions that *u* is zero at center and radial stress is zero at the radius of the particle (hint: substitute $u = u'/r^2$ to simplify).

$$\frac{d^2}{dr^2} u + \frac{2}{r} \frac{du}{dr} - 2\frac{u}{r^2} = \frac{1+v}{1-v} \frac{\Omega}{3} \frac{dc}{dr} \tag{C.17}$$

Following expressions are obtained for radial and tangential stresses after solving the equation (C.17).

$$\hat{\sigma}_r = \frac{3\sigma_r}{\left(\frac{\Omega E}{(1-\nu)}\right)} = \frac{2}{3}\left(\int_0^1 c\ \xi^2 d\xi - \frac{1}{\xi^3}\int_0^{\xi} c\ \xi^2 d\xi\right) \tag{C.18}$$

$$\hat{\sigma}_\theta = \frac{3\sigma_\theta}{\left(\frac{\Omega E}{(1-\nu)}\right)} = \left(2\int_0^1 c\ \xi^2 d\xi + \frac{1}{\xi^3}\int_0^{\xi} c\ \xi^2 d\xi - c\right) \tag{C.19}$$